



**University of Calgary**

**PRISM: University of Calgary's Digital Repository**

---

Graduate Studies

The Vault: Electronic Theses and Dissertations

---

2021-05-07

# Aerodynamic Performance and Starting Behavior of Multi-Bladed Waterpumping Windmills

John, Itoje Harrison

---

John, I. H. (2021). Aerodynamic Performance and Starting Behavior of Multi-Bladed Waterpumping Windmills (Unpublished doctoral thesis). University of Calgary, Calgary, AB.  
<http://hdl.handle.net/1880/113405>  
doctoral thesis

---

University of Calgary graduate students retain copyright ownership and moral rights for their thesis. You may use this material in any way that is permitted by the Copyright Act or through licensing that has been assigned to the document. For uses that are not allowable under copyright legislation or licensing, you are required to seek permission.

*Downloaded from PRISM: <https://prism.ucalgary.ca>*

UNIVERSITY OF CALGARY

Aerodynamic Performance and Starting Behavior of Multi-Bladed Waterpumping  
Windmills

by

Itoje Harrison John

A THESIS  
SUBMITTED TO THE FACULTY OF GRADUATE STUDIES  
IN PARTIAL FULFILLMENT OF THE REQUIREMENTS FOR THE  
DEGREE OF DOCTOR OF PHILOSOPHY

GRADUATE PROGRAM IN MECHANICAL AND MANUFACTURING ENGINEERING

CALGARY, ALBERTA

MAY, 2021

© Itoje Harrison John 2021

# Abstract

Windmills for waterpumping typically operate at low speed and high torque owing to their multi-bladed nature. This low Reynolds number,  $Re$ , operation, however, complicates the rotor aerodynamic behavior due to the mutual interaction between adjacent blades. While studies on aerodynamic and starting performance of windmills indicate that increasing blade number and airfoil type are critical analysis and design parameters, the low  $Re$  behavior of the commonly used cambered blades is still poorly understood.

Accordingly, the rotor performance and starting behavior of a cambered, multi-bladed, waterpumping windmill were experimentally and analytically investigated at low tip speed ratios using three-, six-, twelve-, and twenty-four-bladed rotor configurations based on Wegereef's 1984 blade profile. Comprehensive wind tunnel testings were performed to provide accurate airfoil data at flow conditions typical of the low  $Re$  and high angles of attack experienced by windmills during starting. Implementation of the blade element momentum (BEM) with a generally more accurate, helical vortex theory-based tip loss function or otherwise "finite blade function" for very low speed wind turbines other than the commonly used Prandtl tip loss factor provided insights on the blade elements performance and subsequently, the global performance parameters.

Wind tunnel and theoretical studies showed that design parameters not limited to solidity impact the rotor performance and starting behavior. Increasing the blade number improves the rotor performance coefficients and starting performance by reducing idling time. Generally, there is good agreement between the wind tunnel measurement results and BEM prediction for the range of tip speed ratio considered, except below the optimal tip speed ratio region. In that region, discrepancies due to solidity effects unaccounted for in the BEM prediction were observed and shown to increase with blade number.

The impact of blockage was examined with both low and high blockage wind tunnels and found to be significant. For a given rotor model and varying wind tunnel areas, the blockage effects increase with solidity. Overall, the experiment provided better performance,

highlighting the importance of accounting for high solidity in low wind speed aerodynamic performance prediction. Useful preliminary guides are proposed to optimize the windmill rotor design.

# Acknowledgements

First and foremost, I would like to thank my supervisor, Prof. David Wood, for his unflinching support, profound guidance, and all-around encouragement. His uncommon patience and understanding during the numerous crises in this study were invaluable. His willingness to go the extra mile to help and make himself available for insightful discussions is an excellent source of inspiration to both my research and personal life. The time spent together at TU Delft to resolve blockage effect on small wind turbine performance measurements is invaluable and taught me the humane personae perspective of him outside academics.

I am indebted to the Niger Delta Development Company (NDDC), Nigeria, for sponsoring the first three years of my study and, again, Prof. David Wood for funding the subsequent years through the Schulich Endowment Fund. Thanks are also due to Profs. Gerard van Bussel and Nando Wimmer, both of TU Delft, for making their Open Jet Facility wind tunnel available for testing and to Sam Cawthorne-Nugent and the technical staff for helping out with the experiment.

To my fellow research colleagues, particularly the LTRAC team, too numerous to mention, thank you for all your assistance in the laboratory as well as the conviviality you injected into the whole Ph.D. work. Special thanks to you, Ayman Ashry, for the valuable suggestions and ideas and for helping out with the airfoil measurement. Thanks also to Professor Jerson Vaz of the Faculty of Mechanical Engineering, Institute of Technology, Federal University of Pará, for introducing me to the use of the laboratory during his time at the University of Calgary.

To all the summer intern students whose paths crossed with mine, I say thank you. The support of the technical staff of the Schulich School of Engineering, University of Calgary, is well appreciated.

The final thank you belongs to my family and friends for their tremendous encouragement and support. I want to wholeheartedly thank my wife, Salome, for her steadfast love and standing by me throughout the program. I owe in-depth gratitude to my adorable daughters, Ogheneruno and Oghenemaro, born during the study. The beautiful destressing moments and their innocently understanding my not being fully available to play the role of daddy are cherished. To members of the Nigerian community, both at the University of Calgary and the City of Calgary, thank you for the fun-filled and incredible social activities and moments during the years of this research.

*Dedicated to the loving memories of my father and uncle, Neworld John Itoje and Samson  
Oghenebrorie Itoje*

# Table of Contents

<b>Abstract</b>	ii
<b>Acknowledgements</b>	iv
<b>Dedication</b>	vi
<b>Table of Contents</b>	vii
<b>List of Figures and Illustrations</b>	x
<b>List of Tables</b>	xv
<b>List of Symbols, Abbreviations, and Nomenclature</b>	xvi
<b>1 Introduction</b>	1
1.1 A case for decentralized sustainable energy supply systems . . . . .	1
1.2 Context of current research . . . . .	6
1.3 Problem statement . . . . .	7
1.4 Thesis objectives . . . . .	11
1.5 Thesis structure . . . . .	11
<b>2 Overview of Waterpumping Windmill</b>	13
2.1 Types of wind turbines and its application . . . . .	13
2.2 Large (LWTs) and small (SWTs) wind turbines . . . . .	15
2.2.1 Wind-powered waterpumping technologies . . . . .	16
2.3 Literature review . . . . .	19
2.3.1 Aerodynamic characteristics of waterpumping windmill blades . . . . .	19
2.3.2 Windmill performance . . . . .	25
2.3.3 Starting behavior of SWTs . . . . .	28
2.4 Summary . . . . .	31
<b>3 Airfoil Experimentation</b>	33
3.1 Low Reynolds number airfoils and high incidence . . . . .	33
3.1.1 Aerodynamics of low Reynolds number airfoils . . . . .	35
3.2 Airfoils for SWTs . . . . .	36
3.3 Test setup and airfoil models . . . . .	37

3.4	Measurement of static and dynamic aerodynamic forces . . . . .	42
3.5	Experimental uncertainty analysis . . . . .	46
3.6	Wind tunnel boundary corrections . . . . .	48
3.7	Steady aerodynamic performance . . . . .	53
3.7.1	NACA0012 performance . . . . .	54
3.7.2	Effect of Reynolds number on circular-arc airfoils . . . . .	59
3.7.3	Effect of thickness, camber, aspect ratio and tunnel-blockage on CAAs	62
3.7.4	Circular-arc airfoils hysteresis . . . . .	67
3.8	Unsteady aerodynamic performance . . . . .	68
3.9	Summary . . . . .	71
<b>4</b>	<b>Rotor Aerodynamic Performance Prediction</b>	<b>76</b>
4.1	Introduction . . . . .	77
4.2	Actuator disk model . . . . .	78
4.3	Rotor disk model . . . . .	84
4.4	Blade element theory (BET) . . . . .	87
4.5	Blade element momentum theory (BEM) . . . . .	90
4.6	BEM implementation . . . . .	91
4.7	Finite blade function (Tip and root loss factors) . . . . .	92
4.7.1	Helical vortex theory for tip and root loss . . . . .	93
4.8	Simulated windmill . . . . .	96
4.8.1	Blade element computations . . . . .	97
4.9	Concluding remarks . . . . .	108
<b>5</b>	<b>Starting Analysis</b>	<b>112</b>
5.1	Aerodynamic starting model . . . . .	112
5.1.1	Model description . . . . .	113
5.2	Starting calculations and results . . . . .	117
5.2.1	Starting performance . . . . .	119
5.2.2	Validity of negligible induction in BEM starting analysis . . . . .	123
5.2.3	Effect of increasing blade number on starting performance and runaway conditions . . . . .	124
5.2.4	Effect of unsteadiness . . . . .	127
5.2.5	Effect and sensitivity of starting to pitch angle variation . . . . .	130
5.2.6	Concluding remarks . . . . .	132
<b>6</b>	<b>Windmill and Tunnel Blockage Experimentation</b>	<b>133</b>
6.1	Experimental facilities . . . . .	133
6.1.1	University of Calgary Red Wind Tunnel . . . . .	134
6.1.2	TU Delft Open Jet Facility . . . . .	135
6.2	Experimental setup and measurements . . . . .	135
6.2.1	Windmill experimental model . . . . .	135
6.2.2	Measured parameters and instrument calibration . . . . .	137
6.2.3	Windmill performance experiment . . . . .	145
6.2.4	Starting experiment . . . . .	149

6.2.5	Measurement uncertainty . . . . .	149
6.3	Blockage in open jet wind tunnel (OJT) . . . . .	150
6.3.1	Blockage effect assessment and correction . . . . .	151
<b>7</b>	<b>Windmill and Blockage Experimental Results</b>	<b>154</b>
7.1	Aerodynamic performance . . . . .	154
7.1.1	BEM comparison to Wegereef 1984 and OJF experiments . . . . .	154
7.1.2	BEM Comparison to RWT and OJF experiments . . . . .	157
7.2	Blockage effect on flat disks/plate and windmill rotor . . . . .	160
7.3	OJF experimental starting performance . . . . .	163
7.3.1	Rotor starting performance with different blade numbers . . . . .	166
7.4	Preliminary design considerations for waterpumping windmills optimization .	167
7.5	Summary . . . . .	170
<b>8</b>	<b>Conclusions and Recommendations</b>	<b>171</b>
8.1	Conclusions . . . . .	171
8.2	Significant and original contributions . . . . .	174
8.3	Future work . . . . .	175
<b>Bibliography</b>		<b>177</b>
<b>A Lift and drag coefficients of NACA0012 and Circular-Arc airfoils (CA) series</b>		<b>194</b>
<b>B Drivetrain resistance model</b>		<b>209</b>
<b>C Contribution of the spars to the windmill blade's thrust and torque</b>		<b>213</b>
C.1	Thrust calculation . . . . .	213
C.2	Torque calculation . . . . .	214

# List of Figures and Illustrations

1.1	Population without electricity access. Reproduced from [5] (accessed 5 Sep 2020). . . . .	3
1.2	Human Development Index values, by country grouping, 1990–2017. Reproduced from [7](accessed 5 Sep 2020). . . . .	4
1.3	Small wind turbine global installed capacity. Data from World Wind Energy Association [9] and Statista [14] (accessed 5 Sep 2020). . . . .	4
1.4	Traditional windmills. . . . .	8
1.5	Typical windmill blade:circular arc sheet metal with spars (supporting tubes) [29]. . . . .	9
1.6	Circular-arc airfoil geometrical profile. $c$ = chord, $t$ = thickness, $h$ = camber, $LE$ = leading edge, $TE$ = trailing edge, $\alpha$ = angle of attack and $U_\infty$ = freestream wind speed. . . . .	10
2.1	Vestas V112 3 MW, 3-bladed rotor [40]. . . . .	14
2.2	VAWTs (a) Drag-driven (b) and (c) Lift-driven [40]. . . . .	14
2.3	Schematic of typical wind pumps. Reproduced from [43]. . . . .	18
2.4	Effect of curvature on the aerodynamic characteristics of a rectangular aluminum foil model airfoil with $t = 0.3$ mm and $c = 30$ mm. Each symbol refers to a different camber, as shown in the panel on the figure. Reproduced from [54]. . . . .	22
2.5	Performance of 10% cambered 2% thick steel plate with and without spars at the 50% chord position. $Re$ indicated in legend. Extracted from [26]. . . . .	24
2.6	Tip vortices trailing from a model wind turbine in the DNW 9.5 × 9.5 m wind tunnel ( <a href="http://www.mexnext.org/">http://www.mexnext.org/</a> ). . . . .	27
2.7	Starting of Speedovane in varying wind speeds and computed starting torque coefficients, ( $C_{d0}$ ) [101]. . . . .	30
3.1	Operating path of a 3-bladed waterpumping windmill model. . . . .	35
3.2	Typical airfoil separation characteristics at different regimes of $Re < 10^6$ . Adapted from [106]. . . . .	36
3.3	Red wind tunnel working section (upstream view). . . . .	38
3.4	Schematic of tunnel. . . . .	38
3.5	Experimental set up of airfoil performance measurement. The acrylic side plates were used to form the closed jet tunnel (CJT) working sections and removed for the open jet tunnel (OJT) tests. . . . .	39
3.6	CAA models and profile configuration. . . . .	40

3.7	SolidWorks designed and assembled airfoil sections. . . . .	41
3.8	Open jet tunnel test section with airfoil model. . . . .	44
3.9	Modified open tunnel test section with airfoil model. . . . .	44
3.10	Force coefficients system. . . . .	45
3.11	$C_A$ , $C_N$ , $C_l$ and $C_d$ measurements and their uncertainty for CA1705 at $Re = 1.0 \times 10^5$ in the open test section. . . . .	48
3.12	NACA0012: Wind tunnel uncorrected and corrected lift and drag data for $Re = 1.5 \times 10^5$ . . . . .	53
3.13	$C_l$ and $C_d$ vs $\alpha$ for NACA0012 airfoil study in OJT and CJT sections alongside those reported by Sheldahl and Klimas [64], Rainbird et al. [65] and Worasinchai et al. [67]. The insets represent a magnified and detailed view for a limited range of $0^\circ \leq \alpha \leq 20^\circ$ . . . . .	57
3.14	Open jet tunnel measurements of NACA0012. . . . .	58
3.15	Closed jet tunnel measurements of NACA0012. . . . .	59
3.16	Relationship between $C_l$ and $C_d$ at second stall region for NACA0012. . . . .	60
3.17	$C_l$ and $C_d$ of CA1705 without spar (clean model). . . . .	61
3.18	$C_l$ and $C_d$ of CA1705 with spar. . . . .	62
3.19	Effect of camber, thickness, aspect ratio, tunnel-blockage on lift and drag of the clean CAA in open tunnel condition. . . . .	63
3.20	Effect of camber and thickness on lift and drag of the CAA with spar in the OJT. . . . .	64
3.21	Effect of camber, thickness, aspect ratio, tunnel-blockage on lift and drag of the CAAs compared with Bruining [26] data with no wind tunnel correction applied and labeled “BR” in closed tunnel condition, all at $Re = 6 \times 10^4$ . . .	65
3.22	Effect of camber, thickness, aspect ratio and tunnel-blockage on lift and drag of the CAAs compared with Bruining [26] data with no wind tunnel correction applied and labeled “BR” in a closed tunnel condition, all at $Re = 10^5$ . . .	65
3.23	Lift-to-drag of the circular-arc airfoil compared with uncorrected Bruining [26] data in a closed tunnel condition. . . . .	66
3.24	Hysteresis of $C_l$ and $C_d$ curve for the clean CA1705 in an open jet flow condition. . . . .	68
3.25	Hysteresis of $C_l$ and $C_d$ curve for the CA1705 with spar in an open jet flow condition. . . . .	68
3.26	Unsteady response of CA1604 at $Re = 0.6 \times 10^5$ and $10^5$ ( $\alpha = 45^\circ + 45^\circ \sin 0.02\tau$ ). Error bars represent one standard deviation of the mean force measurements over 5 cycles. . . . .	70
3.27	Effect of reduced frequency, $k$ on the lift coefficient at $Re = 0.6 \times 10^5$ for the clean CA1604 in an open tunnel condition: $\alpha = 45^\circ + 45^\circ \sin k\tau$ . Black arrows shows the pitch-up direction of the unsteady loops. . . . .	72
3.28	Effect of reduced frequency, $k$ on the lift coefficient at $Re = 10^5$ for the clean CA1604 in open tunnel condition: $\alpha = 45^\circ + 45^\circ \sin k\tau$ . Black arrows shows the pitch-up direction of the unsteady loops. . . . .	73
4.1	Flowfield of a wind turbine. Adapted from [136]. . . . .	78
4.2	Flowfield of an actuator disk. Adapted from [136]. . . . .	79

4.3	Pressure and wind speed variation through an axi-symmetric streamtube. Reproduced from [1]. . . . .	80
4.4	Variation of $C_p$ and $C_T$ with $a$ for an ideal, horizontal-axis wind turbine, extracted from [86]. . . . .	83
4.5	Rotor flow states and validity of actuator disk theory. Reproduced from [1]. . . . .	84
4.6	Illustration of the flow downstream of the rotating disk. . . . .	86
4.7	Rotor disk annulus. . . . .	86
4.8	BET force system, extracted from [1]. . . . .	88
4.9	Illustration of velocity and aerodynamic force/torque triangles on a blade element. Extracted from [1]. . . . .	89
4.10	Experimental rotor blade configuration. . . . .	98
4.11	Blade profile of experimental model (extracted from [23]). . . . .	98
4.12	Lift and drag coefficients of the model windmill blade CA1705 section. . . . .	99
4.13	Predicted performance compared to the measurements of Anderson et al. [141], $\square$ , BEM without tip loss; +, BEM with conventional tip loss; *, BEM with modified tip loss. Reproduced from [78]. . . . .	100
4.14	Computed power coefficient compared to TU Delft OJF experimental measurements. Experimental results are in blue. The conventional Prandtl tip loss (CTL) in red and modified tip loss (MTL) in black. . . . .	101
4.15	Computed torque coefficient compared to TU Delft OJF experimental measurements. Experimental results are in blue. The CTL in red and MTL in black. . . . .	102
4.16	Computed thrust coefficient compared to TU Delft OJF experimental measurements. Experimental results are in blue. The CTL in red and MTL in black. . . . .	103
4.17	Blade element performance parameters for $N = 3$ at $\lambda = 1$ . . . . .	104
4.18	Blade element performance parameters for $N = 6$ at $\lambda = 1$ . . . . .	105
4.19	Blade element performance parameters for $N = 12$ at $\lambda = 1$ . . . . .	106
4.20	Blade element performance parameters for $N = 24$ at $\lambda = 1$ . . . . .	107
4.21	Predicted velocity through the rotors for the MTL function. . . . .	108
4.22	Modified tip loss functions. . . . .	109
4.23	Predicted blade circulation of the MTL. . . . .	110
4.24	Predicted distribution of blade element torque and thrust of MTL. . . . .	111
5.1	Illustration of windmill drivetrain and rotor system. . . . .	114
5.2	$C_l$ & $C_d$ for CA2010 without spar, $Re = 6 \times 10^4$ . . . . .	117
5.3	Airfoil performance characteristics. . . . .	119
5.4	Angle of attack variation. . . . .	120
5.5	Reynolds number variation. . . . .	121
5.6	Aerodynamic and drivetrain resistive torque variation. . . . .	122
5.7	Predicted and measured rotational speed for $N = 3$ . . . . .	122
5.8	Starting behavior along the blade span. . . . .	123
5.9	Kinetic energy ratio variation with time at constant wind speed of 6 m/s. . . . .	124
5.10	Comparison of rotational speeds. . . . .	126
5.11	Drivetrain resistive, $Q_R$ and aerodynamic, $Q$ torque of the rotors. . . . .	126

5.12	Drivetrain resistive, $C_{QR}$ and aerodynamic, $C_Q$ torque coefficients of the rotors.	127
5.13	Variation of angle of attack with $Re$ for all rotors.	128
5.14	Spanwise distribution of $a$ for all $N$ for blade elements at the root and tip.	128
5.15	Variation of net torque with time.	129
5.16	Variation of net torque with RPM.	129
5.17	Blade tip pitch rate.	131
5.18	Rotor speed for $N = 3$ with varying pitch angles and no induction.	131
6.1	University of Calgary Red Wind Tunnel (open jet).	134
6.2	TU Delft open jet facility.	136
6.3	24-bladed waterpumping windmill setup in the RWT.	137
6.4	6-bladed waterpumping windmill setup in the OJF measurement section.	138
6.5	Windmill setup in the RWT modified to include a torque sensor.	139
6.6	RWT speed calibration curve.	140
6.7	RWT velocity profile (m/s) operating at 57 Hz measured in the current study.	140
6.8	RWT F/T transducer axis system (F and M represent the force and moments respectively) Retrieved from <a href="https://www.ati-ia.com/products/ft/ft_models.aspx?id=Delta">https://www.ati-ia.com/products/ft/ft_models.aspx?id=Delta</a> [Access date:21-Nov-2019].	142
6.9	OJF F/M axis system (BC is the balance reference center, while F and M represent the force and moments respectvly. Source: OJF external force balance documentation).	143
6.10	MPB70 cross section view.	144
6.11	Modified experimental windmill rotor setup.	146
6.12	Torque calibration curves.	147
6.13	MPB torque calibration against RPM at various input currents for 0–10 V.	147
6.14	Drag measurement in RWT test section. Shown is the circular disk of $\phi=50$ cm.	153
7.1	BEM power coefficient compared to the measurements made by Wegereef and in the OJF.	155
7.2	BEM torque coefficient compared to the measurements made by Wegereef and in the OJF.	155
7.3	Predicted and measured performance of a high solidity, delta wing-bladed rotor, [27].	158
7.4	BEM and measured power coefficient with no blockage correction applied to the RWT results.	158
7.5	BEM and measured torque coefficient with no blockage correction applied to the RWT results.	159
7.6	BEM and measured thrust coefficient with no blockage correction applied to the RWT results.	160
7.7	Drag coefficients of simple geometries at varying distance from the RWT exit.	162
7.8	BET and measured power coefficient with correction applied to the RWT results.	164
7.9	BET and measured torque coefficient with correction applied to the RWT results.	165

7.10 BET and measured thrust coefficient with correction applied to the RWT results. . . . .	165
7.11 Model experimental rotor speed at constant wind speeds. . . . .	167
7.12 Comparison of rotational speeds at different winds speeds. Red lines show $U_{\infty}=5$ m/s, blue lines show $U_{\infty}=10$ m/s, black lines show $U_{\infty}=15$ m/s, the solid line shows $N = 3$ , the dash-dot line shows $N = 6$ , the dotted line shows $N = 12$ and the dashed line shows $N = 24$ . . . . .	168
7.13 Comparison of rotational speeds with rotor experiment at constant wind speed.	169
B.1 Schematic of a generalized Stribeck curve. . . . .	211

# List of Tables

1.1	Comparison of small wind turbine and solar PV technologies. Adapted from [4].	6
1.2	Comparison of horizontal axis rotor types. Extracted from Practical Action, [28] (accessed 5 Jan 2018).	9
2.1	Comparison of small and large wind turbines. Adapted from [33].	16
2.2	Summary of some research on circular-arc airfoils and flat plates.	20
2.3	Important aerodynamic parameters of cambered steel plates. Sourced from [53].	23
2.4	Result of CAA performance at $Re = 10^5$ . The first column shows when a spar was used and its position with respect to blade chord. Reproduced from [26].	23
3.1	Airfoil models and geometry.	40
3.2	Summary of airfoil experimental tests.	42
3.3	Uncertainty measurements values for elemental and propagated error sources.	48
3.4	Summary of NACA0012 studies referenced.	55
5.1	Mass moment of inertia and solidity of rotors.	115
5.2	Starting performance of rotors.	125
6.1	Characteristics of wind tunnels.	133
6.2	ATI Delta SI-330-30 range, resolution and uncertainty. Retrieved from ATI [Access date:21-Nov-2019].	141
6.3	OJF external balance load range. Source: OJF external force balance documentation	143
6.4	MPB70 specifications and coil data.	144
6.5	Uncertainty in windmill experimental measurements.	150
6.6	Characteristics of flat plate and thin disks.	153
7.1	Comparison of OJF and BEM torque and power coefficients.	157
7.2	Starting and running speeds of rotors under no-load.	164
B.1	Drivetrain resistance model parameters	212

# List of Symbols, Abbreviations, and Nomenclature

## Symbols

$a$	Axial induction factor
$A$	Blade/rotor swept area ( $\text{m}^2$ )
$a'$	Tangential/circumferential induction factor
$A_c$	Airfoil cross-sectional area ( $\text{m}^2$ )
$b$	Blade span (m)
$B_R$	Blockage factor
$c$	Airfoil/blade chord (m)
$C_A$	Axial force coefficient
$C_d$	Drag coefficient
$C_l$	Lift coefficient
$C_M$	Quarter-chord moment coefficient
$C_N$	Normal force coefficient
$C_p$	Power coefficient
$C_Q$	Torque coefficient
$C_T$	Thrust coefficient
$D$	Drag (N)
$F$	Force per unit span (N/m)
$F_A$	Axial force per unit span (N/m)
$f_n$	Natural frequency (Hz)
$F_N$	Normal force per unit span (N/m)
$F_p$	Prandtl tip loss factor
$F_U$	Axial finite blade function
$f_v$	Vortex shedding frequency (Hz)
$F_W$	Tangential finite blade function
$h$	Airfoil camber (m)
$H$	Tunnel height (m)
$J$	Rotor inertia ( $\text{kNm}^2$ )
$k$	Reduced frequency
$k_{\alpha,tip}$	Tip pitch rate
$L$	Lift (N)
$M$	Mach number
$N$	Blade number

$p$	Vortex pitch (m)
$Q$	Torque (Nm)
$r$	Blade radius (m)
$R$	Tip blade radius (m)
$Re$	Reynolds number
$t$	Airfoil thickness (m)
$T$	Thrust (N)
$t$	Time (s)
$t$	Vortex radius (m)
$U_\infty$	Free stream wind speed (m/s)
$U_{wb}$	Streamtube average axial velocity at the blade
$U_c$	Cut-in wind speed (m/s)
$U_R$	Uncertainty in measurement result
$U_s$	Starting wind speed (m/s)
$U_T$	Total or effective velocity (m/s)
$w_{wb}$	Streamtube average tangential velocity at the blade
$X$	Axial distance from tunnel exit (m)

### Greek symbols

$\alpha$	Angle of attack (deg)
$\alpha_a$	Amplitude of sinusoidal motion (deg)
$\alpha_m$	Mean of sinusoidal motion (deg)
$\beta$	Prandtl-Glauert factor
$\beta$	Total blade pitch angle (rad)
$\Gamma$	Circulation ( $m^2/s$ )
$\lambda$	Tip speed ratio
$\lambda_r$	Local tip speed ratio
$\mu$	Dynamic viscosity of air (kg/m/s)
$\nu$	Kinematic viscosity of air ( $m^2/s$ )
$\Omega$	Rotor angular speed (rad/sec)
$\omega$	Swirl angular speed (rad/sec)
$\omega_p$	Frequency of oscillation (Hz)
$\phi$	Inflow angle, phase of sinusoidal motion (rad)
$\rho$	Density ( $kg/m^3$ )
$\sigma$	Solidity
$\tau$	Reduced time
$\theta_s$	Separation blockage factor
$\theta_p$	Blade twist angle (rad)
$\varepsilon_{sep}$	Separation blockage
$\varepsilon_T$	Total blockage
$\varepsilon_s$	Solid blockage
$\varepsilon_w$	Wake blockage

### Abbreviations

BE	Blade Element
BET	Blade Element Theory
CAA	Circular-Arc Airfoils

CJT	Closed Jet Tunnel (Modified open tunnel)
CTL	Convectional Prandtl tip loss factor
HAWTs	Horizontal Axis Wind Turbines
KER	Kinetic Energy Ratio
LSB	Laminar Separation Bubble
LWTs	Large Wind Turbines
MTL	Modified Tip Loss factor
OJF	Open Jet Facility
OJT	Open Jet Tunnel (the RWT without side and top walls)
RWT	Red Wind Tunnel
SWTs	Small Wind Turbines
VAWTs	Vertical Axis Wind Turbines

# **Chapter 1**

## **Introduction**

In view of the global quest for sustainable energy systems, a case is advanced for small, decentralized, stand-alone energy supplies as alternatives to the conventional centralized grid system in this study. Rather than electrical power generation, direct mechanical power derivable from wind is suggested. It is argued that small-scale wind turbines (SWTs), such as the typical waterpumping windmill, are critical for engendering a carbon-free economy as well as enduring sustainable development for future generations, especially in developing countries. Against this backdrop, this thesis studies the rotor aerodynamic and starting behavior of waterpumping windmills with a range of blade numbers with the intent of improving their performance, motivated by their inherent simplicity in design and low cost manufacturing and the potential for performance improvement.

### **1.1 A case for decentralized sustainable energy supply systems**

The most critical challenge facing the human race is the stewardship of energy, food, and water owing to fast-depleting natural resources, the increasing anthropogenic impact on the environment, and the rising global population [1]. In recognition of this, the United Nations

(UN) proposed a blueprint tagged the “UN 2030 Agenda for Sustainable Development”, which was subsequently adopted by its member states in 2015 to address these and other related challenges using a holistic and integrative approach. At its heart are 17 actionable plans called the Sustainable Development Goals (SDG), wherein goals 7, 2, and 6 addressed energy, food, and water, respectively [2].

Energy and its services are crucial to enhancing human health and well-being and a country’s economic development [3,4]. However, access to energy in its most versatile form-electricity, is still a huge challenge in developing countries. Even with the growing increase in electricity supply, an estimated 13% of the world population do not have access to electricity [5], of whom 95% reside in sub-Saharan Africa and developing Asia, see Figure 1.1. As shown in the figure, around 80% of the developing countries’ populace dwell in rural areas. It is, therefore, not a coincidence that sub-Saharan Africa and developing Asia are ranked low in the human development index <sup>1</sup> (HDI) values. Viewing Figures 1.1 and 1.2 together show the nexus between access to energy and HDI. To further exacerbate the situation, many of these remote communities lack connection to the existing electrical grid and grid extension, which in many cases may not be economical due to inaccessible terrain and inefficient transmission lines. Hence, decentralized small-scale power energy sources such as solar, wind, and biomass are realistic options that can potentially provide people in rural areas access to energy services from their natural resources.

Given that wind energy is now one of the world’s fastest-growing renewable energy sources [8], it is expected to play a significant role in sustainable energy supply systems now and in the future. Indeed, wind turbine technology has proven to be promising in addressing the urgent need for sustainable energy and mitigating the apparent dangers of relying on transported energy sources. While large or utility wind turbines constitute the bulk of installed wind energy plants worldwide, they are of no benefit to rural locations not connected to the

---

<sup>1</sup>The Human Development Index (HDI) measures the average achievement in key dimensions of human development: a long and healthy life, access to education and a decent standard of living. The HDI is the geometric mean of normalized indices for each of the three dimensions [6].

grid. However, SWTs undoubtedly offer one of the most environmentally benign and cost-competitive technologies to expand access to energy services in remote areas. Also, they are very suitable for grid and building-integrated applications. The diverse use of SWT is evidenced by the relatively sustained growth in capacity from 2010 to 2018, except for a momentary drop in 2017, as illustrated in Figure 1.3. As of 2011, over 330 small wind manufacturers concentrated mainly in China, North America, and several European countries have been identified with the developing nations only playing a small role in the manufacture of SWTs [9]. Sadly, the locations of these manufacturing companies in favor of developed countries have created a barrier to the adoption of this technology in growing economies. Notwithstanding, some professional manufacturers, such as Kijito in Kenya [10], Jober in Colombia [11], Aureka in India [12] and Poldaw in the UK [13], focus on the developing world. A significant aspect of this work is to increase the penetration of SWTs in remote areas through an adequate understanding of their performance.

Small wind turbines are mainly used for rural electrification and waterpumping to meet basic needs: human consumption, livestock watering, and irrigation. Less common applications of SWTs for home heating and water desalination have been reported by [15, 16] and [17] respectively. Waterpumping is one of the earliest wind turbine technology appli-

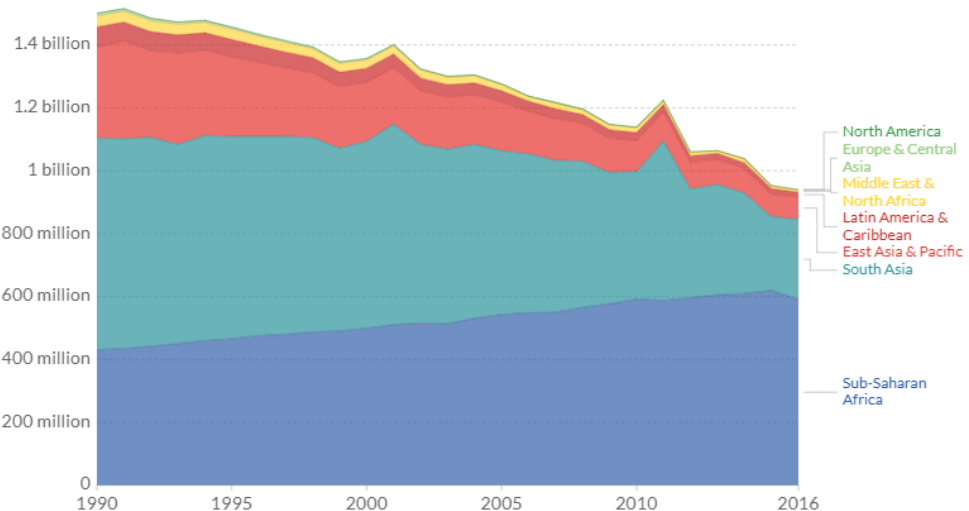


Figure 1.1: Population without electricity access. Reproduced from [5] (accessed 5 Sep 2020).

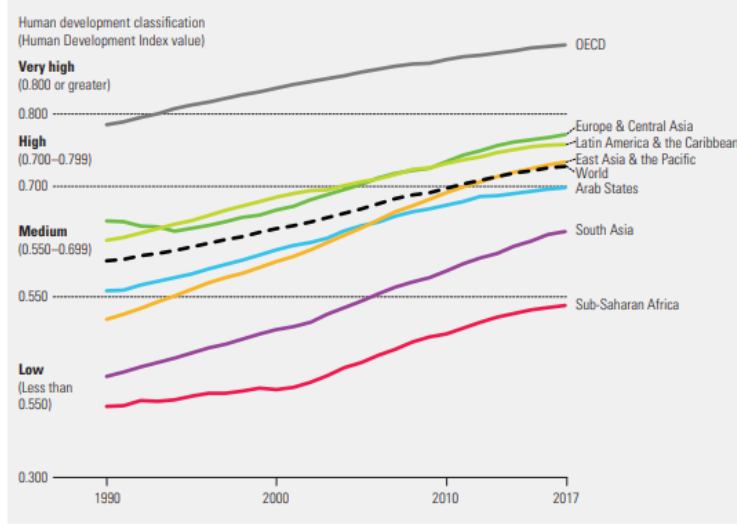


Figure 1.2: Human Development Index values, by country grouping, 1990–2017. Reproduced from [7](accessed 5 Sep 2020).

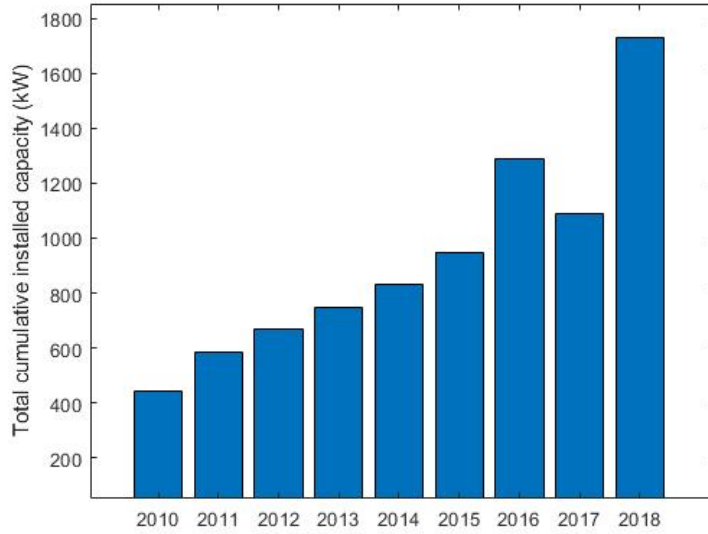


Figure 1.3: Small wind turbine global installed capacity. Data from World Wind Energy Association [9] and Statista [14] (accessed 5 Sep 2020).

cations; however, its use in the contemporary world has slowed. Nonetheless, harnessing the energy of wind to pump water is experiencing a revival. With the generally increasing acceptance of renewable energies, particularly in developing regions, its importance will grow again, thereby promoting rural development [18].

The scarcity of water, an essential source of life, is crucial for the world community,

especially rural dwellers. On a global scale, water use has increased by about one percent per annum since the 1980s, propelled by a mix of population growth, socio-economic change, and changing consumption patterns. The need for global water is anticipated to continue to grow at a comparable pace until 2050, accounting for a rise of 20 to 30% above the current level, primarily due to increasing demand in the industrial and domestic sectors [19]. According to UNESCO [19], three of every ten people have no access to clean drinking water. Nearly 50% of people who drink water from unsafe sources live in sub-Saharan Africa. Consequently, developing nations with rapidly growing populations have serious challenges in meeting their water demand.

Amongst the different renewable energy technological options for off-grid rural water pumping, solar PV and small wind turbines offer the greatest potential. However, which of these technologies is more appropriate? Several factors need to be considered. These include durability, noise level, maintainability, innovativeness, geographical location, life-cycle assessment, and cost-benefit analysis. Table 1.1 presents a comparison of windmills and PV water pumpers. From the perspective of sustainability in tandem with the SDG goals, the SWT is more appropriate. Small-scale wind power sources are economically competitive and environmentally sustainable to meet the water need of people in remote locations with good wind resources. The inspiring story of William Kamkwamba, who built windmills from scrap materials sourced from his village in Malawi, is a testament to the ease of manufacture and adaptability of SWTs. His ingenious work was documented in the book titled *The Boy Who Harnessed the Wind* [20] and was later adapted into a movie <sup>2</sup> in 2019. If SWTs are to be adopted as an alternative in rural areas, they must be cheap and easy to manufacture. However, in many cases, simplistic design and operation come with a penalty in performance efficiency [21]. This thesis seeks to contribute toward designing a technically appropriate and economically viable water pumping windmill suitable for indigenous construction and better adaption to conditions of the developing regions within the broader context of sustainable

---

<sup>2</sup><https://www.netflix.com/ca/title/80200047>

Table 1.1: Comparison of small wind turbine and solar PV technologies. Adapted from [4].

<b>Small wind turbines</b>	<b>Solar photovoltaic</b>
Windmills are effective at any latitude, whether at the poles or top of high mountains.	PV effectiveness decreases at latitudes greater than 45°. Snow and cloud cover reduce their output.
SWT efficiency is independent of time. Efficiency losses are due to additional rugosity caused by dust transported by the wind. This loss remains unchanged over time.	The efficiency of PV panels decreases by approximately one percent per annum.
SWTs have long service lives and are easy to dismantle and recycle.	Retired PVs are electronic waste and are potentially toxic to the environment because they comprise rare-earth metals. Their recyclability is still a subject of debate.
SWT technologies are simple, and scavenged materials can be used to build, maintain, and repair SWTs.	Solar PV is a high technology product that can only be manufactured by few companies in the world. In other words, PV system investment is exclusively for the privileged class that can afford it.
Building and installing SWTs in remote locations can potentially create small industries and jobs for locals.	PV is mostly imported, so the manufacturers become richer to the detriment of the local populace.

development.

## 1.2 Context of current research

This study is a continuation of previous studies by Fagbenro [22], Singh [23] and Vaz et al. [24]. The generic aim of this research is wind tunnel testing and computational investigation of the aerodynamic and starting performance of a small, horizontal axis wind turbine based on the replication of a circular-arc bladed rotor with multiple blade numbers tested by Wegereef [25] for waterpumping application. Fagbenro [22] numerically examined the impact of solidity, a measure of the blade area to the rotor swept area, on the lift and drag of a Bruining [26] model blade. The study suggested that in analytically evaluating windmill performance, solidity effects should be incorporated because of their significance. Singh [23] continued by implementing the suggested solidity corrections in blade element momentum

(BEM) theory prediction but concluded that the effects are insignificant. However, it is not clear under what conditions these effects can be ignored. The starting behavior of a model experimental windmill with blade number,  $N = 3$ , was investigated by [24]. They characterized the drivetrain resistance and showed that the static and dynamic components determine the starting wind speed and runaway rotor speed, respectively. In furtherance of this work, a holistic approach that entails wind tunnel characterization of circular-arc airfoils, rotor aerodynamic performance, and starting behavior investigations using the experimental rotor model of [23] with a range of  $N$  will be examined. In summary, the ultimate goal is to improve BEM prediction for low tip speed ratio and high solidity wind turbines by incorporating solidity effects, if significant, and then optimize the windmill design to maximize starting torque and minimize starting time.

### 1.3 Problem statement

Current aerodynamic research focuses, understandably, on high-speed wind turbines generating electricity on a range of scales. Small wind turbines for direct mechanical drive applications such as waterpumping have not been the subject of much research, even though they are most suitable and convenient to use in rural or off-grid areas. Waterpumping windmills characteristically start under load, and this requires high torque, which is realized mainly by increasing blade number,  $N$  or solidity,  $\sigma$ , which is in the region of 0.5–0.8 for the classical American windmill [27, 28] compared to that of conventional wind turbines given in Table 1.2. This characteristic, however, complicates the rotor aerodynamic behavior due to the mutual interaction between adjacent blades and low Reynolds number,  $Re$ , operation. Typical examples of waterpumping windmills are shown in Figure 1.4. Even though these windmills have been around for several centuries, their aerodynamic performance is not fully understood, particularly the influence of high solidity. Understanding the aerodynamic performance characteristics of cambered blades is both instructive and will provide design



(a) Poldaw 5m diameter, 18-bladed water pumping windmill [13].  
 (b) Kijito 18 ft diameter, 24-bladed water pumping windmill. Photo: Courtesy of Dr. David Wood.

Figure 1.4: Traditional windmills.

guidelines for optimizing the aerodynamic and starting performance of SWTs at low wind speed conditions.

Windmill blades are generally cambered or curved and made from thinly rolled metal sheets with spars consisting of circular tubes running along the blade length. The spars are used to hold the blades and connect them to the rotor hub, as illustrated in Figure 1.5. A typical circular-arc blade and its geometrical features are outlined in Figure 1.6. Quality experimental lift and drag data at appropriate  $Re$  are required for accurate design and performance prediction of SWTs. However, one main challenge is the dearth of aerodynamic data of cambered airfoils at suitable thickness and camber, especially at low  $Re$ . While computational tools such as computational fluid dynamics (CFD) have been used to predict airfoil performance at high  $Re$ , it can not be trusted for  $Re < 500,000$  [30]. Unlike high  $Re$  airfoils, available CFD codes are not sufficiently robust to predict the airfoil performance behavior of low  $Re$  flow due to the complexities associated with it. Under these circumstances,



Figure 1.5: Typical windmill blade:circular arc sheet metal with spars (supporting tubes) [29].

Table 1.2: Comparison of horizontal axis rotor types. Extracted from Practical Action, [28] (accessed 5 Jan 2018).

Type	Starting Torque	Speed	Fabrication method	Power coefficient ( $C_p$ )	Solidity ( $\sigma$ ) (%)
Cretan sail or flat paddles	Medium	Low	Simple	0.05–0.15	50
Cambered plate fan	High	Low	Moderate	0.15–0.30	50–80
Moderate speed aero-generator	Low	Moderate	Moderate	0.20–0.35	5–10
High speed aero-generator	Almost zero	High	Precise	0.30–0.45	5

wind tunnel testing is the most reliable method to obtain the airfoil's polar data.

It is evident from previous studies [31, 32] that lack of quality airfoil data at the appropriate  $Re$  and high  $\alpha$  is one impediment to accurate starting performance analysis. Starting is usually not an issue for large wind turbines because they have blade pitching mechanisms that lower the typically large  $\alpha$  when stationary. On the other hand, most small wind turbines do not have blade pitch adjustments due to high costs. Because the turbines are located close to their supply load, which may be a low wind site (urban dwellings), [33], their starting is entirely dependent on the aerodynamic torque produced by the stationary blades, which is likely to result in poor starting performance [34]. A consequence of poor

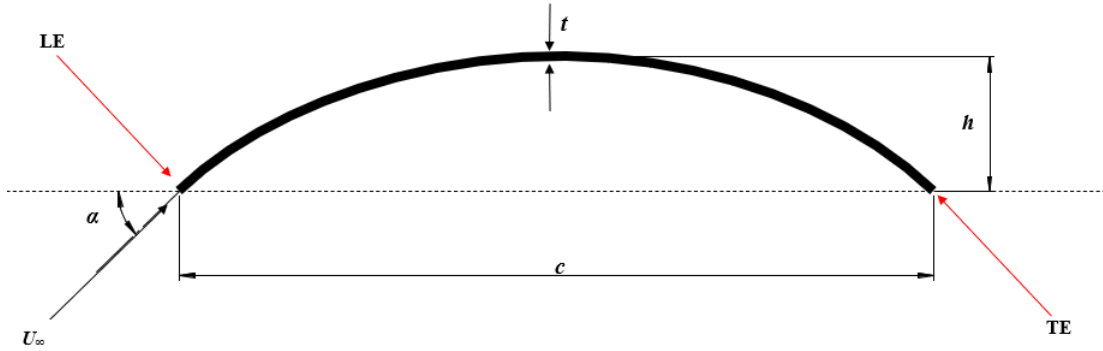


Figure 1.6: Circular-arc airfoil geometrical profile.  $c$  = chord,  $t$  = thickness,  $h$  = camber, LE = leading edge, TE = trailing edge,  $\alpha$  = angle of attack and  $U_\infty$  = freestream wind speed.

starting is the turbine rotor's inability to accelerate to a steady power extraction state in a low wind environment. As reported by Ebert and Wood [35], SWT starting aerodynamics are complex. The problem is a tripartite one, an odd combination of very low  $Re$ , high  $\alpha$ , and unsteadiness. As a result, starting wind speed can be considerably higher than the cut-in wind speed under no-load conditions [34, 35]. This fact is validated by the findings of Sarkis and Pinilla [36], who showed that the maximum efficiency of a waterpumping wind turbine occurs below its starting wind speed and that significant performance improvement can be made with a good aerodynamic blade design. Improvement in starting behavior can increase energy yield from 15–30% depending on the site [37]. Although horizontal axis windmill rotor starting has been investigated for blade number  $\leq 3$ , e.g., [24], this study is unaware of a study with a high solidity (high blade number) using airfoil data at the appropriate  $Re$ .

Performance results of scaled experimental rotor models in wind tunnels can be significantly higher than that of the same model in actual wind conditions due to blockage effect. Blockage ratio,  $B_R$ , measures the size of a model to that of a wind tunnel test section and should be below 10% for its effect to be insignificant [38]. While the blockage impact on low solidity convectional wind turbines is well researched, the impact of high tunnel blockage on the performance of high solidity rotors such as waterpumping windmill, has not been investigated.

## 1.4 Thesis objectives

This work advances the state-of-the-art understanding of the aerodynamics and starting behavior of small wind turbines intended for waterpumping and the influence of various design variables using both analytical and experimental methods. The objectives of this study are summarized as follows:

- Provide a comprehensive wind tunnel airfoil performance dataset for a typical windmill blade performance with different geometrical characteristics at low  $Re$  and high  $\alpha$  under steady and unsteady wind conditions.
- Model and investigate the aerodynamic performance and starting behavior of a windmill rotor with a range of blade number using standard blade element momentum theory (BEM) and compare with wind tunnel testing.
- Experimentally examines the effects of high blockage and the significance of high solidity on windmill rotor aerodynamic performance with a view to incorporate solidity corrections into blade element momentum theory prediction code.

## 1.5 Thesis structure

The remainder of the thesis is set out as follows:

Chapter 2 reviews relevant literature on waterpumping windmills and the critical parameters influencing their aerodynamic performance and starting behavior. In Chapter 3, circular-arc airfoil wind tunnel testing and its performance in both steady and unsteady conditions are described. Blade element momentum theory (BEM) is used in Chapter 4 to predict the rotor model performance with a range of blade number. Also, the impacts of blade element performance parameters are presented. Chapter 5 focuses on the starting performance prediction using BEM. A description of the experimental facilities and the rotor model test is outlined in Chapter 6. Results of the testing for both aerodynamic performance

and starting together with a comparison to a BEM prediction are presented in Chapter 7. Finally, Chapter 8 contains a summary of the significant findings and suggestions for future work.

# Chapter 2

## Overview of Waterpumping Windmill

The provision of water in off-grid and remote locations in developing regions using SWTs has been established as appropriate within the context of sustainability in Chapter 1. In this chapter, literature relevant to waterpumping windmill research is explored. Topics surveyed include wind turbine types and their applications, the distinction between large and small wind turbines, the aerodynamic performance of cambered airfoils, windmill rotor aerodynamic performance, and SWT starting behavior to establish the existing knowledge gap.

### 2.1 Types of wind turbines and its application

Broadly speaking, wind energy converters can be classified into two categories: horizontal axis wind turbines (HAWTs) and vertical axis wind turbines (VAWTs) based on the orientation of the rotor axis. In the HAWTs, the axis of rotation is parallel to the wind direction, as shown in Figure 2.1, while for the VAWTs, the rotation is perpendicular to the wind flow direction. In both types, the aerodynamic propelling force can be either drag or lift. See Figure 2.2 for examples of VAWTs with a great variety of geometries. In addition, there are cases of the combination of both forces in the design of VAWTs, e.g., [39]. Due to its high performance compared to VAWT, the HAWT dominates the utility-scale wind power



Figure 2.1: Vestas V112 3 MW, 3-bladed rotor [40].

generation both onshore and offshore. While VAWTs for water pumping are not as prevalent as HAWTs, it has been suggested that they may play an important role in water supply in the future because of their inherent advantages, such as the ability to accept wind from any direction, ease of manufacture, low noise, and reduced cost. Most of the water pumps in operation are driven by horizontal axis wind turbines, which are the focus of this research.

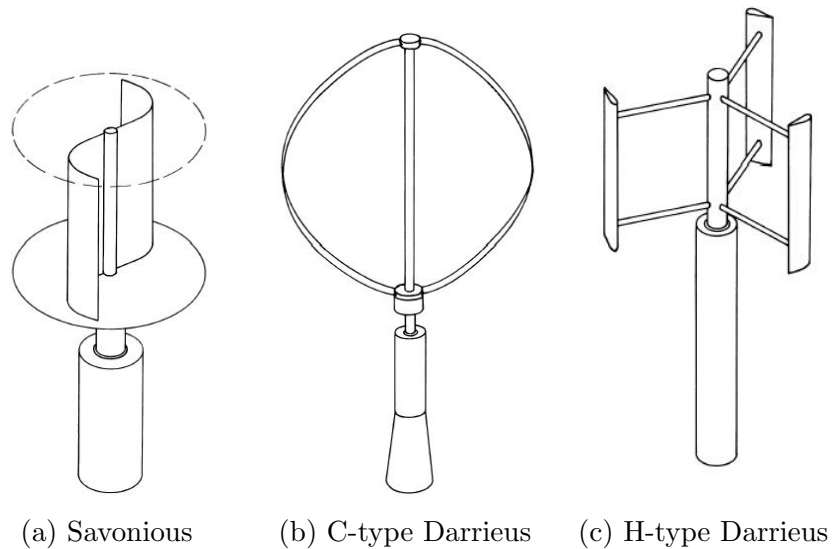


Figure 2.2: VAWTs (a) Drag-driven (b) and (c) Lift-driven [40].

## 2.2 Large (LWTs) and small (SWTs) wind turbines

The general trend in the wind turbine industry is competition between manufacturers to build larger and larger giant wind turbines. The main argument put forward is the economics of scale, though stifling the entry of smaller competitors might also be a factor. Not long after GE<sup>1</sup> built the world's largest wind turbine, a 220 m rotor, 12 MW capacity offshore turbine (Haliade-X), Siemens Gamesa<sup>2</sup> unveiled a 14 MW capacity, 222 m offshore wind turbine (SG 14-222 DD) in a bid to beats out the competition from GE. Due to social imbalances, environmental impacts, and effects on local economies, this approach is not sustainable in the long term. Readers interested in these issues are encouraged to consult Ref. [4] for further details on the sustainability of increasing SWTs penetration. From a technical perspective, SWTs have been defined differently, with several countries setting up different small wind power ranges. The definition by **IEC 61400-2:2013 Wind turbines-Part 2: Small wind turbines** safety standard seems appropriate in this context [41]. It defines a small wind turbine as having a swept area below  $200 \text{ m}^2$ , i.e., when  $D < 16 \text{ m}$ , equivalent to a power rating of approximately 50 kW. While the standard applies only to HAWTs, the “definition” has been conveniently applied to VAWTs, e.g., [34]. Even though there is no clear dividing line between small and large wind turbines, the IEC classification is sufficient for this research.

The fundamental principles governing the operation of SWTs are size-independent. For example, the restriction on the ideal maximum power coefficient called the “Betz–Joukowsky limit” and derived in Chapter 4 is the same for both LWTs and SWTs. Conversely, size-dependent issues are experienced during operation, such as starting performance and cut-in wind speed—the minimum speed at which power is extracted. The significance of these factors for SWTs’ starting performance, discussed in Chapter 5, are encapsulated in the differences between SWTs and LWTs given in Table 2.1.

---

<sup>1</sup><https://www.ge.com/renewableenergy/wind-energy/offshore-wind/haliade-x-offshore-turbine>

<sup>2</sup><https://www.renewableenergyworld.com/2020/05/22/siemens-gamesa-reveals-worlds-largest-wind-turbine/>

Table 2.1: Comparison of small and large wind turbines. Adapted from [33].

SWTs	LWTs
They are usually sited close or adjacent to the supply load, which are often not the windiest locations.	LWTs in wind farms are deliberately sited in windy environments.
SWT generators have significant resistive torque that must be overcome aerodynamically before the blades turn. In addition, due to the high cost, pitch control is rarely used on small wind turbines. Therefore, it is impossible to change the angle of attack of the blade to the prevailing wind conditions. This problem is especially critical during starting.	LWTs have pitching systems that allow for the angle of attack change; thus, sufficient aerodynamic torque is generated to overcome their usually small drivetrain resistive torque.
Low $Re$ largely influences its aerodynamics. In practical terms, these low $Re$ values imply that SWTs bear more similarity to models rather than to a full-sized airplane.	Because of their size, they are operated at a high $Re$ .
SWTs use inexpensive or free yawing systems, such as tail fins or downwind blades. They rely on aerodynamic means such as furling-turning the rotor out of the wind to limit speed or shorting of the generator output.	LWTs have complicated yaw mechanisms to align their rotors to the wind direction.
	LWTs use a brake on the high-speed shaft (between the gearbox and the generator).

### 2.2.1 Wind-powered waterpumping technologies

While there are conflicting speculations about the historical origin of windmills [38, 40], wind has been harnessed as a traditional energy source for centuries and is still commonly used in developing countries and rural areas of developed nations. According to ancient history, the first use of wind power is in the East, and they were reportedly used for the milling of grains. Centuries later, there were reports of the Chinese windmill using wind wheels for draining rice fields. Since the early 13<sup>th</sup> century, wind has been used to pump water in dewatering polders in the Netherlands to prevent flooding and render them more suitable for agricultural purposes [27, 42]. Small wind pumps fabricated from wood have been used in France, Portugal, and Spain to pump seawater to produce salt. Afterward,

the American wind pump made of steel with a multi-bladed, fan-like rotor became the most popular waterpumping technology in the late 19<sup>th</sup> century [27]. The American windmill has undergone modifications to reduce its weight and cost and improve performance, and several technological options have emerged.

Wind energy can be harvested either mechanically or electrically to power a waterpumping wind turbine, or more commonly known as a wind pump. A mechanical wind pump operates by converting the kinetic energy of the wind to useful rotary shaft motion, which is then used to drive a water pump either directly or via a gear system. An electrical wind pump produces electrical output (AC or DC) using a generator, which pumps water directly by connecting to either an AC or DC motor. The choice between a mechanical and electrical wind pump for a given location depends on factors reflected in the advantages and disadvantages of a mechanical wind pump compared to an electrical pump [42, 43]:

- Windmills use a high number of curved steel plate blades, usually at least 10, and are referred to as high solidity rotors. In contrast, electrical wind turbines use about three blades of true airfoils like the convectional wind turbines and are classed as low solidity rotors.
- Mechanical wind pumps must be located directly over the borehole; the best wind speed location is usually not the best water resource location. Electrical wind turbines can be sited at the best wind location, and power generated from the turbine at any nearby location can easily be transmitted to the pumping site.
- Electrical wind turbines use centrifugal pumps, which simplify matching the turbine with the pump; the match is achieved by electronically varying the load. In contrast, reciprocating or positive displacement pumps are used in mechanical wind turbines; matching the wind turbine to the pump is realized mechanically and can be problematic.
- Electrical wind turbines are versatile as surplus electrical power generated can be used

for lighting and other purposes and even stored in a battery.

- Mechanical wind pumps can start at about 2.5–3.5 m/s and are very suitable for low wind speed regions. In contrast, an electrical wind pump requires a mean speed of 4–5 m/s. They, however, become competitive with their counterpart mechanical wind turbine at a higher mean speed of 5–6 m/s.

A complete overview of both pumping systems with the main components and significant differences between each type is shown in Figure 2.3. While the electric pump performs better relative to the mechanical pump, it is not very suited for low wind speed locations. Therefore, further discussion on water pumping windmills will be limited to the direct drive (gearless), mechanical wind pump, the focus of this thesis.

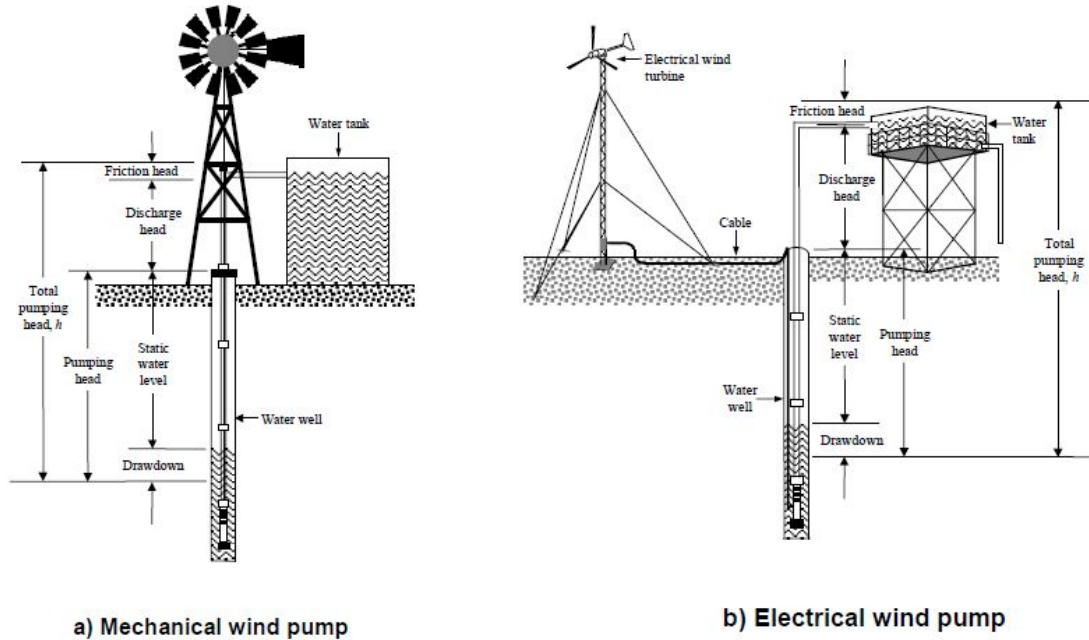


Figure 2.3: Schematic of typical wind pumps. Reproduced from [43].

## 2.3 Literature review

Compared to several other technological solutions developed for waterpumping systems reviewed by Gopal et al. [44], windmill technology still remains relatively inexpensive and easy to manufacture in developing nations. As a result, windmills for waterpumping applications are commonly deployed today because of their perceived role in sustainable energy development, especially in areas facing economic shortages of water.

The overall conversion efficiency of waterpumping windmills are relatively poor, typically around 5 % according to [45] and between 7% –27% reported by [46] and [43], partly because the basic aerodynamic principles are not well understood and their low rotational speed. Poor matching of pumps to rotors and cyclic variation of torque required by the pumps are other factors that affect the efficiency of windpump as an energy converter [45], but are outside the scope of the current treatise. Improving the maximum conversion efficiency requires more studies on the blade aerodynamics, as this ultimately determines the rotor aerodynamics and starting performance in low wind speed environments. Unfortunately, high solidity wind machines are under-researched compared to electricity-generating wind turbines. A better understanding of their aerodynamics will provide valuable information for optimizing the design of windmills for increased efficiency and good starting performance. A brief review of the relevant literature, which provides the rationale for this thesis, is divided into three main parts and presented in the following three subsections.

### 2.3.1 Aerodynamic characteristics of waterpumping windmill blades

Waterpumping windmills characteristically start under load and require high starting torque, which is realized mainly by increasing  $N$  or  $\sigma$ , which is in the region of 0.5–0.8 for the classical American windmill [27, 28]. In designing SWT blades, the focus is usually on finding a compromise between power production and starting torque [33]. First, however, an optimal blade number must be defined for waterpumping. The more blades, the more costly and

complicated the system becomes. Because curved blades made from thinly rolled metal sheets are typically used as the airfoil sections with spars (supporting rods) to sustain the blades, their design process is aerodynamically and structurally simple, and materials can be sourced locally. As such, the blades are attractive for low-speed operating turbines and very suitable for developing regions where access to sustainable energy is still challenging, see Table 1.2.

The exploitation of a windmill potential is limited due to the lack of data for lift,  $L$ , and drag,  $D$ , of the blade in terms of the geometrical parameters, chord,  $c$ , camber,  $h$ , and thickness,  $t$ , especially at low  $Re$  and  $\alpha$  beyond the stall; consistent with the operational regime of high solidity wind turbines. Other essential features that affect the blade's performance are the surface smoothness of the blade and the location of the spar on either the pressure or suction sides of the blade, as depicted in Figure 1.5.

Due to the growing utilization of airfoils operating at  $Re < 10^5$  for various applications, including micro aerial vehicles and sailplanes, there have been increased performance studies, e.g., [47–50]. Selig et al. [48] investigated a wide range of airfoils for different applications, including the S822 and S823 airfoils specifically designed for SWTs, but they require high manufacturing precision, which translates to high cost. However, cambered plate airfoils are proving to be a cost-effective and viable alternative for the development of SWTs and even commercial applications, as demonstrated in recent studies by Kragten [51] and Kummer et al. [52], respectively.

The earliest reported studies on circular-arc airfoils (CAA) were done by Wallis [59] in

Table 2.2: Summary of some research on circular-arc airfoils and flat plates.

Author(s)	$c$ (mm)	$Re$	$t/c$ (%)	$h/c$ (%)	$AR$	$\alpha$ range
Bruining (1979) [26]	400	$6 \times 10^4$ – $3.5 \times 10^5$	2	10	5	$-10^\circ$ – $90^\circ$
Pandey et al. (1988) [53]	304	$2.23 \times 10^5$	0.67	0–14	2	$-20^\circ$ – $90^\circ$
Okamoto et al. (1996) [54]	30	$< 1.14 \times 10^4$ – $1.5 \times 10^4$	1	3–9	6	$-6^\circ$ – $20^\circ$
Okamoto et al. (2005) [55]	30	$< 1 \times 10^4$	5	2–12	2	$-30^\circ$ – $30^\circ$
Tezuka et al. (2008) [56]	100	$6.2 \times 10^4$	1	4	3	$0^\circ$ – $10^\circ$
Okamoto & Ebina (2016) [57]	30	$1 \times 10^3$ – $1 \times 10^4$	1	3–22	3.3	$-5^\circ$ – $25^\circ$
Flay & Piard (2017) [58]	610	$1.16 \times 10^5$ – $4.15 \times 10^5$	4	21–22	4	$-5^\circ$ – $25^\circ$

1946, and Ikui et al. [60] in 1972. From the late 1980's, a considerable number of characterization studies on flat plates and circular-arc airfoils with different geometrical characteristics are summarized in Table 2.2 have been reported. The influence of blade curvature (camber) on CAA performance has been widely studied; see Table 2.2, where  $t$  and  $h$  are usually normalized by  $c$ , and  $AR$  is the aspect ratio-the model span divided by its chord.  $AR$  influences the performance of airfoils which by definition have infinite  $AR$ , but this is not possible to have in a wind tunnel. Okamoto et al. [54], Mueller [61] and Okamoto and Azuma [55] showed aerodynamically that cambered thin CAA plates offer better performance than flat plates at  $10^3 < Re < 10^4$ . An increase in  $h/c$  increases the maximum lift coefficient,  $C_{l,max}$ , lift curve slope, and the corresponding  $\alpha$  due to the likely delay in stall. For example, as shown in Figure 2.4, increasing the camber from 3% to 9% results in an over 55% rise in the magnitude of  $C_{l,max}$ , an indication of the significance of camber in windmill blade design. At the same  $Re$  range, Sunada et al. [62] found that thin airfoils with around 5% camber have a high lift-drag ratio,  $L/D$ , that increases as the maximum camber location moves towards the trailing edge. While [54,55,62] investigations were conducted at limited  $\alpha$  range, Pandey et al. [53] considered  $\alpha$  between  $-20^\circ$  and  $90^\circ$  at a single  $Re$  of  $2.23 \times 10^5$  and wide range of camber given in Table 2.3. As  $h/c$  increases, although the  $C_{l,max}$  increases, the  $C_d$  rises as well thereby lowering the  $C_l/C_d$ . The maximum stall angle,  $\alpha_s$  occur at  $17.30^\circ$  for  $h/c = 0.14$  suggesting stall delay due to high curvature which agrees with [62]. Based on their results, 8% camber gives the highest  $C_l/C_d$  that maximizes  $C_p$  for eight- and twelve-bladed windmill rotors, although the reported theoretical  $C_p$  values appear quite optimistic. The work by [58] at a limited range of  $\alpha$ , however, found that for  $h/c > 20\%$ , flow separation occurs at low  $\alpha$ , causing performance deterioration. The paucity of airfoil data at high camber over a wide range of  $\alpha$  and lower  $Re$  necessitates further investigation.

Several researchers have studied the effects of thickness on CAA, e.g., [54, 61, 62]. As thickness decreases, the airfoil performance improves, especially for CAAs with relative thickness  $< 6\%$ ; that is, the thinner the airfoil, the better its performance. Relatively

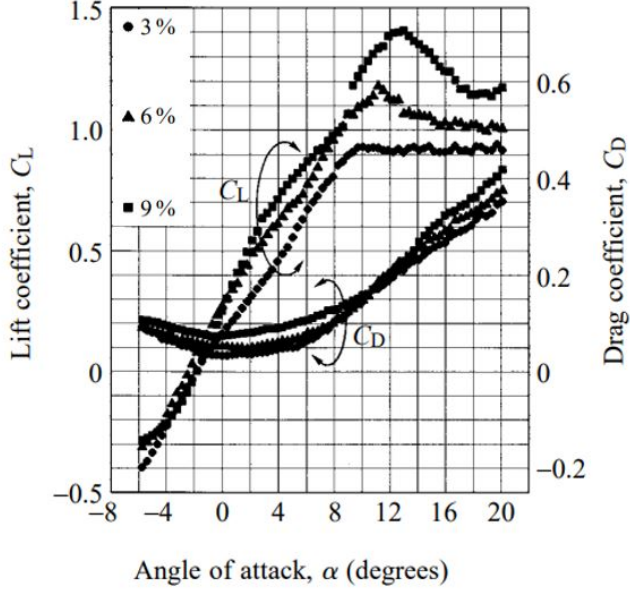


Figure 2.4: Effect of curvature on the aerodynamic characteristics of a rectangular aluminum foil model airfoil with  $t = 0.3$  mm and  $c = 30$  mm. Each symbol refers to a different camber, as shown in the panel on the figure. Reproduced from [54].

thick airfoils ( $t/c > 6\%$ ), in the  $30,000 \leq Re \leq 70,000$  regime can have significant hysteresis effects resulting from laminar separation with transition to turbulent flow that deteriorates their performance [63]. Symmetric airfoil studies investigating thinner airfoils, such as NACA0012 [64, 65], and thicker airfoils, such as NACA0021 [66], have been performed, but data on highly cambered and relatively thick CAAs, especially at lower  $Re$ , are scarce for applications and circumstances where high structural strength is required of the blade. Thus, a combination of geometrical variation of camber and thickness and its effects on performance deserves investigation at  $\alpha$  decreasing from high ( $90^\circ$ ) to low ( $0^\circ$ ), similar to SWTs  $\alpha$  variation during starting.

Bruining [26] provided one of the most comprehensive data sources on CAAs covering a wide range of  $\alpha$  and low  $Re$ , motivated by waterpumping applications. Lift and drag data of a CAA with an aspect ratio of 5 whose characteristics and experimental conditions are given in Table 2.2 were determined. The measurements were carried out with and without spars at five different positions around the blade profile in a closed jet wind tunnel with a turbulence intensity of 0.02%. Because windmill blades typically use spars, determining the

Table 2.3: Important aerodynamic parameters of cambered steel plates. Sourced from [53].

Model h/c	Conditions for maximum $C_l/C_d$			First stall		Minimum $C_d$		Average lift curve slope	Angle for zero lift	Theoretical maximum power coefficient when used in windmill	
	$\alpha$	$C_l/C_d$	$C_l$	$\alpha_{stall}$	$C_{l,max}$	$\alpha$ for min $C_d$	$C_d$			Eight bladed rotor	Twelve bladed rotor
	deg			deg		deg		per rad	deg		
0.00	4.90	13.158	0.52	8.82	0.96	0.00	0.018	6.21	0.0	0.40	0.40
0.002	4.04	21.739	0.72	11.03	1.17	0.10	0.024	5.66	-3.4	0.45	0.45
0.04	3.80	23.809	0.95	11.20	1.40	0.20	0.031	6.77	-4.0	0.45	0.46
0.06	4.00	25.000	1.267	12.60	1.58	0.30	0.040	6.83	-4.0	0.46	0.46
0.10	5.50	20.408	1.318	14.30	1.60	0.27	0.047	6.70	-5.2	0.44	0.46
0.12	7.28	10.526	1.300	14.80	1.42	-0.64	0.090	6.17	-5.2	0.38	0.38
0.14	8.26	7.692	1.250	17.30	1.41	-2.00	0.115	7.16	-5.2	0.35	0.36

Table 2.4: Result of CAA performance at  $Re = 10^5$ . The first column shows when a spar was used and its position with respect to blade chord. Reproduced from [26].

Spar position	Model code	Conditions for $(C_l/C_d)_{max}$			Conditions for stall		$C_{d,min}$	$C_p$ and optimum $\lambda$ for a 4-bladed windmill	
		$\alpha$ degrees	$C_l/C_d$	$C_l$	$\alpha$ degrees	$C_{l,max}$		$\lambda$ for $C_{p,max}$	$C_{p,max}$
—, —	—, —	6	23	1.3	12	1.47	0.06	3.6	0.43
◦	0, +0.0	6	19	1.1	16	1.5	0.06	3.2	0.42
◦	25, -1.55	17	3.4	1.12	21	1.28	0.16	1.00	0.2
◦	25, +1.55	5	18	1.07	12.5	1.3	0.06	3.00	0.41
◦	50, -0.0	16	4.7	1.26	16	1.27	0.16	1.6	0.25
◦	50, -1.55	15	4.8	1.28	15	1.28	0.17	1.6	0.26
◦	50, -4.0	14	4.7	1.2	17	1.24	0.17	1.6	0.25
◦	50, +4.0	5	18	1.16	12	1.35	0.07	3.00	0.41
◦	50, +8.0	17.5	1.2	1.2	11	1.4	0.07	3.00	0.41

optimal spar position that maximizes  $C_l/C_d$  is essential. As shown in Table 2.4, the spar position on the low-pressure side of the blade leads to  $C_l/C_d \leq 5$ , while that on the high-pressure side produce  $L/D$  as high as 20. In other words, the lift and drag characteristics are slightly affected when the spar is placed on the high-pressure (concave) side of the blade. However, a spar on the low-pressure (convex) side led to a significant deterioration in the airfoil characteristics. Hence, the high-pressure side position is adopted in the airfoil experimentation described in Chapter 3 to characterize the CAA at  $Re < 60,000$  appropriate for modeling SWTs starting behavior which was not measured by [26].

A variation in  $Re$  or the presence of a spar affects the performance of airfoils, as illustrated in Figure 2.5. The different profiles exhibit similar patterns [26] showing the second peak

phenomenon also observed in the wind tunnel test results of [53]. Rainbird [65] compared the aerodynamic data of NACA0015 in open and closed wind tunnel sections and attributed the observed differences to the effect of tunnel wall proximity. Worasinchai [67] further studied wind tunnel effects on selected cambered and symmetrical airfoils' measured data and found that flow around the airfoils is significantly influenced. Results of investigations by [65,67,68] showed that polar are sensitive to wind tunnel configuration and airfoil geometry, particularly at high  $\alpha$ . Although an extensive database of high and low  $Re$  is available, the results are mostly limited to conventional airfoils. Thus, it is imperative to examine the wind tunnel wall effect on CAA's measured data and their "second stall behavior". In circumstances where wind shear, gust, or yaw causes unsteadiness, there is a periodic change in apparent wind velocity and  $\alpha$  in the routine operation of wind turbines. Therefore accurate prediction of SWTs performance will require low  $Re$  dynamic airfoil data over a wide range of  $\alpha$  and reduced frequencies,  $k$ , which are typically scarce and have not been documented for circular-arc airfoil used in windmills.

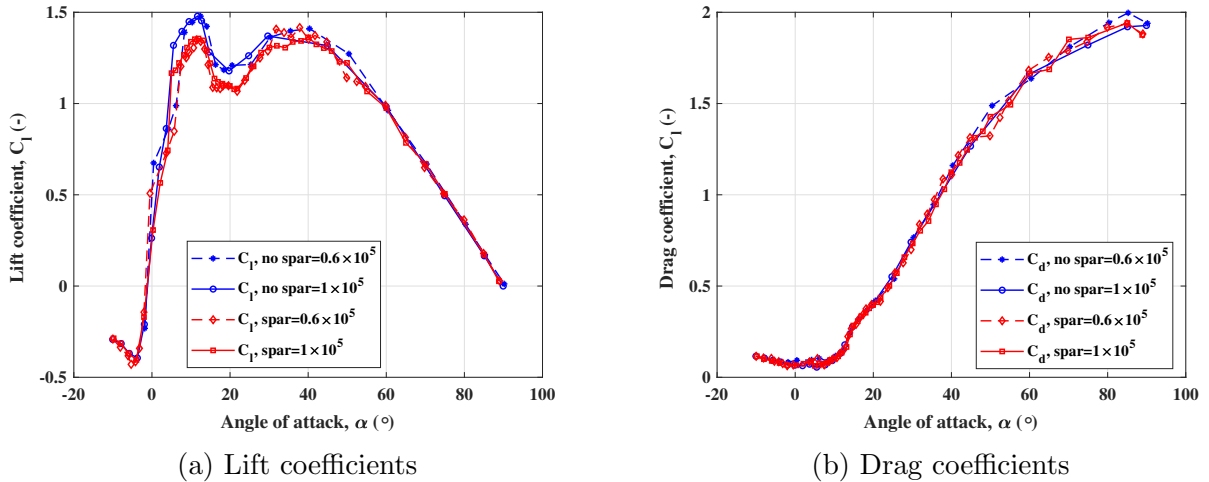


Figure 2.5: Performance of 10% cambered 2% thick steel plate with and without spars at the 50% chord position.  $Re$  indicated in legend. Extracted from [26].

### 2.3.2 Windmill performance

Given their slow rotation and high solidity, windmill aerodynamic performance differs significantly from conventional wind turbines due to the blade-to-blade interaction, low tip speed ratio,  $\lambda$ , operation, and, consequently, low  $Re$  [27]. Although studies over the last four decades, e.g., Bragg and Schmidt, [69], Nathan, [70], Cleijne et al., [71], Manwell et al., [72], Rijs and Smulders, [73] Rijs et al., [74] focused on design analysis, field and laboratory testing, and construction of waterpumping windmills that include performance matching, and mechanical coupling of wind pumps to turbines, they overlooked the impact of solidity on their rotor performance. This factor is also neglected by agencies such as the defunct Consultancy Services Wind Energy Developing Countries (CWD), the former Steering Committee Wind Energy Developing Countries (SWD) of the Netherlands, [75] and the Intermediate Technology Development Group (ITDG), which is now Practical Action of the UK, [28] established to undertake research and development activities aimed at providing low-cost windpumps in developing regions. CWD's wind turbines for driving water pumps are of low solidity and high tip speed ratios. Hence, much of their research efforts were geared towards alleviating the need for high torque at start-up and preventing excessive pump rod accelerations for piston pump types. Although these configurations are designed for low wind speed regions where overall water pumping efficiency should be maximized, they are relatively complex. As a result, they are not easy to maintain and repair by the rural populace who lack the needed technical training.

The effect of variable  $N$  or equivalently  $\sigma$  with regards to windmill performance was studied by Wegereef [25] who experimented on a scaled model of ITDG windmill. He measured the performance of  $N = 6, 12$ , and  $24$  bladed rotors with identical blades in a wind tunnel. While the work showed significant increments in starting torque with increased blade root (twist) angles, there was no report on thrust measurements and validation of the torque and power results, rendering the analysis incomplete and necessitating a thorough performance assessment of the model. In his work, Morcos [76] compared the performance of circular-arc

airfoil sections with different rotor solidities but did not validate his analytical prediction with experimental data. Recent works by Tokuyama et al. [77] determined the optimal design configurations of a small turbine and found that the optimal performance of a rotor with diameter  $< 100$  cm and operating at constant tip speed ratio is at  $Re = 10^5$  regardless of the disparity in solidity. However, this study was for a NACA4418 airfoil section. Sarkis and Pinilla [36] studied a scale model of a commercial fast running low solidity rotor and improved its performance by redesigning its rotor, resulting in a better wind to water conversion efficiency. Intriguingly, not much has been reported on solidity interaction between the rotor blades with cambered profiles, particularly as  $N$  increases.

BEM is a valuable and convenient tool for aerodynamic performance prediction and design of wind turbines, even with the availability of sophisticated computational fluid dynamics software. The BEM simplicity derives from the assumption that the discretized blade elements behave as isolated airfoils and act independently of the other elements. Because BEM prediction is based on an actuator disk equivalent to an infinite blade number, the concept of tip loss is used to correct the computed aerodynamic loading and power. The most common versions of BEM are based on the Prandtl simplified tip loss function, but it is inexact near the blade's hub at any tip speed ratio, and inaccurate over the entire blade span at low tip speed ratios [78]. Moreover, BEM is strictly valid only in the limit of  $\sigma \downarrow 0$ . For high  $\sigma$  like the windmills of Figures 1.4, the approximation that the blade elements behave as airfoils is invalidated. Usually, blades of wind turbines in rotation shed helical vortices into their wake, as demonstrated by the flow visualization of two of the three-bladed experimental rotor in Figure 2.6. Because the vortices impact on the velocity over the blades and forces acting on them, tip loss factor computations based on the helical vortex theory are recently being developed and implemented in BEM [79–81], particularly for the conventional three-bladed rotor. But this theory has not been applied to high solidity windmills performance analysis.

Cascade theory, a two-dimensional accounting method for finite solidity and often used

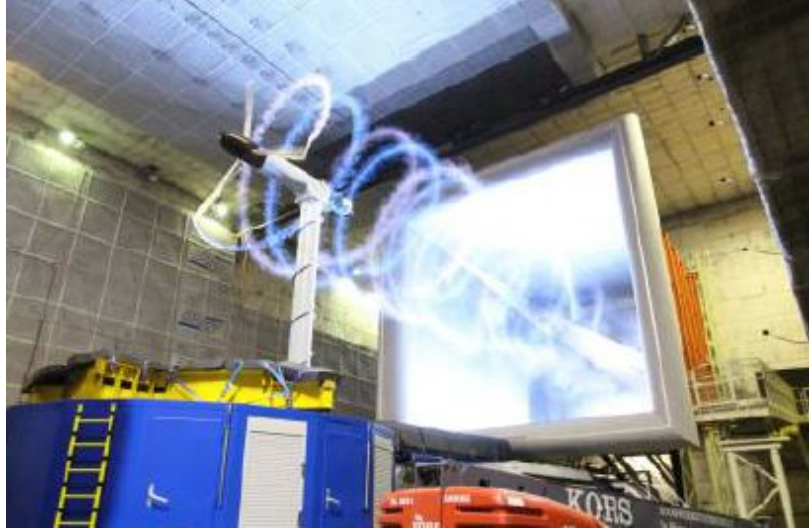


Figure 2.6: Tip vortices trailing from a model wind turbine in the DNW  $9.5 \times 9.5$  m wind tunnel (<http://www.mexnext.org/>).

in turbomachinery, has been employed to account for blade-to-blade interaction in wind turbine performance analysis by BEM modification, e.g., [82–84]. In BEM analysis, the blade elements are assumed to behave as airfoils with zero solidity. However, airfoils in cascade represented by an infinite row of equally spaced airfoils are the same as blade elements of finite solidity. Islam et al. [82] demonstrated that modified BEM using two-dimensional cascade gave better results than a standard BEM for high solidity multi-bladed wind turbine rotors, though with a penalty in computational time [82]. Fagbenro et al. [22] studied high solidity effects on a circular-arc-bladed windmill rotor. Their computational study showed that solidity influences lift and drag coefficients, which agrees with the findings of Yan [85] even for low solidity rotors. Singh [23] examined the effect of solidity on the performance parameters of 6, 12, and 24 bladed rotors that replicate that tested in [25]. Comparing BEM with wind tunnel measurement allowed the author to conclude that the solidity effects are negligible. However, the design conditions under which the solidity is insignificant are unclear. Part of the current study is a further investigation of solidity using the same model in [23] to examine and understand the aerodynamics of multi-bladed windmills.

Performance data from a scaled experimental rotor model in a wind tunnel are higher

than data from the same turbine tested in real wind conditions. The difference is due to blockage, which alters the flow around the model in a finite wind tunnel. For testing in small wind tunnels, the rotor swept area and chord length are maximized to obtain  $Re$  for which there are available  $C_l$  and  $C_d$  data, resulting in a high rotor projected area to tunnel area, called the blockage ratio ( $B_R$ ). Significant performance data on circular-arc bladed windmill rotors are available from the work of Pandey et al. [53] and Bruining [26], see Tables 2.3 and 2.4, respectively. They reported optimistic rotor performances probably because limited or no tunnel blockage corrections were applied to their  $L$  and  $D$  data or the rotor performance coefficients. Blockage effect has been shown to be significant, especially when the rotor area is  $> 10\%$  of the working section cross-section [38]. It is typically more significant in a closed test section than an open one, where the unconstrained streamlines can mimic some features of an unbounded flow. Moreover, in a closed tunnel, the Betz-Joukowsky limit, or ideal maximum  $C_p$ , has been reported to be exceeded, analogous to a shrouded wind turbine rotor [86]. A great variety of blockage assessment and correction studies have been conducted for HAWTs, and VAWTs in closed and open jet tunnels, e.g., [87–90]. Even though tunnel blockage as high as 48% [88] has been investigated, its influence on rotor aerodynamic performance with varying  $N$  and high  $\sigma$  typical of a waterpumping wind turbine has not been dealt with in-depth. Thus, a greater understanding of the relevant aerodynamics is a precursor to an optimal windmill blade design.

### 2.3.3 Starting behavior of SWTs

While many studies have focused on HAWTs design for aerodynamic performance improvement, e.g., [91–94], only a few have examined the starting behavior. A recent investigation was conducted by Ebert and Wood [35] on a 5 m diameter, two-bladed 5 kW wind turbine. The analysis showed that a complete starting sequence comprises two phases. The first is a long period of slow acceleration, in which the turbine accelerates slowly with the angle of attack decreasing from its high initial value at the stationary position until the blade reaches

the region of maximum ( $C_l/C_d$ ). In the second phase, the turbine goes through a short period of rapid acceleration to the useful power extraction region, generating high torque. Thus, starting performance is dominated by high  $\alpha$ , with the power extraction occurring at a low  $\alpha$  and high ( $C_l/C_d$ ). Mayer et al. [95] examined the effects of blade pitching angle on a similar small HAWT as in [35]. Starting was observed for a range of pitch angles from  $0^\circ$  to  $35^\circ$  degrees in steps of  $5^\circ$ . They found that the idling period decreased with an increase in pitch angle owing to reduced  $\alpha$ . By comparing measurement data with the rotor acceleration prediction, a better agreement was found for higher pitch angles for the range of wind speeds investigated.

Further study on the starting performance of a small HAWT was described by Wright and Wood [32]. The authors field-tested a three-bladed 2 m diameter HAWT and showed from BEM that while the starting torque is generated largely at the blade root, the power extraction torque is produced at the tip region of the blade. They used approximate generic formula and a combination of interpolated airfoil performance data of different airfoils for estimating  $C_l$  and  $C_d$  at a high  $\alpha$  due to the shortage of such data at the incidence angle (up to  $90^\circ$ ) and at low  $Re$ . Also, in the study, the authors noted the need to accurately characterize the drivetrain resistance of SWTs because their cogging torque increases with decreasing turbine size. Considering the importance of increasing the energy output of wind turbines in low wind speed conditions, particularly small turbines in which a much higher starting torque is required, [96]; better starting is an important issue for SWTs design. Improvement in starting behavior can potentially increase energy yield from 15-30% depending on the site, [97], and up to 40% depending on the load, [37]. Later studies by [98] concurred with the findings of [32] and assert that the idling period can be reduced by increasing the blade chord length and twist angles near the hub.

The magnitude of starting torque generated by a SWT such as a windmill when it is in imminent motion is important to starting. The windmill may come to rest during a period of lull. For it to come into operation rapidly as the wind speed rises again and operate in

low winds regime, the starting torque must be reasonably high and sufficient to overcome the internal friction of the system [99]. The need to accurately characterize the internal friction or drivetrain resistance has been reported as early as the turn of the 20th century. For example, Perry [100] performed some dynamometric experiments on a windmill that include the determination of starting torque and drivetrain resistance. In the early 1950s, a further attempt to measure the starting torque coefficients of windmills via a start and stop experiment was carried out by Sanuki [101], with Figure 2.7, showing the impact of  $N$  and varying wind speeds on the starting behavior of a Speedovane akin to a windmill. In the ensuing years, the research slowed due to growing alternatives to mechanical wind pumps. Currently, drivetrain resistance is becoming an increasingly critical issue in SWTs, especially as it is an important design factor for low wind speed starting in HAWTs, [24, 102, 103] and VAWTs [104, 105].

Vaz et al. [24] investigated the effect of bearing friction on the drivetrain resistance of a small HAWT, notably during its transition from the high static to low dynamic resistive torque in predicting the starting performance and runaway, defined as the maximum

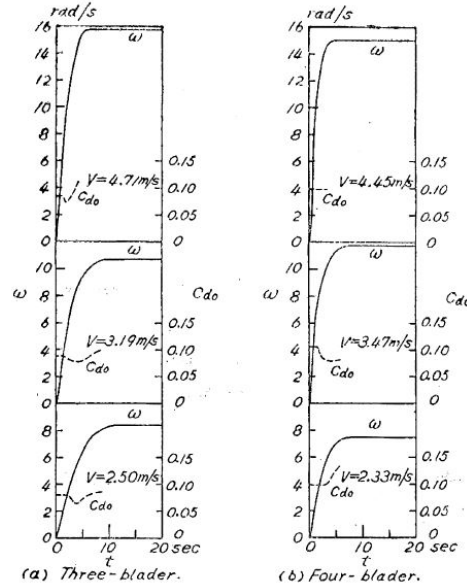


Figure 2.7: Starting of Speedovane in varying wind speeds and computed starting torque coefficients, ( $C_{d0}$ ) [101].

aerodynamically possible rotor speed for the no-load condition. As wind turbines must be operated below the runaway point to produce power safely, its estimation at the rotor design stage is important. Their bearing frictional analysis showed that the static to dynamic resistive torque ratio is about 7:1, which is a significant variation compared to cogging torque (stationary and rotating) in permanent magnet generators (PMG). The authors found that starting wind speed is higher than the cut-in wind speed. They concluded that low wind turbine aerodynamics and accurate drivetrain resistance models could minimize the starting wind speed and broaden the operating range for optimal rotor performance. However, their study assumed no induction and was limited to a three-bladed rotor.

This author is unaware of any reported research, experimental or analytical, that has investigated the starting behavior of high solidity, circular-arc-airfoil horizontal rotors with  $C_l$  and  $C_d$  data at the appropriate  $Re$  and high  $\alpha$  in a high blockage tunnel. As such, the model in [24] will be further investigated with a range of blade numbers,  $N$ , and  $\sigma$  comparable to that of a typical waterpumping windmill.

## 2.4 Summary

Based on the literature review, the aerodynamics of a circular-arc bladed windmill with a high  $N$  or otherwise significant  $\sigma$  is still poorly understood. Experimenting with a wide range of blade numbers and comparing the results with BEM (zero solidity) prediction will help determine if solidity effects are present and, if so, their significance at low  $Re$  operation.

The accuracy of BEM is dependent on the quality of the aerodynamic data of airfoil. Although there are low  $Re$  and high  $\alpha$  airfoil performance data for camber airfoil, there is still a lack of data for certain geometrical characteristic combinations such as high camber and thickness ratio, appropriate to a given application and  $Re$  requirement.

Further, vortex theory is not used in most standard BEM versions to compute tip loss, even though all blades in rotation shed helical vortices in their wake, which alters the velocity

over the blades and the resultant forces acting on them. Application of a vortex-based tip loss factor for finite blade correction in a windmill with varying blade numbers will increase the understanding of the physics affecting windmill performance and correct the inaccuracies of using Prandtl tip loss over the blade span at low  $\lambda$ .

Starting is a critical operational issue for SWT, especially in low wind speed conditions, because of the virtual lack of pitching mechanism and high drivetrain resistance. Accurate airfoil data at very low  $Re$  corresponding to the starting wind speed is required to model its starting behavior correctly. An attempt at modeling or experimentally investigating high  $\sigma$  (high  $N$ ) turbines has not been reported to the authors' knowledge.

Wind tunnel blockage significantly affects rotor test measurements. However, most blockage studies have focused on low  $\sigma$ , high  $\lambda$  machines. While the aerodynamics of high  $\sigma$  and low  $\lambda$  is complicated because of mutual blade interaction, the combined effect of high  $\sigma$  and high blockage on the rotor aerodynamic performance has not appeared in the open literature and therefore requires experimental investigation.

# Chapter 3

## Airfoil Experimentation

This study intends to replicate and extend the circular-arc airfoil (CAA) model of Bruining [26] to that of Wegereef [25]. Thus this chapter discusses airfoil performance at low  $Re$  and its behavior at high angles of attack, particularly relating to the starting of small wind turbines such as waterpumping windmills. A brief description of the University of Calgary Red Wind Tunnel (RWT), where all the airfoil experiments were conducted, is presented here, with further information in Chapter 6. In addition, detailed descriptions of the static and dynamic force measurement techniques, data acquisition equipment, airfoil performance, tunnel boundary corrections, and uncertainty estimates are provided. Further, the influence of airfoil geometrical features such as camber and thickness ratios on specific operational low  $Re$  airfoil performance are examined. Hysteresis and quasi-steady behavior of the CAA are also explored. Finally, for the first time, the dynamic lift and drag were measured for an airfoil pitching over a wide range of angles and reduced frequencies.  $L$  and  $D$  data of the studied airfoils are provided in Appendix A for reference purposes.

### 3.1 Low Reynolds number airfoils and high incidence

There has been a growing interest in the design and development of low  $Re$  airfoils for several applications such as small aerial vehicles (SAV) [61, 106] and, of course, SWTs [107–109].

Reynolds numbers based on the airfoil’s chord length ranging between  $10^4$ – $10^5$  are termed *low Re* and their flows are significantly different, more complicated than flows at  $Re > 10^6$ . Thus, investigations are needed to obtain adequate understanding and then propose design guides for their intended applications. In terms of  $L/D$ , a given airfoil performance improves monotonically with  $Re$ ; however, at  $Re < 10^6$ , the same airfoil suffers performance degradation worse than that of even a simple flat plate [106]. Such loss in aerodynamic performance due to high drag necessitates an improved understanding of the impact of different geometries such as relative thickness and camber.

As is the case with aircraft, an SAV typically operates within a limited range of  $\alpha$ , in most instances up to stall, so post-stall aerodynamic performance data are of little or no interest to commercial and military aviation industries. On the other hand, SWT performance, including starting, requires low  $Re$  lift and drag data at both pre-stall and beyond stall regimes. Although an extensive database of  $C_l$  and  $C_d$  data from wind tunnel testing is available for SWT aerodynamic design and performance analysis at and below stall, until recently, there is a scarcity of such data at high  $\alpha$  and  $Re < 10^5$ , possibly due to the difficulty in accurately measuring the small forces, pressure differences and velocities involved [33, 63]. This challenge is understandable, as only designers interested in SWT starting are concerned about measuring  $\alpha$  in the extreme range.

The  $\alpha$  and  $Re$  variation along the span of a 0.68 m diameter model windmill blade’s tip and root during starting is shown in Figure 3.1. Clearly, starting investigation is important for SWTs because of the very large  $\alpha$  experienced by the blades. The blade’s starting from rest to a wind speed of 6 m/s were calculated as depicted in the curves indicating starting, which is completed as soon as power production begins. Note that the constant  $\alpha$  is for the stationary blades, and the blades operate at ranges of  $Re$ , which is due entirely to changes in velocity along the entire blade span shown. Further discussion on the experimental model of Figure 3.1 is reserved for Chapter 4.

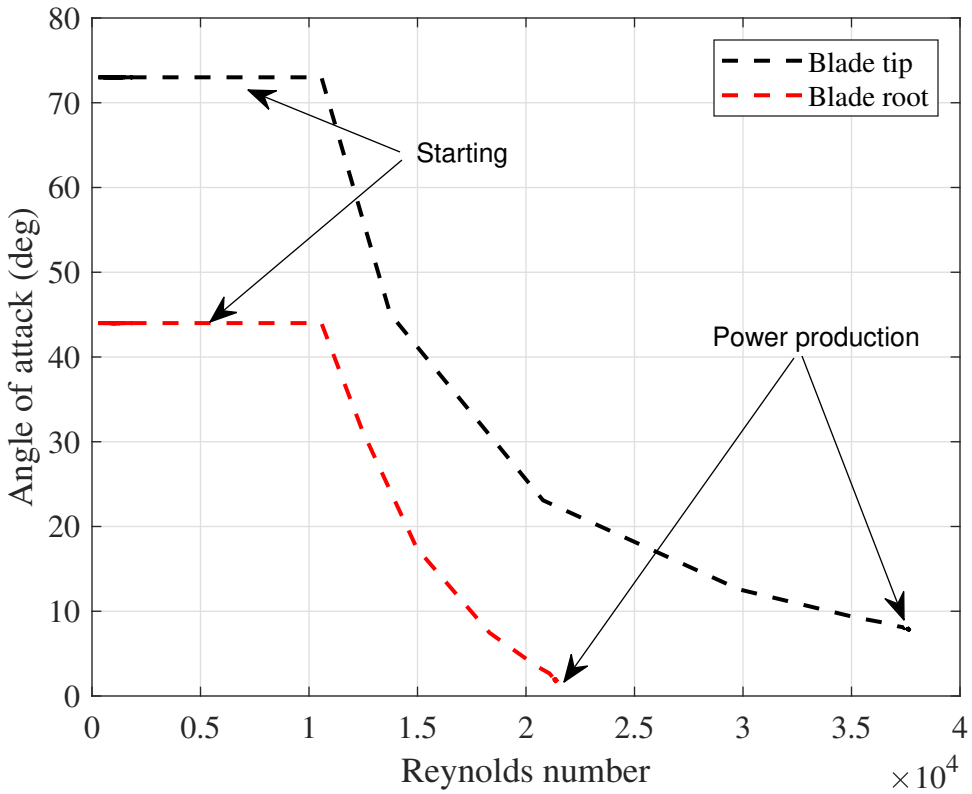


Figure 3.1: Operating path of a 3-bladed waterpumping windmill model.

### 3.1.1 Aerodynamics of low Reynolds number airfoils

It is instructive to understand the underlying characteristics of low  $Re$  number airfoil aerodynamics before examining the impact of geometrical parameters on their performance. Airfoils at high  $Re > 10^6$  are well understood. For these high  $Re$  airfoils, the boundary layer at first is laminar from the leading edge. The extent of the laminar flow decreased with an increase in  $Re$  before transitioning to turbulent flow with a negligible effect on the airfoil performance. However, at low  $Re$ , the flow is fundamentally different, exhibiting unusual aerodynamics characteristics and becoming more complex. Its boundary layer separates due to low kinetic energy; that is, it physically detaches from the airfoil surface—the resulting unstable flow transitions to turbulent flow in the free air. If the  $Re$  is very low or the point of laminar separation is sufficiently far aft, the flow will not reattach and becomes fully separated. The occurrence of laminar separation closer to the leading edge, the transition to turbulence,

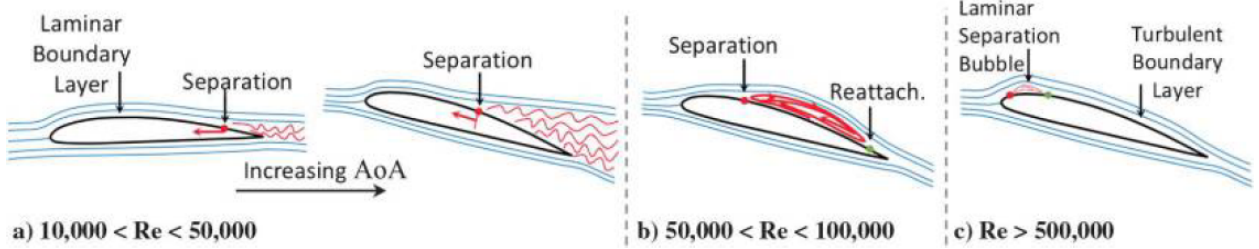


Figure 3.2: Typical airfoil separation characteristics at different regimes of  $Re < 10^6$ . Adapted from [106].

and ensuing reattachment is aptly referred to as the “laminar separation bubble” (LSB). The reluctance of the boundary layer to transition naturally is responsible for the degrading airfoil performance with decreasing  $Re$ .

LSB length and behavior are dependent on the airfoil type,  $Re$ , and  $\alpha$ , typically moving toward the leading edge with increasing  $\alpha$ , as illustrated in Figure 3.2. Airfoil drag reduction is mainly achieved by decreasing the size and extent of the bubble. The lowering of the impact of LSB is of great importance at low  $Re$ , which is usually achieved with proper airfoil designs [110]. However, this design development is beyond the scope of the current study. Interested readers are advised to consult Ref. [47] for further information.

## 3.2 Airfoils for SWTs

SWTs operate in low  $Re$  flow regimes, where laminar separation bubble effects can severely degrade their performance. While airfoil sections designed for the outer part of large blades may be suitable for SWTs as their thickness is  $< 20\%$ , root airfoils with greater thickness are not. Thick airfoils can have leading edge separation at very low  $\alpha$ . Hence, airfoils are being developed explicitly for SWTs applications. Notable airfoil developments for high aerodynamic performance were studied by Tangler and Somes [111] and Selig and Giguere [112] for stall-regulated, variable pitch, variable rpm and changing windspeeds rotors. Recent computational studies include that by Osei et al. [113] and Leloudas et al. [114]; however, only very few incorporated starting performance in their airfoil design e.g. [108, 109, 115].

Additionally, large  $\alpha$  up to  $90^\circ$  are not considered by most of these studies, which are, therefore, of little benefit to fixed pitch SWT starting performance prediction analysis.

### 3.3 Test setup and airfoil models

#### Experimental facility and measurement techniques

Part of the original intent of this study is to replicate and extend the measurements on an airfoil model of Bruning [26] to that of Wegereef [25] and measure the static and dynamic forces of the model in the University of Calgary RWT at low  $Re$ . It has a square cross-section of  $1 \times 1$  m and a length of 9.6 m with a 5.76:1 contraction ratio (see Figure 3.4). Its combined turbulence intensity and unsteadiness were determined to be 0.3%. Further details about the tunnel are provided in Chapter 6. As seen in Figure 3.3, the tunnel needs modification for airfoil testing. Thus, a test stand that houses the driving mechanism assembly and to which the model and measuring equipment are affixed was built and then attached to the adjustable t-slot horizontal bar downwind of the tunnel contraction, as shown in Figure 3.5. Note that the test section in Figure 3.5 is modified to an approximately closed test section with acrylic plates on all four sides (i.e., top, bottom, left, and right sides). The purpose is to investigate the influence of wind tunnel configuration on the airfoil's performance, in particular, is to check for the presence of "second stall" phenomenon at high  $\alpha$  in closed jet tunnels according to [68].

#### Airfoil models

The profile of the airfoils tested are circular-arc, designated CAYYXX following and expanding on the notation adopted by [116]. The circular-arc sections are indicated by the capital letters CA, followed by a four-digit number wherein YY and XX, respectively, denote the camber and thickness in percent of the chord length. In Table 3.1, the geometrical characteristics of the three circular-arc airfoils and NACA0012 are presented. The CAA models



Figure 3.3: Red wind tunnel working section (upstream view).

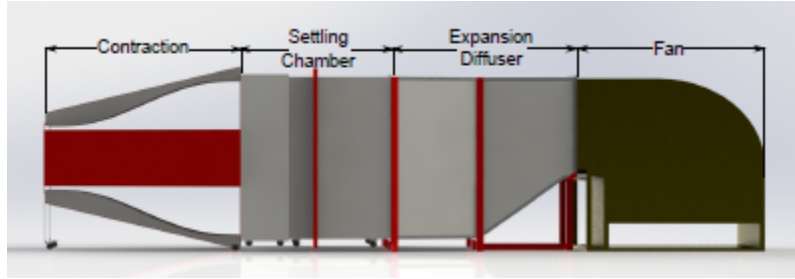


Figure 3.4: Schematic of tunnel.

are shown in Figure 3.6 with varying thickness, ( $t/c$ ), camber, ( $h/c$ ), chord-to-tunnel height ratio, ( $c/H$ ), span,  $b$  and aspect ratios ( $AR$ ), intended to investigate the effect of a change in these variables on the lift and drag performance characteristics. At  $\alpha = 90^\circ$ , the maximum tunnel blockage of CA2010, CA1705, CA1604 and NACA0012 are 6 %, 13.83 %, 10.83 % and 10.88 % respectively. To validate the RWT measurements, the NACA0012, one of the

most common and widely researched airfoils with a large bank of experimental and numerical data, was selected. The models were confined between the adjustable top and bottom acrylic end plates spanning the height of the test section.

As suggested by [117], the ends of the top and bottom plates were equipped with a 3D printed super-elliptic leading edge to minimize the possibility of leading-edge flow separation. The model airfoils were designed in SolidWorks and manufactured by fused deposition modeling (FDM) using PLA. Due to the 3D-printer dimension and for convenience, each model was printed in several sections of equal height depending on the model span, with a mean surface tolerance of  $\pm 0.01$ , as illustrated in Figure 3.7. The sections are then glued

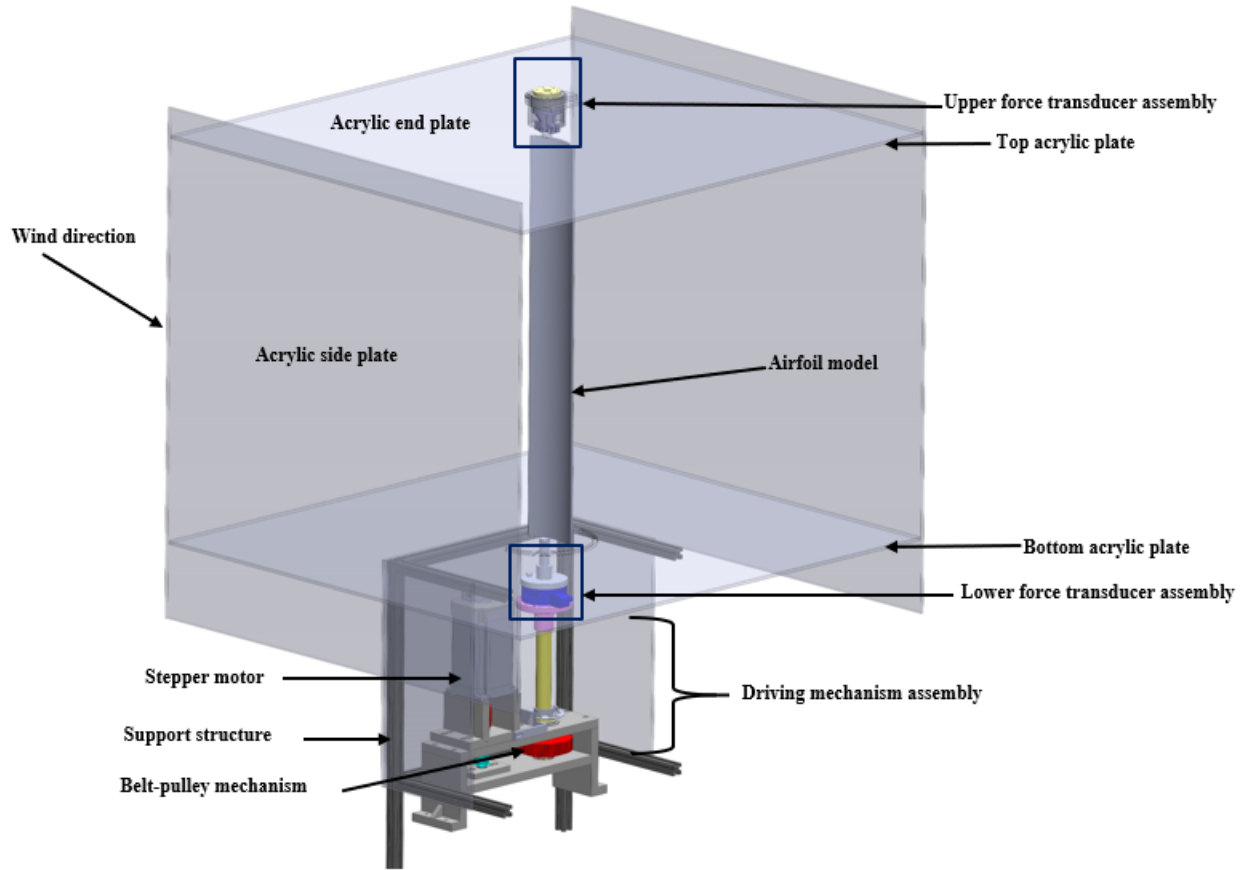


Figure 3.5: Experimental set up of airfoil performance measurement. The acrylic side plates were used to form the closed jet tunnel (CJT) working sections and removed for the open jet tunnel (OJT) tests.

together on a  $1/8''$ ,  $3/16''$  and  $1/4''$  shaft appropriate to the thickness of the models which goes through the quarter chord centreline of the airfoil. The shaft extends out of both ends of the models into two aluminum tubes for easy mounting. Small gaps due to manufacturing errors were filled with an all-purpose filler. As surface precision is not typically high with FDM, the assembled models were sanded to obtain a relatively fine finish. Finally, the models were coated with WEST SYSTEM® epoxy for a smooth surface finish. Each model was aligned for zero yaw during installation by ensuring that the leading and trailing edges were perpendicular to the lower and upper acrylic plates using a combination of an  $8''$  torpedo level and T square.

Table 3.1: Airfoil models and geometry.

Profile name	$c$ (mm)	$b$ (mm)	$t/c$ (%)	$h/c$ (%)	$c/H$	$AR$
CA2010	100	600	10	20	0.1	6
CA1705	165	840	5	17	0.17	5.2
CA1604	190	570	4	16	0.19	3
NACA0012	150	725	12	-	0.15	4.8

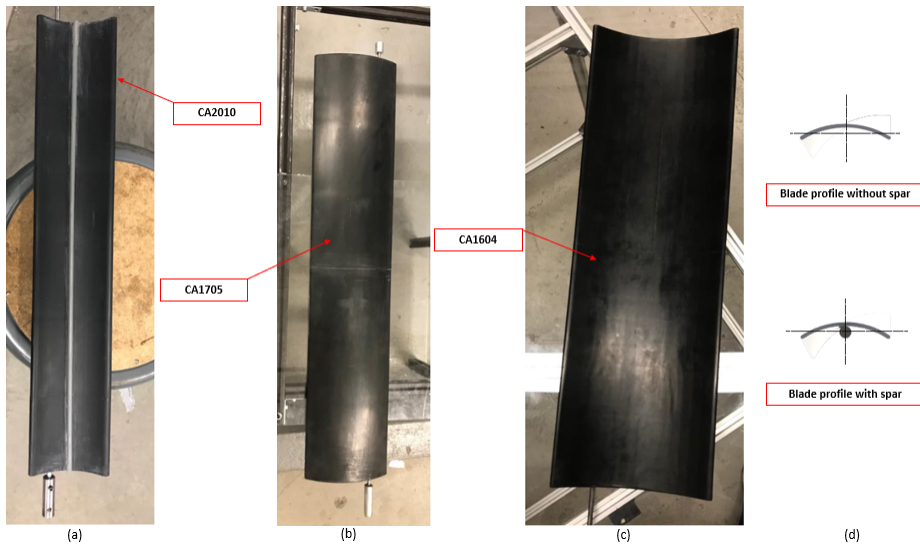


Figure 3.6: CAA models and profile configuration.

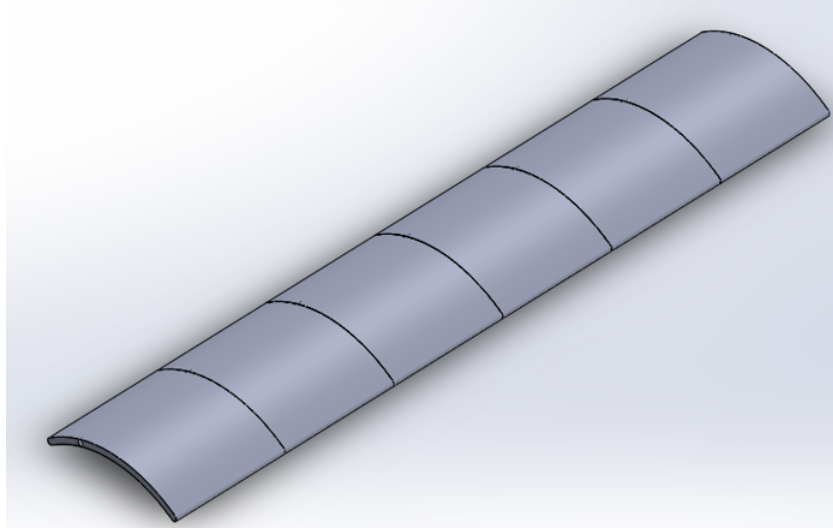


Figure 3.7: SolidWorks designed and assembled airfoil sections.

### Test matrix

The testing was quite extensive. It entailed measurements of CAAs without and with a spar ( $1/4"$  diameter PVC rod glued to the  $0.5c$  position on the high-pressure side of the airfoil, which maximizes the lift-drag ratio as suggested by Bruining [26], see Figure 3.6. The steady-state tests involved force measurements conducted at wind velocities ranging from 2 to 15 m/s corresponding to three  $Re$  for both increasing  $\alpha$  from  $-10^\circ$  to  $90^\circ$  and decreasing  $\alpha$  from  $90^\circ$  to  $-10^\circ$  to document any aerodynamic hysteresis. However, the CA2010 testing was extended to eight  $Re$  to obtain a wide range of data for large cambered and thick circular-arc airfoil, typically rare in the open literature. Unsteady measurements were conducted only for the arbitrarily selected CA1604 airfoil model at the  $Re$ , reduced frequencies,  $k$ , amplitude angle,  $\alpha_a$ , and mean angles of attack,  $\alpha_m$ , listed in Table 3.2 along with the steady measurement tests. Each of the experiments was conducted at least twice to determine its repeatability.

## 3.4 Measurement of static and dynamic aerodynamic forces

While the static measurements were conducted in both open-jet (OJT) and closed-jet (modified open jet) (CJT) flow conditions, as shown in Figures 3.8 and 3.9, the dynamic force measurement were done only in open jet flow condition. For both test conditions, the models were mounted vertically at the center of the wind tunnel test section between two ATI six-axis force/torque transducers (F/T) shown in Figure 3.5. F/T (Mini40 IP68) force sensing range is 20 N in the x- and y-direction with a resolution of 1/200 N. The lower F/T has a force resolution of 1/160 N and a maximum sensing capacity of 32 N in the x- and y-direction. The upper F/T (Gamma SI-32-2.5) was mounted on a spherical rod and rotated freely with the airfoil, just like the lower F/T. The F/T sensors output voltage signals in the range of  $\pm 10$  V and were connected to National Instruments data acquisition cards,

Table 3.2: Summary of airfoil experimental tests.

<i><b>Steady test conditions</b></i>				
Tunnel Type	Open jet tunnel			Closed jet tunnel
Airfoil type	Spar	No spar	Spar	No Spar
Nature of $\alpha$	Increasing $\alpha$	Decreasing $\alpha$	Increasing $\alpha$	Decreasing $\alpha$
<b>Airfoil section</b>	<b>Nominal Re</b>			
CA2010	30,000, 40,000, 50,000, 60,000, 70,000, 80,000, 90,000, 100,000			
CA1705	30,000, 60,000, 100,000			
CA1604	30,000, 60,000, 100,000			
NACA0012	86,000, 150,000			
<i><b>Unsteady test conditions</b></i>				
Tunnel type	Open jet tunnel			
Airfoil type	No spar (clean model)			
k	0.01, 0.02, 0.03, 0.04, 0.05, 0.06			
$\alpha_m$	45			
$\alpha_a$	45			
Cycles	5			
<b>Airfoil section</b>	<b>Nominal Re</b>			
CA1604	60,000, 100,000			

NI-DAQ 6212, consisting of 16 channels with a resolution of 16 bits that receive the analog transducer signals and convert them to force and moment using the calibration matrix furnished by ATI. Using an external trigger, the two cards were synchronized to start acquisition simultaneously. Two 4.5 mm thick and  $900 \times 900$  mm acrylic sheets were used to isolate the free ends of the model from the tunnel upper and lower wall boundary layers and serve as a support. Spaces between the model and the sheets were nominally less than 2 mm. In the closed tunnel section shown in Figure 3.9, two side walls of acrylic sheets with dimensions  $900 \times 900 \times 45$  mm were mounted to simulate a closed test section.

Motion was generated by a pulley-belt system shown in the test stand of Figure 3.5 and driven by a stepper motor (86STH156 NEMA-34 Bipolar Gearless Large Stepper). The motor commands coded on an Arduino board, send the motion parameters such as initial angle, final angle, step angle and speed for the steady experiment, whereas  $\alpha_m$ ,  $\alpha_a$ , and frequency,  $w_p$  parameters were sent to produce sinusoidal motion for the unsteady test. The driver module has a resolution of 256 micro-steps, equivalent to a motor angle of  $0.00703^\circ$ . To accurately evaluate the angle position, the stepper motor was integrated with an optical encoder having a resolution of  $0.0625^\circ$ . Given that the motor torque rating is increased by a factor of 4 from 10 Nm, the maximum rotor speed is reduced by a similar factor to 350 rpm.

Because the measured static force is a sum of the aerodynamic, inertial, and frictional forces acting on the models, the aerodynamic load of interest is obtained by a difference between the measured force for a given run and the force at  $U_\infty = 0$  (i.e., when wind tunnel is off). A GUI MATLAB program was used to acquire the static force readings for  $\alpha$  in increments of  $5^\circ$  after specifying the flow settings and motion parameters at a sampling rate of 20 Hz. With the force transducers pitching with the model, the unsteady data were recorded at 200 Hz. For the dynamic test, tare deduction and low-pass filtering were applied when processing the unsteady data. Tare deduction eliminates the force contributions due to steady and unsteady inertia and friction associated with the test setup. The measured

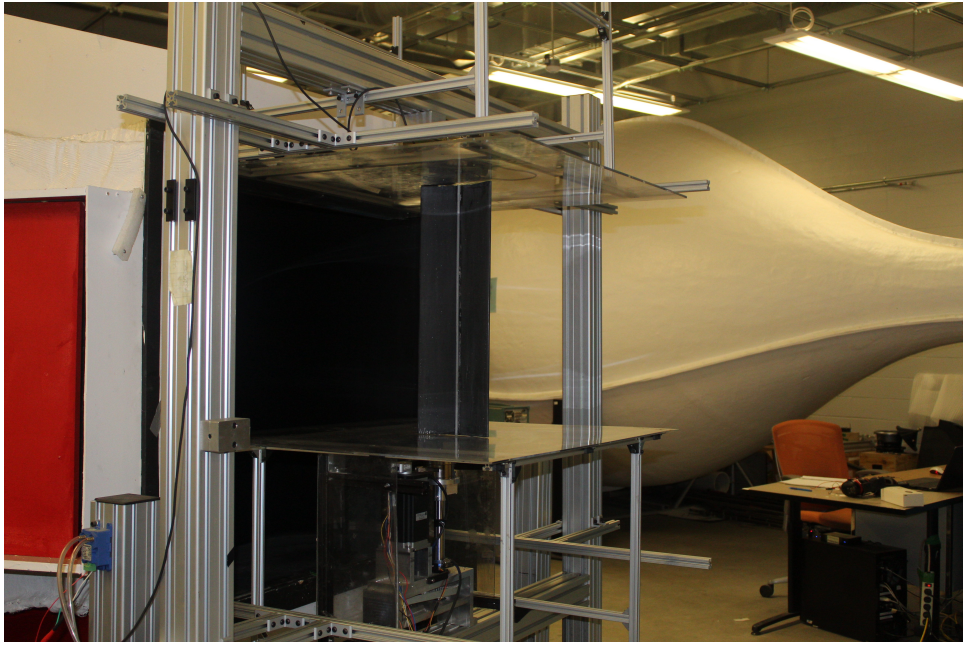


Figure 3.8: Open jet tunnel test section with airfoil model.



Figure 3.9: Modified open tunnel test section with airfoil model.

forces at  $U_\infty = 0$  were systematically subtracted from the force measured at the same reduced frequency as the free stream. More importantly, the unsteady tare subtraction is expected to expunge the non-circulatory parts of the aerodynamic loading, such as added mass and inertia owing to accelerating air around the model. However, these effects are only significant

for reduced pitch rate,  $k_p > 0.2$  [118] that is, at much higher frequencies than those used here.

The system of forces acting on the airfoil relative to the chord and the wind directions are illustrated in Figure 3.10. The normal forces,  $F_N$ , and the axial forces,  $F_A$ , were measured directly by the sensors and their total calculated by the addition of the force readings from the upper and lower F/T, and then their force coefficients are computed according to

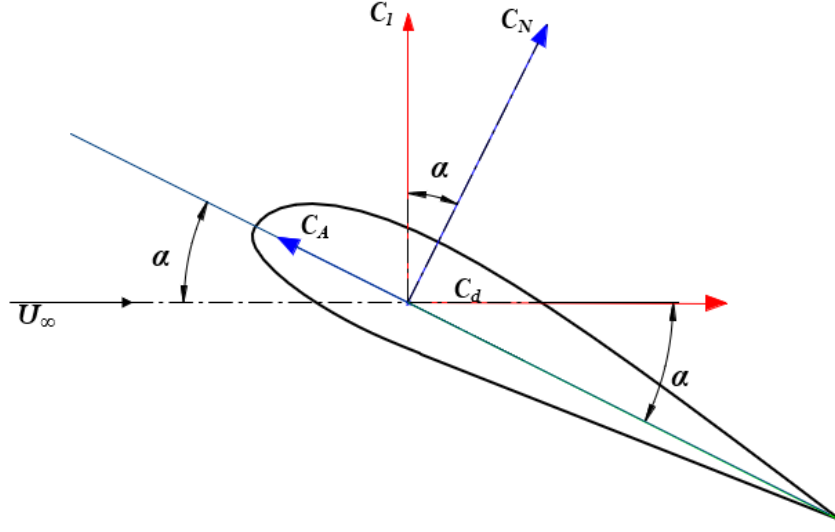


Figure 3.10: Force coefficients system.

$$C_N = \frac{F_{N1} + F_{N2}}{\frac{1}{2}\rho U_\infty^2 bc} \quad (3.1)$$

and

$$C_A = \frac{F_{A1} + F_{A2}}{\frac{1}{2}\rho U_\infty^2 bc} \quad (3.2)$$

where subscripts “1” and “2” denotes the lower and upper force measurements. The lift and drag coefficients are then obtained as:

$$C_l = C_N \cos \alpha + C_A \sin \alpha \quad (3.3)$$

and

$$C_d = C_N \sin \alpha - C_A \cos \alpha \quad (3.4)$$

### 3.5 Experimental uncertainty analysis

For completeness, experimental results are presented along with their associated uncertainties, defined as the difference between the value of experimental measurement and the true value of a measured property. Basically, there are two types of uncertainties: systematic and random. Systematic uncertainties are due to constant (bias) offset, wrong calibration, temperature drift, and unaccounted friction; unpredictable variation in experimental conditions constitutes random uncertainty. Several measuring instruments and physical variables are involved, so the uncertainty must be carefully estimated to determine the accuracy of the results. Analysis of these uncertainties entails identifying and quantifying measurement errors, primarily originating from instrument inaccuracies, reading accuracy, angle of attack settings, data acquisition, and data reduction. For a given set of measurements, the uncertainty in the value of a result,  $R$ , a function of physical variables, is

$$R = R(X_1, X_2, X_3, \dots, X_N) \quad (3.5)$$

is given by [119]

$$U_R = \left\{ \sum_{i=1}^N \left( \frac{\partial R}{\partial X_i} B_i \right)^2 + \tau \sum_{i=1}^N \left( \frac{\partial R}{\partial X_i} S_i \right)^2 \right\}^{1/2} \quad (3.6)$$

where  $U_R$  is the overall uncertainty at the 95% confidence level obtained by root-sum-squares (RSS) summation,  $\frac{\partial R}{\partial X_i} B_i$  and  $\frac{\partial R}{\partial X_i} S_i$  represent respectively the contribution from systematic (bias) and random (precision) errors from any one of the variable,  $X_i$ .  $\tau$  is the Student's multiplier for the quoted confidence level and degrees of freedom of the precision index. Note Eq. (3.6) is valid so long as the following assumptions hold [119]:

1. Each measurement variable is independent.

2. Repeated runs of each dataset follow a normal distribution.
3. Initial estimates for each measurement are at the same odds (i.e., at 95% confidence level).

In a more simplistic form, Eq. (3.6) is expressed as

$$U_R = \sqrt{\left(\frac{\partial R}{\partial X_1} U_{X_1}\right)^2 + \left(\frac{\partial R}{\partial X_2} U_{X_2}\right)^2 + \dots + \left(\frac{\partial R}{\partial X_N} U_{X_N}\right)^2} \quad (3.7)$$

Using these variables, the propagated uncertainties in the axial and normal force coefficients directions were derived and expressed as

$$U_{C_N} = \sqrt{\frac{U_{F_{N1}}^2 + U_{F_{N2}}^2}{(F_{N1} + F_{N2})^2} + \frac{U_b^2}{b^2} + \frac{U_c^2}{c^2} + \frac{U_\rho^2}{\rho^2} + \frac{4U_\infty^2}{U_\infty^2}} \quad (3.8)$$

$$U_{C_A} = \sqrt{\frac{U_{F_{A1}}^2 + U_{F_{A2}}^2}{(F_{A1} + F_{A2})^2} + \frac{U_b^2}{b^2} + \frac{U_c^2}{c^2} + \frac{U_\rho^2}{\rho^2} + \frac{4U_\infty^2}{U_\infty^2}} \quad (3.9)$$

Following from Eq. (3.7), the uncertainties in the lift and drag coefficients of Eqs. (3.3) and (3.4) are:

$$U_{C_l} = \sqrt{U_{C_{N1}}^2 \cos(\alpha_1)^2 + U_{C_{A1}}^2 \sin(\alpha_1)^2 + U_{\alpha_1}^2 (C_{A1} \cos(\alpha_1) - C_{N1} \sin(\alpha_1))^2} \quad (3.10)$$

$$U_{C_d} = \sqrt{U_{C_{A1}}^2 \cos(\alpha_1)^2 + U_{C_{N1}}^2 \sin(\alpha_1)^2 + U_{\alpha_1}^2 (C_{N1} \cos(\alpha_1) + C_{A1} \sin(\alpha_1))^2} \quad (3.11)$$

Table 3.3 presents the uncertainty estimates of the measured and calculated variables according to Eq. (3.7) with respect to a defined reference. A close observation shows that in comparison to other variables, the error in velocity is the highest, resulting in a high  $Re$  error. This is due largely to its dependence on the uncertainty of the measured ambient conditions of the wind tunnel and, of course, the data acquisition process.

Graphical plots of the uncertainties associated with a representative force measurement in the form of error bars are depicted in Figure 3.11(a) for typical measurements of  $C_N$  and

Table 3.3: Uncertainty measurements values for elemental and propagated error sources.

Variable	Units	Mean reference	Absolute uncertainty	Relative uncertainty
c	m	0.1638	$\pm 9.1 \times 10^{-5}$	$\pm 0.056 \%$
b	m	0.8395	$\pm 5.2 \times 10^{-4}$	$\pm 0.062 \%$
$\alpha$	deg	4.875	$\pm 0.125$	$\pm 2.56 \%$
$\rho$	kg/m <sup>3</sup>	1.029	$\pm 0.006$	$\pm 0.58 \%$
T	deg	24.85	$\pm 1.0115$	$\pm 0.34 \%$
p	Pa	$8.8 \times 10^4$	$\pm 400.05$	$\pm 0.45 \%$
$U_\infty$	m/s	9.16	$\pm 0.2962$	$\pm 3.23 \%$
$Re$	-	$1 \times 10^5$	$\pm 3.25 \times 10^3$	$\pm 3.25 \%$

$C_A$  and Figure 3.11(b) for  $C_l$  and  $C_d$ . For reference, at  $\alpha = 20^\circ$ , the nominal  $C_l$  is 1.698 with an absolute uncertainty of  $\pm 0.02$ , while the nominal  $C_d$  is 0.4146 with absolute uncertainty is  $\pm 0.06$ .

## 3.6 Wind tunnel boundary corrections

Flow conditions in a finite wind tunnel are different from those of an unbounded (free) flow. Extraneous forces due to boundary effects are produced in both open and closed jet tunnels, which must be accounted for in the aerodynamic force coefficients computation.

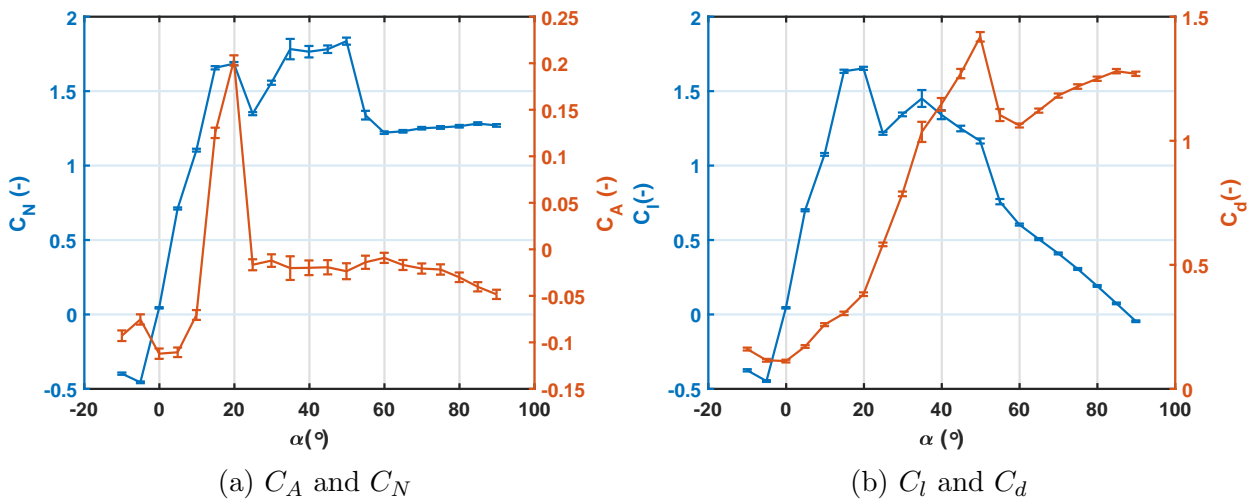


Figure 3.11:  $C_A$ ,  $C_N$ ,  $C_l$  and  $C_d$  measurements and their uncertainty for CA1705 at  $Re = 1.0 \times 10^5$  in the open test section.

Also, a longitudinal static pressure drop occurs in the closed jet test section. While there are many studies on closed jet tunnels such as [120,121], at low  $\alpha$  and low blockage, only a few studies have investigated high blockage over a wide range of  $\alpha$  up to  $180^\circ$  such as [122]. The boundaries in two-dimensional testing cause the following phenomena in both closed and open test sections [47,123,124]:

1. Horizontal buoyancy: an extra drag force that results from static pressure drop along the test section due to the thickness of the boundary layer at the walls increasing along the tunnel. Usually, the buoyancy effects are considered in the freestream velocity corrections. With an open test section, the pressure drop is negligibly small, and so is the effect of buoyancy.
2. Solid blockage: produces a reduction in the effective area due to the physical presence of the model within a test section. It is a function of the model size and test section dimensions.
3. Wake blockage: results from a low velocity within the airfoil wake compared to the free stream. Wake blockage is proportional to the wake size and thus to the measured drag force on the model. For flows beyond the post-stall region, separation occurs at the suction side, giving rise to separation blockage. The effect of the separated flows over the airfoil requires correction.
4. Streamline curvature: owing to the physical constraints of the tunnel boundaries, the normal curvature of free air as it passes over a lifting body such as an airfoil is altered, increasing the airfoil's effective camber as the streamlines are squeezed together. For a closed wind tunnel section, streamline curvature increases lift and quarter chord pitching moment and angle of attack, while the drag is unaffected. However, for an open tunnel, the measured drag and lift are overestimated and underestimated, respectively [121].

5. Downwash: the airfoil is made to either span the tunnel dimensions or confined between the infinite walls of large dimensions compared to the airfoil section dimension to ensure two-dimensionality in airfoil section testing. Usually, the open jet exceeds the airfoil span as it does in this study. Thus, the velocity at any point of the lifting line results from the free stream and an induced velocity orthogonal to the free flow direction. The downwash velocity tends to lower the  $\alpha$  and the  $C_l$  and, at the same time, increases the  $C_d$ .

For open jet flow, the flow freely expands, so solid and wake blockage are usually neglected; however, the streamline curvature and downwash may be significant. Therefore streamline curvature, and downwash corrections need to be applied to the lift and drag coefficients. Based on conflicting assumptions, both methods cannot be applied simultaneously, according to Fuglsang et al. [123]. For the present study, the correction applied is that due to Brooks et al. [125] and is given by

$$C_m = C_{mu} - \frac{\sigma_a}{2} C_{lu} \quad (3.12)$$

$$\alpha = \alpha_u - \frac{\sqrt{3\sigma_a}}{\pi} C_{lu} - \frac{\sqrt{2\sigma_a}}{\pi} C_{lu} - \frac{\sqrt{\sigma_a}}{\pi} 4C_{mu} \quad (3.13)$$

$$C_d = C_{du} + \left[ -\frac{\sqrt{3\sigma_a}}{\pi} C_{lu} \right] C_{lu} \quad (3.14)$$

For the above,

$$\sigma_a = \frac{\pi^2}{48} \left( \frac{c}{H} \right)^2 \quad (3.15)$$

where  $C_{mu}$  is the measured pitching moment coefficient,  $\alpha_u$  is the uncorrected angle of attack, and  $C_{du}$  is the measured drag coefficient. Similarly, the measured aerodynamic forces in CJT, which approximate a closed test section, include the contribution from the solid, wake, and separation blockages and are corrected using the approach of Garner et al. [120]. The solid

blockage correction factor,  $\varepsilon_s$  according to [120, 126] is calculated as follows:

$$\varepsilon_s = 0.524 \left[ 1 + 1.2\beta \left( \frac{t}{c} \right) \right] \frac{A_c}{\beta^3 H^2} \quad (3.16)$$

where  $A_c$  denotes the cross-sectional area of the airfoil, and  $\beta$  is the Prandtl-Glauert factor that accounts for the compressibility effect, which is a function of  $M$ , the Mach number. For incompressible flows considered here,  $M$  was set to zero, therefore  $\beta \approx 1$ .

The wake blockage correction factor,  $\varepsilon_w$  [120, 126] is:

$$\varepsilon_w = 0.25 \left( \frac{c}{H} \right) \frac{1 + 0.4M^2}{\beta^2} C_{du} \quad (3.17)$$

The classical method for correcting separated flow is based on experimental results of a bluff body with edge separation. Maskell [124] conducted a series of experiments on a flat plate with varying  $AR$  in a closed jet wind tunnel. The results yield

$$\varepsilon_{sep} = 0.5\theta_s \left( \frac{t}{c} \right) C_{du} \quad (3.18)$$

where  $\theta_s$  is the separation blockage factor. Based on [124], the separation factor for two-dimensional flow was suggested to be 0.96 [126]. Eq. (3.18) is valid for low blockage in the pre-stall region and was determined from separated flows of a flat plate, whose applicability to airfoil over a wide range of  $\alpha$  is questionable. Thus, Kang et al. [122] developed a separation blockage correction for high blockage at large  $\alpha$  up to  $180^\circ$  for the airfoil of a wind turbine. The separation blockage is defined as

$$\varepsilon_{sep} = \begin{cases} \frac{1}{6} \left( \frac{c/h}{1-c/h} \right) C_{ds}, & \text{for } 0^\circ \leq \alpha \leq 90^\circ \\ \frac{1}{3} \left( \frac{c/h}{1-c/h} \right) C_{ds}, & \text{for } 90^\circ \leq \alpha \leq 180^\circ \end{cases} \quad (3.19)$$

where  $C_{ds} = C_{du} - C_{di} - C_{dm}$  is the separation drag coefficient,  $C_{di}$  is the induced drag coefficient and  $C_{dm}$  is the minimum drag coefficient. Because this study involves measurement

at large  $\alpha$ , Eq (3.19) was used to compute  $\varepsilon_{sep}$ .

In addition to the effects of blockage on the wind tunnel data, lift interference between the airfoil and the tunnel boundaries needs to be considered. On the assumption that the model is located at the center of the test section, the extra corrections on  $\alpha$ ,  $C_l$ ,  $C_d$  and  $C_m$  are:

$$\Delta\alpha = \frac{\pi c^2}{96\beta H^2} (C_{lu} + 4C_{mu}) - \frac{7\pi^3 c^4 C_{lu}}{30720\beta^3 H^4} \quad (3.20)$$

$$\Delta C_l = C_{lu} \left\{ -\frac{\pi^2}{48} \left( \frac{c}{\beta H} \right)^2 + \frac{7\pi^4}{3072} \left( \frac{c}{\beta H} \right)^4 \right\} \quad (3.21)$$

$$\Delta C_d = (C_{dm} + C_{ds})(1 + 0.4M^2)\varepsilon_s \quad (3.22)$$

$$\Delta C_m = C_{lu} \left\{ \frac{\pi^2}{192} \left( \frac{c}{\beta H} \right)^2 - \frac{7\pi^4}{15360} \left( \frac{c}{\beta H} \right)^4 \right\} \quad (3.23)$$

Therefore, the final corrections for the dynamic pressure, angle of attack, lift coefficient, drag coefficient, and pitching moment coefficient as given by [120, 122, 126] are:

$$q = q_u(1 + \varepsilon_T(2 - M^2)) \quad (3.24)$$

$$\alpha = \alpha_u + \Delta\alpha \quad (3.25)$$

$$C_l = (C_{lu} + \Delta C_l) \frac{q_u}{q} \quad (3.26)$$

$$C_d = (C_{du} + \Delta C_d) \frac{q_u}{q} \quad (3.27)$$

$$C_m = (C_{lu} + \Delta C_m) \frac{q_u}{q} \quad (3.28)$$

where,  $q_u$ , is the uncorrected dynamic pressure, and  $\varepsilon_T = \varepsilon_s + \varepsilon_w + \varepsilon_{sep}$ .

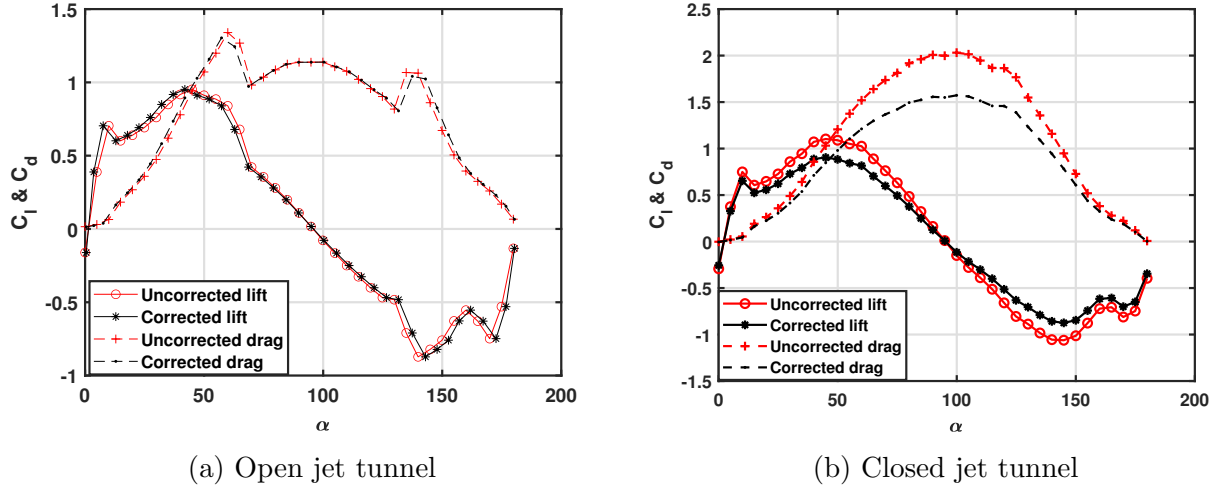


Figure 3.12: NACA0012: Wind tunnel uncorrected and corrected lift and drag data for  $Re = 1.5 \times 10^5$ .

Figure 3.12 compares the corrections in the open jet test section to that of the closed one. It can be seen that the effect on the former is nearly negligible but very significant for the latter, especially for  $C_d$  in the post-stall region.

### 3.7 Steady aerodynamic performance

In this section, the static lift and drag coefficients results of the CAAs detailed in Table 3.2 are presented and discussed. The pitch moment coefficients,  $C_m$  were obtained but only used in the  $\alpha$  correction formula, though useful in self-acting variable pitch VAWTs [127], no further analysis of it is presented in the remainder of this chapter since it is not important for HAWTs. The corrected aerodynamic data are presented in Appendix A for reference as they are also valuable for applications such as MAV [106] and sails [58], where aerodynamic data of highly cambered airfoils at low  $Re$  are desirable.

### 3.7.1 NACA0012 performance

Independent measurements obtained from different tunnel facilities rarely give consistent results even with the same airfoil model and geometry. This fact is substantiated by the assessment study on an extensive database of experimental results of NACA0012 obtained in more than 40 wind tunnels done by McCroskey [128] for higher  $Re$ . Wind tunnel data for  $Re$  below  $10^5$  are no exemption, and even worse, especially because laminar separation and the formation and collapse of LSBs make performance difficult to predict. For this flow regime, a small variation in  $Re$  or turbulence level can significantly affect the airfoil performance; therefore, it is imperative to compare the RWT airfoil performance results at different  $Re$  with those obtained from other facilities.

To validate the directly measured loads obtained from this study, NACA0012, a popular and widely researched airfoil, was tested at two  $Re$ s of  $0.86 \times 10^5$ , and  $1.5 \times 10^5$  and compared with published results at one test condition ( $Re = 1.5 \times 10^5$ ). Beyond validation, these results also provide insight into the effects of low  $Re$  on airfoil performance. All of the test data of the present work relate to corrected closed and open test sections for the stated  $Re$ . While the open tunnel measurements were corrected for streamline curvature only using Eqs. (3.12–3.14), solid and wake/separation blockages were corrected for in the closed tunnel results using Eqs. (3.25–3.28). The variation of lift,  $C_l$  and drag,  $C_d$  coefficients over the  $180^\circ$  range of  $\alpha$  are presented in Figures 3.13a and 3.13b, respectively.

Airfoil performance coefficients from the open test (OJT) are plotted together with those from the modified open test section (CJT). Data from selected studies, specifically Sheldahl and Klimas [64], Rainbird et al. [65] and Worasinchai et al. [67] are also plotted for comparison. These references and those of this study are summarized in Table 3.4 highlighting important factors that influence airfoil aerodynamic performance measurement in different wind tunnels.

For a range of  $\alpha$ , one can observe that in the inset of Figure 3.13a,  $C_l$  is almost linear in  $\alpha$  up to the first stall, whereas  $C_d$  begins to experience a rapid increase as depicted in the

Table 3.4: Summary of NACA0012 studies referenced.

Source	$Re (\times 10^5)$	c/H	AR	I	Tunnel type
Sheldahl and Klimas [64] <sup>a</sup>	1.6	0.07	6.0	1.38 <sup>b</sup>	Closed
Rainbird [65]	1.5	0.27	3.5	0.15%	Closed <sup>c</sup>
	1.5	0.32	3.0	0.15%	Closed
Worasinchai et al. [67]	1.5	0.24	4.1	1% <sup>d</sup>	Open
Current study	1.5	0.15	4.8	0.3%	Open and closed <sup>e</sup>

<sup>a</sup> Not measured, data extrapolated from higher to lower  $Re$ .

<sup>b</sup> Turbulence factor given instead for correcting  $Re$ .

<sup>c</sup> Adaptive tunnel with slatted walls.

<sup>d</sup> Not given in Ref. [67], but because the same tunnel was used in [68], the reported value was assumed.

<sup>e</sup> Adapted open test section.

inset of Figure 3.13b. The OJT results are considered the base case in this study; its peak  $C_l$  is 0.72 at  $10^\circ$  and compares fairly well with that reported by [65] for  $c/H = 0.27$  but at a slightly increased  $\alpha = 10.6^\circ$ . At a larger  $c/H = 0.32$  for [65], a 24% increase in the peak  $C_l$  was obtained, which is slightly greater than that measured by Sheldahl and Klimas at a modestly increased  $Re$  of  $1.6 \times 10^5$ . Compared to OJT, the CJT measurements recorded a slightly reduced peak  $C_l=0.65$  at  $\alpha = 9.6^\circ$  similar in magnitude to those of [64, 65]. However, the highest  $\alpha$  corresponding to peak lift was reported by [67]. This stall delay is possibly due to the larger turbulence intensity of [67], which also lowers the measured lift.

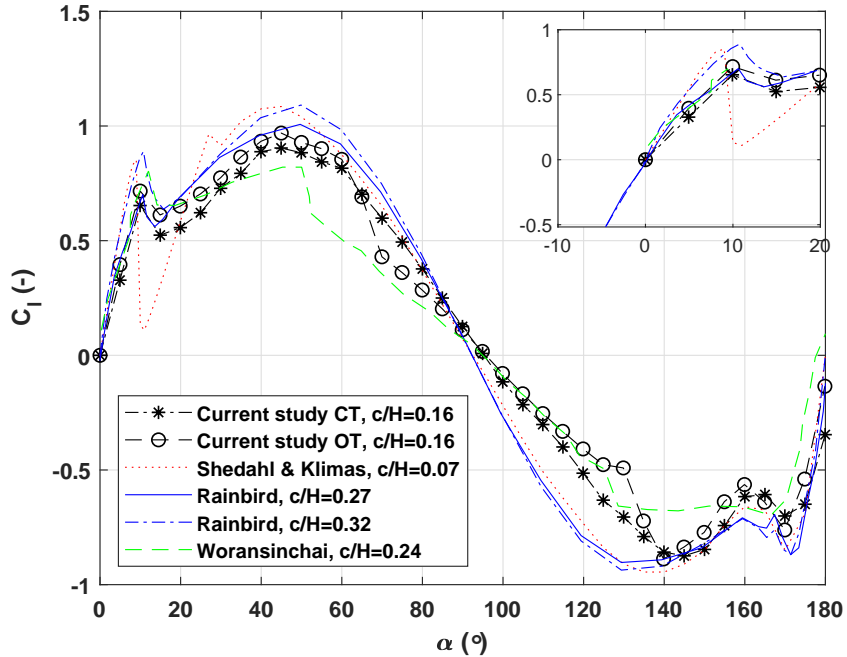
Tunnel blockage, measured by the chord-tunnel height ratio,  $c/H$ , is another factor that influences the airfoil performance wherein it increases the lift in the case of [65] even with blockage correction. Generally, slight discrepancies between the results of these experimental studies exist, which is not surprising. Airfoil model contour accuracy, surface roughness, and sensitivity of the airfoil boundary layer to freestream turbulence at low  $Re$  affect the laminar separation bubble. The airfoil surface roughness due to 3D printing as in the current study may impact the  $C_d$  performance of the airfoil at low  $\alpha$ . Three-dimensional effects due to endplates, though small, may be present, especially for directly measured forces where significant interference effects are likely to be induced on the airfoil resulting in loss of lift

and increased drag [129].

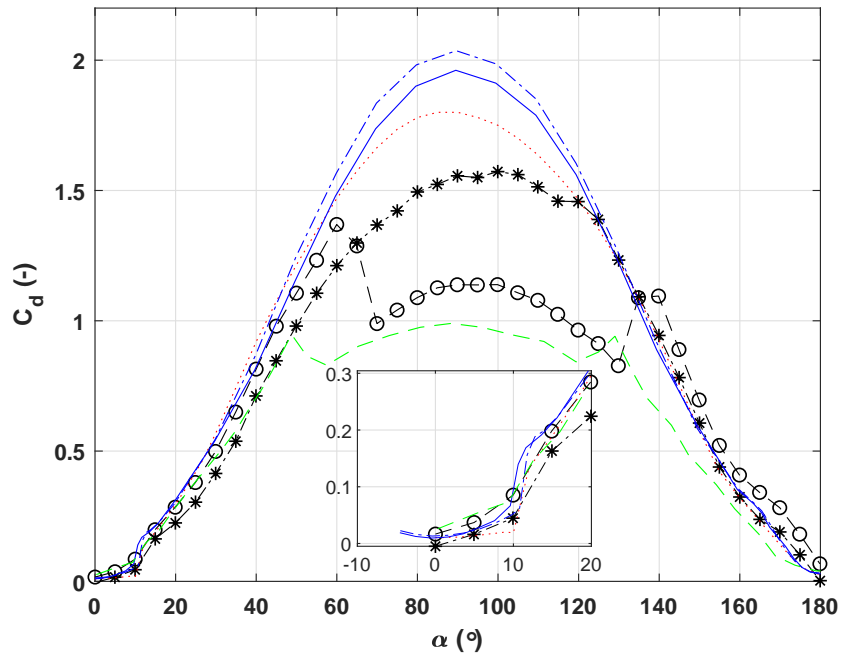
Beyond stall, the lift curves of Figure 3.13a drop gradually before slowly increasing to their post-stall peak values except for Klimas and Sheldahl [64], which falls very rapidly. The  $C_l$  falls to a value of 0.6 before rising to a 0.95 post-stall peak at  $\approx 42^\circ$ . The Sheldahl lift curve exhibits quite different characteristics beyond stall where  $C_l$  reduces significantly before sharply increasing to a second peak. While the underlying physics behind the dramatic loss in lift and sudden recovery in the post-stall regime is not exactly clear, it is pertinent to mention that their aerodynamic data were obtained using a computer code that extends the measured high  $Re$  values to low  $Re < 3.5 \times 10^5$  [64], without explicitly accounting for the changes in the flow. A close observation of Figure 3.13a reveals an interesting phenomenon at around  $65^\circ$ : the “second stall”, captured in the open tunnels of the current study and in that of [67] but not in the closed tunnels of [64, 65] or in that of the present study. The lift coefficient of OJT gradually increases from its minimum post-stall value of 0.61 at  $15^\circ$  to 0.97 at  $45^\circ$  before slowly dropping to 0.43 at  $70^\circ$ . When the LE of the airfoil is facing the wind at about  $90^\circ$ , the airfoil characteristics are mirrored, with a more gradual stall observed at  $170^\circ$  and a sudden second stall at  $140^\circ$ .

Flow visualization studies such as [68] suggest that the “second stall” occurs when the point of flow separation adjacent to the LE of an airfoil moves from the low-pressure side to the high-pressure side, leading to sudden changes in the wake structure. Similarly, second stall behavior was noticed in the measurements of [67] but with the second stall occurring earlier at around  $52^\circ$ . No discernable second stall was seen for the closed tunnels measurements of either the current study or the referenced data of [64, 65].

The drag coefficient of [65] reported a maximum of a little above 2 for  $c/H = 0.32$  consistent with [130] and a little less than 2 for  $c/H = 0.27$ , which is close to the values of a two-dimensional normal flat plate [131]. While Sheldahl and Klimas reported a lower  $C_d = 1.8$ , that from the CJT is considerably lower at  $C_d = 1.6$ . The  $C_d$  curves of Worasinchai [143] and the OJT show a sudden drop in the second stall angles, confirming the presence of



(a)  $C_l$  vs  $\alpha$

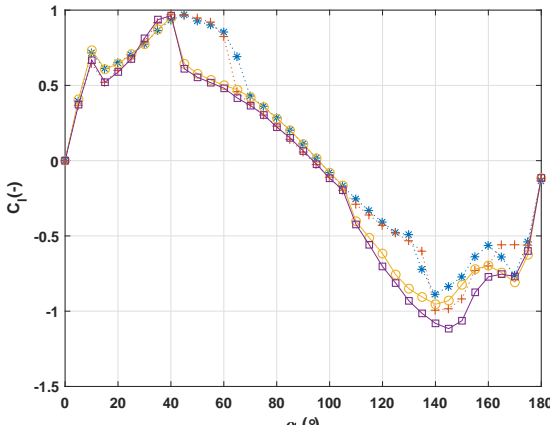


(b)  $C_d$  vs  $\alpha$

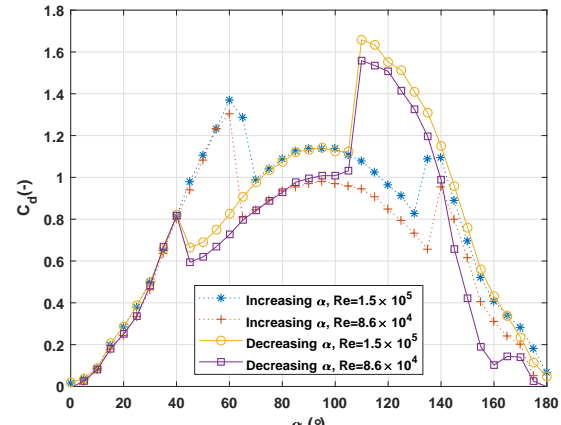
Figure 3.13:  $C_l$  and  $C_d$  vs  $\alpha$  for NACA0012 airfoil study in OJT and CJT sections alongside those reported by Sheldahl and Klimas [64], Rainbird et al. [65] and Woransinchai et al. [67]. The insets represent a magnified and detailed view for a limited range of  $0^\circ \leq \alpha \leq 20^\circ$ .

the second stall phenomenon. The observed discrepancies in the  $C_d$  curves are likely to be attributable to the factors listed in Table 3.4.

Disparities in flow behavior were observed between  $Res$  of  $1.5 \times 10^5$  and  $0.86 \times 10^5$  in Figures 3.14 and 3.15 for increasing  $\alpha$ . Most significant are the  $C_d$  values for  $Re = 0.86 \times 10^5$  at  $\alpha > 60^\circ$  in Figure 3.14(b) and at around  $\alpha > 40$  in Figure 3.15(b), which are surprisingly lower than that at  $Re = 1.5 \times 10^5$ , a departure from usual airfoil flow behavior with increasing  $Re$ . However, a computation and plot of  $C_l/C_d$  in Figure 3.16 for both the open and closed tunnel measurements produced much the same curve. The large  $\alpha$  probably changes the mechanism of pressure distribution on the lower and upper surface of the airfoil, giving rise to a higher drag force, which is compensated for by the increased lift. Apparently, the second stall does not appear to alter the direction of the total force, which explains the near constancy of  $C_l/C_d$ . It will be interesting to gain further insight into the fundamental physics of the pressure distribution; unfortunately, the pressure measurement data are unavailable with the direct force measurement used in the current study. Flow visualization studies, such as particle image velocimetry (PIV), are another useful tool to help with the physical mechanism of the flow. From these results, the performance characteristics of NACA0012 are  $Re$  sensitive, consistent with the findings of [106] for  $Re < 10^6$ .



(a)  $C_l$  vs  $\alpha$



(b)  $C_d$  vs  $\alpha$

Figure 3.14: Open jet tunnel measurements of NACA0012.

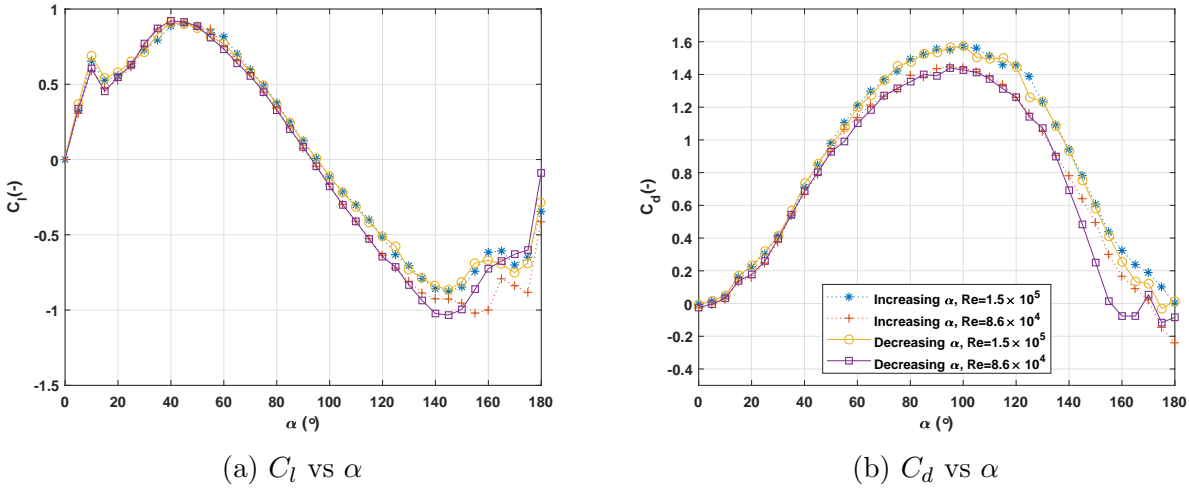


Figure 3.15: Closed jet tunnel measurements of NACA0012.

Hysteresis in airfoils is due to the difference in  $C_l$ ,  $C_d$  or  $C_m$  at a given  $\alpha$  when  $\alpha$  is approached from a higher and then a lower value. It can be viewed as the limiting case of unsteady behavior in which the reducing frequency,  $k \rightarrow 0$ , is significant for starting. Its effects on NACA0012 were cursorily examined. Also shown in Figures 3.14 and 3.15 is a comparison of the measured force coefficients acting on the airfoil over an increasing  $\alpha$  range from 0 to 180° and a decreasing  $\alpha$  range from 180 to 0° in the open and closed tunnels for two  $Re$ s. A larger hysteresis loop occurring around the post-stall peak region exists for the OJT compared to the CJT. The reason is not evident from the results but may be due to gross laminar separation coupled with the second stall phenomenon.

### 3.7.2 Effect of Reynolds number on circular-arc airfoils

The effect of  $Re$  variation on the aerodynamic characteristics of a CAA, both with and without (clean model) a spar at the 0.5c position, was examined using the CA1705 airfoil model. Figure 3.17 shows the corrected  $C_l$  and  $C_d$  at three  $Re$  under different wind tunnel testing conditions: open and closed. As shown in Figure 3.17(a), the lift coefficient at zero angle of attack,  $C_{l(\alpha=0)}$  is almost zero; thus, it appears that for the  $Re$  range considered, the wind tunnel does not see the curvature of the profile, similar to observation reported

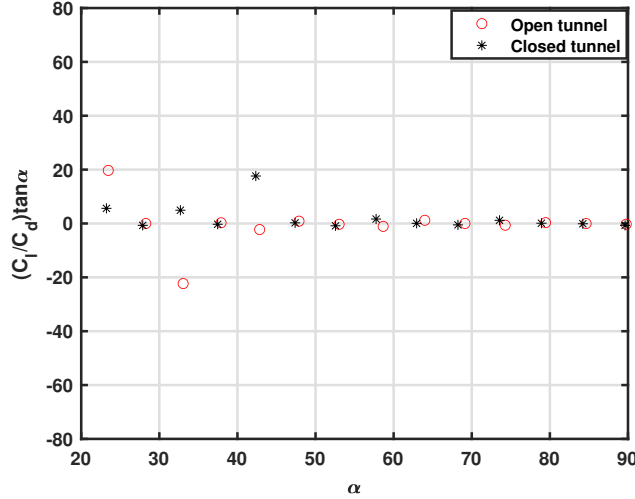


Figure 3.16: Relationship between  $C_l$  and  $C_d$  at second stall region for NACA0012.

by Flay et al. [58] for  $Re \leq 2.26 \times 10^5$ . In general, the  $C_l$  curves for the investigated  $Re$ s agree well up to the stall at around  $\alpha = 18^\circ$ ; this stall delay is due to the high curvature of the airfoil model (see Okamoto and Ebina [57]). For  $Re = 3 \times 10^4$ ,  $C_l$  rises steadily as  $\alpha$  increases until a point where it suddenly jumps to its peak value of 1.8. Surprisingly, this peak value is 15% higher than that of  $Re = 6 \times 10^4$  and  $10^5$ , in which virtual plateaus are reached at  $18^\circ < \alpha < 23^\circ$ . The occurrence of plateaus may be due to the presence of LSB. The boundary layers, which are initially laminar separate due to adverse pressure gradient, then transition to turbulent flow and reattach as a strong turbulent boundary layer [58]. However, this peak is followed by an abrupt drop in the lift for all  $Re$  cases due perhaps to leading edge stall, although  $Re = 3 \times 10^4$  is marginally different from the other two higher  $Re$ . The lift then gradually drop until  $\alpha = 52^\circ$ ,  $57^\circ$ , and  $62^\circ$ , corresponding to  $Re = 3 \times 10^4$ ,  $6 \times 10^4$ , and  $10^5$ , respectively where an abrupt drop in  $C_l$  is observed; this abrupt drop is an indication of the second stall phenomenon.

The  $C_d$  increases according to the increase of  $C_l$ . Similar to  $C_l$ , the  $C_d$  of  $Re = 3 \times 10^4$  is significantly higher than that of  $Re = 6 \times 10^4$  and  $10^5$ , which must be due to the mechanism of the pressure distribution around the airfoil. The  $C_d$  matches for all  $Re$  cases up until  $\alpha = 18^\circ$ , beyond which the  $C_d$  at  $Re = 3 \times 10^4$  increasingly deviates from  $Re = 6 \times 10^4$  and

$10^5$  with  $\alpha$ . Compared to Figure 3.17(a), the closed tunnel  $C_l$  values are slightly lower than those of Figure 3.17(b), possibly due to the quasi-closed section and the applied blockage correction formulae. However, most noticeable in Figure 3.17(b) is the absence of second stall behavior, which agrees with previous NACA0012 CJT measurements in this study.

The  $C_l$  and  $C_d$  of the OJT and CJT measurements of the airfoil model with a spar are presented in Figure 3.18. Compared to Figure 3.17(a), not many changes in the performance characteristics are observed for the three  $Re$  cases. In Figure 3.18(a), there is a considerable rise in  $C_d$  especially for  $Re < 6 \times 10^4$  while the  $C_l$  curves remain almost unchanged. The influence of the spar is remarkably evident in the closed tunnel section measurements shown in Figure 3.18(b). Curiously, the second stall phenomenon can be seen for  $Re = 3 \times 10^4$  and  $10^5$ . While this is not very clear, the mechanical vibrations caused by the rigid coupling of the drive system to the wind tunnel test stand and the wakes of the model supports, though reduced, may have influenced the flow aerodynamics.

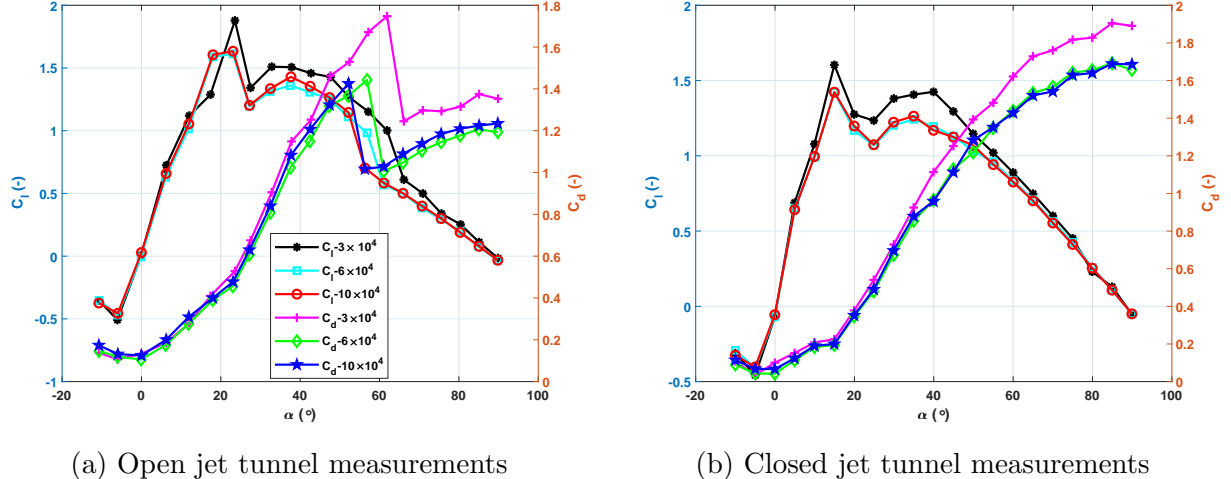


Figure 3.17:  $C_l$  and  $C_d$  of CA1705 without spar (clean model).

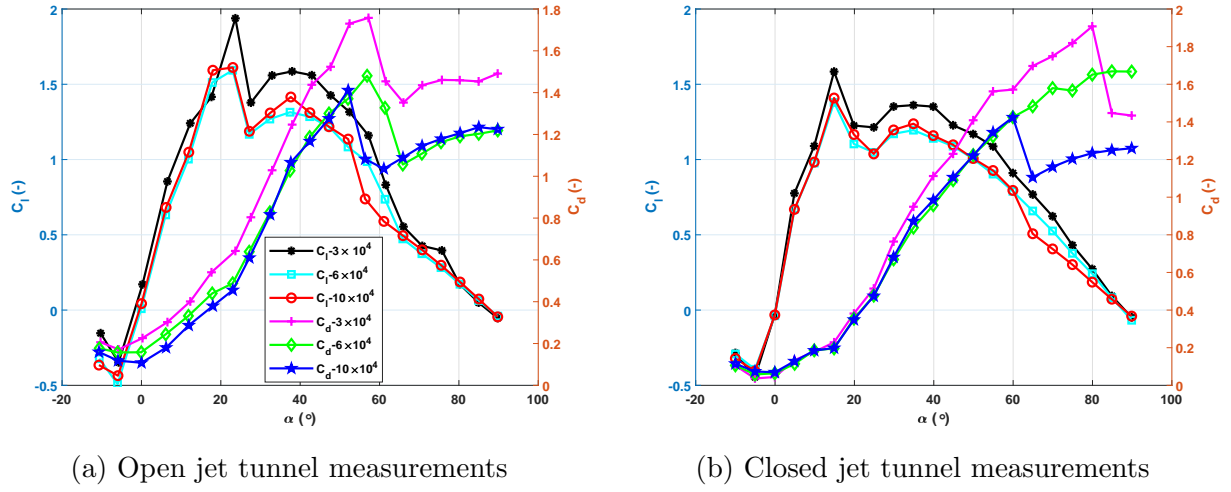


Figure 3.18:  $C_l$  and  $C_d$  of CA1705 with spar.

### 3.7.3 Effect of thickness, camber, aspect ratio and tunnel-blockage on CAAs

It has been established that even nominally identical airfoils tested under the same nominal conditions in different wind tunnels often result in considerable discrepancies, especially at low  $Re$ . Therefore, significant variation would be expected of airfoils with a mix of geometrical parameters. In this study, three CAAs with a combination of geometrical features fabricated from the same material using the same fabrication technique to minimize surface roughness and better contour accuracy were tested under supposedly similar conditions at  $Re$  of  $6 \times 10^4$  and  $10^5$ . Figure 3.19a compares the lift and drag curves obtained for the three sections of varying camber ( $h/c$ ), thickness, ( $t/c$ ) aspect ratio, ( $AR$ ), and tunnel blockage ( $c/H$ ). Lift curves of CA1705 and CA2010 are in close agreement in the pre-stall region and are steeper compared to that of CA1604 at  $Re = 6 \times 10^4$  (see Figure 3.19a). The results also show that as  $h/c$  and  $t/c$  are increased, so does the  $C_l$  curve and  $C_{l_{max}}$ , but this is not always the case as there are limits beyond which performance deterioration sets in. The  $C_{l_{max}}$  of CA1705 and CA1604 are the same because of their geometrical similarity, as depicted in Figure 3.19b. Though increasing  $t/c$  reduces lift, the effect of  $h/c$  is clearly more pronounced

in the case of  $Re = 6 \times 10^4$ . A substantial increase of 26% and 45% in  $C_{l_{max}}$  was observed as  $h/c$  increased from 16% to 17% and 20% respectively.

Although the testing was conducted to ensure two-dimensionality, it is likely that AR influences the airfoil performance. As AR increases, the lift increases in relation to  $h/c$ . Therefore, it is not surprising that CA2010, the airfoil model with the highest AR, has the highest  $C_{l_{max}}$ , but this is accompanied by a noticeable drag penalty, as shown in the  $C_d$  curve of Figure 3.19a. Furthermore, the second stall behavior can be seen in the three airfoil models operating at  $Re = 10^5$ ; it is obviously absent in the CA2010 model. This absence is possibly due to the large camber and relative thickness of the airfoil, which alters the flow physics around the airfoil contour and its operating Re. The above results emphasize that low  $Re$  airfoil performance characteristics at high  $\alpha$  are influenced by wind tunnel configuration, airfoil geometry and  $Re$ .

The results of experimental studies on the aerodynamic characteristics of the three airfoil profiles with spars are presented in Figure 3.20a and 3.20b, showing a similar trend with the clean CAAs. A considerable increase in the maximum  $C_d$  was observed because of the presence of the spar. In addition, the high degree of scatter in Figures 3.20a and 3.20b is due to unsteadiness arising from flow separation. These results, along with that of the clean

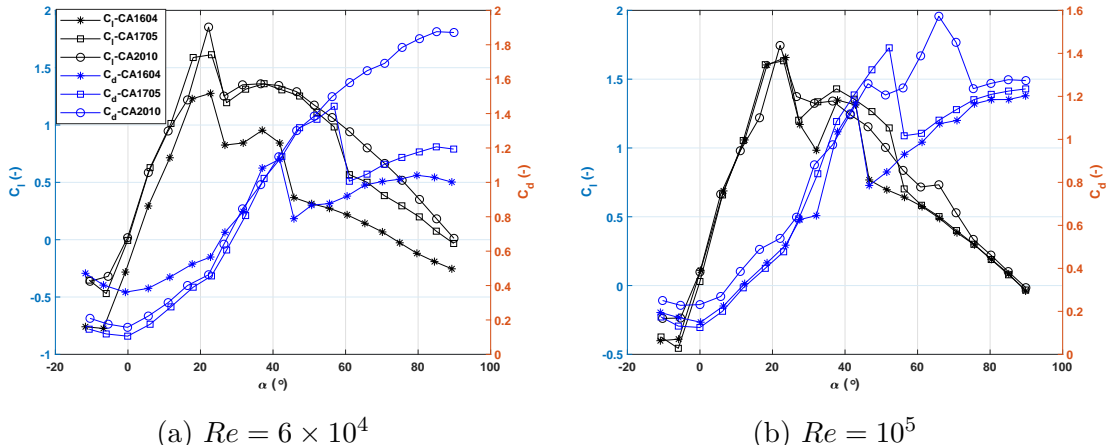


Figure 3.19: Effect of camber, thickness, aspect ratio, tunnel-blockage on lift and drag of the clean CAA in open tunnel condition.

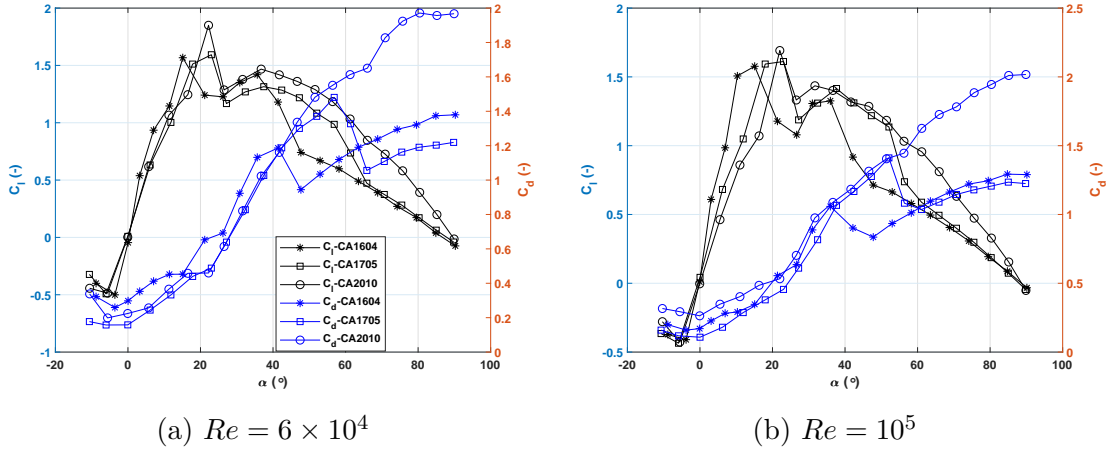


Figure 3.20: Effect of camber and thickness on lift and drag of the CAA with spar in the OJT.

airfoil, are important and used for predicting the aerodynamic and starting performance of the windmill blade sections discussed in Chapters 4 and 5.

As stated earlier, the original intent of this study was to replicate the airfoil model of Bruining [26], but that was not possible due to the limiting dimensions of the 3D printer. Hence all the tested airfoil sections were designed and printed with large cambers than that of [26] to ensure they rigidly adhere to the print bed; otherwise, the printed object might tip over, flex, or vibrate, resulting in warpage or deformation.

Performance results of the clean CAAs measured in the OJT were compared to Bruining's 2% thick and 10% cambered plate tested in a closed tunnel with a turbulence intensity of 0.02%, an order of magnitude less than that of the RWT at the same  $\alpha$  range and selected  $Res$  for the current study. Its  $AR$  and  $c/H$  are, respectively, 5 and 0.12 as reported in [26], and it is designated "BR1002", following the naming convention used for the CAAs. At  $Re = 6 \times 10^4$ , the slopes are non-linear in the pre-stall region, as shown in Figure 3.21(a). The lift curve of BR1002 is much steeper than those of the current study and closest in agreement to that of CA1604, possibly due to its relatively thin contour. Thus, the thinner the airfoil, the steeper the lift slope. In general, the double peaks of lift are observed over the whole  $\alpha$  range, resulting in a non-monotonic behavior. The first peak is typically higher than

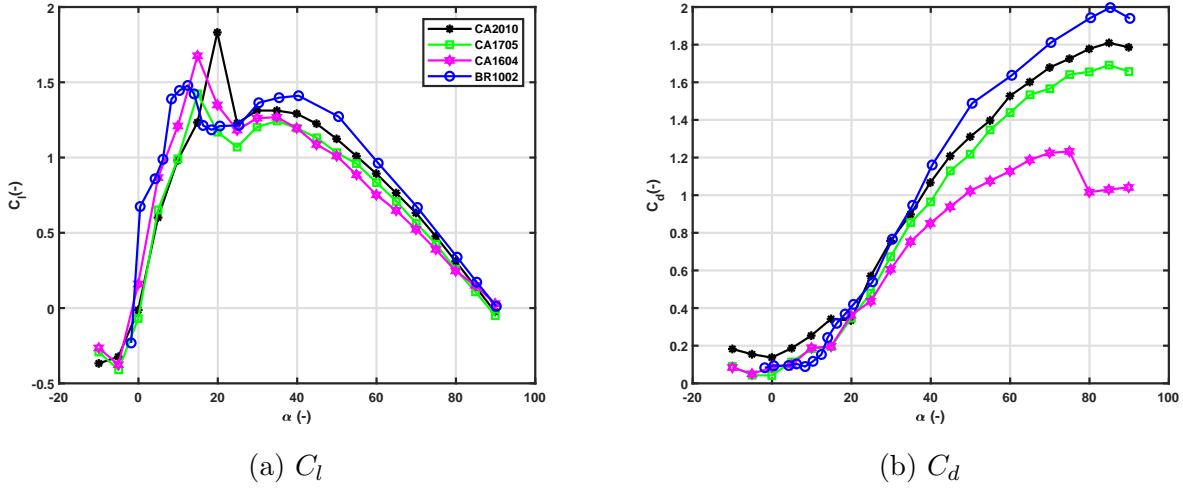


Figure 3.21: Effect of camber, thickness, aspect ratio, tunnel-blockage on lift and drag of the CAAs compared with Bruining [26] data with no wind tunnel correction applied and labeled “BR” in closed tunnel condition, all at  $Re = 6 \times 10^4$ .

the second. The first peak was found between  $11.7^\circ$  and  $19.9^\circ$  and occurred at higher  $\alpha$  with increasing  $t/c$  and  $h/c$ . The CA2010 model with maximum camber (20%) and maximum thickness (10%) stalled at  $19.9^\circ$ , followed by that of CA1604, CA1705, and BR1002, in that order. Between  $29^\circ$  and  $34^\circ$ , the second peak of  $C_l$  for each of the different airfoils model was

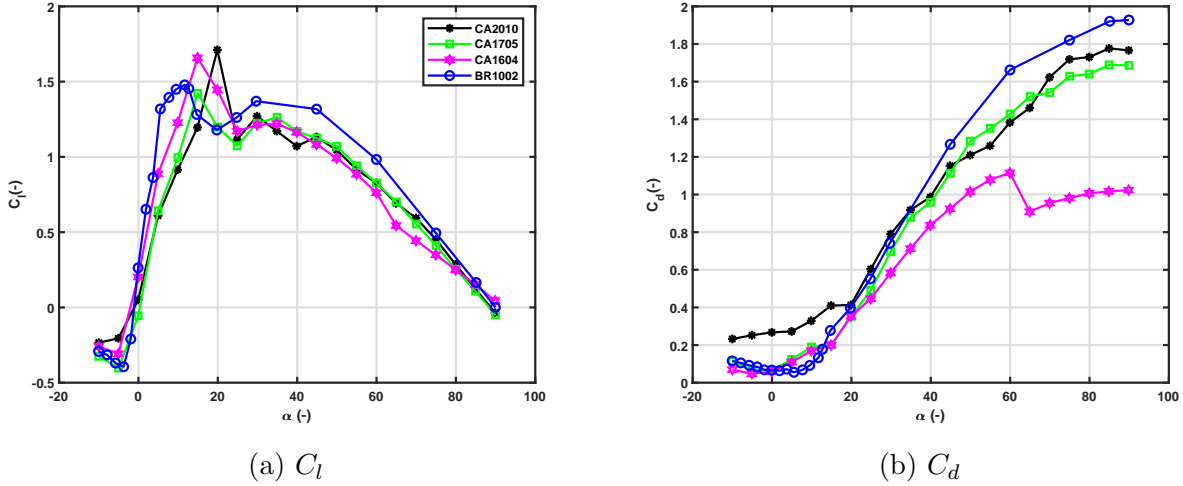


Figure 3.22: Effect of camber, thickness, aspect ratio and tunnel-blockage on lift and drag of the CAAs compared with Bruining [26] data with no wind tunnel correction applied and labeled “BR” in a closed tunnel condition, all at  $Re = 10^5$ .

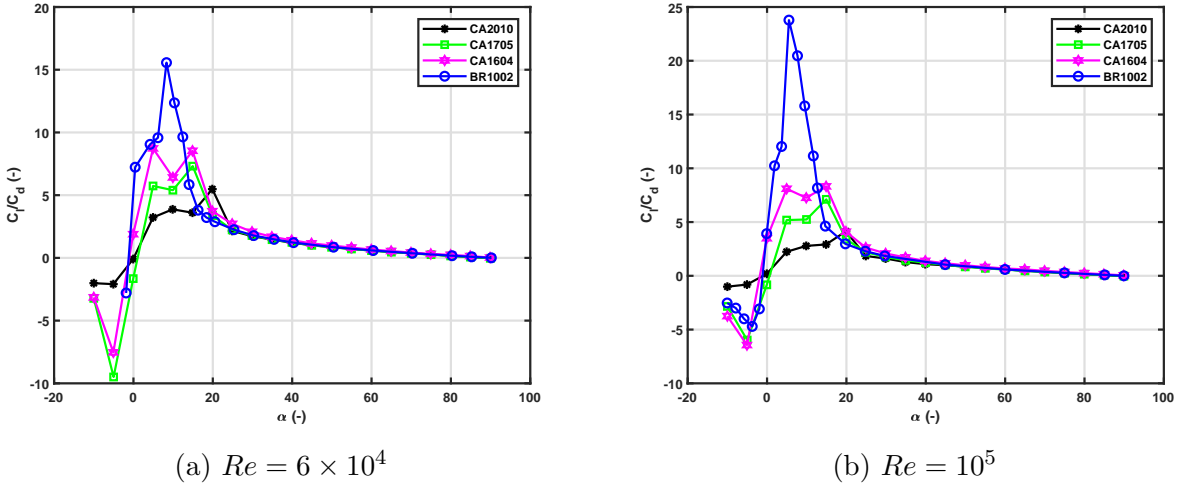


Figure 3.23: Lift-to-drag of the circular-arc airfoil compared with uncorrected Bruining [26] data in a closed tunnel condition.

observed, with the  $C_l$  of BR1002 highest between  $24^\circ \leq \alpha \leq 85^\circ$ . Above  $85^\circ$ , it drops below that of CA1604. The  $\alpha$  corresponding to zero lift is negative except for CA1705 because the models'  $t/c$  differs just as much as the  $h/c$ , the airfoil behavior will not follow the expected trend in circular-arc airfoil performance.

Figure 3.21(b) shows that although, BR1002 has higher  $C_d$  values particularly at  $29^\circ < \alpha < 90^\circ$ , its values from  $-10^\circ$  up to stall are relatively lower, resulting in the maximum  $C_l/C_d$  shown in Figure 3.23. Comparing the other three, decreasing  $h/c$  and  $t/c$  decreases the  $C_d$ . The highest values of  $C_d$  were observed between  $80^\circ$  and  $90^\circ$ . The maximum  $C_d$  of BR1002 is 2.0, which is 62%, 18.1%, and 10.3% more than that of CA1604, CA1705, and CA2010, respectively, probably due to the simple tunnel blockage correction employed by Bruining [26], which only corrected the tunnel wall static pressure used in computing the flow velocity. Even though the testing was conducted in a closed jet condition, the second stall phenomenon was observed with CA1604, probably because it presents the maximum  $c/H$  and the lowest AR.

Increasing the  $Re$  by an order of magnitude from  $10^4$  to  $10^5$ , as shown in Figure 3.22, is explained using Figure 3.23. While a rapid rise in  $C_l/C_d$  can be seen for BR1002, slow,

gradual variations are associated with the three other airfoil models. According to Mueller [132], interference effects between the airfoil and the endplates due to flow separation and formation of a “corner vortex” can affect as much as 10% of the airfoil span, which can spike the drag values, especially at  $Re < 100,000$ . Moreover, the turbulent intensity of the RWT is an order of magnitude higher than that at which the BR1002 was investigated.

### 3.7.4 Circular-arc airfoils hysteresis

Lift and drag hysteresis is commonly associated with round-nosed, thick, cambered airfoils, especially at  $Re < 3 \times 10^5$  [132] and is important in a steady lift and drag performance because starting in SWTs tend to proceed from high to low  $\alpha$ . Although experimental data were obtained for the CA2010, CA1705, and CA1604 with and without a spar for both the closed and open jet flow conditions for the  $Re$  range from  $3 \times 10^4$  to  $10^5$ , only the data of CA1705 for  $Re = 6 \times 10^4$  and  $10^5$  will be analyzed.

Hysteresis was present for all the  $Re$  investigated. Some representative results are shown in Figures 3.24 and 3.25 where, interestingly, hysteresis was not seen until post-stall, near the second peak lift. The  $\alpha$  for the hysteresis lies between  $32^\circ$  and  $61^\circ$  for  $Re = 6 \times 10^4$ , as shown in Figure 3.24(a). By increasing the  $Re$  to  $10^5$ , the size of the hysteresis region is reduced by about  $5^\circ$ . With spars, the hysteresis regions are slightly changed and the ranges for Figures 3.24 and 3.25 are  $32^\circ \leq \alpha \leq 66^\circ$  and  $32^\circ \leq \alpha \leq 61^\circ$ , respectively. In all the cases, the hysteresis loop is clockwise for both the  $C_l$  and  $C_d$  profiles, as illustrated in Figure 3.24(b) (see arrow direction). This finding implies that as  $C_l$  drops,  $C_d$  reduces. In terms of performance coefficient, no significant variation resulted from the hysteresis, for example, at  $\alpha = 37^\circ$ ,  $C_l = 1.36$  and  $C_l/C_d = 1.45$ , when  $\alpha$  is in the increasing branch of the loop. Conversely, when  $\alpha$  is decreasing in the other half of the loop,  $C_l = 0.9363$  and  $C_l/C_d = 1.52$ . A 4% increment is not likely to influence static airfoil performance.

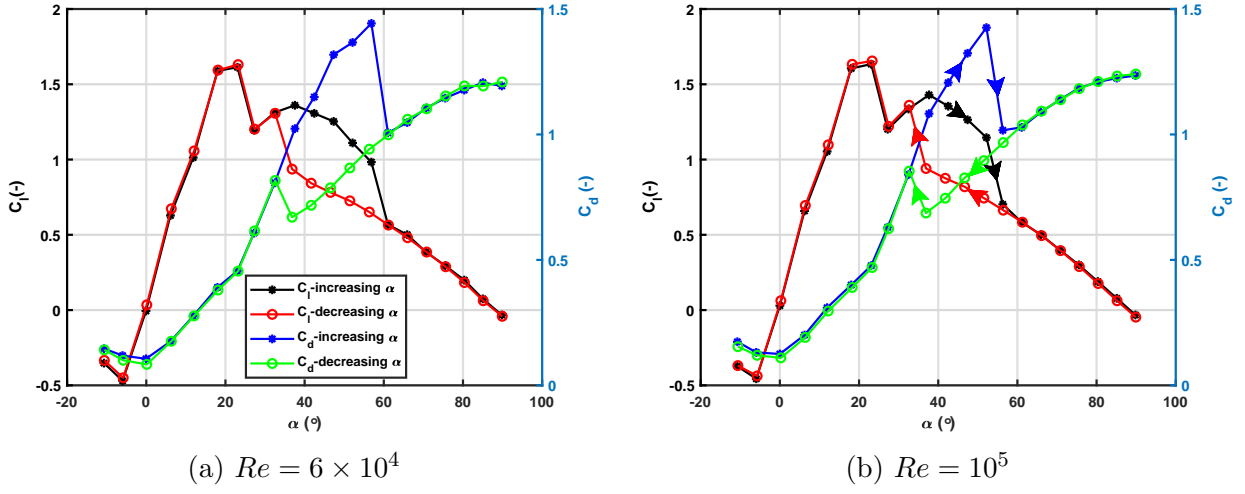


Figure 3.24: Hysteresis of  $C_l$  and  $C_d$  curve for the clean CA1705 in an open jet flow condition.

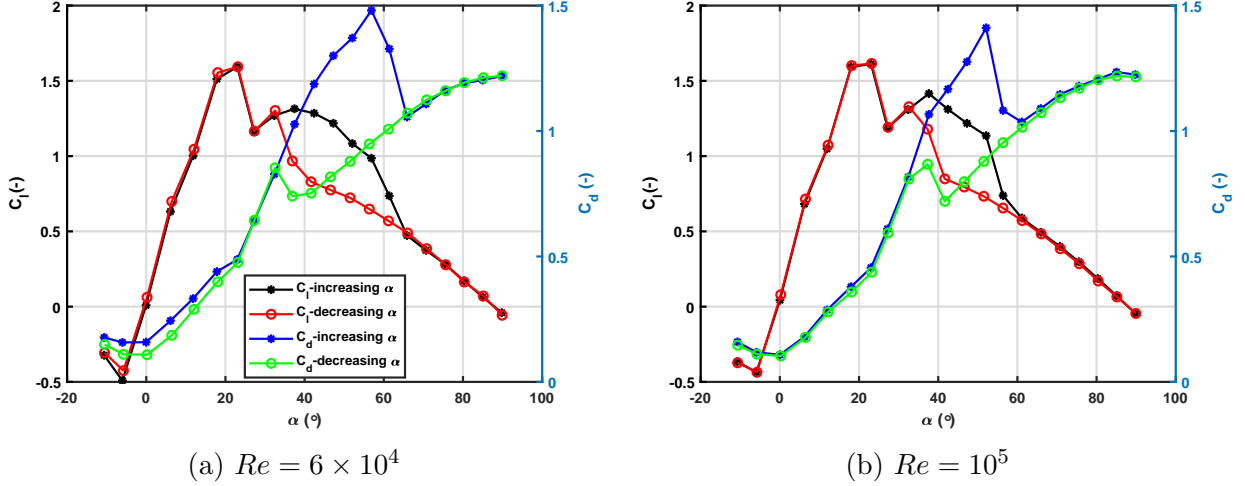


Figure 3.25: Hysteresis of  $C_l$  and  $C_d$  curve for the CA1705 with spar in an open jet flow condition.

### 3.8 Unsteady aerodynamic performance

Unsteady tests have been conducted on the CA1604 models without a spar at two different  $Re = 6 \times 10^4$  and  $10^5$ . The airfoil model was pitched at a chordwise pivot location of  $0.25c$  following a sinusoidal path in the canonical form of  $\alpha = \alpha_m + \alpha_a \sin k\tau$ , where  $\tau$  is the

reduced time,  $\tau = 2U_\infty t/c$  at various reduced frequencies,  $k$  given by

$$k = \omega_p c / 2U_\infty \quad (3.29)$$

achieved by adjusting the oscillating pitch frequency,  $\omega_p$  of the sinusoidal motion. The experiments were, however limited to  $k \leq 0.6$  to ensure that the vortex shedding frequency,  $f_v$  is well below the natural frequency,  $f_n$  of the experimental setup i.e.,  $f_v < f_n$ .

Before examining the airfoil response to unsteady aerodynamics, it is necessary to discuss the usefulness of the  $k$  values tested in the present work. In many normal operating events such as wind shear or a wind turbine in yaw, the frequency is the rate of rotation. As will be shown in Chapter 4 the velocity at the tip of a rotor blade is

$$U_T = \sqrt{U_1^2 + (\Omega R)^2} \quad (3.30)$$

If the turbine is at optimum performance, the velocity at the blade becomes

$$U_1 = 2/3U_\infty \quad (3.31)$$

Thus, by combining Eqs. 3.29, 3.30, and 3.31, the reduced frequency becomes

$$k \approx \frac{c\lambda}{2R\sqrt{\lambda + 4/9}} \quad (3.32)$$

For the windmill rotor tested in this work (see Chapter 4),  $c/R = 0.118$  and  $k < 0.05$ . Although  $k$  will increase towards the blade root, the experiments conducted cover typical values of  $k$  for the power-producing part of the blade.

The airfoil response at  $k = 0.02$  for  $Re = 0.6 \times 10^5$  and  $10^5$  along with the error bars, a representation of one standard deviation from the average of the measurements of  $C_l$  and  $C_d$  for 5 cycles of oscillation, are shown in Figure 3.26. As indicated in the Figure, the

measurements show good repeatability for all loops except for  $C_d$  at  $\alpha > 50^\circ$  up to near  $90^\circ$  for both  $Res$ . It appears that there are flow stability issues around this range of  $\alpha$ .

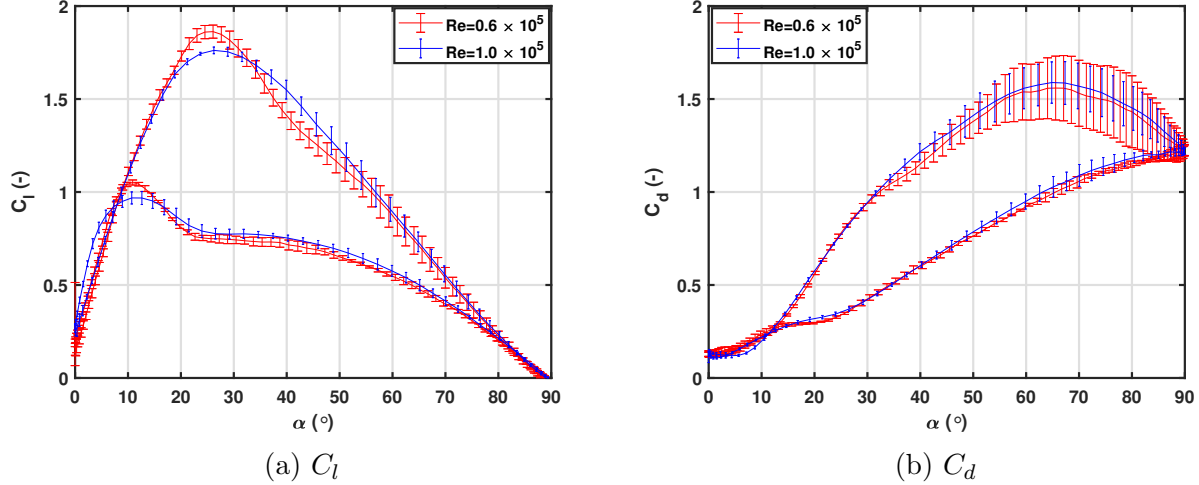


Figure 3.26: Unsteady response of CA1604 at  $Re = 0.6 \times 10^5$  and  $10^5$  ( $\alpha = 45^\circ + 45^\circ \sin 0.02\tau$ ). Error bars represent one standard deviation of the mean force measurements over 5 cycles.

The effects of  $k$  on the  $C_l$  in response to the sinusoidal motion described by  $\alpha = 45^\circ + 45^\circ \sin k\tau$  is illustrated in Figure 3.27 for the CA1604 airfoil. The steady  $C_l$  slope agrees with the unsteady measurements (pitch-up motion indicated by the black arrowheads, in Figure 3.27(a), especially at  $\alpha < 10^\circ$  where the  $C_l$  slope increases with  $k$  with a slight deviation occurring up to the stall. This deviation is attributable to the tunnel blockage correction applied only to the steady data. Peak  $C_l$ , as well as its corresponding  $\alpha$ , increases monotonically with increasing  $k$ . For  $k = 0.6$ , peak  $C_l$  is  $\approx 2$  occurring at  $\alpha \approx 30^\circ$ , 1.2 times its counterpart steady-state peak lift value. In all cases of  $k$ , the dynamic hysteresis loop differs from the static one.

At  $k > 0.4$ , the  $\alpha$  for peak lift saturates at about  $30^\circ$ , even with a modest increase in the peak lift coefficient. Strictly speaking, the unsteady measurements considered here are at best quasi-steady in nature because  $0.01 \leq k \leq 0.06$ , although Leishman [133] defined the upper limit of  $k$  as 0.05 for this flow type. Hence the relatively low overshoot in the lift, unaccompanied with load fluctuations, implies the unsteadiness effects are negligible.

According to Granlund et al. [118], the unsteady response for all the cases is due to stall delay, as  $C_l$  depicts no appreciable departure from the steady evolution at low  $\alpha$  and the linear region extending up to a delayed stall  $\alpha$  as  $k$  rises.

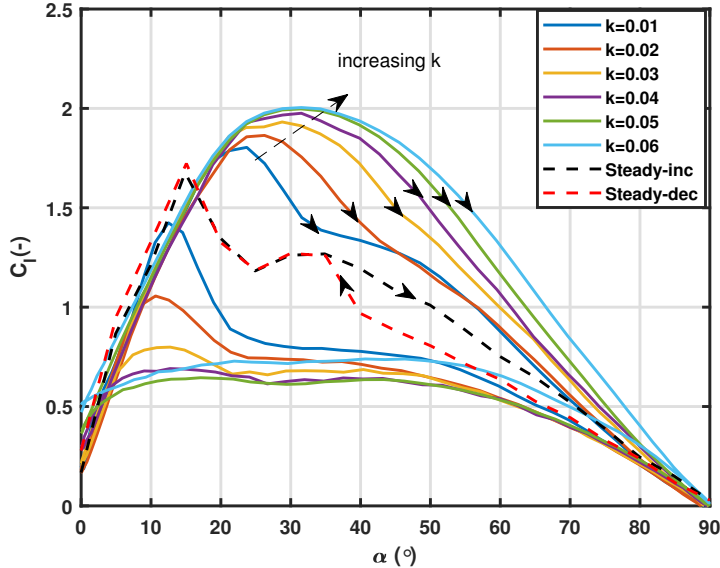
In Figure 3.27(b), the  $C_d$  also demonstrates an overall increase with  $k$  following the same trend as  $C_l$ . The unsteady pitch-up motion  $C_d$  curves maintain proximity to the steady curve for all  $k$  up to  $10^\circ$ . Beyond  $\alpha > 10^\circ$ , noticeable departures from the steady curve can be seen. By comparing Figure 3.27(a) to Figure 3.27(b), it was observed that the  $C_d$  increased appreciably more than  $C_l$ . For example at  $k = 0.06$ , the magnitude of  $C_d$  is 2.181, a nearly 60% increase of the maximum steady  $C_d$ , while the corresponding  $C_l$  increased by just 20%. This large difference in increment is due to the dynamic motion and airfoil characteristics.

Figure 3.28 presents the  $C_l$  and  $C_d$  for  $Re = 10^5$ , where  $k$  increased from 0.01 to 0.06. The airfoil response are comparable to that obtained at  $Re = 6 \times 10^4$ . However, looking at Figure 3.28(a), the  $C_l$  increase is non-monotonic with the increase in  $k$ . On the one hand, the peak  $C_l$  is lower than that of Figure 3.27(a), suggesting that the effect of unsteadiness is  $Re$  dependent. On the other hand, while  $C_d$  of Figure 3.28(b) rises with increasing  $k$ , it is slightly higher than that of  $Re = 6 \times 10^4$  in Figure 3.27(b) for  $k = 0.06$ . Leading to the conclusion that  $k$  greatly influences the aerodynamic behavior of the flow around the airfoil, and for  $k < 0.06$ , the flow behavior is  $Re$  dependent.

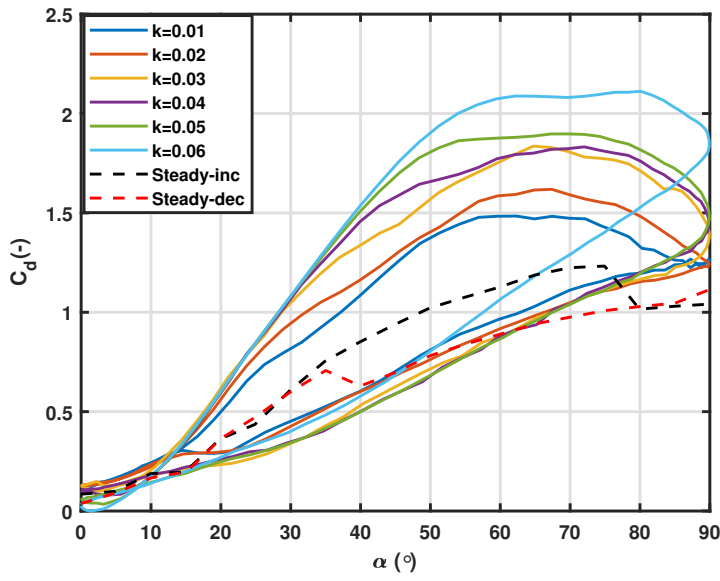
## 3.9 Summary

Static performance characterization of three circular-arc airfoils without and with a spar: CA2010, CA1705, and CA1604 at nominal  $30,000 \leq Re \leq 100,000$  and NACA0012 at  $Re$  of 86,000 and 150,000 were investigated under two tunnel conditions and presented in this chapter alongside the dynamic (quasi-steady) open tunnel performance of CA1604.

The open tunnel performance of NACA0012 at comparable  $Re$  agrees with studies by Sheldahl and Klimas [64], Rainbird et al. [65] and Worasinchai et al. [67] for the pre-stall

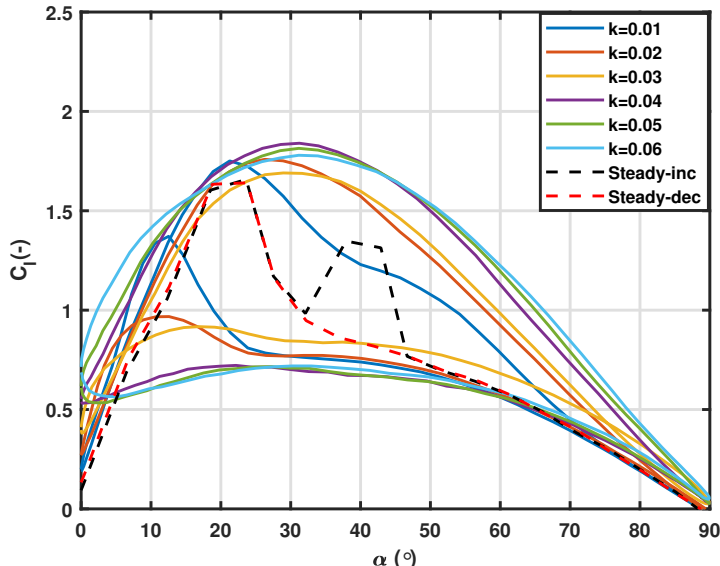


(a)  $C_l$

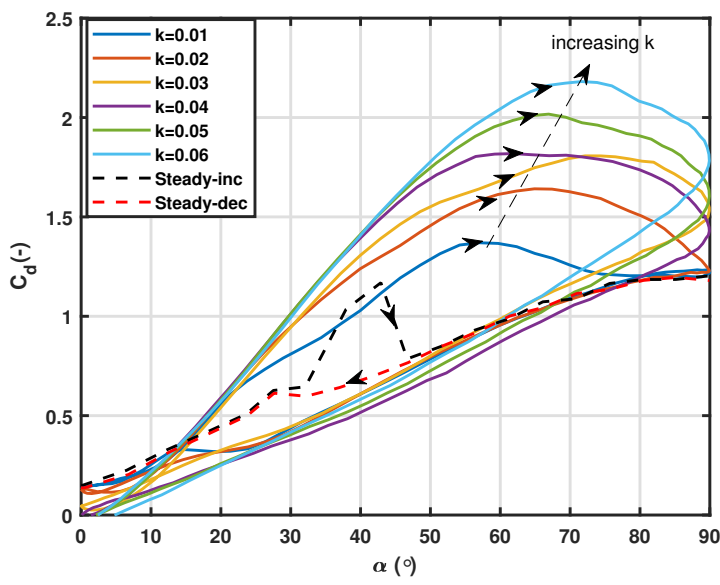


(b)  $C_d$

Figure 3.27: Effect of reduced frequency,  $k$  on the lift coefficient at  $Re = 0.6 \times 10^5$  for the clean CA1604 in an open tunnel condition:  $\alpha = 45^\circ + 45^\circ \sin k\tau$ . Black arrows shows the pitch-up direction of the unsteady loops.



(a)  $C_l$



(b)  $C_d$

Figure 3.28: Effect of reduced frequency,  $k$  on the lift coefficient at  $Re = 10^5$  for the clean CA1604 in open tunnel condition:  $\alpha = 45^\circ + 45^\circ \sin k\tau$ . Black arrows shows the pitch-up direction of the unsteady loops.

region. The airfoil properties and wind tunnel test section configuration influence the performance of the airfoil. The discernable discrepancies between the results were likely due to the impact of the parameters mentioned above on the flow behavior around the airfoil. A significant finding of this study is the low  $Re$  sensitivity of NACA0012, contrary to most literature reports, e.g., [67].

A “second stall” phenomenon due to the translation of the flow separation point near the leading edge from the suction to the pressure side of the airfoil, giving rise to abrupt changes in the wake structure, was observed not only for the open test section as hypothesized by [68] but also for the closed test section depending on the  $Re$  and tunnel blockage, effectively defined as the  $c/H$  ratio. The open tunnel measurements evinced a large hysteresis loop compared to the closed tunnel measurements, surprisingly around the post-stall region.

The effects of rare combinations of thickness, camber, and aspect ratios on the performance of circular-arc airfoils revealed that the gain in the lift by increased camber and thickness, and even AR, is accompanied by a penalty in drag; in other words, a high lift obtained expectedly resulted in a corresponding high drag. With a spar at the 0.5c chord position, the airfoil performance drops due to increased drag in both closed and open tunnel conditions. However, the overall performance depends on a mix of these factors. The lift-to-drag ratio of BR1002 [26] on a relatively cambered profile is at least three times that of CA1604 due to its thinner geometry and low turbulence intensity of the test section, thereby emphasizing the importance of low turbulence in low  $Re$  airfoil investigation. Like the NACA airfoil section, hysteresis was observed only in the post-stall region, implying less significant variation in static aerodynamic performance.

Unsteady force measurements have clearly shown the effects of unsteadiness with regard to aerodynamic airfoil performance, wherein the static forces are dynamically increased, and the stall angle of attack is delayed beyond the static stall angle. As  $k$  increases,  $C_l$  and  $C_d$  strictly increases for  $Re = 60,000$  without an accompanying load fluctuation due to the range of  $k$  investigated, virtually in the quasi-steady flow regime. An order of magnitude

change in  $Re$  from  $10^4$  to  $10^5$  increases the  $C_l$  non-monotonically, while the  $C_d$  unexpectedly grows monotonically with values higher than that of the low  $Re$ . This suggests that for  $k \leq 0.06$ ,  $Re$  might be important.

As observed in several studies, there are differences between data showing the occurrence of a second stall measured in different wind tunnels. Thus, while CFD is a complementary tool for determining the characteristics of an airfoil, it can not be trusted to predict low  $Re$  airfoil performance around the stall region.

# Chapter 4

## Rotor Aerodynamic Performance Prediction

Part of the overall aim of this study is to assess the accuracy of the blade element momentum theory (BEM) for aerodynamic (presented in this chapter) and starting (given in Chapter 5) performance prediction of a waterpumping windmill with blade number,  $3 \leq N \leq 24$  experimented on in Chapter 6. The basic principles of BEM will be explored to highlight the performance parameters and their optimal conditions, particularly with regard to low tip speed ratio,  $\lambda$ , and high solidity,  $\sigma$ , rotors. A BEM code *power\_calc* will be implemented to calculate the loads, hence the thrust, torque, and power of a 0.68 m, waterpumping windmill rotor model with a range of  $N$ . Apart from the traditional Prandtl tip loss function for correcting for finite blade number, ( $N < \infty$ ), a vortex-based tip loss, otherwise known as finite blade function suitable for low  $\lambda$  operation, will be shown to more accurately predict the rotor performance. Further, the influence of blade element performance parameters on the global parameters for the various  $N$  cases will be examined.

## 4.1 Introduction

In contrast to a propeller that expels energy into the air from another energy source, wind turbines extract mechanical energy from the kinetic energy of moving air–wind. Both aerodynamic machines are similar in terms of the general principles of energy conversion. Hence the same theoretical approach can be applied for analyzing their performance using the propeller theory independently developed from two classical methods called momentum theory and blade element theory (BET).

In wind turbine aerodynamics, the propeller theory is known as the blade element momentum (BEM) theory, a fusion of momentum theory and blade element theory. Even with the development of sophisticated high-fidelity simulation tools, the BEM is and will remain an essential modeling tool for aerodynamic prediction and analysis due to its accuracy and simplicity 78. BEM can easily and swiftly be deployed as an objective function in a multi-dimensional optimization such as incipient rotor blade design with respect to aerodynamic and structural performance, e.g., [134]. It has also been used to optimize SWTs blades for efficient power production and improved starting at low wind speed, e.g., [115].

The actuator disk model theory, which will be discussed in Section 4.2, is the basis for the BEM model. The momentum theory, a component of the BEM model, was initially developed by W.J.M Rankine in 1865 and later improved by R.E Froude in 1889. Its theory is based on determining the forces acting on the rotor to produce the fluid motion. While the BEM provides a theoretical limit on the power that can be extracted from the wind, it is unable to predict the performance of the wind turbine blade as a function of the blade geometrical parameters. The BET was originated by W. Froude in 1878 and further developed by S. Drzewiecki [1, 135]. Contrary to the momentum theory, the BET deals with the forces generated by the blades due to the fluid motion. Further historical developments of the BEM up to the mid-1970s are available in Ref. [135].

## 4.2 Actuator disk model

Significant simplifications to the complexities of a wind turbine due, for example, to environmental conditions and operational requirements, need to be applied to gain a fundamental understanding of its performance. Assume that a wind turbine such as in Figure 4.1 extracts kinetic energy from the flow passing through the actuator disk area with a surface of discontinuous pressure, as shown in Figure 4.2. The wind turbine rotor is idealized as an infinitely thin porous disk of diameter,  $D$ , whose area,  $A$  is defined as  $\pi D^2/4$  and equal to the area swept by the rotor blades. Another way is to view the rotor as a model with an infinite number of infinitely thin blades.

The one-dimensional analysis undertaken here assumes that the flow is incompressible and steady. Also, the velocity is uniform at each cross-section of the streamtube, including at the rotor disk. Thus the velocities and pressure do not vary with radius. Because of the uniform cross-sectional flow, the effects of viscosity are negligible within the streamtube, and so there are no rotational effects (zero vorticity). The streamlines bounding the streamtubes prevent any mass, momentum, and energy flux across the bounding surface of the streamtube. Furthermore, the disk does not impart any swirl to the flow because it is assumed to be stationary.

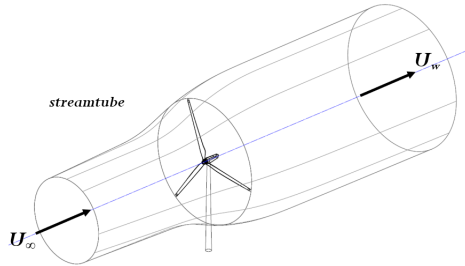


Figure 4.1: Flowfield of a wind turbine. Adapted from [136].

As the flow passes through the actuator disk, it extracts momentum and energy resulting in a gradual decrease in the velocity inside the streamtube. In satisfying the law of conservation of mass, the streamtube expands. Figure 4.3 presents a graphical illustration of the flow field behavior, where  $U_\infty$  is the uniform wind speed,  $P$  is the pressure, and  $A$  is

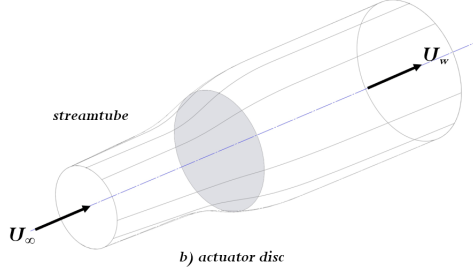


Figure 4.2: Flowfield of an actuator disk. Adapted from [136].

the cross-sectional area of the tube. Conditions for the inlet plane (upstream) are defined by subscripts  $\infty$ , and conditions at the exit plane (downstream) are defined by subscript  $w$ . Numbers 1 and 2, respectively, represent the conditions in the wind direction on the upwind side of the disk and upwind on the downwind side of the rotor disk. Fluids entering the streamtube at uniform wind speed,  $U_\infty$ , and ambient pressure,  $P_\infty$ , continuously decelerate inside the streamtube as they approach the actuator disk. Because no work transfer occurs, the kinetic energy loss results in a pressure increase, leading to the streamtube expansion. The wind upstream is reduced to  $U_1$  and further reduced to  $U_w$  at the actuator disk and exit plane, respectively. Along the streamtube, the mass flow rate is the same at any point. Because no mass flux crosses the bounding surface of the streamtube control volume, the conservation equation is

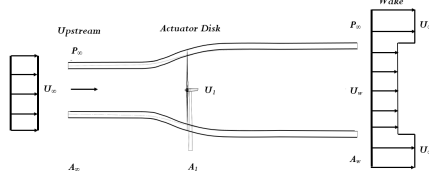
$$\dot{m} = \rho A_\infty U_\infty = \rho A_1 U_1 = \rho A_w U_w \quad (4.1)$$

$\rho$  is the fluid density, and for incompressible flow ( $\rho=\text{constant}$ ), Eq. (4.1) reduces to volume flow rates

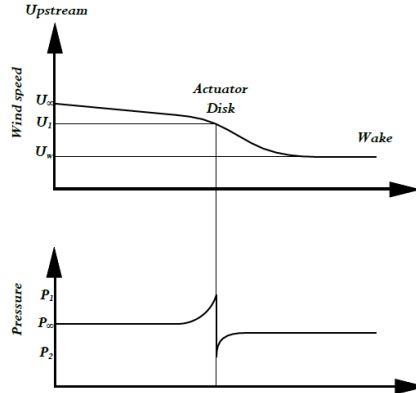
$$\dot{Q} = A_\infty U_\infty = A_1 U_1 = A_w U_w \quad (4.2)$$

Volume flow rates are usually symbolized as  $Q$ , but defined here as  $\dot{Q}$  to differentiate it from  $Q$  used to represent torque in this thesis.

A thrust force,  $T$  in the streamwise direction, which is essentially a drag force due to Newton's law of motion causes a change in axial momentum. The thrust force is:



(a) Schematic of actuator disk in streamtube



(b) Pressure and wind speed distribution

Figure 4.3: Pressure and wind speed variation through an axi-symmetric streamtube. Reproduced from [1].

$$\text{Axial momentum, } T = \dot{m}(U_\infty - U_w) = \rho A_1 U_1 (U_\infty - U_w) \quad (4.3)$$

Also, the thrust force,  $T$ , due to the pressure drop across the disk, can be expressed as

$$\text{Thrust force, } T = (P_1 - P_2)A_1 \quad (4.4)$$

By equating Eqs. (4.3) and (4.4), a relation for pressure is obtained:

$$P_1 - P_2 = \rho U_1 (U_\infty - U_w) \quad (4.5)$$

Furthermore, the actuator disk extracts kinetic energy from the wind at a power,  $P$ , equal to the difference between kinetic energy fluxes at the intake and exit of the streamtube control volume as

$$P = \frac{1}{2}\dot{m}(U_\infty^2 - U_w^2) \quad (4.6)$$

Wind speeds  $U_1$  and  $U_w$  needs to be determined to calculate thrust and power of Eqs. (4.3) and (4.6). Applying the Bernoulli equation to the far upstream (entrance plane) to just in front of the rotor and from just after the disk to far downstream in the wake and combining the resulting equations gives a relation for the pressure drop:

$$P_1 - P_2 = \frac{1}{2}\rho(U_\infty^2 - U_w^2) \quad (4.7)$$

Equating Eqs.(4.5) and (4.7) by simple manipulation gives a relation for  $U_1$  as

$$U_1 = \frac{U_\infty + U_w}{2} \quad (4.8)$$

The velocity at the rotor disk is the arithmetic average of the velocities entering and exiting the streamtube. The amount by which the freestream uniform wind speed decreases is the axial velocity deficit. The fraction of reduction is known as the axial induction factor,  $a$

$$\text{Axial induction factor, } a = \frac{U_\infty - U_1}{U_\infty} = 1 - \frac{U_1}{U_\infty} \quad (4.9)$$

Note that  $U_1/U_\infty$  is the dimensionless wind speed at the actuator disk normalized by the freestream wind speed,  $U_\infty$ . From Eq. (4.8), the wind speeds at the actuator disk and exit of the streamtube become

$$U_1 = U_\infty(1 - a); U_w = U_\infty(1 - 2a) \quad (4.10)$$

Inserting Eq. (4.10) into Eqs. (4.3) and (4.6) leads to simplified definitions of thrust and power in terms of the  $U_\infty$  and  $a$ ,  $\rho$ , and  $A$  as:

$$T = 2\rho A_1 U_\infty^2 a(1 - a) \quad (4.11)$$

$$P = 2\rho A_1 U_\infty^3 a(1-a)^2 \quad (4.12)$$

Eqs. (4.11) and (4.12) are then normalized by the product of the dynamic pressure acting on the actuator disk and area of the disk,  $1/2\rho U_\infty^2 A_1$ , and the available power in the wind passing through the rotor disk area,  $1/2\rho U_\infty^3 A_1$ , respectively, to give:

$$\text{Thrust coefficient, } C_T = \frac{2\rho A_1 U_\infty^2 a(1-a)}{1/2\rho U_\infty^2 A_1} = 4a(1-a) \quad (4.13)$$

$$\text{Power coefficient, } C_p = \frac{2\rho A_1 U_\infty^3 a(1-a)^2}{1/2\rho U_\infty^3 A_1} = 4a(1-a)^2 \quad (4.14)$$

Maximum power occurs when  $dC_p/da = 0$ . From Eq. (4.14), this occurs at  $a = 1/3$ , so

$$C_{p,max} = 16/27 \approx 0.593 \quad (4.15)$$

Eq. (4.15) is called the “Betz-Joukowsky limit” and shown in Figure 4.4 for  $a = 1/3$ ,  $U_1/U_\infty = 2/3$  and  $U_w/U_\infty = 1/3$  in Eq. 4.14. This derivation shows that, at most, the kinetic energy capture is limited to 59.3%. In a similar form, at optimum performance,  $C_T = 8/9$  and has a maximum of unity when  $a = 1/2$ , found from setting the derivative of Eq. (4.13) equal to zero. Eqs. 4.13 is also shown graphically in Figure 4.4.

Experiments have revealed that the assumptions of an ideal wind turbine leading to Eq. (4.11) are only valid for  $a$  approximately less than 0.4. When  $a > 1/2$ , the flow is reversed at the exit of the streamtube. This flow state is known as the turbulent wake state, which violates the assumptions of one-dimensional, inviscid, and irrotational flow of the actuator disk model.

$C_T$  measurements as a function of  $a$  for different rotor states showing the validity limit of the actuator disk theory is presented in Figure 4.5. Also shown is the experimental data by Glauert [99] with  $C_T > 1$ , which contravenes the momentum theory prediction. He suggested

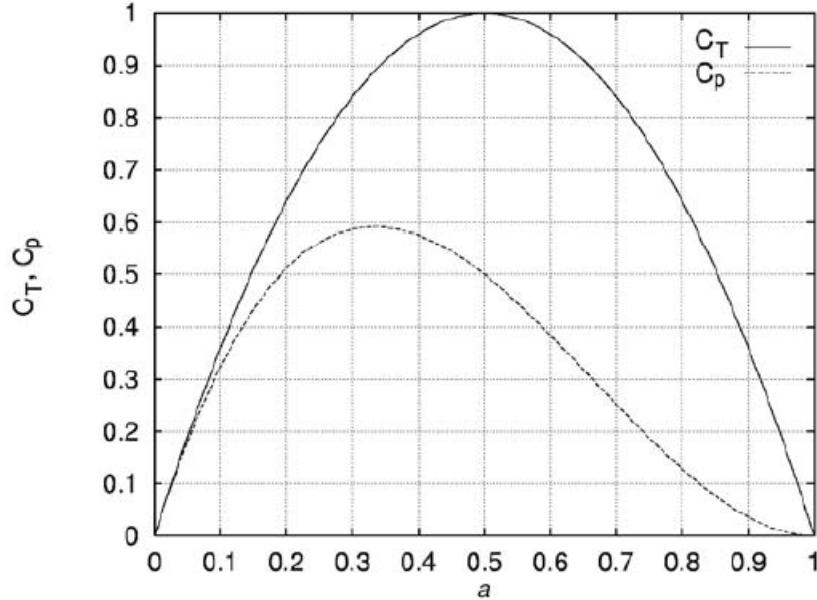


Figure 4.4: Variation of  $C_p$  and  $C_T$  with  $a$  for an ideal, horizontal-axis wind turbine, extracted from [86].

a high thrust (axial induction) correction equation, a modification of Eq. (4.13), indicated by the solid lines at  $a_T > 0.4$ , which is the transition point from low to high thrust and given as:

$$C_T = 4a(1 - a) + 2 \quad (4.16)$$

An alternate high thrust correction model reportedly used in the blade element calculations of [33, 137–139] is

$$C_T = \begin{cases} 4a(1 - a) & a \leq a_c \\ 4[a^2 + (1 - 2a_c)a] & a > a_c \end{cases} \quad (4.17)$$

where  $a_c$ , is the critical axial induction factor = 1/3. This correction is implemented in the BEM code employed in this study and discussed subsequently. Fortunately, the actuator disk operates in the windmill state for  $0 < a \leq 0.5$ , which is the range for wind turbine rotors and, of course, waterpumping windmills, so high thrust corrections are perhaps theoretically less critical, especially for design and performance analysis, as is the case of the current

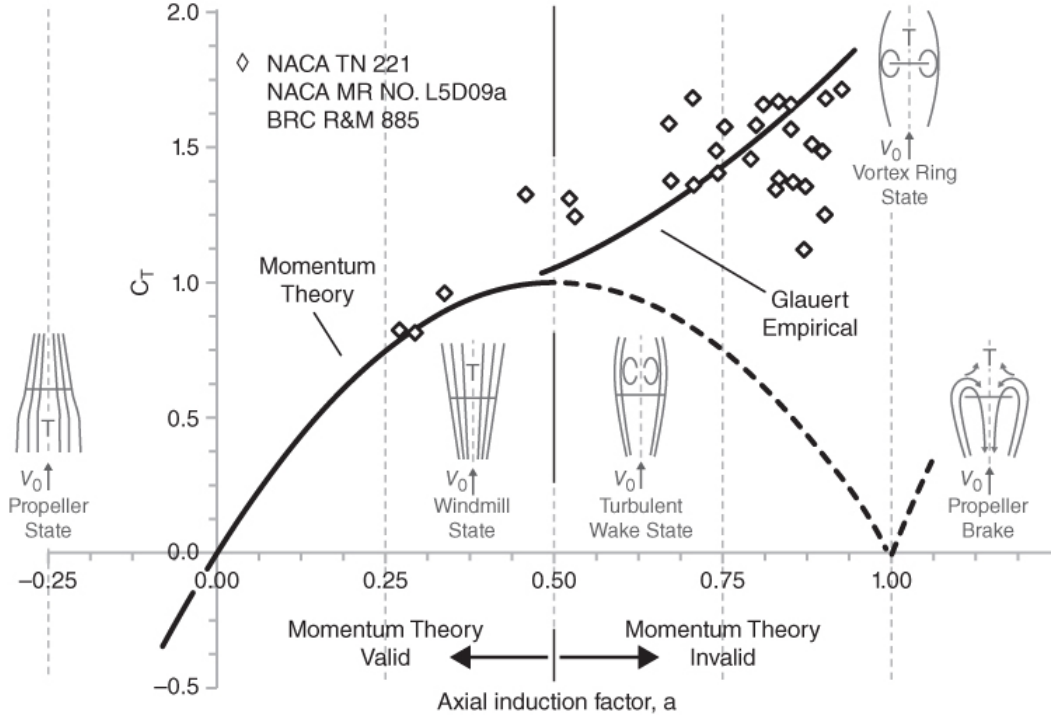


Figure 4.5: Rotor flow states and validity of actuator disk theory. Reproduced from [1].

study [33].

### 4.3 Rotor disk model

For the previous analysis, the tangential induction factor,  $a'$ , to be defined later, is zero. In other words, the rotor thrust and power are exclusively dependent on  $a$ , giving rise to the maximum theoretical  $C_p$ , the Betz-Joukowsky limit. In the rotor disk theory described in this section, the momentum analysis is modified to allow the actuator disk to affect tangential flow downstream of the wake. The added angular momentum and kinetic energy lead to a reduction in the maximum theoretical  $C_p$ , a direct consequence of the sustained wake rotation. Because the angular kinetic energy is due to the rotor disk reaction, the wake rotation is directly opposite to that of the rotor blades depicted in Figure 4.6.

To incorporate variations in parameters involved along the blade in Figure 4.7, an annular streamtube model will be used. The rotor torque is equivalent to the change in wake angular

momentum. For an annulus of width,  $dr$  at location  $r$ , the incremental torque and power are defined as:

$$dQ = d\dot{m}r^2\omega \quad (4.18)$$

$$dP = d\dot{m}r^2\omega\Omega \quad (4.19)$$

Here,  $\omega$  and  $\Omega$  are, respectively, the swirl and rotor angular speed. Recall that from Eq. (4.1),  $d\dot{m} = \rho U_1 dA_1$  with  $dA = 2\pi r dr$  being the area of the rotor disk annulus. By introducing the tangential induction factor,  $a'$  defined as

$$a' = \frac{\omega}{2\Omega} \quad (4.20)$$

and substituting Eq. (4.20) into Eqs. (4.18) and (4.19) gives a relations in terms of  $a$ ,  $a'$ ,  $U_\infty$ ,  $r$  and  $\Omega$

$$dQ = 4\pi\rho U_\infty (1 - a)a'\Omega r^3 dr \quad (4.21)$$

$$dP = 4\pi\rho U_\infty (1 - a)a'\Omega^2 r^3 dr \quad (4.22)$$

The total torque and power are determined by integrating  $dQ$  and  $dP$  from 0 to  $R$  to obtain

$$dQ = 4\pi\rho U_\infty \Omega \int_0^R a'(1 - a)r^3 dr \quad (4.23)$$

$$dP = 4\pi\rho U_\infty \Omega^2 \int_0^R a'(1 - a)r^3 dr \quad (4.24)$$

or in dimensionless forms as

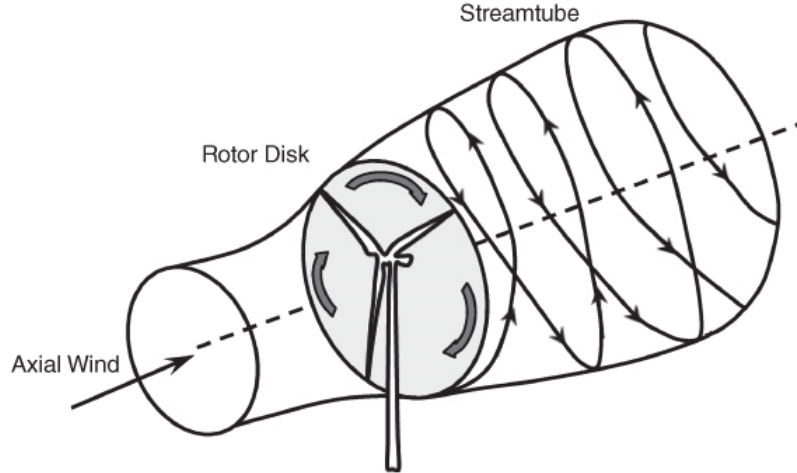


Figure 4.6: Illustration of the flow downstream of the rotating disk.

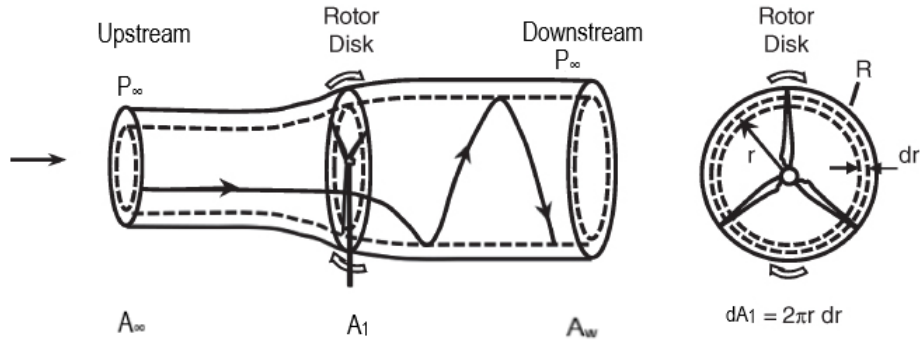


Figure 4.7: Rotor disk annulus.

$$\text{Torque coefficient, } C_Q = \frac{8}{\lambda^3} \int_0^\lambda a'(1-a) \lambda_r^3 d\lambda_r \quad (4.25)$$

$$\text{Power coefficient, } C_p = \frac{8}{\lambda^2} \int_0^\lambda a'(1-a) \lambda_r^3 d\lambda_r \quad (4.26)$$

where  $\lambda = \Omega R / U_\infty$  is the tip speed ratio, which describes the ratio of the angular velocity at the edge of the rotor disk to the incoming wind speed, and  $\lambda_r = \Omega r / U_\infty$ , or  $\lambda r / R$ , defines the fraction of  $\lambda$  seen at a local disk annulus. As is the case with no rotation, the optimum rotor performance with wake was obtained when

$$a = 1/3; a' = \frac{a(1-a)}{\lambda_r^2} = \frac{2/9}{\lambda_r^2} \quad (4.27)$$

Thus, wake rotation is less significant near the rotor tip because as  $r \rightarrow R$ ,  $a' \rightarrow 0$ .

Comparing Eqs. 4.25 and 4.26 gives the following:

$$C_P = C_Q \lambda \quad (4.28)$$

that relates the power and torque coefficients.  $C_Q$  is useful and appears to be the most important in describing direct-drive waterpumping wind turbines, where the torque from the rotor must match that of the pumping load. The value of  $C_Q$  at  $\lambda = 0$  is of significance because it defines the ability of the wind turbine rotor to start the water pump under load conditions. Kentfield [27], therefore, suggested another useful but less fundamentally derived performance parameter termed the water flow rate coefficient,  $C_W$  for describing the potential waterpumping capacity of directly driven water pumps with a reciprocating positive displacement piston pump. He computed  $C_W$  as

$$C_W = \lambda_{run} C_{Q(\lambda=0)} \quad (4.29)$$

Here,  $\lambda_{run}$  is the runaway value of  $\lambda$  in a no-load condition or, otherwise, the maximum  $\lambda$ .

## 4.4 Blade element theory (BET)

The analysis of Sections 4.2 and 4.3 furnished us with formulae to compute the power extracted and thrust acting on the wind turbine rotor. It also provided the theoretical limit of the extractable wind power. However, the performance prediction did not consider the rotor blade design and geometrical parameters. This deficit is remedied by considering individual rotor blades in motion and subdividing each into discrete blade elements. The lift and drag forces acting on a blade element depicted in Figure 4.8 are the same as those

of the same airfoil section at the same angle of attack and resultant velocity. Note that the blade elements are assumed to operate independently of each other: no radial variation in velocity (pressure gradient).

The component velocity for each blade element is summarized in Figure 4.9. The total or resultant velocity as seen by a blade element is a vector sum of the wind speed,  $U_1$ , and the circumferential velocity, which is a combination of  $\Omega r$  and  $w$

$$U_T = \sqrt{[U_\infty(1-a)]^2 + [\Omega r(1+a')]^2}$$

in dimensionless form (4.30)

$$U_T = \sqrt{[(1-a)]^2 + [(1+a')\lambda_r]^2}$$

Both the wind speed and circumferential velocities are modified by both the axial and tangential induction factors. The force/torque acting on the blade element is also shown in Figure 4.9. Here,  $\alpha$  is the angle of attack (or incidence angle), defined as the angle between the blade element's chord line and  $U_T$ .  $\beta$  is the angular distance from the plane of rotation to the element's chord line. The total blade pitch is equal to the sum of the blade twist specified by the blade geometry and the blade pitch. For zero pitch,  $\beta$  is equal to the blade

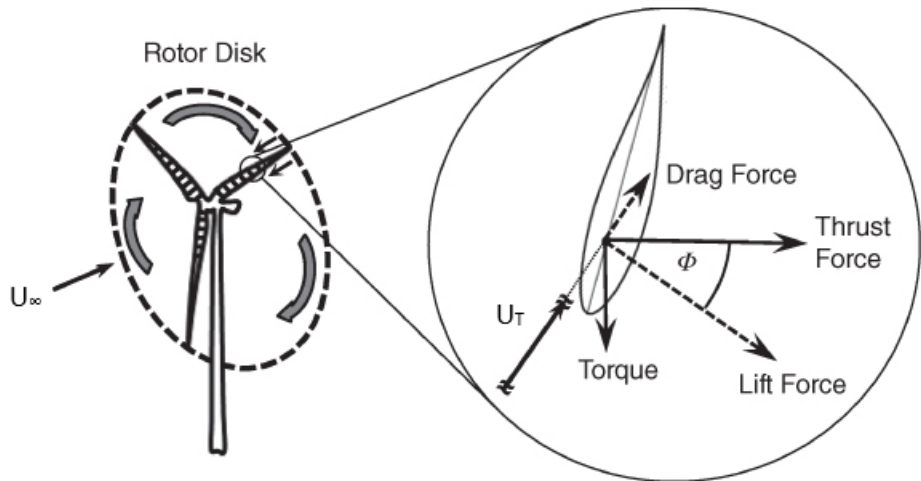


Figure 4.8: BET force system, extracted from [1].

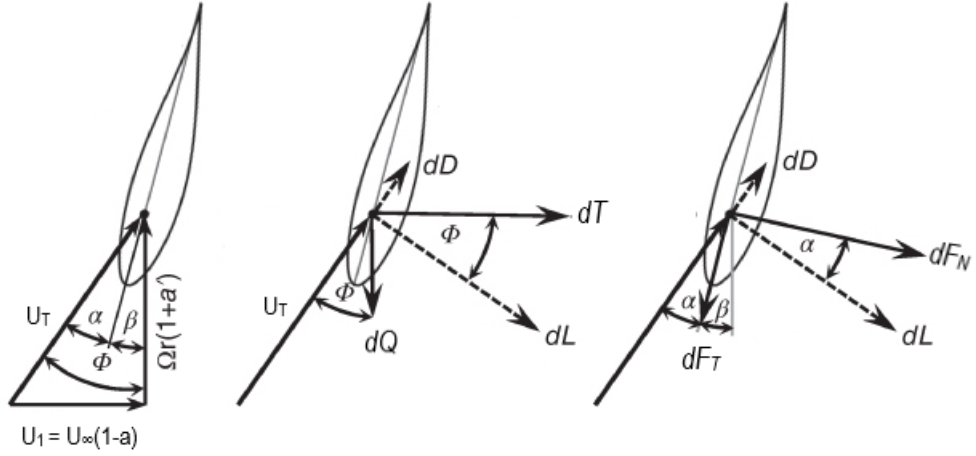


Figure 4.9: Illustration of velocity and aerodynamic force/torque triangles on a blade element. Extracted from [1].

twist. The last of the angles in Figure 4.9 is between the plane of rotation and  $U_T$  and is known as the blade inflow angle. The relation between the three angles is given by

$$\phi = \alpha + \beta \quad (4.31)$$

Also from the geometry,

$$\tan \phi = \frac{U_1(1 - a)}{\lambda r(1 + a')} = \frac{1 - a}{\lambda r(1 + a')} \quad (4.32)$$

Additional relations derived from the velocity triangle are represented as follows:

$$\sin \phi = \frac{U_1(1 - a)}{U_T} \quad (4.33)$$

$$\cos \phi = \frac{\Omega r(1 + a')}{U_T} \quad (4.34)$$

As illustrated in Figure 4.9, while the lift acts normal to  $U_T$ , the drag acts in the direction

of  $U_T$ . It is already assumed that the lift and drag forces acting on a blade element are no different from those of an airfoil of an equivalent section,  $\alpha$ , and  $U_T$ . Based on these assumptions, the blade element lift and drag can be formulated as:

$$dL = \frac{1}{2}\rho U_T^2 C_l c dr \text{ and } dD = \frac{1}{2}\rho U_T^2 C_d c dr \quad (4.35)$$

where  $C_l$  and  $C_d$  are the lift and drag coefficients, respectively, and  $c$  is the chord length. The force on a blade element in Figure 4.9, can be resolved into the axial and circumferential components of interest to obtain the incremental thrust,  $dT$ , and incremental torque,  $dQ$  from the lift and drag forces.

$$dT = dL \cos \phi + dD \sin \phi \text{ and } dQ = (dL \sin \phi - dD \cos \phi)r \quad (4.36)$$

For an  $N$ -bladed rotor, the total thrust and total torque on the  $N$  blade element are:

$$dT = \frac{1}{2}\rho U_T^2 c N (C_l \cos \phi + C_d \sin \phi) dr = \frac{1}{2}\rho U_T^2 c N C_a dr \quad (4.37)$$

$$dQ = \frac{1}{2}\rho U_T^2 c N (C_l \sin \phi - C_d \cos \phi) r dr = \frac{1}{2}\rho U_T^2 c N C'_a r dr \quad (4.38)$$

Here,  $C_a = C_l \cos \phi + C_d \sin \phi$  is the normal force coefficient and  $C_a' = C_l \sin \phi - C_d \cos \phi$  is the tangential force coefficient.

## 4.5 Blade element momentum theory (BEM)

As stated before, BEM is a synthesis of momentum and blade element theories. Basically, it balances the forces on each blade element against the changes in axial and tangential momentum in the annular streamtube that intersects the element to determine the rotor performance. Comparing Eq. (4.11) to Eq. (4.37) gives

$$a(1-a) = \frac{U_T^2 C_a \sigma}{U_\infty^2} \quad (4.39)$$

In Eq. (4.39),  $\sigma$  is the local solidity defined as

$$\sigma = Nc/2\pi r \quad (4.40)$$

Combining Eqs. (4.23) and (4.38) and substituting Eq. (4.39) yields

$$a' = aC'_a/C_a \lambda_r \quad (4.41)$$

By initializing the values of  $a$  and  $a'$ ,  $\phi$  can be determined from Eq. (4.32) and then the  $C_l$  and  $C_d$  and so on and so forth. The calculation is iterative and dependent on  $a$  alone, pending when, for a given blade element, Eqs. (4.11) and (4.23) balance Eqs. (4.37) and (4.38), respectively.

## 4.6 BEM implementation

Having introduced the theory and fundamental equations in Section 4.5, next is the code for implementation. Several open-access codes are available, such as *Qblade*<sup>1</sup> developed at TU Berlin, *XTurb*<sup>2</sup> developed at Penn State University and *power\_calc*<sup>3</sup> developed at the University of Calgary. *power\_calc* written by Professor David Wood was used in this study because it is written in MATLAB, a widely used numerical computing tool; therefore, it can easily be adapted to a given rotor application. Moreover, it includes a versatile and more accurate tip and root loss formulation, making it suitable for SWTs such as a waterpumping windmill that operates at low values of  $\lambda$ , atypical of conventional wind turbines.

---

<sup>1</sup><https://sourceforge.net/projects/qblade/> (accessed 28 May 2020)

<sup>2</sup><https://www.rotoraero.psu.edu/xturb-psu/> (accessed 28 May 2020)

<sup>3</sup><http://extras.springer.com/2011/978-1-84996-174-5> (accessed 28 May 2020)

## 4.7 Finite blade function (Tip and root loss factors)

Several corrections, namely high axial induction, stall delay, solidity, and finite blade number ( $N < \infty$ ) have been suggested to correct the standard BEM. The importance of accurately representing the last ensues from the fact that an approximately 5-10% [80] drop in rotor performance for the typical case of  $N = 3$  is observed for an actual wind turbine compared to an ideal rotor. In BEM, the assumption is that the radial elements operate as two-dimensional airfoil sections with no radial flow along the blade span; in reality, higher pressure upstream flow passes around the blade tip and root to the lower pressure downstream flow, thus generating vortices that trail downstream into the wake. These tip vortices lower the lift and, therefore, the generated torque and the power output. Indeed, the concept of tip loss originated by Prandtl accounts for the difference between the physical mechanism of an actuator disk with an infinite number of blades ( $N = \infty$ ) and an actual wind turbine with a finite number of blades ( $N < \infty$ ).

Finite blade correction is not limited to either the hub or tip, but the whole blade span, hence Wood [140] appropriately referred to it as “Finite Blade function”. It is hoped that this appellation will catch on with time in the wind turbine community.

To simulate a wind turbine with ( $N < \infty$ ), tip loss effects are included in the BEM computation using the Prandtl tip loss function,  $F_p$ , defined as the ratio between the average induced velocity in the streamtube and that induced at the blades. Normalizing by the wind speed and expressing the Prandtl tip loss function in terms of the axial induction factor,  $F_p = a/a_b$  and  $F_p \rightarrow 0$  as  $r \rightarrow R$ . The simple and BEM-compliant form of  $F_p$  due to Glauert [99] is

$$F_p = \frac{2}{\pi} \cos^{-1} \left[ \exp \left( -\frac{N(1-r)}{2r \sin \phi} \right) \right] \quad (4.42)$$

Note that  $r$  in Eq. (4.42) is normalized by the blade tip radius. Following the Prandtl tip loss function,  $F_p$ , the implementation of *power\_calc* is based on Ref. [33] and references [137, 138]

therein. Eqs. (4.39) and (4.41) are then rewritten as

$$\frac{a_b F_p (1 - a_b F)}{(1 - a_b F)^2} = \frac{\sigma C_a}{4 \sin^2 \phi} \quad (4.43)$$

$$\frac{a'_b F_p (1 - a_b)}{(1 - a_b F)(1 + a'_b)} = \frac{\sigma C_{a'}}{4 \sin \phi \cos \phi} \quad (4.44)$$

By incorporating  $F_p$  into the high thrust correction, Eq. (4.17) is modified to

$$f_a = \begin{cases} a_b F_p (1 - a_b F) & a_b \leq a_c \\ 4[a_c^2 F_p^2 + (1 - 2a_c F)a_b F_p] & a_b > a_c \end{cases} \quad (4.45)$$

The final expressions for induction factors deployed in the code become

$$a_b = \frac{2 + Y_1 - \sqrt{4Y_1(1 - F) + Y_1^2}}{2(1 + F_p Y_1)} \quad (4.46)$$

$$a'_b = \frac{1}{(1 - aF_p)Y_2/(1 - a) - 1} \quad (4.47)$$

Here,  $Y_1$  and  $Y_2$  are intermediate functions

$$Y_1 = \frac{4F_p \sin^2 \phi}{\sigma C_a} \quad (4.48)$$

$$Y_2 = \frac{4F_p \sin \phi \cos \phi}{\sigma C_{a'}} \quad (4.49)$$

#### 4.7.1 Helical vortex theory for tip and root loss

The helical trailing vorticity of a rotating blade was originally modeled by Prandtl as semi-infinite two-dimensional laminae and implemented by Glauert [99] as such. It is easily and

rapidly computed in BEM codes but is known to be accurate for  $\lambda$  in excess of about 7 for a typical modern wind turbine operating in practice. This limitation means that for low  $\lambda$  applications such as water pumping windmills,  $F_p$  is insufficient to account for the finite blade number effect. Various alternatives to  $F_p$  have been developed using helical vortex theory for use in BEM code by Branlard [79], Schmitz and Maniaci [81] and Wood et.al [80]. In general, the authors approximated the induced velocity field of a semi-infinite helical vortex sheet in the wake of a wind turbine rotor. Following from [80] and using their Eq. (19), Wood [78] developed a more general analytic tip loss formulation that can easily be absorbed into a BEM program. Accordingly, the equations for the induced velocities by an expanding helical vortex at radius,  $r$ , by a semi-infinite vortex of the pitch,  $p$ , and radius,  $t$ , were derived. In the following discussion, the salient equations reproduced here are strictly based on [78]. The departures from the streamtube average axial,  $U_{wb}$ , and tangential,  $w_{wb}$ , velocities at the blade due to trailing vorticity in the wake are approximated respectively as

$$U_{wb}(r) \sim \frac{1}{4\pi} \int_0^r \frac{\partial \Gamma}{\partial t} \left[ \frac{p^2(t) + t^2}{p^2(t) + r^2} \right]^{1/4} \left[ \frac{-N}{p(t)(1 - e^{\xi N})} + \frac{1}{24} \left( \frac{2p^2(t) + 9t^2}{(p^2(t) + t^2)^{3/2}} - \frac{2p^2(t) - 3r^2}{(p^2(t) + r^2)^{3/2}} \right) \log(1 - e^{\xi N}) \right] dt + \frac{1}{4\pi} \int_r^1 \frac{\partial \Gamma}{\partial t} \left[ \frac{p^2(t) + t^2}{p^2(t) + r^2} \right]^{1/4} \left[ \frac{N}{p(t)(1 - e^{\xi N})} + \frac{1}{24} \left( \frac{2p^2(t) + 9t^2}{(p^2(t) + t^2)^{3/2}} - \frac{2p^2(t) - 3r^2}{(p^2(t) + r^2)^{3/2}} \right) \log(1 - e^{\xi N}) \right] dt \quad (4.50)$$

$$w_{wb}(r) \sim \frac{1}{4\pi} \int_0^r \frac{p(t)}{r} \frac{\partial \Gamma}{\partial t} \left[ \frac{p^2(t) + t^2}{p^2(t) + r^2} \right]^{1/4} \left[ \frac{-N}{p(t)(1 - e^{\xi N})} + \frac{1}{24} \left( \frac{2p^2(t) + 9t^2}{(p^2(t) + t^2)^{3/2}} - \frac{2p^2(t) - 3r^2}{(p^2(t) + r^2)^{3/2}} \right) \log(1 - e^{\xi N}) \right] dt + \frac{1}{4\pi} \int_r^1 \frac{p(t)}{r} \frac{\partial \Gamma}{\partial t} \left[ \frac{p^2(t) + t^2}{p^2(t) + r^2} \right]^{1/4} \left[ \frac{N}{p(t)(1 - e^{\xi N})} + \frac{1}{24} \left( \frac{2p^2(t) + 9t^2}{(p^2(t) + t^2)^{3/2}} - \frac{2p^2(t) - 3r^2}{(p^2(t) + r^2)^{3/2}} \right) \log(1 - e^{\xi N}) \right] dt \quad (4.51)$$

where  $\frac{\partial \Gamma}{\partial t}$  is the rate of change of vortex strength and

$$e^\xi = \frac{r[p(t) + \sqrt{p^2(t) + t^2}] \exp \sqrt{1 + r^2/p^2(t)}}{t[p(t) + \sqrt{p^2(t) + r^2}] \exp \sqrt{1 + t^2/p^2(t)}} \quad (4.52)$$

Wood [78] also observed that the finite blade function in the axial flow,  $F_u$  can be different from that in the tangential flow direction,  $F_w$ . While  $F_u = F_w$  for the ideal case of a Betz-Goldstein rotor, the inequality between  $F_u$  and  $F_w$  needs to be maintained for general analytic application. Resulting in

$$F_u = a/(a + U_{wb}) \quad (4.53)$$

and

$$F_w = a'/(a' + w_{wb}) \quad (4.54)$$

It is important to note that as  $\lambda$  increases,  $F_u$  and  $F_w$  asymptote to  $F_p$ . They are expected to be more accurate at low  $\lambda$ . In the BEM implementation, the  $F_p$  terms in Eqs. (4.48) and (4.49) are replaced by  $F_u$  and  $F_w$ , respectively, as

$$Y'_1 = \frac{4F_u \sin^2 \phi}{\sigma C_a} \quad (4.55)$$

and

$$Y'_2 = \frac{4F_w \sin \phi \cos \phi}{\sigma C_{a'}} \quad (4.56)$$

Following from which the induction factors on the blade are then computed using

$$a_b = \frac{1}{Y'_1 + 1} \quad (4.57)$$

$$a'_b = \frac{1}{Y'_2 - 1} \quad (4.58)$$

To determine  $F_u$  and  $F_w$ , the blade element  $p$  and circulation,  $\Gamma$ , contained in Eqs. (4.50) and (4.51) are required and obtained using

$$a = a'_b F_u = N\Gamma/(4\pi p) \quad (4.59)$$

and

$$\lambda r a' = \lambda r a'_b F_w = N\Gamma/(4\pi r) \quad (4.60)$$

$$\Gamma = \frac{1}{2} U_T C_l \left( 1 - \frac{C_d}{C_l \tan \phi} \right) \quad (4.61)$$

The helical vortex theory, unfortunately, does not account for high thrust or high axial induction. However, the thrust correction equation is obtained from

$$dC_T/dr = 8[a_c^2 + (1 - 2a_c)a_b]F_u r \quad (4.62)$$

where

$$a_b = 1 + Y'_1 \left( \frac{1}{2} - a_c^2 \right) - \frac{\sqrt{Y'_1}}{2} \sqrt{4 + Y'_1 + 4a_c(a_c - 2 - Y'_1(1 - a_c))} \quad (4.63)$$

## 4.8 Simulated windmill

To analyze the aerodynamic performance of the waterpumping windmill using BEM, a previously used turbine model that replicated the experimental rotor of Wegereef [25] and referred to in the work of Singh [23] was simulated. The rotor design and fabrication are detailed in [23]. They are such that the hub can carry different numbers and perhaps types of blades up to a maximum of 24, as depicted in Figure 4.10. The rotor is of diameter 0.68 m, and the blades are made from ABS plastic via rapid prototyping to ensure precision and homogeneity

in their profile. The blade model has a constant chord and thickness of 0.04 m and 0.002 m, respectively, and a span of 0.2 m. All configurations used identical circular arc blades with 15% camber, typical of water pumps, and twist angle varying from  $46^\circ$  at the blade root of  $0.42R$  to  $17^\circ$  at the blade tip of  $0.83R$ . On the concave (high pressure) side of the blades, similar to the scaled rotor of Wegereef, spars of  $1/4''$  diameter (15.88% chord) that extends out from the rotor hub were mounted at the 50% chord position to maximize the  $C_l/C_d$ , as suggested by [26], as well as for reinforcement and attachment to the rotor hub (see Figure 4.11). The CA1705 with performance characteristics shown in Figure 4.12 was used in the simulation because it has geometrical characteristics similar to Wegereef's [25] blade profile.

#### 4.8.1 Blade element computations

The blades of Figure 4.11 were divided into 20 equispaced blade elements from the root to the tip. The BEM analyses use two-dimensional lift and drag data for the blade sections without and with spars at  $Re = 0.6 \times 10^5$  and  $10^5$  for  $\alpha$  between  $-10^\circ$  and  $90^\circ$  obtained in Chapter 3 and shown in Figure 4.12. While wind tunnel blockage corrections were applied to the airfoil data used here, no corrections were done for either stall delay or solidity effects. The blade element calculations were iterated for all elements to within a convergence tolerance of  $10^{-4}$ .

The *power\_calc* code has been validated in [78] and shown to predict the performance of high  $\lambda$  and low  $\sigma$  typical of convectional wind turbines with reasonable accuracy. The computed power and thrust coefficients compared to the experimental data of two-bladed rotor measurements of Anderson et al. [141] are presented in Figure 4.13. While conventional Prandtl,  $F_p$ , and modified tip loss,  $F_u$  and  $F_w$ , reduce the power to within about 10% of the no tip loss case, very little change can be observed for the thrust. However, the experimental results are well in agreement for  $C_P$  obtained using both tip loss methods.

For low  $\lambda$  and increasing rotor  $\sigma$ , as in the case of the simulated multi-bladed windmill

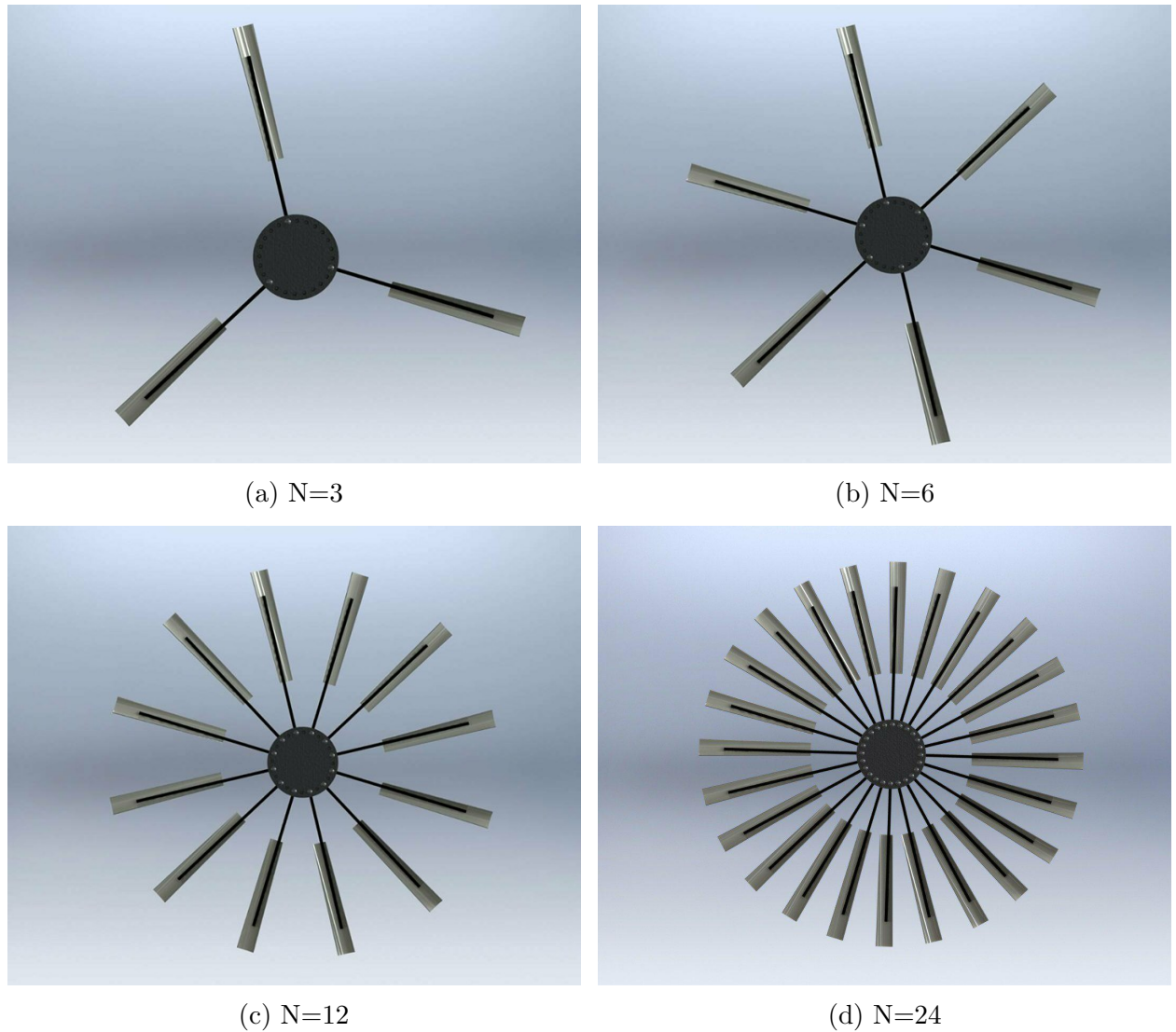


Figure 4.10: Experimental rotor blade configuration.

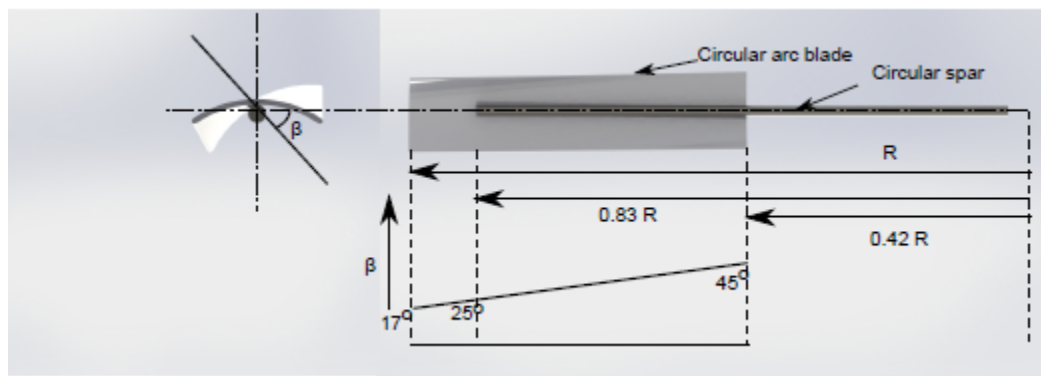


Figure 4.11: Blade profile of experimental model (extracted from [23]).

model, the influence of  $F_p$ , and  $F_u$  and  $F_w$  on the performance was examined and then compared with measurements obtained from the negligible blockage open jet facility (OJF) of TU Delft. The simulations were performed at a wind speed of 15 m/s, and the testing details are given in Chapter 6. As shown in Figure 4.14, the BEM prediction of  $C_p$  using  $F_u$  and  $F_w$  (modified tip loss–MTL) is more accurate for  $N = 3, 6, 12$  and  $24$ , but the difference with  $F_p$  (convectional Prandtl tip loss–CTL) decreases as  $N \rightarrow \infty$ . A similar trend is also observed for  $C_Q$ , as given in Figure 4.15 because of the direct relationship between torque and power. However, at low  $\lambda$ , the BEM under-predicts the torque primarily because of the high  $\sigma$ , which is most obvious in  $N = 24$ . The extent of deviation due to the rotor solidity effect could not be shown due to the unavailability of test data at the lower  $\lambda$  up to the zero-speed region of the curves. Using both CTL and MTL,  $C_T$  in Figure 4.16 was over-predicted for  $N = 3, 6$  and  $12$ , contrary to that of the high  $\lambda$  and low  $\sigma$  rotor of Figure 4.13, but underestimated that of  $N = 24$ , see Figure 4.13(b).

There are noticeable differences between the BEM predicted global parameters  $C_p$ ,  $C_Q$  and  $C_T$  using the CTL and MTL functions as reflected in the blade element, (BE), performance parameters over the entire range of  $\lambda$ . The behavior follows about the same pattern for all  $N$ . Figures 4.17, 4.18, 4.19 and 4.20 present comparisons of the BE performance

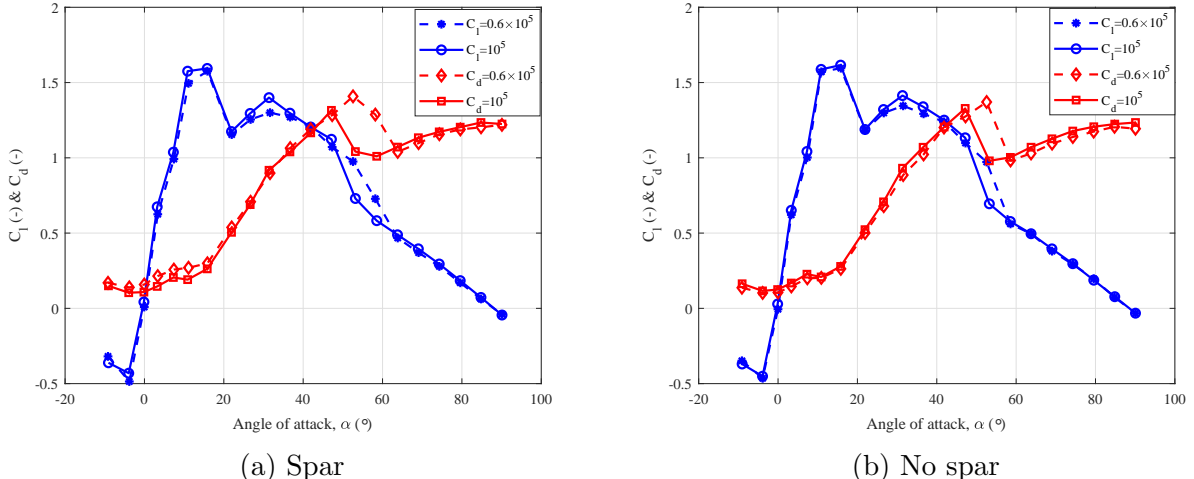


Figure 4.12: Lift and drag coefficients of the model windmill blade CA1705 section.

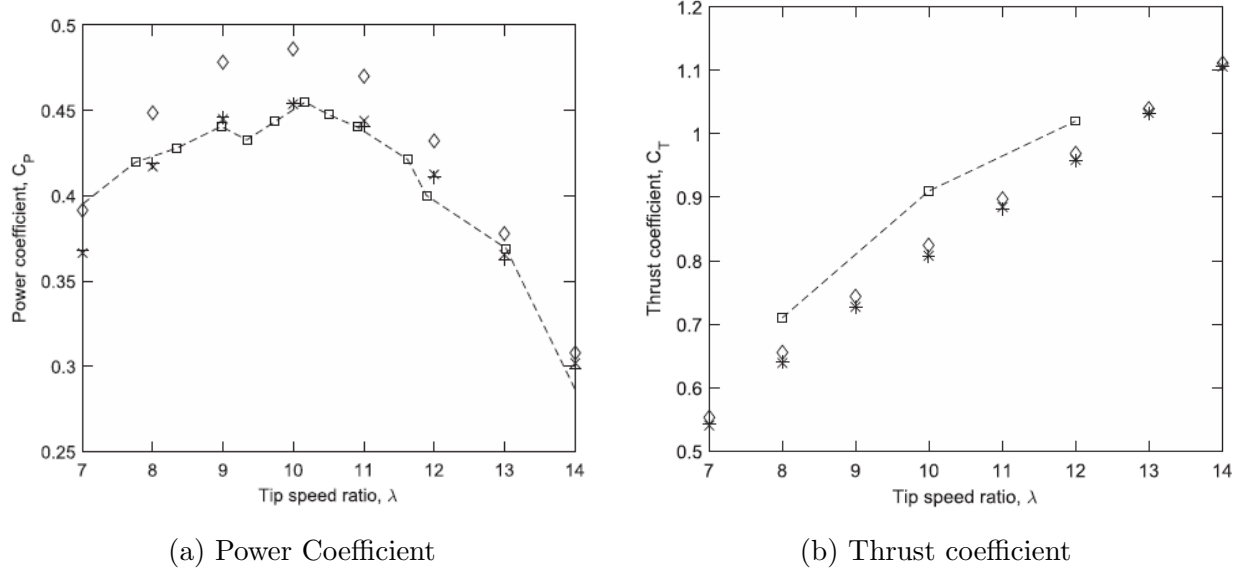


Figure 4.13: Predicted performance compared to the measurements of Anderson et al. [141],  $\square$ ,  $\diamond$ , BEM without tip loss;  $+$ , BEM with conventional tip loss;  $*$ , BEM with modified tip loss. Reproduced from [78].

parameters for  $N = 3, 6, 12$  and  $24$ , respectively, at a representative  $\lambda = 1$ . This value is chosen for two reason: (a)  $\lambda_{opt}$ , that is the  $\lambda$  that corresponds to maximum power coefficient,  $C_{p,max}$  is between  $0.9$  and  $1.4$  for each  $N$ , and (b) to have a common basis for comparing the implications of the BE parameters on the global parameters for each  $N$ .

For  $N = 3$ , although  $F_u$  and  $F_w$  matched closely across the blade span, there is a marginal difference around the blade mid-span as shown in Figure 4.17(a). Of significance is  $F_u$  and  $F_w$  that exceed unity and are far higher than  $F_p$ , which is widely believed to be inaccurate at low values of  $\lambda$  [78]. The low value of  $F_p$  is responsible for the underestimated  $C_p$ , especially on the right side of the torque and power spectrum of Figures 4.14 and 4.15 respectively. Figure 4.17(b) shows  $\Gamma$  is relatively uniform along the span and will expectedly increase with increasing  $\lambda$  as it approaches  $\lambda_{opt}$  for the 3-bladed rotor case. The differences from  $r/R = 0.5$  to  $r/R = 1$  are reflective of the difference in the  $C_P$  due to the two methods. The MTL function more accurately predicts the measurements near to and at the tip, where  $\Gamma$  due to  $F_u$  and  $F_w$  is greater, and hence more power is produced. Figures 4.17(c) and

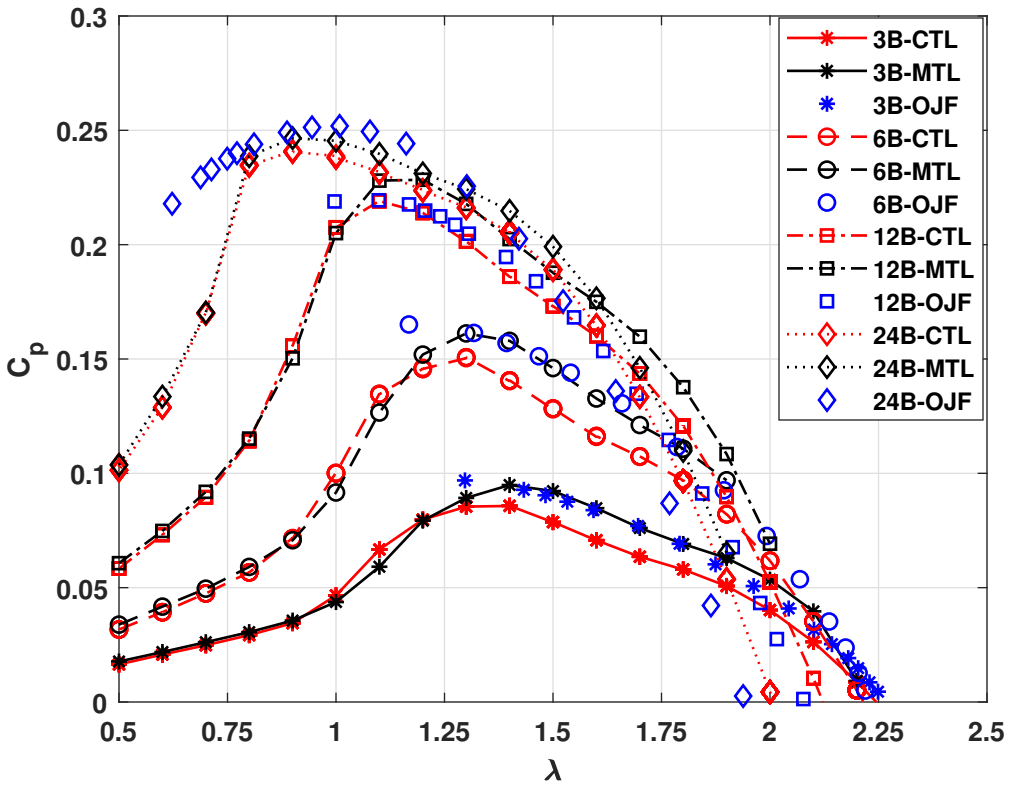


Figure 4.14: Computed power coefficient compared to TU Delft OJF experimental measurements. Experimental results are in blue. The conventional Prandtl tip loss (CTL) in red and modified tip loss (MTL) in black.

4.17(d) compare the distribution of forces and flow along the blades for the blade element torque and thrust, respectively. The increase near the tip region is because of the increasing contribution of  $\Omega r$  to  $U_T$ . Hence, most of the power and thrust are produced in that region. In the light of these differences,  $F_u$  and  $F_w$  predict the near tip performance with reasonable accuracy. Bear in mind that as much as 40% of the blade radius near the root of Figure 4.11 is not captured in the BEM analysis. However, the relations derived in Appendix C were used to estimate the torque and thrust of the spars not due to the blade (see Figure 4.11) and then used to correct the presented experimental data. Because most of the power is produced near the tip, it is less likely that power produced at  $r/R \leq 0.4$ , will significantly affect the rotor aerodynamic performance.

Keeping  $\lambda$  constant and increasing  $N$  from 3 to 6 or  $\sigma$  from 0.11 to 0.22 did not signif-

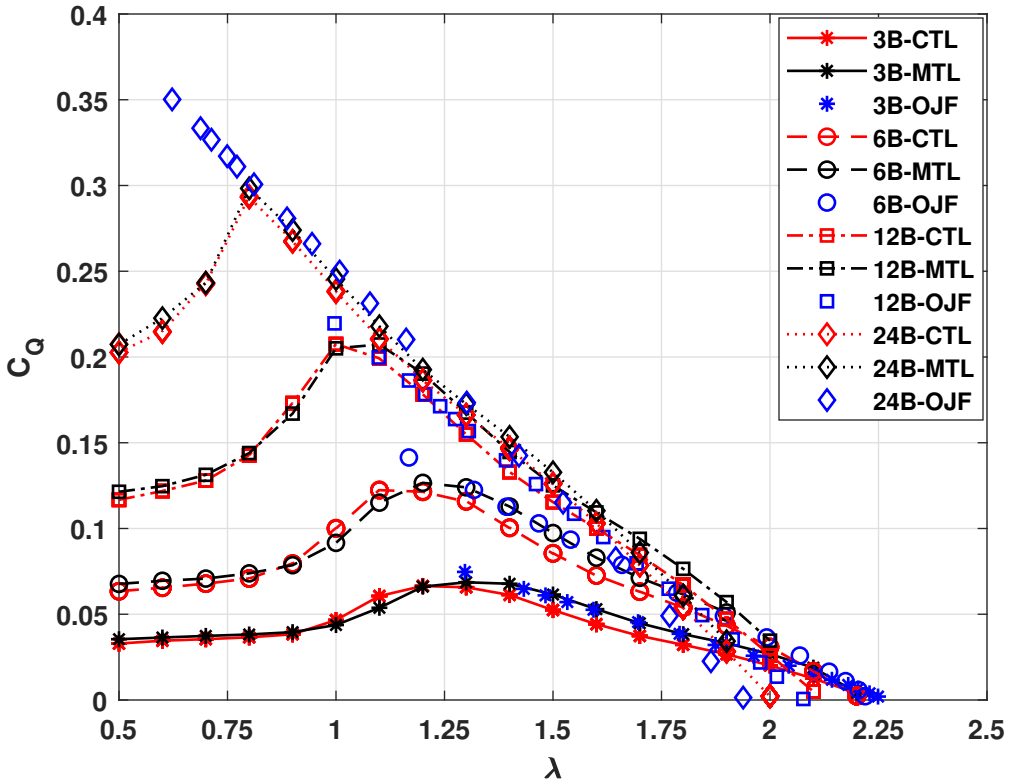


Figure 4.15: Computed torque coefficient compared to TU Delft OJF experimental measurements. Experimental results are in blue. The CTL in red and MTL in black.

icantly change the difference between  $F_u$  and  $F_w$ , and  $F_p$  of Figure 4.18(a), except at the inner blade section where there is improved agreement.  $F_u$  and  $F_w$  closely match. At the  $\lambda$  considered, which is below  $\lambda_{opt}$ , the BE parameters of Figures 4.18(b), 4.18(c) and 4.18(d) are reflective of the global parameters. Further increase in  $N$  from 6 to 12, improves the agreement of  $F_u$  and  $F_w$ , and  $F_p$  as illustrated in Figure 4.19(a); it appears that as  $N \rightarrow \infty$ ,  $F_u = F_w$ . The correspondence of  $\Gamma$ , elemental torque, and thrust as respectively depicted in Figures 4.19(b), 4.19(c) and 4.19(d) due to both tip loss function methods explains the improved agreement in the results. For a much larger  $N$ , or a correspondingly high  $\sigma$ , only slight differences can be observed at both the root and tip of the blade, which, of course, are the regions of vortex generation. The result of Figure 4.20(a) therefore suggests that  $F_u$  and  $F_w$  are nearly equal to  $F_p$ . In general, as  $N$  approaches  $\infty$ , equivalent to the ideal

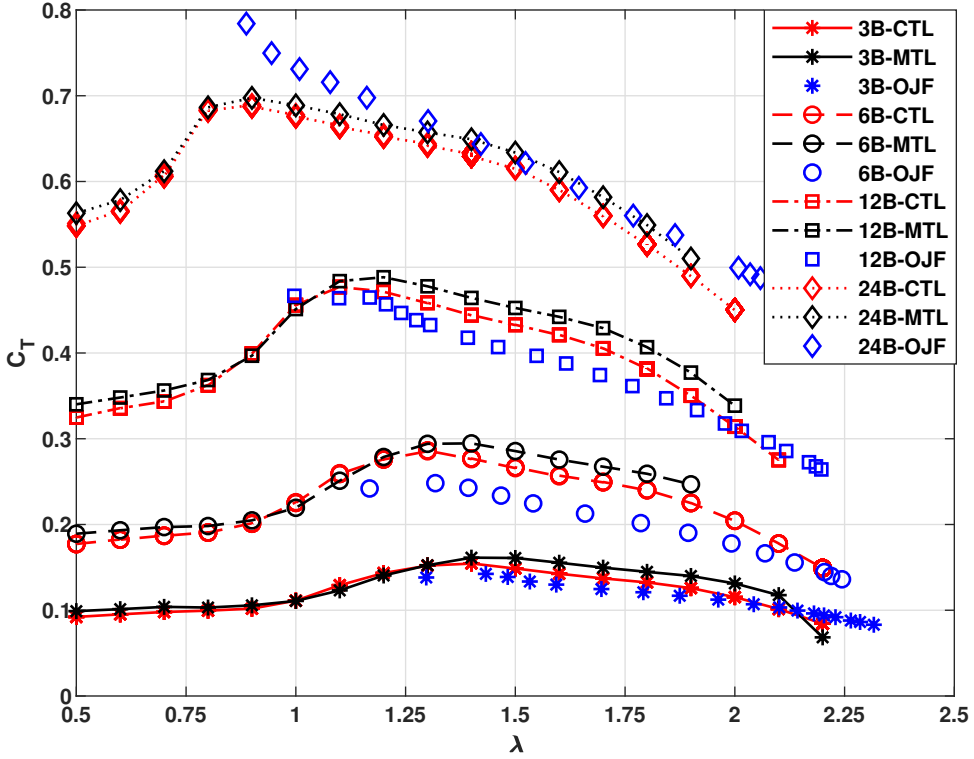


Figure 4.16: Computed thrust coefficient compared to TU Delft OJF experimental measurements. Experimental results are in blue. The CTL in red and MTL in black.

rotor disk, the correspondence of the two tip loss methods improves. Evaluating the tip loss effect at the optimal tip speed ratio, which will be considered next, is of interest to wind turbine designers because it provides a sound basis for informed decisions that can improve aerodynamic designs. For all  $N$  cases investigated, the performance prediction due to  $F_u$  and  $F_w$  are in good agreement with the test data. Thus, all subsequent BEM calculations will use the modified tip loss function.

The impact of the BE performance parameters based on  $F_u$  and  $F_w$  was further examined at  $\lambda = 0.5, 1.0$  and  $1.5$  for each  $N$  case. An illustration of the dimensionless velocity variation at the blades computed as  $U_1/U_\infty = 1 - a$  is given in Figure 4.21 with the magnitude of  $U_1/U_\infty$  decreasing with  $N$ . For a given  $N$ , increased velocity reduction occurs at the blade. Otherwise,  $a$  increases with increasing  $\lambda$ . The near constancy of  $U_1/U_\infty$  across the blade

span reduces with  $\lambda$ . At  $\lambda = 0.5$ , it is largely flat, except near the tips where it rises due to tip loss correction. Increasing  $\lambda$  to 1 decreases the uniformity ratio, which becomes more non-uniform and drops to a minimum near  $r/R = 0.9$  for  $\lambda = 1.5$ . Figure 4.22 presents a comparison of  $F_u$  and  $F_w$ , and  $F_p$  for all cases of  $N$ . As can be observed, at  $\lambda = 1$ , the tip loss exceeds unity at around 60–70% of the blade span for the case of  $N = 3$  (see Figure 4.22(a)) and  $0.7 < r/R < 0.9$  for  $N = 6$  in Figure 4.22(b) rather than near the axis of rotation as alluded to by Wood et al. [80].  $F_u$  and  $F_w > 1$ , according to Wood and Okulov [142], is due to the inclusion of non-linear angular momentum terms in the BEM for  $N < \infty$ . However, the correctness of the peak at locations further away from the hub may be connected to the

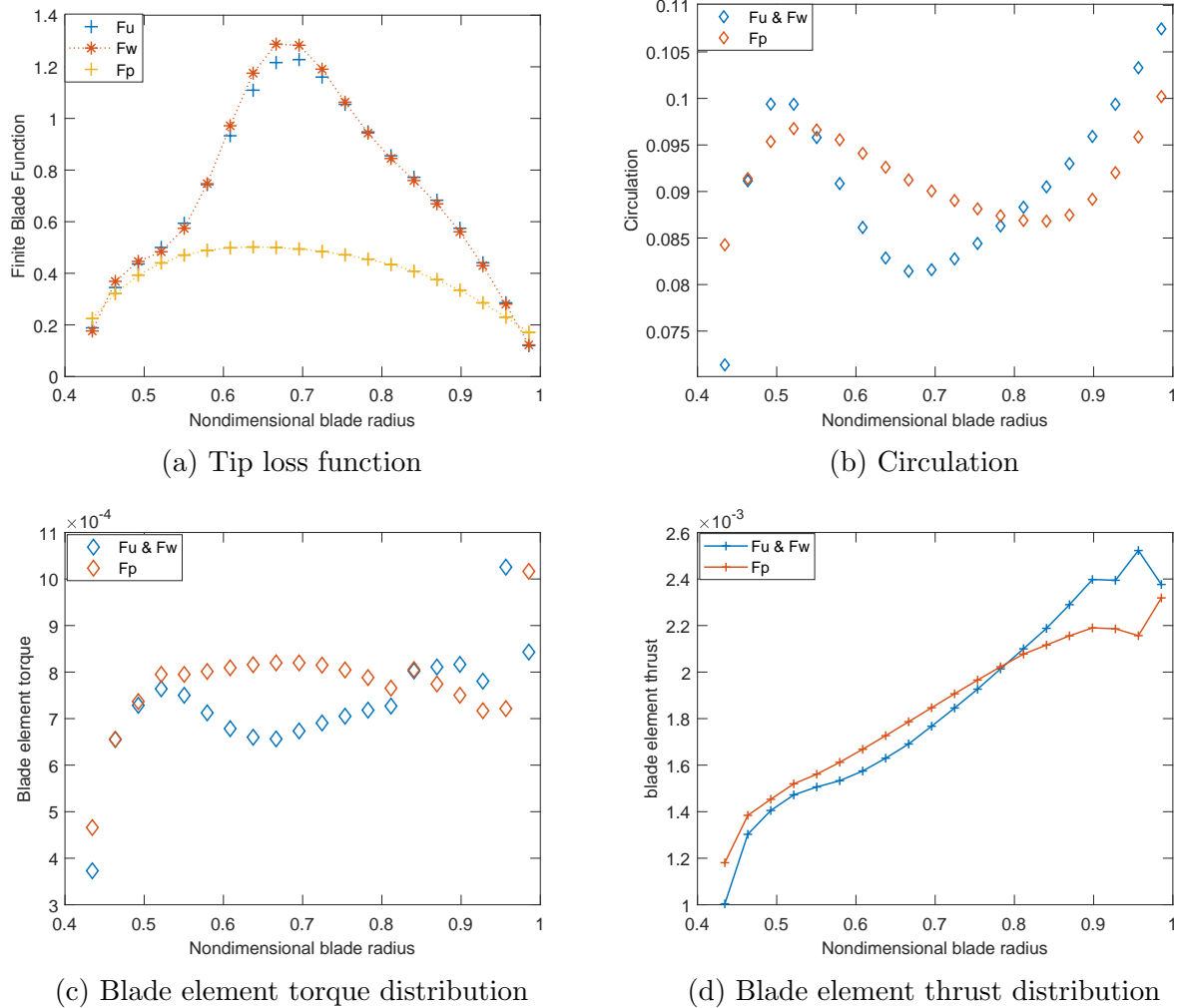


Figure 4.17: Blade element performance parameters for  $N = 3$  at  $\lambda = 1$ .

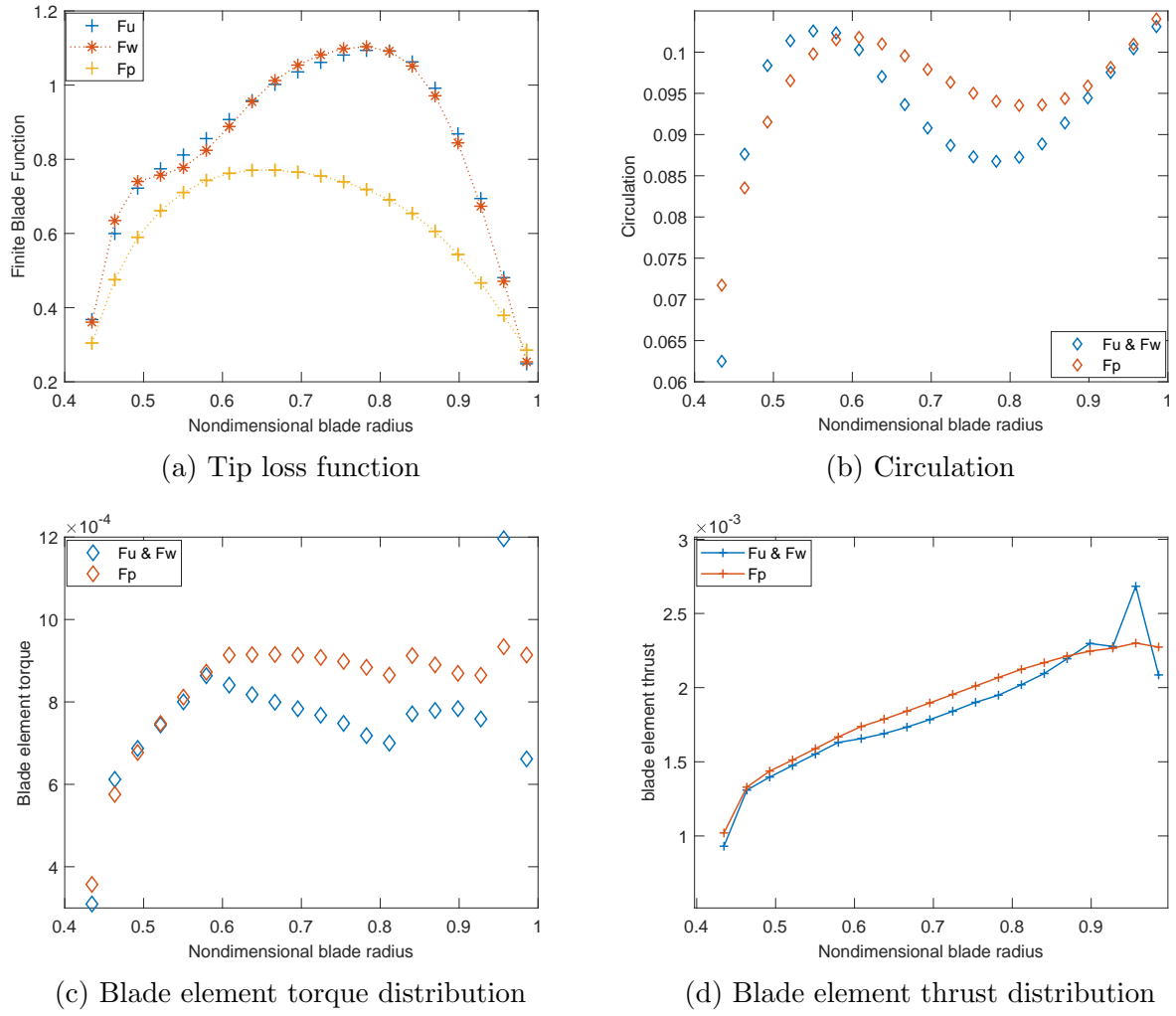


Figure 4.18: Blade element performance parameters for  $N = 6$  at  $\lambda = 1$ .

smoothness of the sectional airfoil lift and drag data known to determine the smoothness of  $F_u$ , and  $F_w$  curves [80]. Notice that as  $N$  increases, the local peaks reduce, and the evenness of the distribution increases, thereby reducing the discrepancies at the respective  $\lambda$ . For the range of  $\lambda$  considered, the importance of non-linearity varies non-monotonically. For example, at  $\lambda = 0.5$ ,  $F_u$  and  $F_w$  are either less than or around unity, but at  $\lambda = 1$ , they are relatively large due to increased significance of the non-linear terms, which then reduces at  $\lambda = 1.5$ . This agrees with Wood and Okulov's [142] finding that the non-linear terms peak when  $0.8 \leq \lambda \leq 1.5$ .

$\Gamma$  normalized by  $(\frac{1}{2}U_T c C_l)$ , is generally uniform along the blade span for all examined  $\lambda$  and

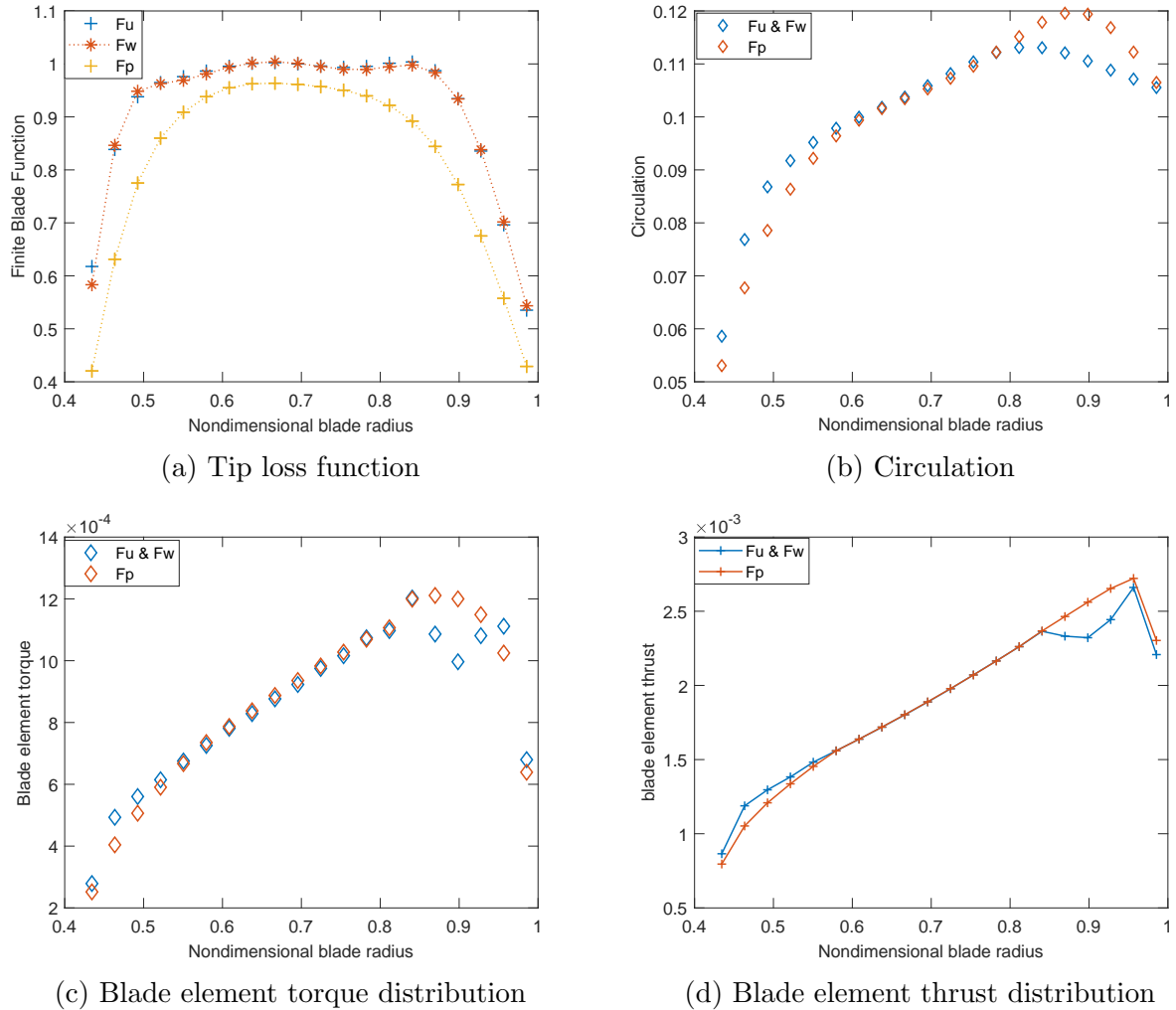


Figure 4.19: Blade element performance parameters for  $N = 12$  at  $\lambda = 1$ .

cases of  $N$ , as shown in Figure 4.23. In each plot, the curves with the highest peak represent the optimum value of  $\lambda$ . Again, near the tip circulation decrease is due to the tip loss correction, such that  $\Gamma\lambda$  will be approximately constant. Notice that the variation of  $\Gamma$  with  $\lambda$  is dependent on optimum  $\lambda$ ; as an example, for  $N = 3$ ,  $\Gamma$  tends to increase with increasing  $\lambda$ , as illustrated in Figure 4.23(a). However, when  $N = 24$ ,  $\Gamma$  is highest for  $\lambda = 1$ , which is close to  $\lambda_{opt}$  and lowest for  $\lambda = 1.5$ , as shown in Figure 4.23(d). Because the local torque is directly due to the local circulation, the curves of the blade elemental torque of Figures 4.24(a-d) closely match those of Figure 4.23. The plot is such that multiplying a given  $\lambda$  by the sum of the torques gives the blade element contribution to  $C_p$ . At  $\lambda = 0.5$ , the blade

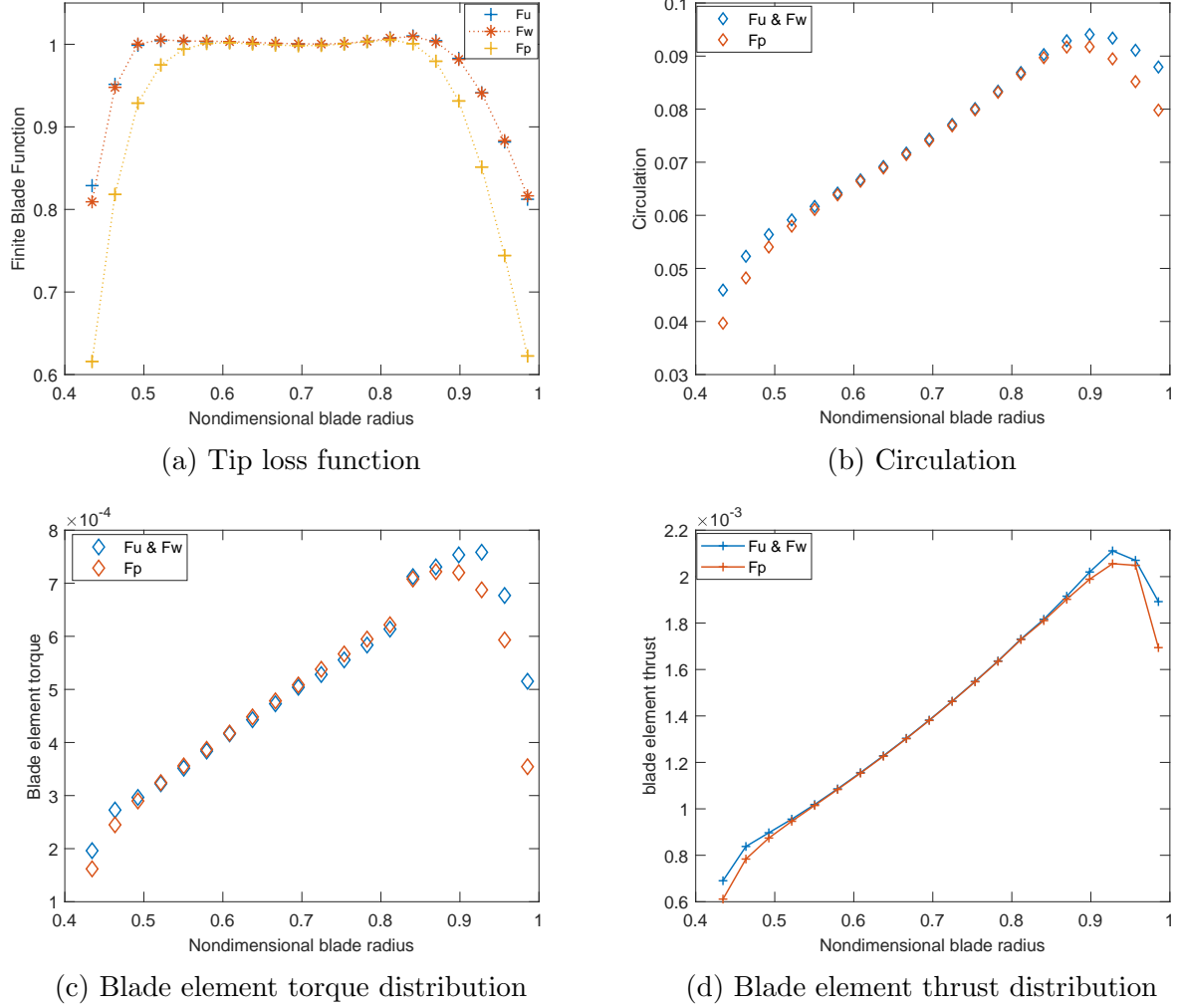


Figure 4.20: Blade element performance parameters for  $N = 24$  at  $\lambda = 1$ .

element torque is relatively constant for all  $N$ , except for  $N = 24$ , where it peaked around  $r/R = 0.55$  before falling to a nearly constant value. The maximum BE torque occurs at the optimum  $\lambda$  for each  $N$  case. As  $N$  increases, the BE torque magnitude decreases, following Figure 4.21. As shown in Figures 4.24(e-h), similar to Figures 4.24(a-d), the magnitude of the BE thrust decreases with  $N$ . The thrust value increases spanwise due to the increased contribution of  $\Omega r$  and is largest at  $\lambda_{opt}$  occurring near  $\lambda = 1.5$  for  $N = 3$  and 6. The effect of finite blade correction is seen near the tip. Unevenness observed in the MTL curves is possibly due to unresolved numerical convergence issues, also observed in [140].

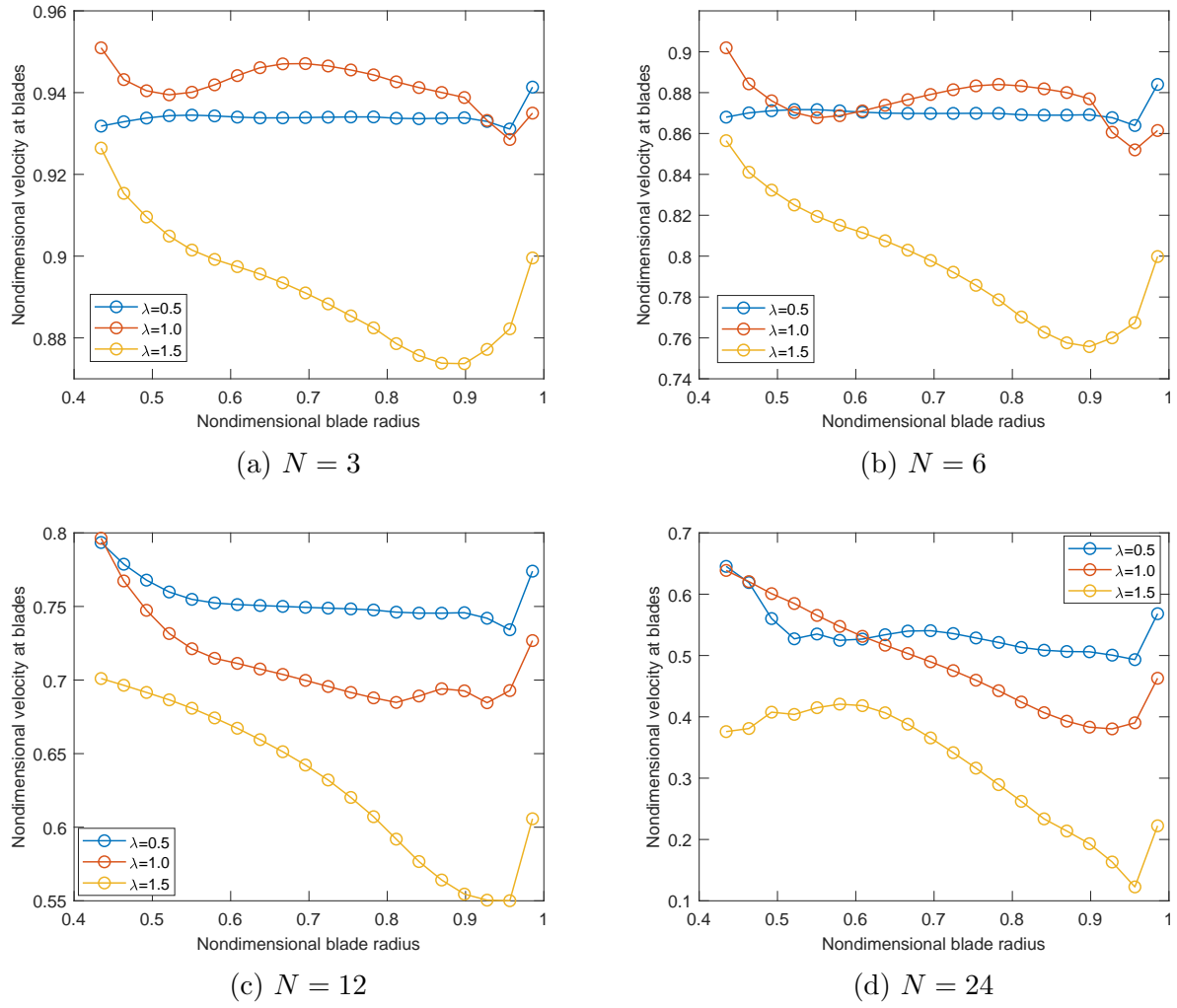


Figure 4.21: Predicted velocity through the rotors for the MTL function.

## 4.9 Concluding remarks

The fundamental BEM theory has been explored, and its accuracy in predicting the performance of a 0.68 m waterpumping windmill model with different blade numbers was evaluated. The BEM with modified tip loss predicted the global performance parameters, namely,  $C_T$ ,  $C_Q$ , and  $C_p$  with reasonable accuracy, better than the traditional Prandtl tip loss function. Unlike  $F_p$  that is restricted to  $\leq 1$ ,  $F_U$  and  $F_W$ , which are based on the helical vortex theory and can be different in both the axial and azimuthal directions, are not limited to unity due to the inclusion of non-linear momentum terms usually excluded in standard BEM analy-

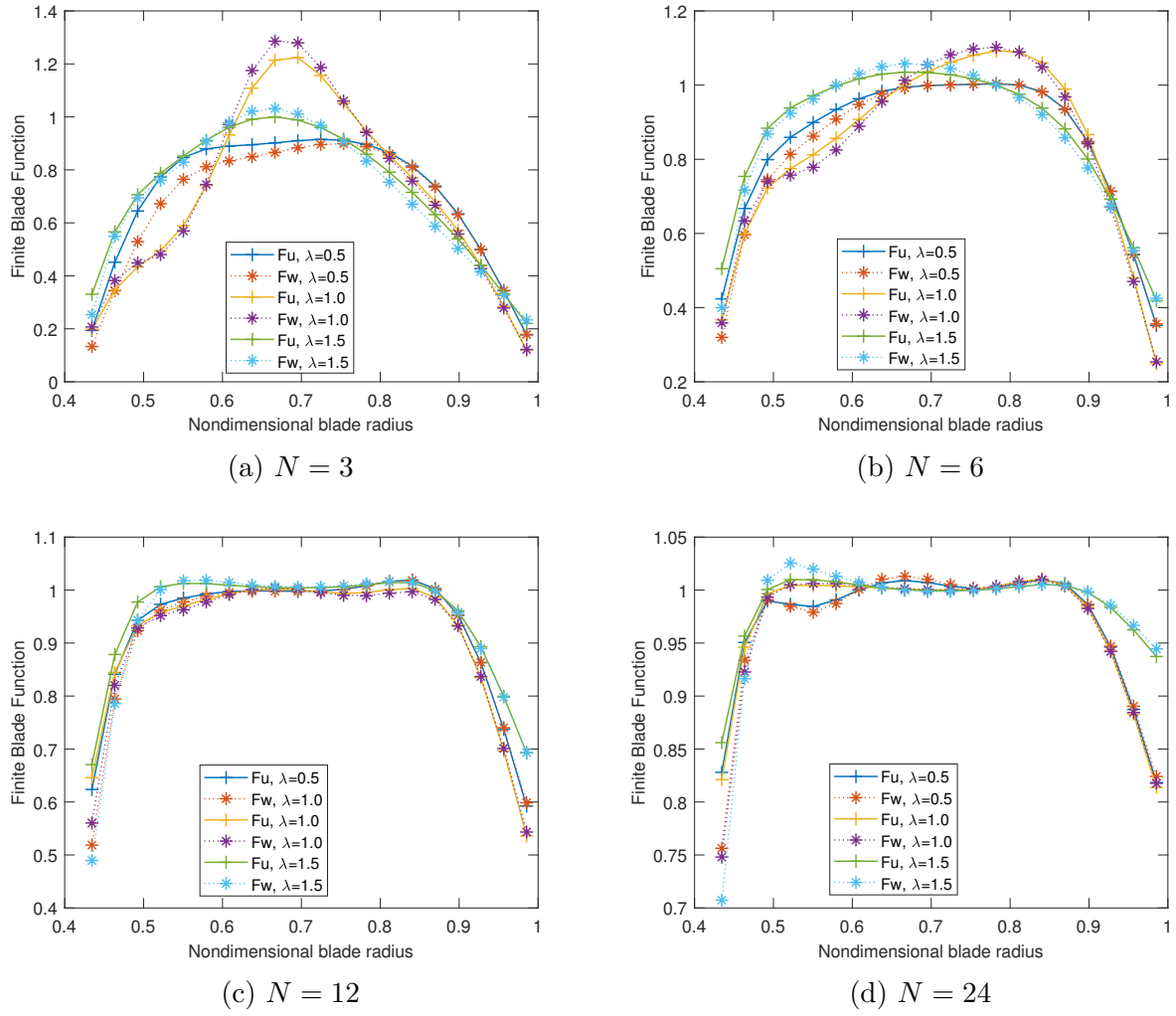


Figure 4.22: Modified tip loss functions.

sis. As  $N$  increases,  $F_U$  and  $F_W$  asymptote to  $F_p$ . A better agreement was also obtained for the high  $\lambda$  range considered. The effect of variable  $N$  was examined; an increase in  $N$  increases the maximum power and thrust coefficients while lowering  $\lambda_{opt}$ ; that is, shifting the curves leftward. Whereas BEM accurately predicts the maximum  $C_p$ , it significantly under-predicts the maximum torque at very low  $\lambda$ , due to high  $\sigma$ , very obvious for  $N = 24$ , indicating that water pumping windmills generate much more starting torque than anticipated. However, the unavailability of experimental data at the small values of  $\lambda$  investigated in this study makes it impossible to draw a firm conclusion on the significance of solidity. Starting behavior of the model windmill is considered in chapter 5.

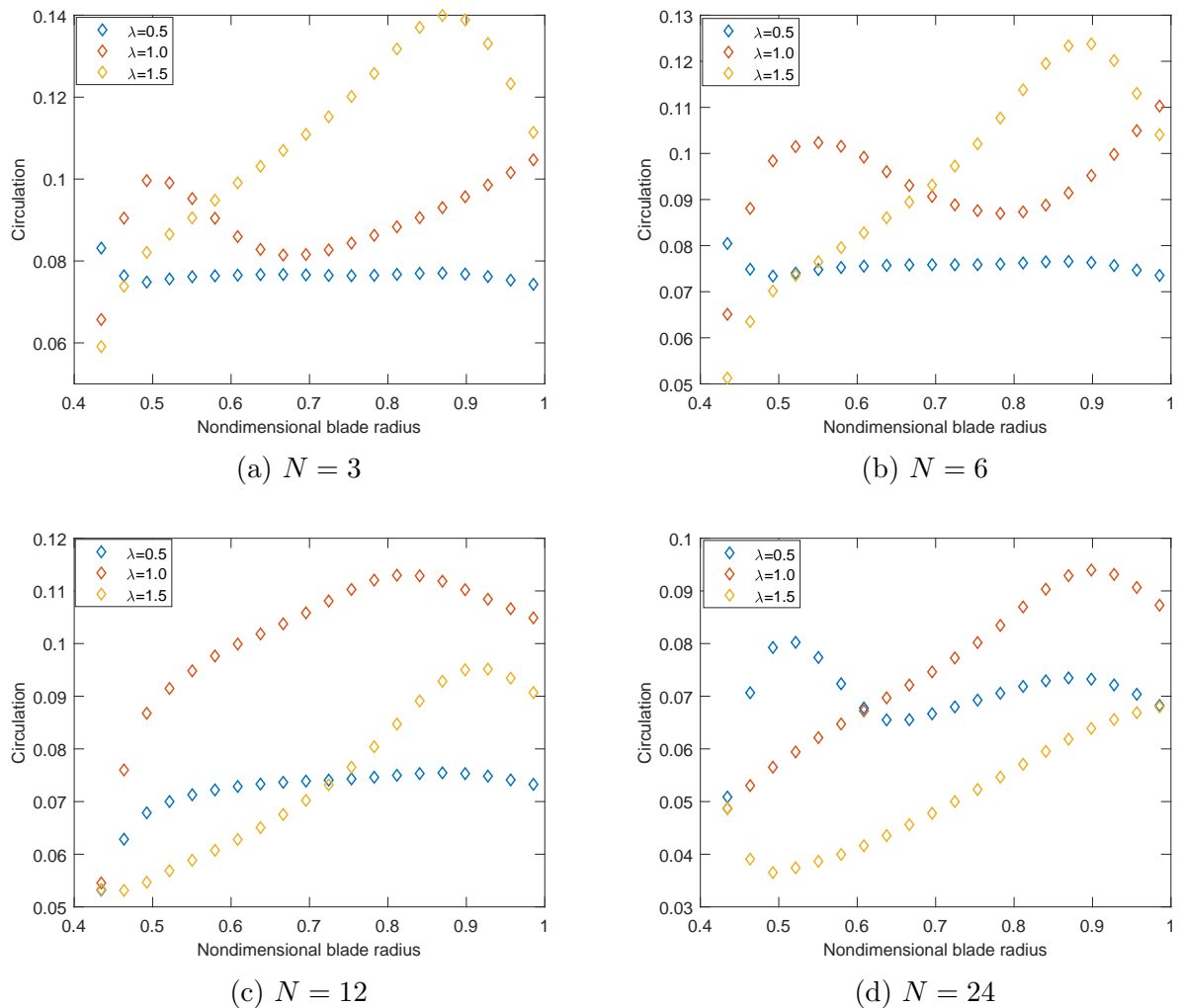


Figure 4.23: Predicted blade circulation of the MTL.

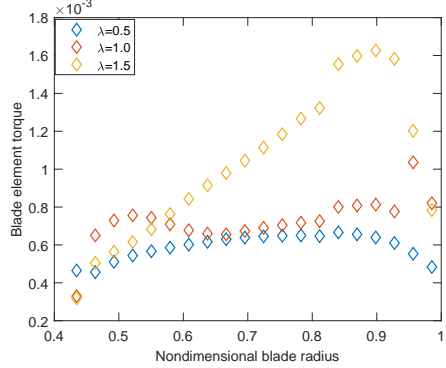
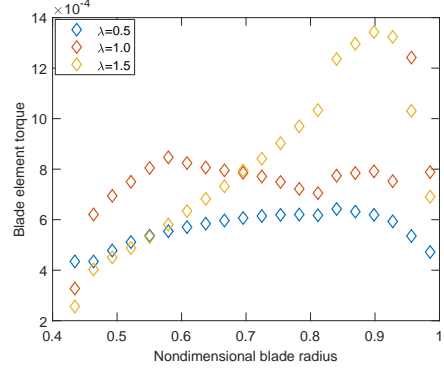
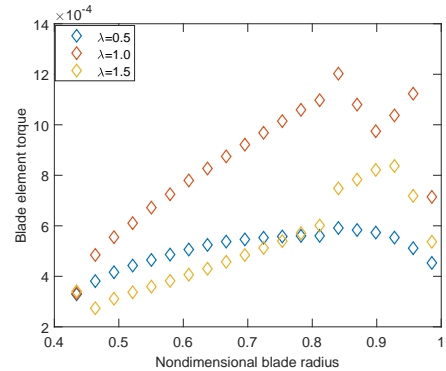
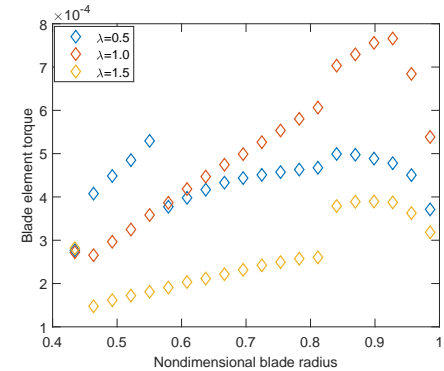
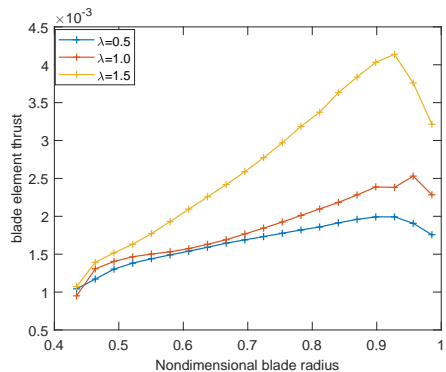
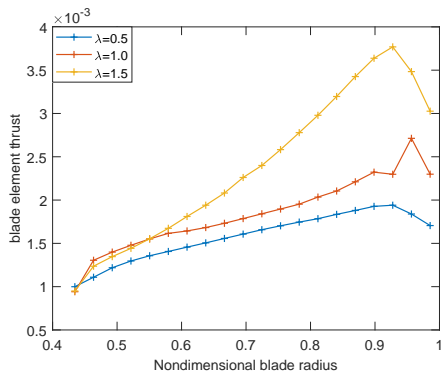
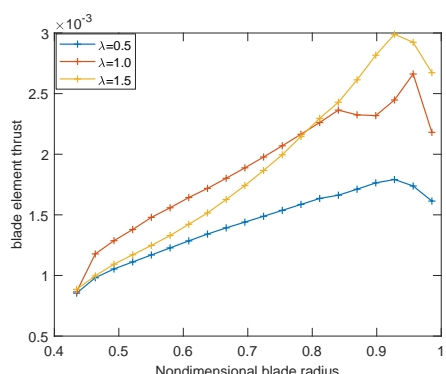
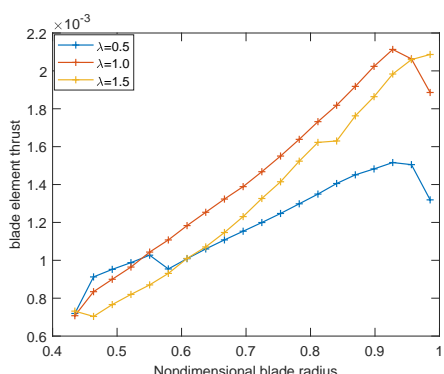
(a)  $N = 3$ (b)  $N = 6$ (c)  $N = 12$ (d)  $N = 24$ (e)  $N = 3$ (f)  $N = 6$ (g)  $N = 12$ (h)  $N = 24$ 

Figure 4.24: Predicted distribution of blade element torque and thrust of MTL.

# Chapter 5

## Starting Analysis

In this chapter, a quasi-steady-state starting model using the characterized drivetrain resistance of the magnetic particle brake (MPB70) by Vaz et al. [24] is developed for the windmill model introduced in Section 4.8. The model validation with experimental measurements from the OJF and RWT for the case of  $N = 3$  is also presented. Furthermore, results of the BEM prediction for starting and runaway speeds are presented for each  $N$ . Finally, kinetic energy ratio, KER, and reduced pitch rate,  $k_\alpha$  are used to determine the validity of the starting model assuming no induction and negligible unsteadiness, respectively on the performance of  $N = 3, 6, 12$ , and  $24$ .

### 5.1 Aerodynamic starting model

Better starting is important for windmills that have maximum pumping efficiency at very low wind speeds. Because of the implication of starting on the performance of SWTs, there must be a compromise between high performance and improved starting on their blade design. Blades designed for power production only will most likely require a high cut-in wind speed, which will be of less practical use in low wind speeds regions [33]. Therefore, the rotor blades must generate enough aerodynamic torque to overcome the combined resistive torque in their generators and drivetrain system. Considering that the aerodynamic torque,  $Q$ , must scale

with the cube of rotor radius, that is  $Q \sim R^3$ , it is not then surprising that starting can be a significant problem for SWTs. The typical resistance of a SWT is the cogging torque of a permanent magnet generator (PMG) and the frictional torque in bearings or gearbox systems, if present.

For SWTs, two types of torque determine their starting: aerodynamic torque, which is due to the forces acting on the blades, and the torque due to the bearing friction on the rotor shaft and the cogging torque on generators, which is referred to as drivetrain resistance torque. As detailed in [35], starting aerodynamics is complicated, primarily influenced by the high  $\alpha$ , very low  $Re$ , and unsteady flow. However, the Blade element momentum (BEM) theory has been shown to predict the starting behavior of a small HAWT with accuracy provided its acceleration is slow enough for a simple quasi-steady-state approximation [32, 34].

### 5.1.1 Model description

The starting prediction model is based on Newton's second law of motion applied to the small wind turbine rotor illustrated in Figure 5.1. Details of the circular-arc bladed windmill model, as well as the geometrical characteristics of airfoil, have been provided in Figures 4.10 and 4.11. The model comprises two deep-groove ball bearings in the Magnetic Particle Brake (MPB) and the windmill rotor. Fundamentally, the starting angular acceleration,  $\alpha$ , is mathematically expressed as

$$\alpha = \frac{Q_{net}}{J} \quad (5.1)$$

where  $Q_{net}$  is the net torque accelerating the windmill rotor divided by the total moment of inertia,  $J$ . Eq. 5.1 can then be expressed in terms of angular speed,  $\Omega$  as

$$\frac{d\Omega}{dt} = \frac{Q - Q_r}{J} \quad (5.2)$$

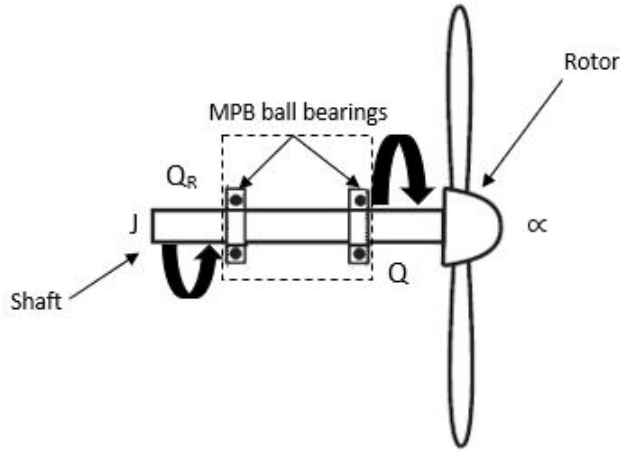


Figure 5.1: Illustration of windmill drivetrain and rotor system.

where  $Q$  already defined, is the aerodynamic torque,  $Q_R$  is the drivetrain resistive torque due largely to the frictional resistance of the MPB bearings, and  $d\Omega/dt$  is the rate of change of angular rotor speed. In terms of  $\lambda$ , Eq. (5.2) easily becomes

$$\frac{d\lambda}{dt} = \frac{R(Q - Q_r)}{J} \quad (5.3)$$

From Eq. (5.3) starting is only possible if and when  $Q > Q_r$ .

### Drivetrain resistance model

In place of a generator, the windmill model uses an MPB70 whose resistive torque is defined in terms of the aerodynamic load imposed by the flow on the turbine,  $T_a(n)$ , computed from BEM, constant drag torque of MPB70,  $Q_{MPB}$ , turbine rotational speed (rpm),  $n$ , and Stribeck rotational speed (rpm),  $n_{st}$ . Vaz et al. [24] characterized the drivetrain resistance of the MPB70 so the model equation is used in the current study. The development of the

equation is given in Appendix B.  $Q_R$  from Eq. (B.11) is

$$Q_R = \left[ 2.15 \left[ 0.0794 + \frac{0.0132T_a(n)^4}{\sin[3.3T_a(n)^{0.24}]} \right]^{0.333} + 40.5 \right] \exp \left[ - \left( \frac{n}{n_{st}} \right)^{0.26} \right] \\ + 15.0954n + 0.0134 [3T_a(n) - 0.3801] [0.00053042 + 0.0001163T_a(n)]^{0.55} \\ + 0.0967n^{0.67} + 0.5Q_{MPB} \quad (5.4)$$

### Moment of inertia

Rotor inertia is an important factor that influences starting and is dependent on the airfoil type, size, and the blade material, and is given by

$$J_B = N\rho_m \int A_m r^2 dr \quad (5.5)$$

where  $N$  is the number of blades,  $\rho_m$  is the density of the material,  $r$ , is the radius, and  $A_m$  is the area of the rotating components at radius  $r$ . For this study, the windmill consists of the following parts: blades, spars, rotor disk (hub), and the MPB and encoder rotating shafts. Based on their determined mass and geometry, the inertia of each part is calculated using Eq. (5.5), except for the rotor disk where  $N$  drops out of Eq. (5.5). The inertia of the MPB and the optical encoder rotating shafts were extracted from the manufacturer's datasheet. Then, the total inertia,  $J$  of the system, is obtained by the sum of the component inertias. Table 5.1 presents the total mass moment of inertia of the four rotors investigated in this study, which is shown to be increasing with solidity and proportional to  $N$ , so that  $J \approx J_B$ .

Table 5.1: Mass moment of inertia and solidity of rotors.

$N$	$J$ (kgm <sup>2</sup> )	$\sigma$ (-)
3	0.0134	0.11
6	0.0243	0.22
12	0.0463	0.45
24	0.0902	0.90

## Polar data

During starting, wind turbine blades operate between zero to low wind speed conditions and consequently, in a low  $Re$  regime. When stationary (i.e., rotational speed of the turbine is zero) and there is no induction, the blades generate aerodynamic torque purely from the lift [33]. However, as the blades begin to rotate,  $\alpha$  can be as high as  $90^\circ$  or even greater, as shown in Figure 5.2. SWTs start when the aerodynamic torque acting on the blades is high enough to overcome the combined resistive torque of the generator and drivetrain system. This can only happen when  $\alpha$  drops considerably, and the  $C_l$  and  $C_d$  increase and decrease, respectively.

Furthermore, the paucity of reliable airfoil data, particularly in the post-stall region, poses difficulty in analyzing its starting behavior. Most available  $C_l$  and  $C_d$  data are only for incidence up to  $20^\circ$  (pre-stall region) and high  $Re$ . As a result, early studies such as [32, 127] on small VAWTs and HAWTs starting, either interpolate and extrapolate available pre-stall airfoil data or use a generic empirical formula based on a flat plate for estimating higher  $\alpha$  lift and drag data or a combination of both methods. Airfoil data obtained by extrapolation from high to low  $Re$  such as Sheldahl and Klimas [64] are suspect, especially because low  $Re$  airfoil behavior, for example, laminar separation bubbles formation and collapse are obviously not captured; see Chapter 3. As noted by Mayer et al. [95], airfoil aerodynamic data obtained in this manner causes uncertainty in starting analyses. Hence, Du [31] and Worasinchai [143] performed wind tunnel measurements of their airfoils at low  $Re$  of interest and high  $\alpha$  prior to their investigation on starting. Accurate modeling requires lift and drag at the appropriate  $Re$  and  $\alpha$  up to  $90^\circ$  for HAWTs and the full incidence range for VAWTs.

The model investigated in the current study have been studied for  $N = 3$  using aerodynamic dataset of Bruining [26] by Vaz et al. [24]. Static lift and drag coefficients data of the circular-arc airfoils sections that comprise the blade of the windmills in this study were measured in the RWT and used as input aerodynamic dataset to the model to correctly predict the windmill starting behavior. Details of the wind tunnel measurements are reported in

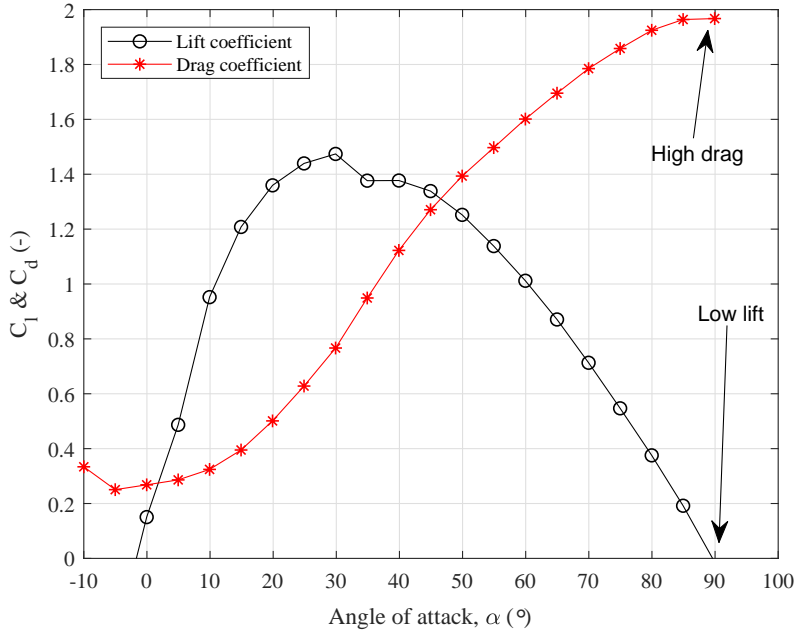


Figure 5.2:  $C_l$  &  $C_d$  for CA2010 without spar,  $Re = 6 \times 10^4$ .

Chapter 3. The airfoil's performance is presented in Figure 5.3. The performance is shown with and without the spar located at the  $0.5c$  position at nominal  $Re$  of  $3 \times 10^4$ – $4 \times 10^4$ , corresponding to representative starting of the windmill in low wind speed for increasing  $\alpha$ , from  $-10^\circ$  to  $90^\circ$  and at decreasing  $\alpha$ , from  $-90^\circ$  to  $10^\circ$ .

## 5.2 Starting calculations and results

The starting analysis model employed the standard 4<sup>th</sup> order Runge-Kutta numerical method to solve the ordinary differential equation of Eq. (5.2). In other words, it predicts the starting performance based on a time-stepping basis. For convenience, the calculations used a minimum time step of 0.5 s for  $N=3, 6$  and 12, and 1 s for  $N=24$ . Halving the time steps introduced computational errors. However, no significant change was seen in the predicted  $\Omega$  for increased time steps. As is the standard procedure with BEM, the blade is divided into several elements, 30 in this case. Figure 4.9 shows an element along with its velocities triangle and forces. Eq. (4.30) gives the total velocity as seen by the blade element reproduced here

for convenience.

$$U_T = \sqrt{[(1-a)]^2 + [(1+a')\lambda_r]^2} \quad (5.6)$$

Based on the computed  $U_T$  from Eq. (5.6) the corresponding chord-based  $Re = U_T c/v$  and  $\alpha = \arctan[U_\infty(1-a)/\Omega r(1+a')] - \theta_p$  can be obtained. Then  $C_l$  and  $C_d$  are determined by interpolation from Figure 5.3. Note all terms here have their standard definitions.

Usually, the blades are stationary during starting, so the rotor does not extract energy from the wind. In that case, the axial velocity at the blade is the same as the upstream wind speed,  $U_\infty$ , implying no deceleration occurs through the blades. Therefore, the axial and circumferential induction factors depicted in Figure 4.9 are zero, i.e.,  $a = 0$  and  $a' = 0$ , respectively. The effective velocity seen by the blade element for negligible induction is then computed using:

$$U_T = \sqrt{(U_\infty^2 + \Omega^2 r^2)} \quad (5.7)$$

For consistency with the assumption of no induction, three-dimensional effects such as tip loss were not considered in the starting BEM analysis. The torque contribution from each element is determined and then integrated from the blade hub,  $r_h$ , to blade tip,  $r_t$ , to find the total torque acting on the number of the blades,  $N$ , using

$$Q = \frac{1}{2} \rho U_T^2 N \int_{r_h}^{r_t} (C_l \sin \phi(r) - C_d \cos \phi(r)) cr dr \quad (5.8)$$

To compare the starting prediction with experimental measurements, the torque and thrust contribution of the spars not modeled in BEM are calculated using Eqs. (C.8) and (C.6) in Appendix C and added to the BEM computed torque and thrust.

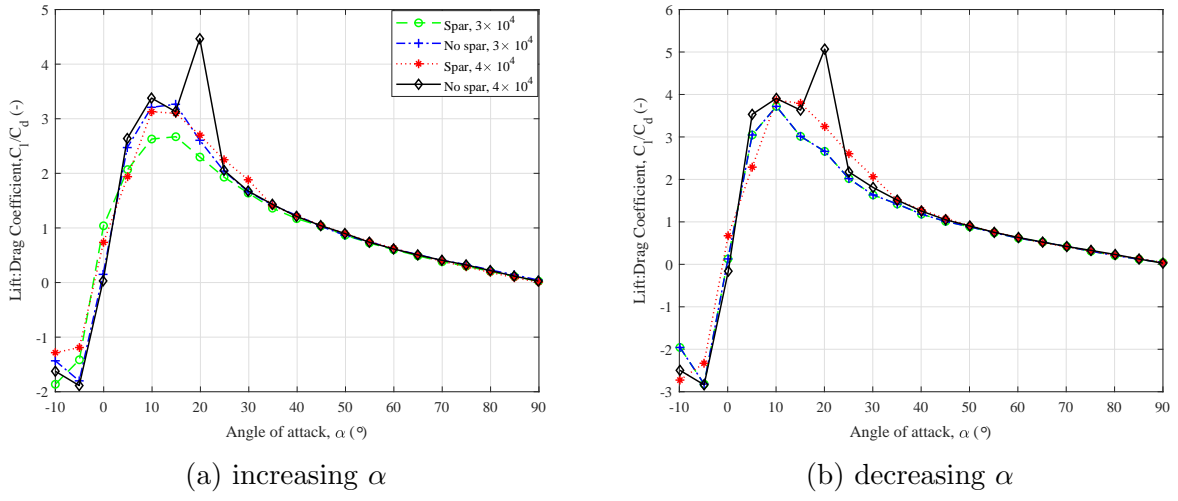


Figure 5.3: Airfoil performance characteristics.

### 5.2.1 Starting performance

The performance investigation begins with  $N = 3$ , taken as the baseline rotor because the BEM analysis with the  $L$  and  $D$  of the airfoil at this  $N$  is most accurate at low  $\lambda$  and avoids the complications of solidity. The starting of the  $N = 3$  rotor is predicted using experimentally acquired wind speed data. The minimum speed,  $U_s$  at which the stationary blades start turning, was determined through wind tunnel testing and found to be  $\approx 6$  m/s for sustained rotation, see Chapters 6 and 7. As the wind speed increases from zero (at  $t = 0$ ), the usually high  $\alpha = 73^\circ$ , see Figure 5.4 and very low  $Re \approx 1350$  (Figure 5.5) for the blade element at the tip both remain constant due to the near constancy of  $U_T$ , before decreasing and increasing respectively, as illustrated in Figure 3.1. Similarly, the blade root and other blade elements follow this trend, which continues until after 12 s of idling. At around  $t = 16$  s,  $\alpha$  at the blade tip drops to  $\approx 7^\circ$ , which is  $3^\circ$  and  $8^\circ$  lower than the angle for the maximum  $C_l/C_d$  for the airfoil with and without a spar, respectively. At this point, the aerodynamic torque coefficient,  $C_Q$ , attains its highest value, which corresponds to the maximum  $C_l/C_d$  and coincides with the lowest  $C_{QR}$  as seen in Figure 5.6. Notice the transition from high static to low dynamic torque following the Stribeck curve of Figure B.1.

Further, the starting sequence as described by [35] is clearly delineated by the idling phase

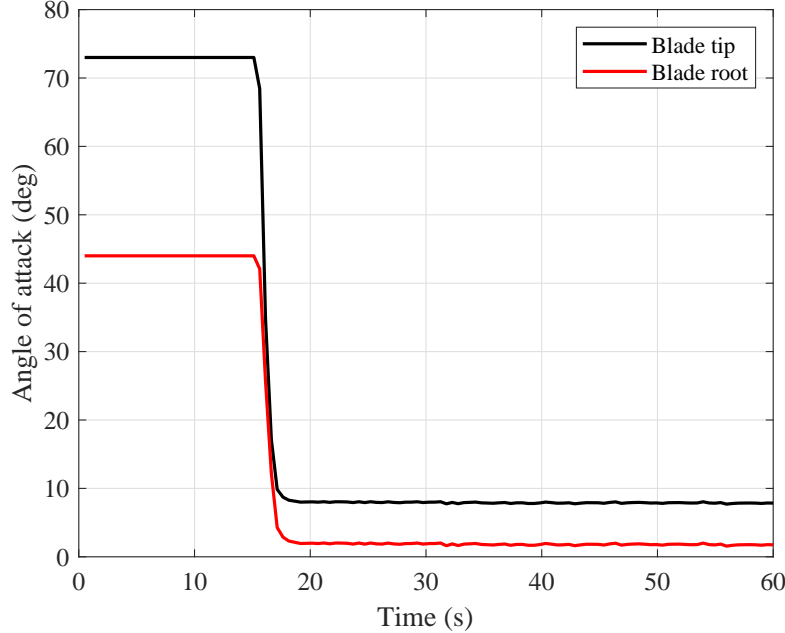


Figure 5.4: Angle of attack variation.

$(C_{QR} > C_Q)$ , where the rotor is slowly accelerating during idling and  $\alpha$  is decreasing, and the rapid acceleration phase,  $(C_{QR} < C_Q)$ , where the  $C_{QR}$  falls and  $C_Q$  rises. This continues until a steady-state point,  $d\Omega/dt = 0$ ,  $(C_{QR} \approx C_Q)$ , which is the runaway  $\Omega$  of the turbine, with the net torque  $\approx 0$  for the rotor. Note, however, that the resistive torque depends on the axial thrust produced by the blades computed from BEM and is also a function of  $n$  given by:

$$T_a(n) = \frac{1}{2}\rho U_T^2 N c (C_l \sin \phi(r) + C_d \cos \phi(r)) \int_{r_h}^{r_t} dr \quad (5.9)$$

The resulting theoretical curve for the rotor angular velocity of the windmill rotor for  $N = 3$  as the wind speed increases to a steady-state value of 5.5 m/s from zero (stationary position), as generated from BEM using Eq. (5.2) is presented in Figure 5.7. The prediction code was validated by comparing it with the experimental model results in the RWT and OJF wind tunnels, as shown in Figure 5.7. The simulated rotor experiences a more rapid rotor

acceleration compared to the tests. While the simulation over-predicted the final or steady-state rotor speed,  $\Omega_t$ , of the OJF by 2.5%, it under-predicted the RWT by 3.4%. Compared to the tests, the BEM under-predicted the starting wind speed to be 3.9 m/s, a 22% decrease from the measured values.

In the transient regime or acceleration phase of the starting sequence, the blades see a combination of extremely low values of  $Re$  and very high  $\alpha$ , particularly at the blade root where most of the starting torque is produced as illustrated in Figure 5.8. It is not clear the cause of the discrepancy observed in Figure 5.7. Nonetheless, it is instructive to mention that the spars cover 42% (nearly half) of the blade radius from the hub. Thus, the spar relations mentioned earlier may not sufficiently capture the physical and mechanical influence of the spars on the starting aerodynamics. Also, the small size of the test model makes it sensitive to parameter changes that might increase the impact of the spar on the flow aerodynamics.

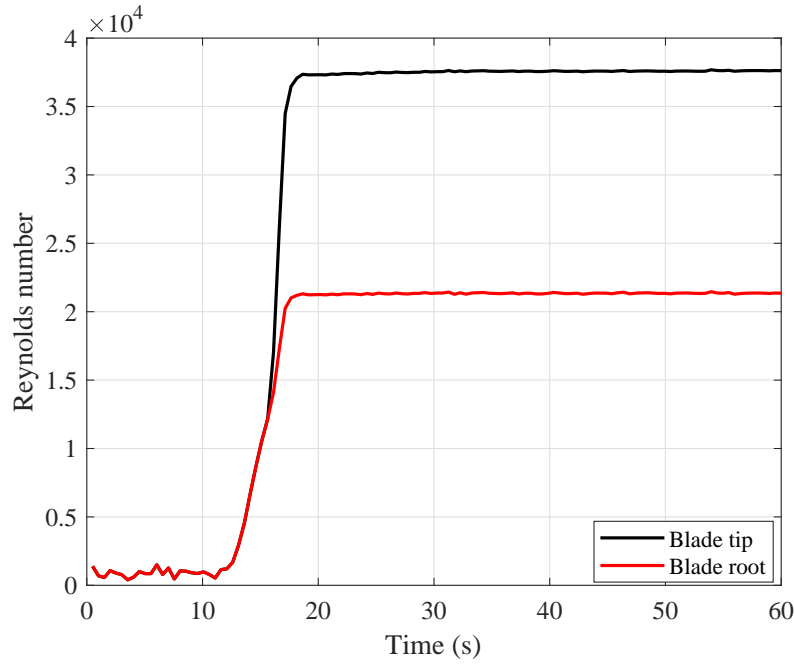


Figure 5.5: Reynolds number variation.

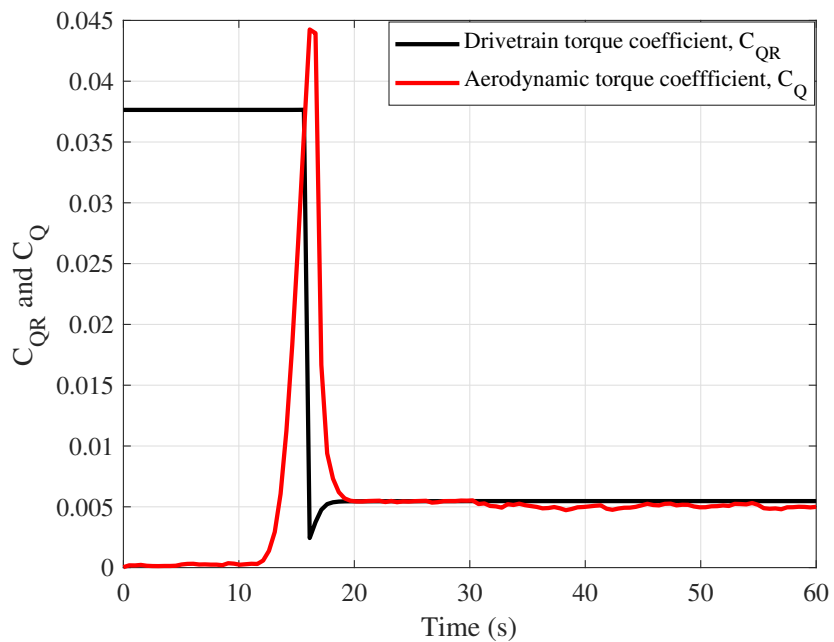


Figure 5.6: Aerodynamic and drivetrain resistive torque variation.

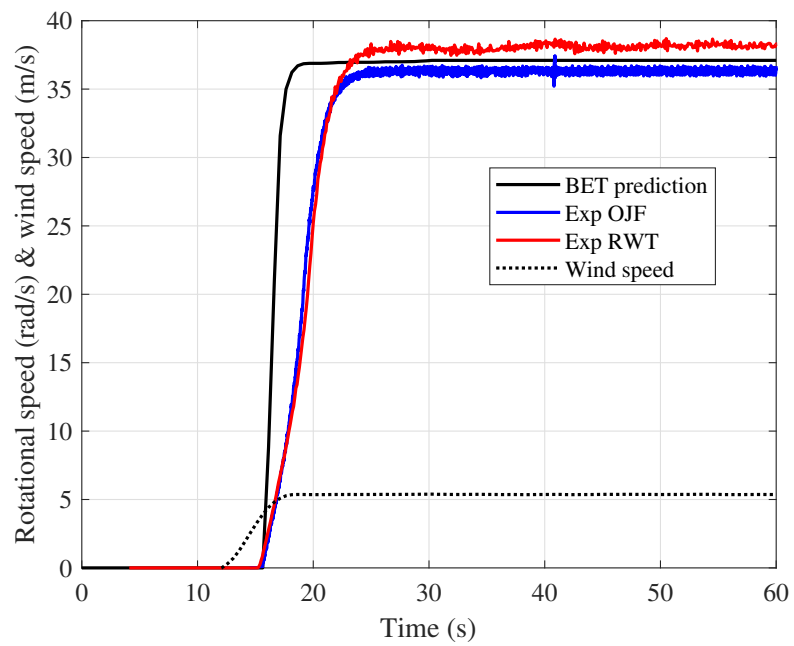


Figure 5.7: Predicted and measured rotational speed for  $N = 3$ .

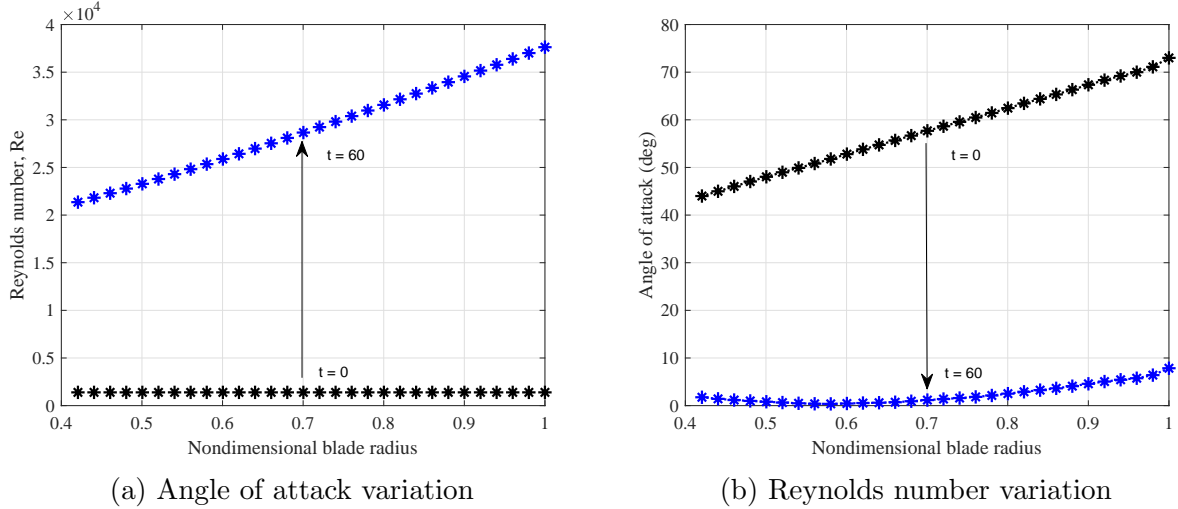


Figure 5.8: Starting behavior along the blade span.

### 5.2.2 Validity of negligible induction in BEM starting analysis

It is pertinent that the effect of  $a$  and  $a'$  both equal to zero employed in the blade element analysis be justified. Negligible induction implies that no energy is extracted by the stationary blades, though a rotating one must, at the least, extract kinetic energy solely for accelerating the rotor. The validity of these assumptions is examined by computing the ratio of the rotor kinetic energy up to the commencement of rapid acceleration to the kinetic energy of the wind flowing through the rotor up to the starting time,  $t_s$ .

$$KER = \frac{J\Omega^2(t_s)}{\rho\pi R^2 \int_0^{t_s} U_s^3(t) dt} \quad (5.10)$$

This ratio is small during the starting sequence, provided the stated assumptions remain valid. By application of Eq. (5.10), the  $KER$  is calculated and plotted in Figure 5.9. Maximum values of  $KER$  are 0.02, 0.09, 0.25, and 0.5 for  $N = 3, 6, 12$  and 24, respectively, which all occur at the transition between the transient and steady-state regimes.  $KER$  decreases for all  $N$  from their maximum values, while the  $\Omega$  remains constant during the steady-state ( $d\Omega/dt$ ). Although  $KER$  is less than unity for all  $N$  as depicted in Figure 5.9, the values are quite significant, particularly for  $N = 12$  and 24 compared to  $KER = 0.0014$

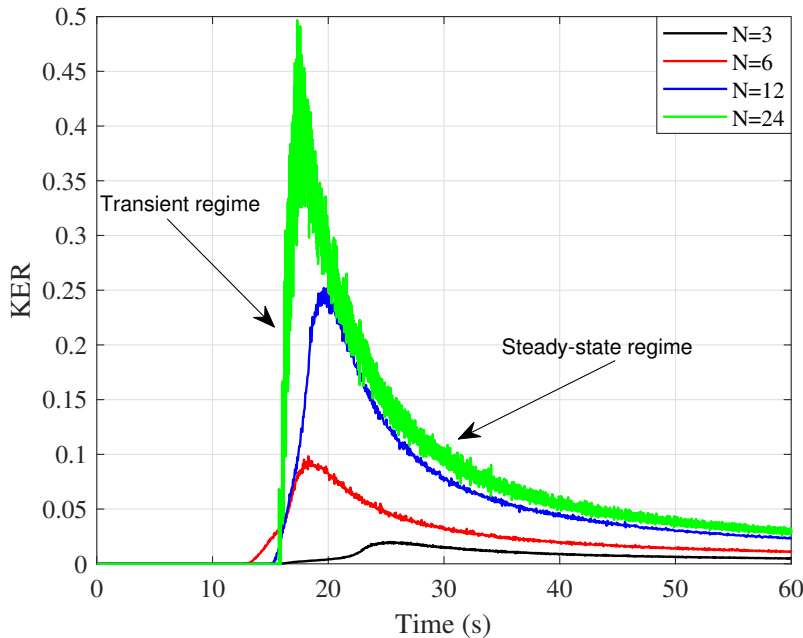


Figure 5.9: Kinetic energy ratio variation with time at constant wind speed of 6 m/s.

reported for a small HAWT by Wright and Wood [32]. Thus, the assumption of negligible induction is not sufficiently justified. Based on the knowledge of the significance of induction on the windmill starting investigation, further and subsequent analyses were implemented with induction and the results discussed in Section 5.2.3. Also, for consistency, the finite blade function (tip and root loss factors) described in Chapter 4 are included.

### 5.2.3 Effect of increasing blade number on starting performance and runaway conditions

For an ideal situation, that is, no friction ( $Q_R=0$ ) and no cascade effects, starting is independent of  $N$  because by comparing Eqs. (5.1) to (5.2),  $N$  cancels out and  $J$  in Table 5.1 is largely due to blades. Depending on the rotor configuration, the blades contribute between 82 to 97% of the total inertia. However, these effects influence starting for practical situations. The effects of increasing  $N$  and  $\sigma$  in Table 5.1 on the model starting performance prediction and their comparison to the baseline rotor,  $N = 3$  are shown in Figure 5.10. As

presented in Table 5.2, it is apparent that as the  $N$  increases, the idling period,  $T_s$ , which is the interval during which the blades accelerate slowly as  $\alpha$  slowly reduces, reduces slightly owing to a relatively small increase in the net starting torque, because of an increment in  $J$ . For example,  $T_s$  drops by 2.5%, 3.0% and 3.5% for  $N = 6, 12$  and  $24$ , respectively, compared to  $N = 3$ . Also, relative to the baseline rotor, an increase in  $\sigma$  by increasing  $N$  results in a 7%, 6.7%, and 6% decrease in the minimum wind starting speed,  $U_s$ , for  $N = 6, 12$  and  $24$ , respectively, thereby aiding the quick starting of the rotors. Notice that for  $6 \leq N \leq 24$ , the runaway speed changes less significantly. For  $N=24$ , the  $U_s$  is predicted to be as low as 3.2 m/s, which is encouraging for regions with low wind speed.

The addition of more blades to the baseline rotor increases  $Q$ , while  $Q_R$  remains unchanged as it is theoretically independent of  $N$ , as shown in Figure 5.11. Figure 5.12 compares the dimensionless aerodynamic,  $C_Q$  and drivetrain resistive,  $C_{QR}$ , torque for all  $N$ . As  $N$  increases from 3, the maximum  $C_Q$ , which corresponds to the point where the lift-drag ratio is maximized by factors of 1.2, 1.6 and 1.8 for  $N = 6, 12$  and  $24$ . Clearly, one of the easiest ways of enhancing starting performance is by increasing  $N$ ; however, this adds to the cost of the blades, which is around 7% [34] of the total cost of an SWT. Fortunately, this study is concerned with cambered plates or circular-arc airfoils, which are cheap in both material and manufacture.

Table 5.2: Starting performance of rotors.

$N$	$U_s$ (m/s)	Idling time (s)	Rotor runaway speed (rad/s)
3	5.824	17.14	36.90
6	4.181	14.62	29.86
12	3.261	14.12	30.24
24	3.202	13.61	30.96

The apparent effect of induction can be seen in the way  $\alpha$  changes with  $Re$ . As  $N$  decreases, the  $\alpha$  seen by the blade elements, for example, is higher at the tip and root, as shown in Figure 5.13 and is typical of the conventional 3-bladed rotor. As expected, this change is due to the increasing induction effect of  $N$ , shown in Figure 5.14. The sudden

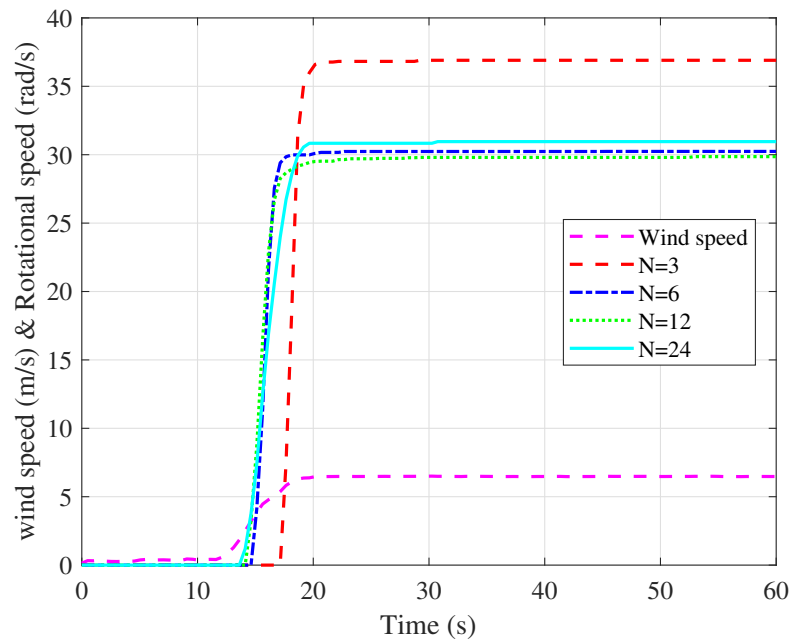


Figure 5.10: Comparison of rotational speeds.

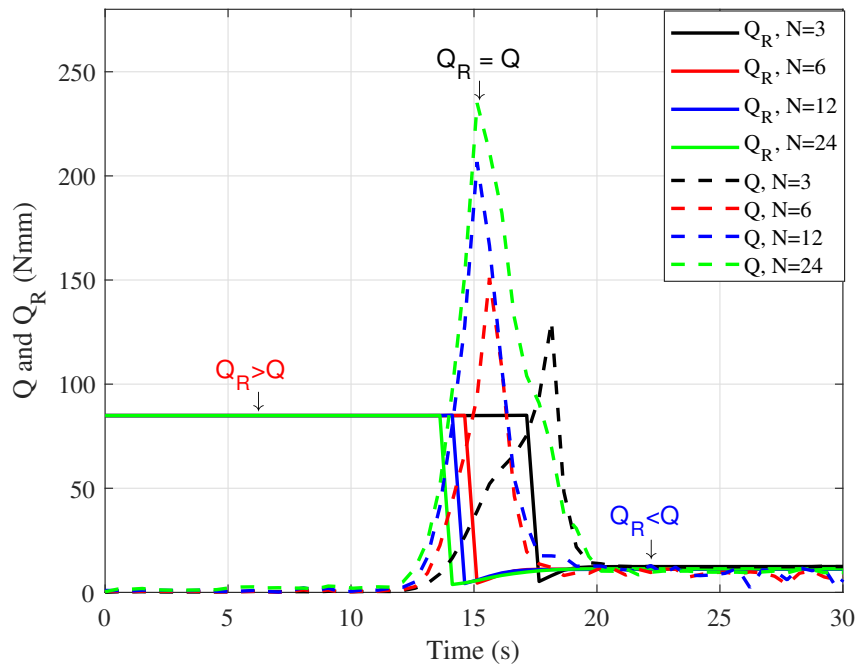


Figure 5.11: Drivetrain resistive,  $Q_R$  and aerodynamic,  $Q$  torque of the rotors.

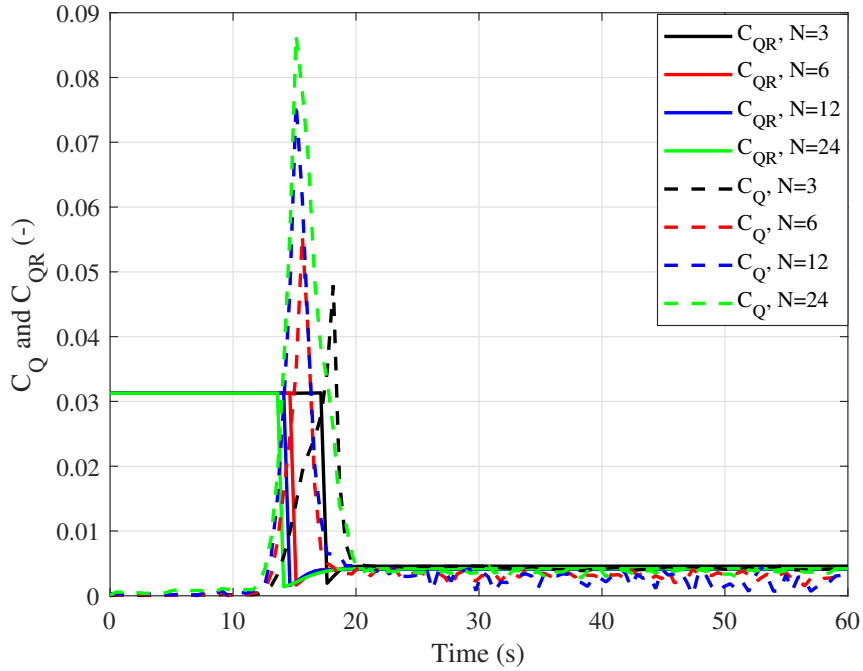


Figure 5.12: Drivetrain resistive,  $C_{QR}$  and aerodynamic,  $C_Q$  torque coefficients of the rotors.

drop in  $a$  near the tip of the blades may be due to the absence of spars at  $r/R \geq 0.83$ . Furthermore, considering the small size of the model, the values of  $a$  are surprisingly high.

Figure 5.15 presents a comparison of the net torque,  $Q_{net} = Q - Q_R$  with the starting duration for the four rotor cases. Compared to Figure 5.11, the observable change is in the transient phase of the starting sequence, where  $Q_R > Q$ . Beyond this region,  $Q_{net}$  approaches the maximum value for all  $N$ , which agree with Figure 5.11. The corresponding RPM at this point decreases with  $N$ , as shown in Figure 5.16 plotted such that the product of  $Q_{net}$  and RPM equals the rotational power of the windmill rotors. As  $N$  increases, the maximum RPM decreases, so is the  $Q_{net}$ . The implication is that the high  $N$  rotor operates at a lower speed and hence lower noise.

#### 5.2.4 Effect of unsteadiness

The effect of unsteadiness is intricate and not easy to quantify due to the combined variation in  $U_T$  and  $\alpha$ . Nonetheless, changes in the  $\alpha$  are usually estimated using a dimensionless

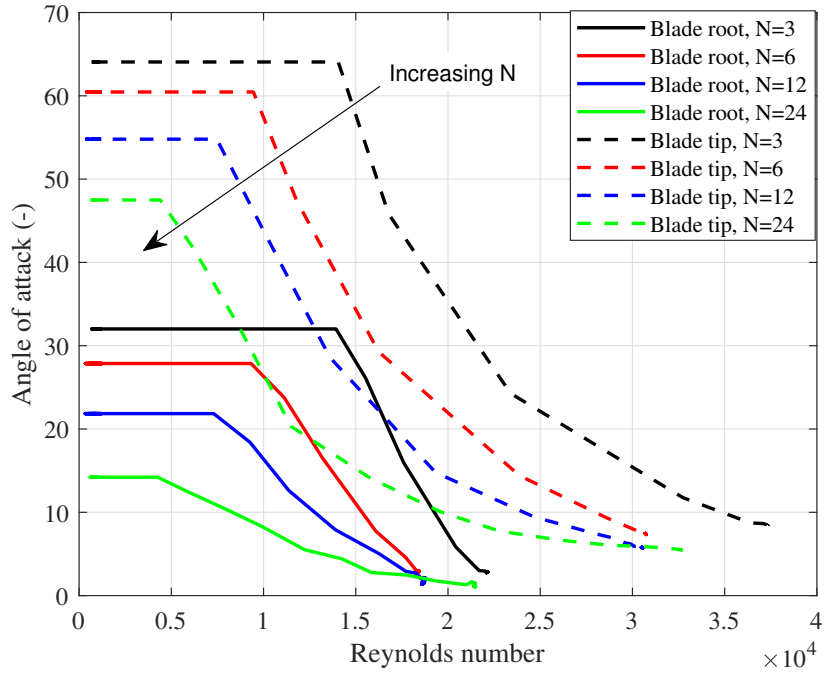


Figure 5.13: Variation of angle of attack with  $Re$  for all rotors.

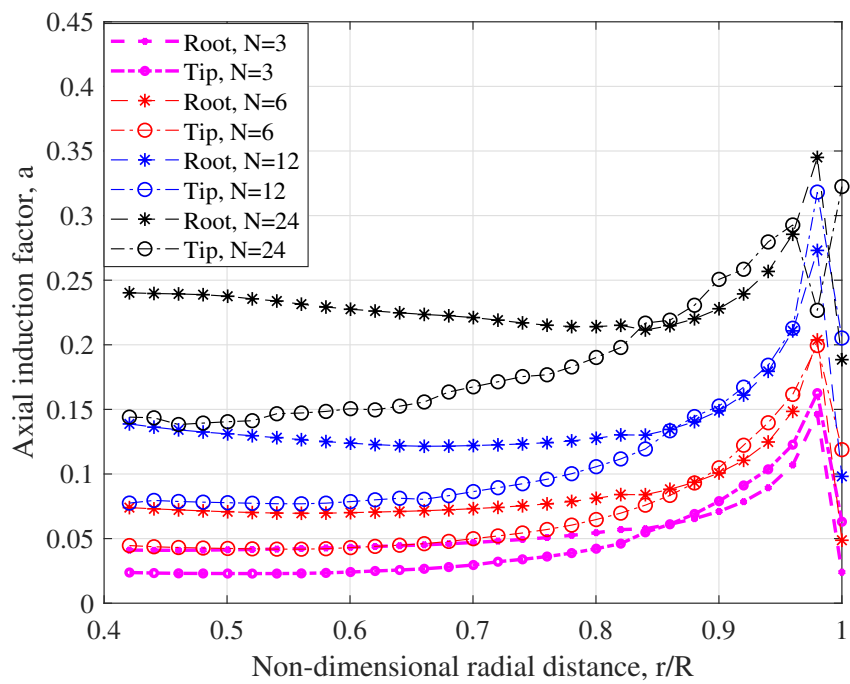


Figure 5.14: Spanwise distribution of  $a$  for all  $N$  for blade elements at the root and tip.

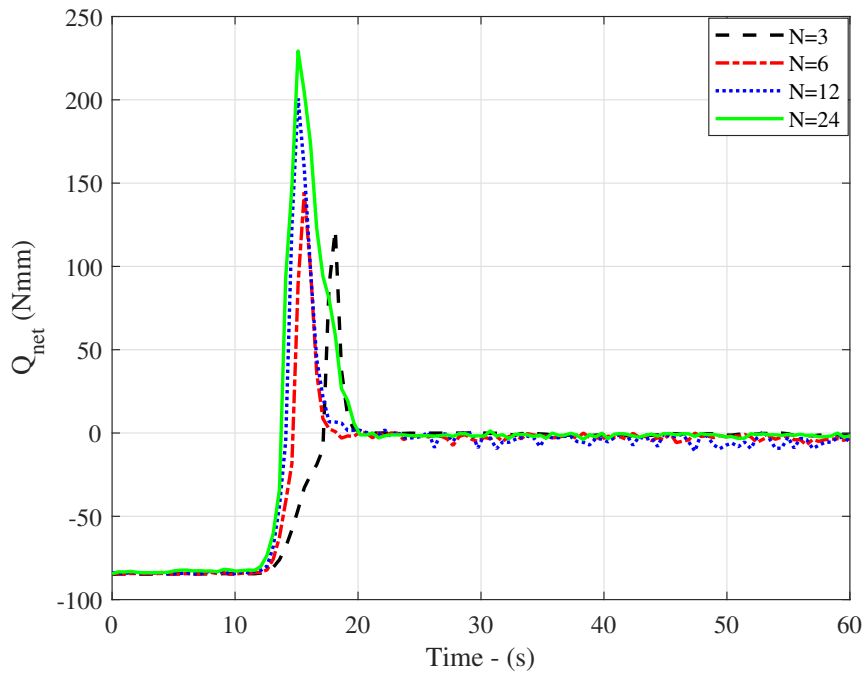


Figure 5.15: Variation of net torque with time.

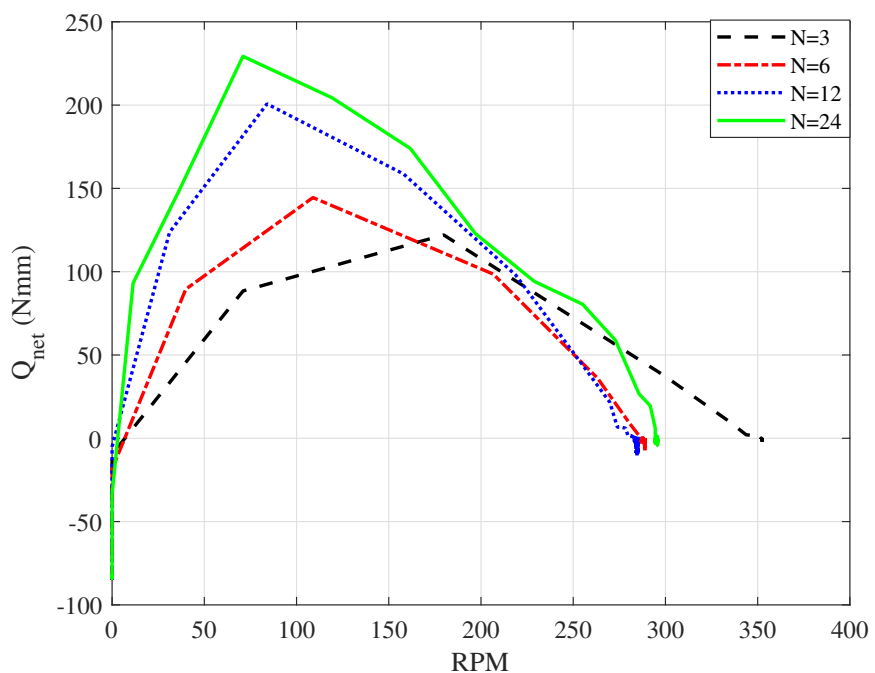


Figure 5.16: Variation of net torque with RPM.

parameter such as “reduced frequency”,  $k_\alpha$ , expressed as

$$k_\alpha = \frac{|\dot{\alpha}|c}{2U_T} \quad (5.11)$$

where  $\dot{\alpha} = \frac{d\alpha}{dt}$

From [35] the reduced frequency formula at the tip of a blade is given by

$$k_{\alpha,tip}(t) \approx \frac{|\dot{\alpha}|c}{2[1 + \lambda^2]^{3/2}U_\infty} \quad (5.12)$$

where  $\dot{\alpha} = \tan^{-1}[U_\infty/\Omega R]$  measured in rad/s.

According to Leishman [133], if  $0 \leq k_{\alpha,tip} \leq 0.05$ , the flow can then be considered quasi-steady; that is the effects of unsteadiness are usually small. The pitch rates for the blade tip were computed using Eq. (5.12) in the BEM analysis, and the largest values for  $N = 3, 6, 12$ , and  $24$  are as shown in Figure 5.17. For the present model, the blade profile chord length is constant, and  $\lambda_r \sim r$ ,  $k_\alpha$  would remain largely unchanged along the blade. Since these values are smaller than 0.05 by around an order of magnitude, it is less likely to alter the lift and drag data at any section of the airfoil.

### 5.2.5 Effect and sensitivity of starting to pitch angle variation

To investigate the effect of pitch angle,  $\theta_p$ , variation on the aerodynamic starting performance of the windmill, the baseline rotor with pitch angle,  $-1.5^\circ \leq \theta_p \leq 1.5^\circ$  in steps of  $0.5^\circ$  is considered. For a constant  $J$ , the effect of pitch variation is expected to follow the same trend. Hence no attempt was made to investigate other rotors. The variation in rotational speed with different  $\theta_p$  is plotted in Figure 5.18. Decreasing  $\theta_p$  from 0 to  $-1.5^\circ$  over-predicts the runaway speed due to lowering  $\alpha$  and the subsequent increase in starting torque,  $Q$  and vice versa. It is seen that within the tested range, the steady rotation velocity matches the experimental measurements in the OJF and RWT only at  $\theta_p = 0.5^\circ$  &  $-1^\circ$  respectively. Curiously, however, there is no observable change in the idling time; it may though unlikely,

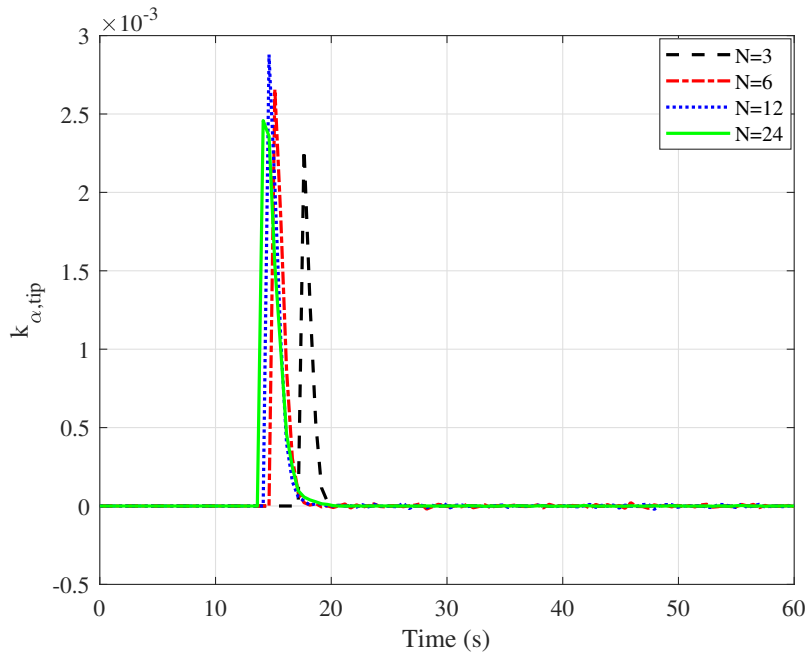


Figure 5.17: Blade tip pitch rate.

be due to the small size of the test turbine.

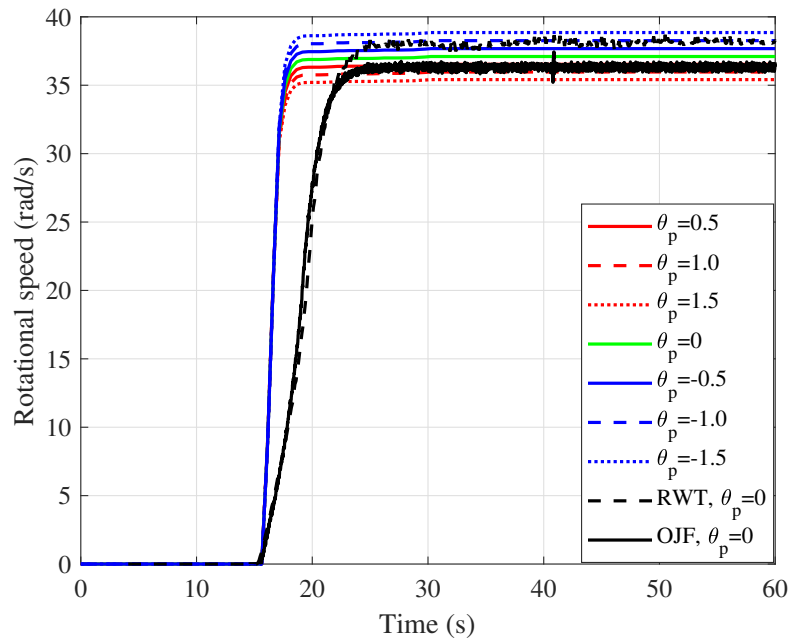


Figure 5.18: Rotor speed for  $N = 3$  with varying pitch angles and no induction.

### 5.2.6 Concluding remarks

The effects of variable  $N$  or otherwise  $\sigma$  on the starting performance prediction of a windmill model have been evaluated. Increasing  $N$  increases the starting aerodynamic torque and reduces the starting speed and the idling time of the rotor. The assumption of negligible induction was invalid for  $N > 3$ , as demonstrated by the significant high kinetic energy ratios,  $KER$ . Furthermore, the application of a quasi-steady-state BEM for predicting the rotor acceleration at no load was shown to be sufficient as the reduced frequencies,  $k$  for unsteadiness effects, are within acceptable ranges for all  $N$ . Considering the small size of the model and the resulting very low chord-based  $Re$ , the complications associated with low  $Re$  aerodynamics and the aerodynamic influence of the spars and the dynamics of MPB70 need to be understood to improve the starting model in the future.

# Chapter 6

## Windmill and Tunnel Blockage

### Experimentation

This chapter describes the wind tunnel test sections, the windmill aerodynamic and starting performance experiments conducted on the windmill rotor model with a wide range of blades starting from three and doubling incrementally to twenty-four as discussed in Section 4.8. The description also includes the data acquisition methods, blockage impact on thin solid disks tested in the *high blockage* red wind tunnel (RWT), and its correction.

#### 6.1 Experimental facilities

The tests for this study were performed at the University of Calgary high blockage red wind tunnel (RWT) and the Delft University of Technology (TU Delft) low blockage open jet facility (OJF) wind tunnel. Both tunnels are low speed and of the open jet type. The main characteristics of the tunnels are summarized in Table 6.1.

Table 6.1: Characteristics of wind tunnels.

Name	Location	Type	Test section (m)	Cross section	Maximum speed (m/s)
OJF	TU Delft	Closed circuit	$2.85 \times 2.85$	Octagonal	35
RWT	University of Calgary	Open circuit	$1 \times 1$	Square	18

### 6.1.1 University of Calgary Red Wind Tunnel

The Red Wind Tunnel (RWT) is one of the two wind tunnels housed in the Laboratory for Turbulence Research in Aerodynamics and Flow Controls (LTRAC) at the University of Calgary. It is an open jet (atmospheric pressure) blower wind tunnel and 9.6 m long, as shown in Figure 6.1. Airflow in the RWT is driven by a fan located in the downstream fan housing powered by a 25 hp electric motor. Air flows into the diffuser, which comprises first a vertical section and then into a horizontal one. Curved nylon screens are placed at the entry of each diffuser section to regulate the flow and prevent flow separation from the diffuser walls. Honeycombs made from polycarbonate measuring 50 mm in width and 0.064 mm in wall thickness with 6 mm cell diameter are positioned to straighten the inlet flow and break up any large scale flow structures 0.914 m downstream of the diffuser outlet. In the settling chamber, the flow passes through four nylons screens with approximate resistance of 59.05 % mounted at 0.203, 0.305, 0.46, and 0.508 m measured from the settling chamber outlet to reduce velocity deviations and turbulence. The resulting low turbulence flow is then blown into the open test section via a contraction chamber with a contraction ratio of 5.76:1.

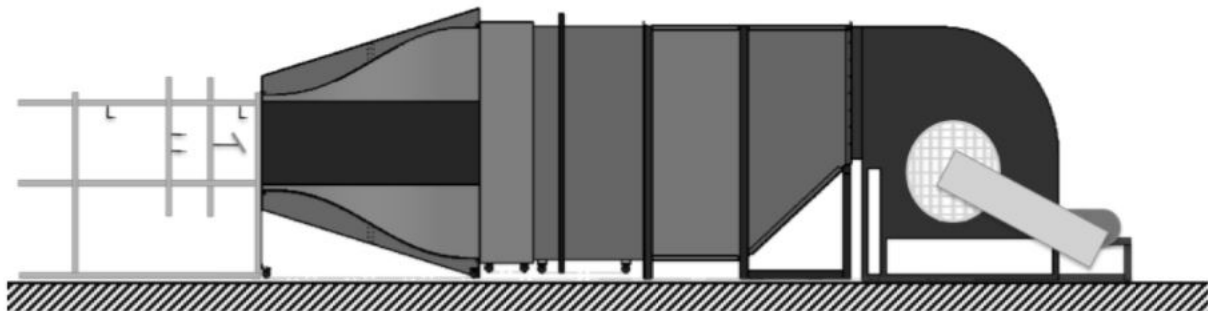


Figure 6.1: University of Calgary Red Wind Tunnel (open jet).

### 6.1.2 TU Delft Open Jet Facility

The Open Jet Facility (OJF)<sup>1</sup> is housed in a room measuring 13 m wide by 8 m high; see Figures 6.2a and 6.2b for the schematic layout and test section, respectively. A large fan powered by a 500 kW electric motor drives the airflow in the OJF. Just after the fan, the flow passes through a long diffuser guided by two rows of corner vanes in such a way that the airflow is rotated by 180°. Flow separation is prevented in a second, short diffuser with a wire mesh. Next, the flow goes through five fine mesh screens in the settling chamber to minimize the airflow velocity fluctuations and turbulence. The consequent laminar flow is then blown into the open test section through a contraction as an even jet stream. Then the air is cooled at the end of the test section to extract the heat added during the process using a huge 350 kW cooling radiation system. Finally, before re-entering the fan to begin the loop, the airflow direction is again turned 180° by two corner vanes.

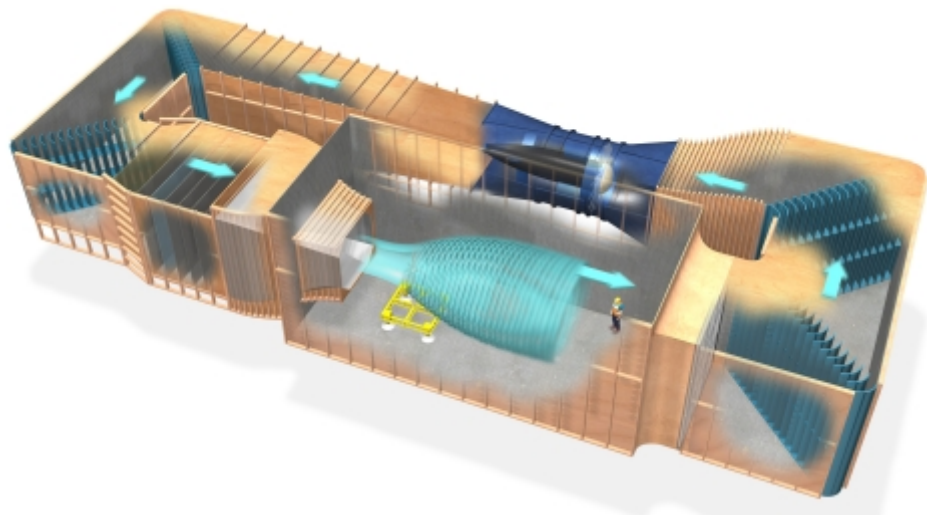
## 6.2 Experimental setup and measurements

### 6.2.1 Windmill experimental model

The geometrical and aerodynamic features of the circular-arc blade of the water pumping experimental windmill model with  $3 \leq N \leq 24$  used in this study were presented in Section 4.8 of Chapter 4; see Figures 4.10 and 4.11. For all  $N$ , the blade pitch angle was the same and equal to zero at the blade tip. The setup of the experiment in the RWT as designed and constructed by [23] is given in Figure 6.3, with the leeward side of the wind tunnel showing the main measuring instruments: optical encoder, Magnetic Particle Brake (MPB), and force transducer. These sensors are described in the next section. Figure 6.4 shows the same model with  $N = 6$  tested in the OJF, which is nearly *nine* times the test section area of the RWT resulting, relative to the model in a blockage ratio of < 5%.

---

<sup>1</sup><https://www.tudelft.nl/en/ae/organization/departments/aerodynamics-wind-energy-flight-performance-and-propulsion/facilities/low-speed-wind-tunnels/open-jet-facility/>



(a) Schematic



(b) Working section

Figure 6.2: TU Delft open jet facility.

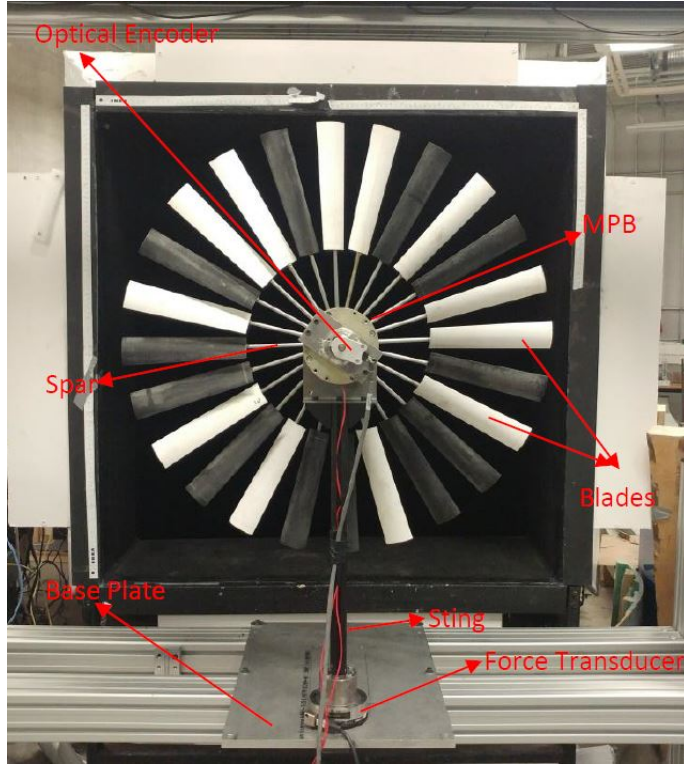


Figure 6.3: 24-bladed waterpumping windmill setup in the RWT.

The experimental setup was later modified to include a torque sensor to directly measure the resulting rotor torque to address the drawback of the MPB. Figure 6.5 shows the setup with the included torque sensor. Test on the modified setup was only conducted in the high blockage wind tunnel to examine the possible impact of blockage and calibrate the MPB.

### 6.2.2 Measured parameters and instrument calibration

#### Wind speed

The wind speed in the RWT was measured using a pitot-static tube connected to the Ashcroft® CXLdp differential pressure transmitter having an accuracy of 0.4 % and installed in front of the rotor and at a larger radius. The CXLdp determines the flow stagnation and static pressure difference from the pitot tube's respective stagnation and static ports. The air density is computed from the ambient laboratory conditions, i.e., the temperature and pressure; the flow velocity is obtained using the well-known Bernoulli's equation. A simple



Figure 6.4: 6-bladed water pumping windmill setup in the OJF measurement section.

in-house MATLAB-based program was used to acquire voltage signals via a NI myDAQ at a sampling rate of 100 Hz for 30 s. Because the RWT fan is controlled by a variable frequency drive (VFD), the flow speed is adjusted through a variation of the drive's frequency. Calibration was done to express the flow speed in terms of the tunnel's frequency, and the resulting calibration curve with its line of best fit is represented in Figure 6.6. Surveys were conducted to determine the flow uniformity, wherein a transverse system was used to position the pitot tube at different locations throughout a plane normal to the freestream. At 57 Hz, the tunnel produces a mean wind speed of 14.7 m/s, with the turbulence intensity measured to be less than 0.3%. The mapped velocity contour depicted in Figure 6.7 shows a 4% variation in the velocity at the tunnel's center, which is considered sufficiently uniform

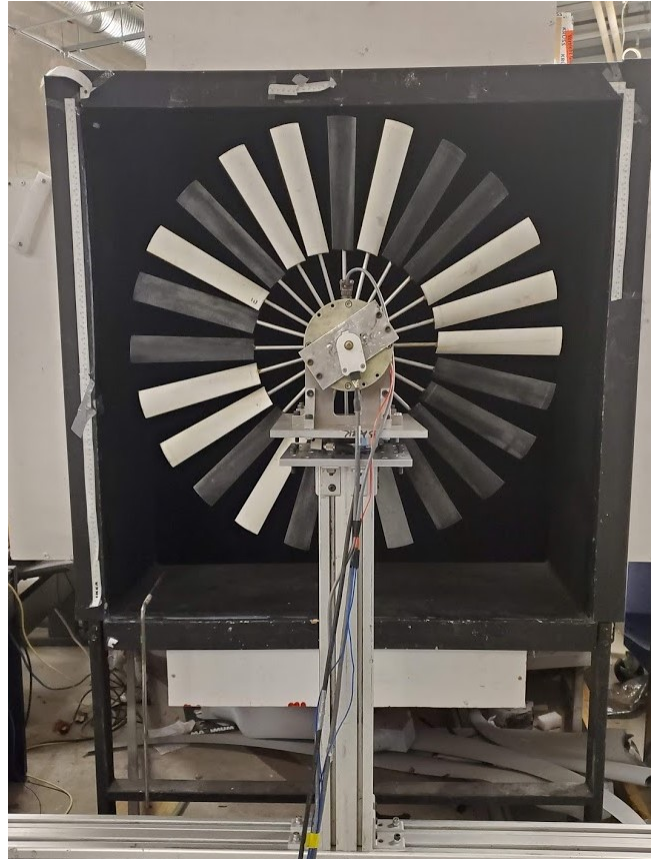


Figure 6.5: Windmill setup in the RWT modified to include a torque sensor.

for this study.

Inbuilt pitot tubes measure the flow speed in the OJF. The required tunnel speed is set and controlled remotely from a control room with the aid of a LabVIEW code. Turbulent intensity is reported to be in the range of 0.1-0.7% for wind speeds of 3–12 m/s [144]; the turbulence level for the 15 m/s wind speed investigated in this study is in the region of 0.25% [145].

### Rotor speed

A US digital Hollow Bore Optical Encoder model no HB5M-360-250-IE-D-H with a resolution of 1 cycle per revolution was employed for the rotational speed measurement. A MATLAB program was written to read time-dependent data via the National Instruments NI-DAQ USB 6212 16 bit, 16, analog inputs AD acquisition card at a sampling rate of 100 Hz.

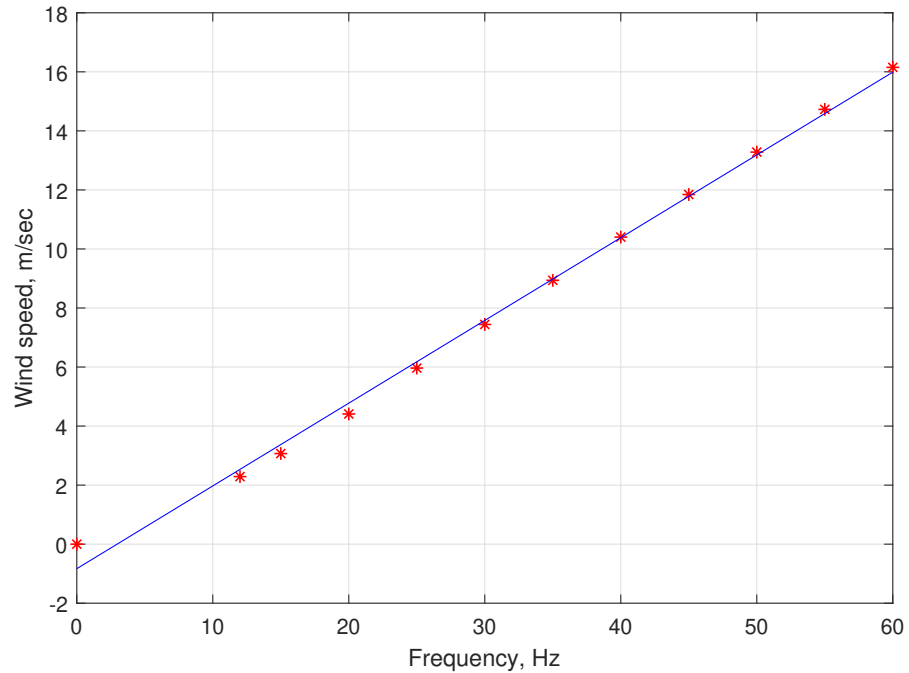


Figure 6.6: RWT speed calibration curve.

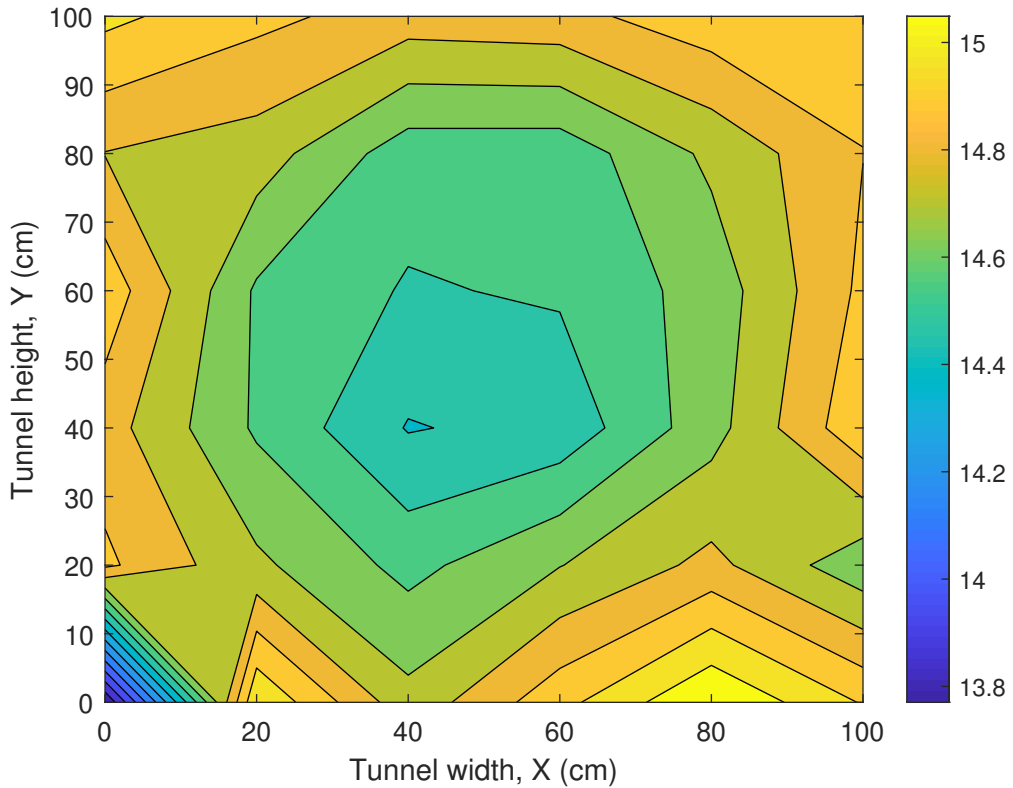


Figure 6.7: RWT velocity profile (m/s) operating at 57 Hz measured in the current study.

Table 6.2: ATI Delta SI-330-30 range, resolution and uncertainty. Retrieved from ATI [Access date:21-Nov-2019].

Force and Moments	Fx	Fy	Fz	Mx	My	Mz
Sensing range	330 N	330 N	990 N	30 N	30 N	30 N
Resolution	1/16 N	1/16 N	1/8 N	5/1333 Nm	5/1333 Nm	5/1333 Nm
Measurement uncertainty (%) <sup>a</sup>	1.25	1.25	1.25	1.25	1.25	1.25

<sup>a</sup>95 % confidence level

With the rotor rotation direction clockwise when viewed from the rear of the windmill and a rotational speed range of 0 to 1000 rpm, the instantaneous rpm measurements for 30 seconds were averaged and recorded for prescribed values depending on the MPB input resistive torque. A stroboscope was used to confirm the measurement of the optical encoder.

### Force and moment

In the RWT, instantaneous forces and moments acting on the windmill model were measured using an ATI Delta SI-330-30 six-component force/torque sensor mounted, for the original set up, at the base of the sting (tower) and fixed to a plate. In the modified setup, the force/torque sensor is mounted between two plates: a lower plate bolted to the sting and an upper plate where the rotor, torque sensor, and MPB are connected and affixed to the plate. The reason for the position in the modified setup is not to exceed the force and moment measurement range of the force transducer given in Table 6.2 together with its resolution and measuring accuracy. The orthogonal forces and moments in the Cartesian coordinates are illustrated in Figure 6.8; however, the interest of this study is the axial rotor thrust or the force in the streamwise direction. Like the optical encoder, measured data were acquired using the National Instruments NI-DAQ USB-6212 with the aid of a MATLAB program. Although the rotor thrust measurement includes the thrust due to the rotor disk, spars from the periphery of the rotor disk to the blade root and sting, the aerodynamic thrust acting on the blades was obtained by subtracting these forces from the measured rotor thrust for the wind speed under experimentation.

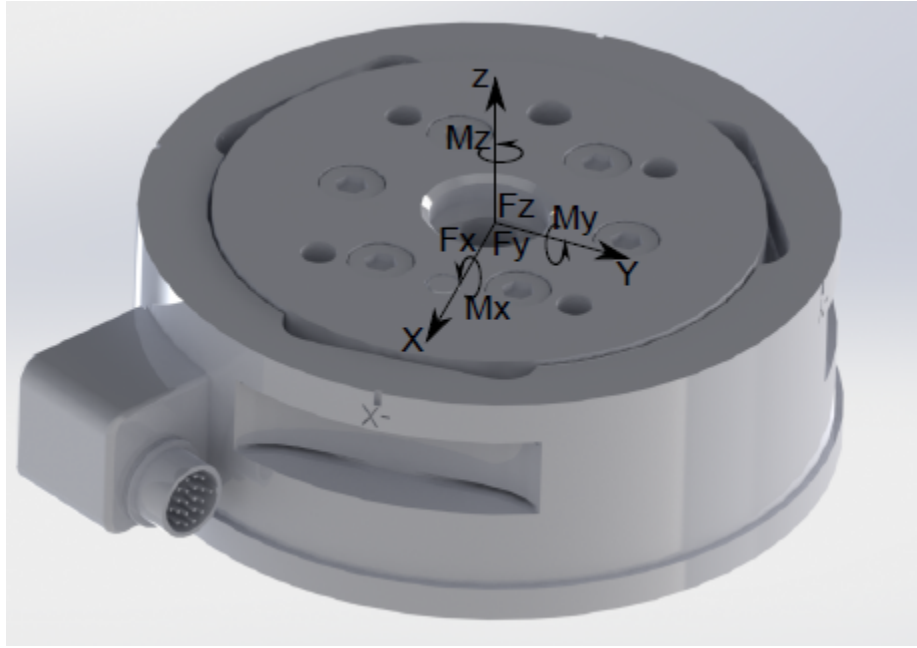


Figure 6.8: RWT F/T transducer axis system (F and M represent the force and moments respectively) Retrieved from [https://www.ati-ia.com/products/ft/ft\\_models.aspx?id=Delta](https://www.ati-ia.com/products/ft/ft_models.aspx?id=Delta) [Access date:21-Nov-2019].

Forces and moments measurements were done in the OJF using their external balance, specifically designed and manufactured for TU Delft by the Dutch National Aerospace Laboratory (NRL). It has six load sensors (Wheatstone bridges) that sense the forces and moments in the three orthogonal axes; that is, it is a six-component balance. As before, the loading in the axial direction (streamwise), as illustrated in Figure 6.9, is the force of interest. The balance measurements give a  $\pm 6\%$  error on average, which is deemed reasonably accurate. The balance is mounted on an adjustable table. The windmill model and tower system are fixed to the balance plate while ensuring the load limit in any coordinate direction is not exceeded (see Table 6.3). Signals from the balance are acquired using NI 9237 at a sampling frequency of 2 kHz for 30 s for each run using an in-house LabVIEW code.

## Torque

In the first instance, torque on the rotor was measured with an MPB, model MPB70. The choice of the MPB is primarily influenced by its ability to very accurately control torque,

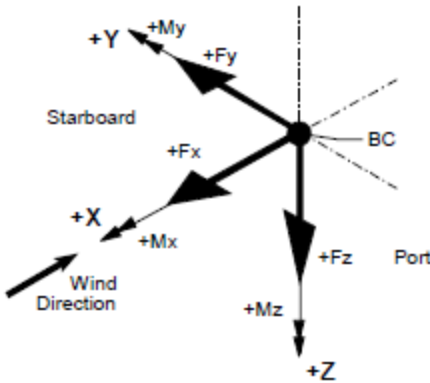


Figure 6.9: OJF F/M axis system (BC is the balance reference center, while F and M represent the force and moments respectively. Source: OJF external force balance documentation).

due to its almost torque-versus-current linear relationship and hence control the speed of the rotor shown in Figure 6.10. The MPB is a unique electromagnetic brake in that it offers a wide range of operations and provides the required torque that depends only on the circuit current. Torque is infinitely variable from disengaged (zero torque) to rated torque, as given in Table 6.4. Very importantly, the rotor power output was varied by adjusting the input resistive torque (load). While the produced torque is slip-speed (proportional to shaft rotational speed), independent according to the Manufacturer; an advantage for some applications, this, however, is a minus for torque measurement in wind tunnel testing where it was established to be dependent on the rotor speed as delineated in Section 6.2.1. As illustrated in Figure 6.10, when no input current is applied, the magnetic powder moves freely within the cavity allowing for free rotation of the input shaft, implying zero torque generation. However, with a non-zero current, a magnetic flux chain is formed which binds

Table 6.3: OJF external balance load range. Source: OJF external force balance documentation

Fx	Fy	Fz	Mx	My	Mz
<b>Maximum simultaneous loads</b>					
± 250 N	± 500 N	± 500 N	± 500 Nm	± 550 Nm	± 50 Nm
<b>Maximum single loads</b>					
± 250 N	± 600 N	± 3500 N	± 550 Nm	± 500 Nm	± 1250 Nm

the particles and connects the housing and the shaft together. With increasing current, the magnetic flux strength builds up, thereby increasing the torque.

Because of the inaccuracies of the MPB torque readings, a rotary torque sensor, TQ513-062 manufactured by Omega Engineering, was used as shown in the modified setup (see Figure 6.11). It is mounted between the rotor and the MPB, with the “active end” facing the rotor where the torque is measured. The torque sensor is positioned as close as possible to the rotor blade to minimize the total stress on the torque sensor shaft and not exceed the maximum stress value for the model. With a maximum operating speed of 5000 rpm, the sensor can measure up to 7.06 Nm of torque. The sensor is a full Wheatstone bridge strain gauge type with  $mV/V$  range electrical output, which is relatively small for NI DAQ equipment to precisely acquire. For low noise distortion and clear signal capture, a voltage amplifier, IAA100 analog amplifier with voltage output, a product of FUTEK, was used for in-line amplification.

The torque sensor was calibrated using a simple test system utilizing reference dead-weights ranging from 100 – 3000 g with a fixed lever arm of 24 cm, giving equivalent torque of 0.50–7.04 Nm. The measured average uncertainty was estimated to be  $\pm 0.11$  Nm ( $\pm 0.5$

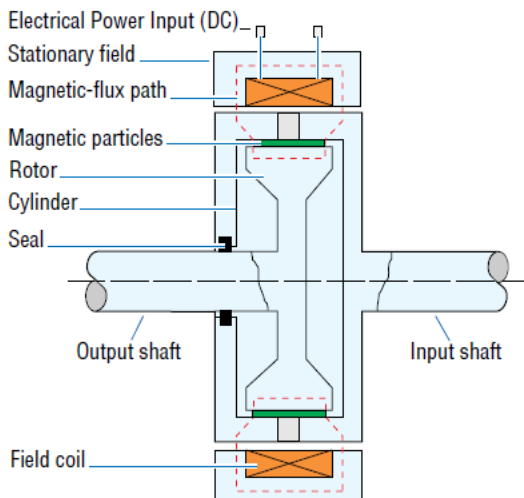


Figure 6.10: MPB70 cross section view.

Table 6.4: MPB70 specifications and coil data.

Parameter	Value
Torque range (Nm)	0.11-7.91
Drag (resistance) torque (Nm)	0.11
Shaft Inertia ( $\text{kgm}^2$ )	$2.35 \times 10^{-5}$
Maximum speed (rpm)	1000
Maximum heat dissipation (Watts)	100
Resistance (Ohms)	35
Rated Voltage (VDC)	24

(%) for both the clockwise (CW) and counter-clockwise (CCW) directions; see Figure 6.12b. As before, a simple MATLAB program was used to acquire data with the aid of an NI USB-6212 A/D converter with 16 channels and 16-bit resolution. This device has a sample rate of 400 kS/s.

In calibrating the MPB, the measured rotor speed, input current, and torque were curve fitted using the MATLAB curve fitting tool. The resulting calibration curves are shown in Figure 6.13. As can be seen,  $Q$  is nearly independent of RPM for  $0.5 \leq Q \leq 2.0$  Nm. Beyond this range, the significance of RPM increases and is highest for  $Q = 7$  Nm. Thus, for the present experiment, the measured torque range is between 0.27 and 6 Nm depending on  $N$ .

### 6.2.3 Windmill performance experiment

Experimental testing was executed with three, six, twelve, and twenty-four blades at wind speeds of 5, 6, 7, 10, and 15 m/s in both the RWT and OJF using the original set up. With the modified setup, measurements were only conducted in the high blockage tunnel because the need for the test only became evident after testing has been concluded at TU Delft, the Netherlands. However, the TU Delft measurements were corrected retrospectively. Based on the blade chord  $Re$ , aerodynamic performance and validation analysis will be limited to only test data at 15 m/s, which gives the highest  $Re$ . For the RWT, speeds were recorded with and without the windmill rotor for each test case to correct for the effect of blockage, which will be discussed in Section 6.3. Prior to starting the experiment, the setup was mounted, secured, and checked to ensure all connections were in place. The tunnel was then switched on and set to the required speed, and the flow was allowed to stabilize. Current is transmitted to the MPB via a DC power supply. The MATLAB code is executed to acquire data for 30 s for the first reading at zero current supplied to MPB. Data acquired are the axial force, torque, and RPM at the runaway condition (equivalent to maximum  $\lambda$ ). The current is then increased to a value that causes a significant change in rotor speed. However, the increment is dependent on the rotor blade configuration ( $N$ ) and wind speed, and the measured values

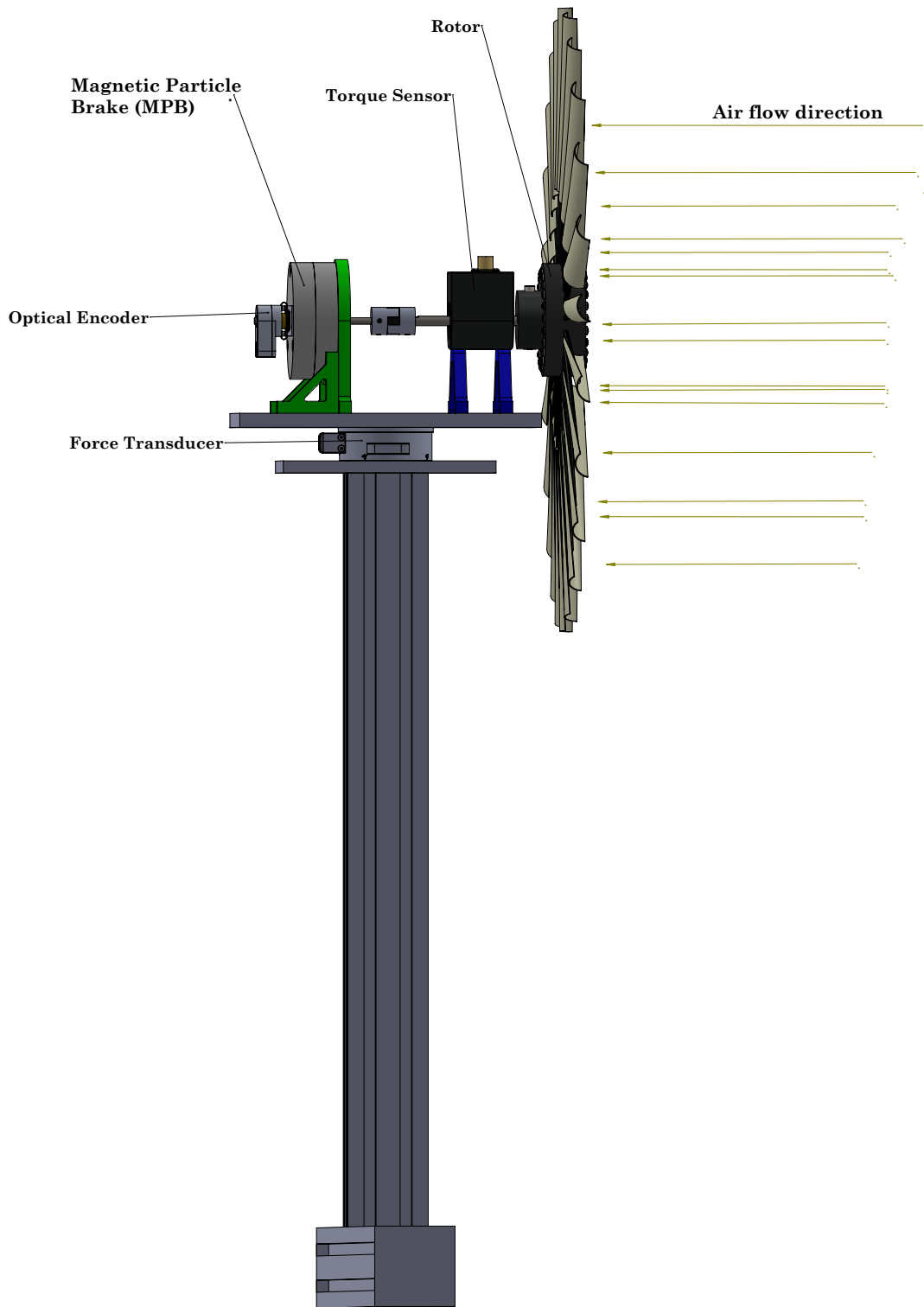
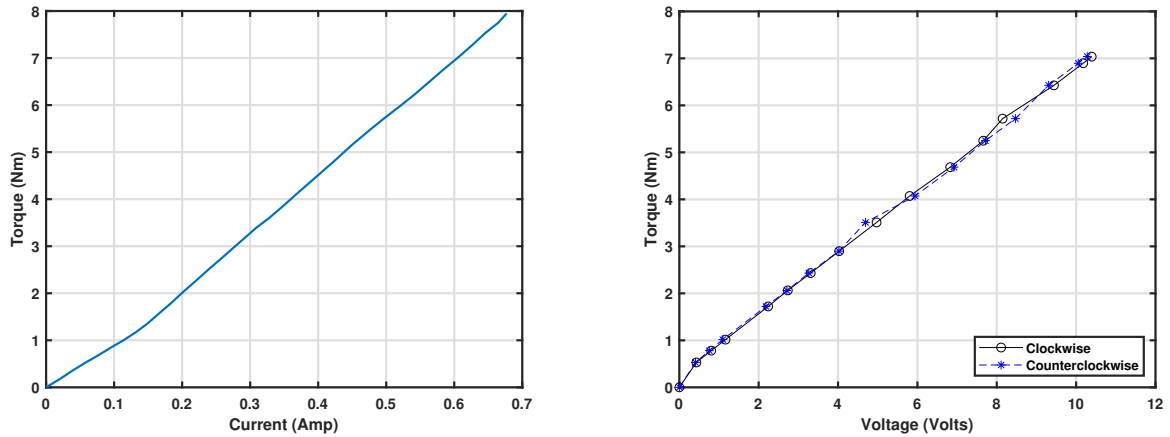


Figure 6.11: Modified experimental windmill rotor setup.



(a) MPB70 (Extracted from PrecisionTork, Retrieved 05-Dec-2019) (b) TQ 513-062 sensor vs voltage relation as determined in current study

Figure 6.12: Torque calibration curves.

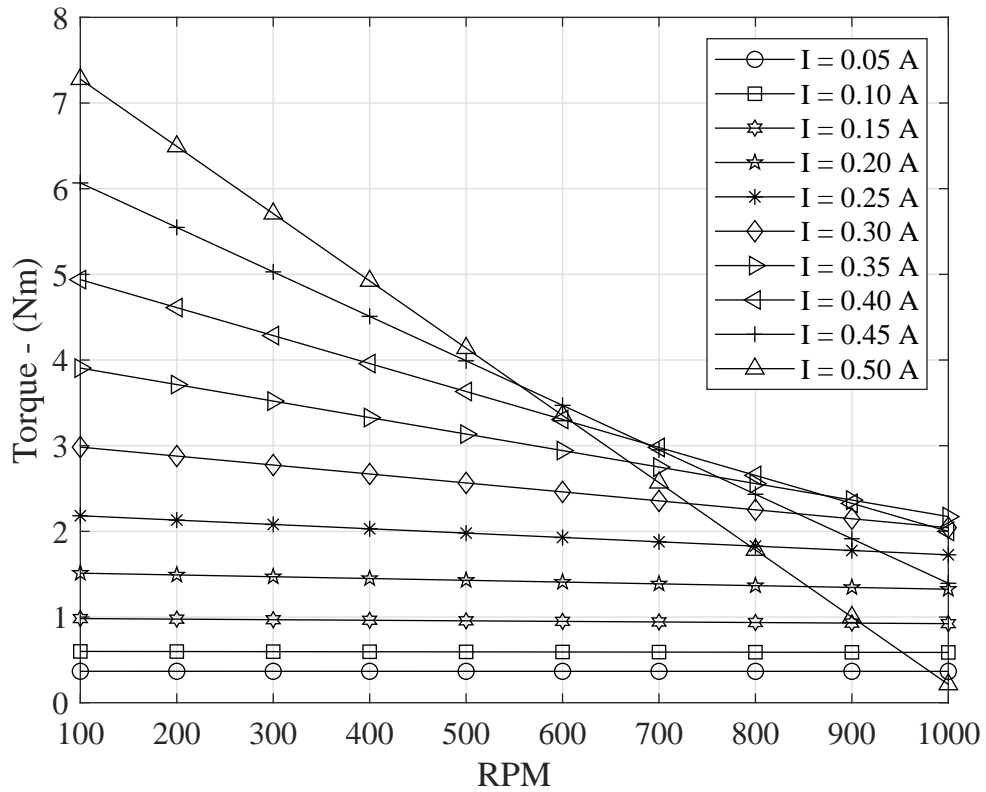


Figure 6.13: MPB torque calibration against RPM at various input currents for 0–10 V.

are recorded. This step is repeated up until the rotor stops turning completely or stalls.

The thrust,  $T$ , torque,  $Q$ , and hence power,  $P$ , which is the product of  $Q$  and rotational

speed,  $\Omega$  were determined from the measured axial force, torque, and rotational speed. As is the convention in fluid machinery, the windmill operational performances are usually expressed in appropriate dimensionless forms. The first of these interesting quantities is the blade thrust,  $T$ , which is not as crucial for wind turbines as propellers, primarily designed for thrust production. However, the blade thrust must be incorporated in the tower and foundation design because it is typically transmitted to the turbine tower. The dimensionless thrust termed thrust coefficient,  $C_T$ , is defined as

$$C_T = \frac{T_{net}}{\frac{1}{2}\rho U_\infty^2 \pi R^2} \quad (6.1)$$

where  $T_{net}$  is the difference between the measured thrust,  $T_m$  which is due to the setup, and the thrust due to the combined effect on the setup, that is not part of the aerodynamic thrust (blade thrust),  $T_{c'}$ , derived in Appendix C. Depending on  $\lambda$  and  $N$ , the contribution of the spars to  $T$  averages between 6-14%. The most useful parameter for describing the performance of windmills, particularly the direct drive water pump, in which the rotor torque must balance the pump load torque, is the torque coefficient,  $C_Q$  expressed as

$$C_Q = \frac{Q_{net}}{\frac{1}{2}\rho U_\infty^2 \pi R^3} \quad (6.2)$$

where  $Q_{net}$  is the difference between the measured torque,  $Q_{net}$ , which is due to the blades and spars, and the torque due to the spars that are not part of blades,  $Q_{b'}$ ; see Appendix C. Again, depending on  $\lambda$  and  $N$ ,  $Q$  due to the spar can be as high as 16%, particularly at runaway  $\lambda$  for the  $U_\infty$  tested.

Another relevant parameter is the power coefficient,  $C_P$ , which is the ratio of the actual power produced to the power in the undisturbed wind, mathematically stated as

$$C_P = \frac{P}{\frac{1}{2}\rho U_\infty^2 A} = \frac{Q_{net}\Omega}{\frac{1}{2}\rho U_\infty^2 \pi R^2} \quad (6.3)$$

Even though  $C_P$  is often treated as aerodynamic efficiency of wind turbine [33], it is strictly

not one. It is a function of the tip speed ratio,  $\lambda$ , given as

$$\lambda = \frac{\Omega R}{U_\infty} \quad (6.4)$$

### 6.2.4 Starting experiment

The objectives here are first to determine the starting wind speed for the various rotors. As has been stated previously, this speed can be significantly higher than the cut-in wind speed. A second objective is to determine the runaway speed (maximum aerodynamically possible rotor speed under no-load condition) for varying upstream wind conditions. The testing was conducted at constant speeds. The tunnel is powered on and set to run at the rotor starting speed already determined by a trial and error approach. The three, six, twelve, and twenty-four-bladed rotors accelerate from rest (stationary position) to their steady-state rotor speed values. Using the MPB, sufficient braking torque is applied to the rotors to completely stop their motion for a few seconds, after which the rotors are suddenly released and allowed to accelerate to their runaway speeds. The time dependence rotor speeds are then measured using the relevant instrumentation and acquired with the previously described NI card for the aerodynamic performance testing.

### 6.2.5 Measurement uncertainty

The uncertainties associated with coefficients of thrust,  $C_T$ , equal to  $f(T_{net}, \rho, U_\infty, R)$  torque,  $C_Q$ , equal to  $f(Q_{net}, \rho, U_\infty, R)$  and power,  $C_p$ , equal to  $f(Q_{net}, \Omega, \rho, U_\infty, R)$ , based on Eq. 3.6, are evaluated using

$$\Delta C_T = \sqrt{\left(\frac{\partial f}{\partial T_{net}} \Delta T_{net}\right)^2 + \left(\frac{\partial f}{\partial \rho} \Delta \rho\right)^2 + \left(\frac{\partial f}{\partial U_\infty} \Delta U_\infty\right)^2 + \left(\frac{\partial f}{\partial R} \Delta R\right)^2} \quad (6.5)$$

$$\Delta C_Q = \sqrt{\left(\frac{\partial f}{\partial Q_{net}} \Delta Q_{net}\right)^2 + \left(\frac{\partial f}{\partial \rho} \Delta \rho\right)^2 + \left(\frac{\partial f}{\partial U_\infty} \Delta U_\infty\right)^2 + \left(\frac{\partial f}{\partial R} \Delta R\right)^2} \quad (6.6)$$

$$\Delta C_p = \sqrt{\left(\frac{\partial f}{\partial Q_{net}} \Delta Q_{net}\right)^2 + \left(\frac{\partial f}{\partial \Omega} \Delta \Omega\right)^2 + \left(\frac{\partial f}{\partial \rho} \Delta \rho\right)^2 + \left(\frac{\partial f}{\partial U_\infty} \Delta U_\infty\right)^2 + \left(\frac{\partial f}{\partial R} \Delta R\right)^2} \quad (6.7)$$

The dimensionless forms of Eqs. 6.5, 6.6 and 6.7 are expressed as

$$U_{C_T} = \sqrt{\left(\frac{\Delta T_{net}}{T}\right)^2 + \left(\frac{\Delta \rho}{\rho}\right)^2 + \left(2 \frac{\Delta U_\infty}{U_\infty}\right)^2 + \left(2 \frac{\Delta R}{R}\right)^2} \quad (6.8)$$

$$U_{C_Q} = \sqrt{\left(\frac{\Delta Q_{net}}{Q}\right)^2 + \left(\frac{\Delta \rho}{\rho}\right)^2 + \left(2 \frac{\Delta U_\infty}{U_\infty}\right)^2 + \left(3 \frac{\Delta R}{R}\right)^2} \quad (6.9)$$

$$U_{C_p} = \sqrt{\left(\frac{\Delta Q_{net}}{Q}\right)^2 + \left(\frac{\Delta \Omega}{\Omega}\right)^2 + \left(\frac{\Delta \rho}{\rho}\right)^2 + \left(3 \frac{\Delta U_\infty}{U_\infty}\right)^2 + \left(2 \frac{\Delta R}{R}\right)^2} \quad (6.10)$$

The error bounds associated with the measuring equipment for the RWT are given in Table 6.5. The accuracy of the OJF wind speed and thrust measurement is 0.5% and  $\pm 0.075N$ , respectively and utilizing Eqs. 6.8, 6.9 and 6.10, the propagated uncertainty estimates for  $C_T$ ,  $C_Q$  and  $C_p$  are computed.

### 6.3 Blockage in open jet wind tunnel (OJT)

Wind turbine performance in real wind conditions often differs from that of similar models tested in wind tunnels due to the confined, limited, and bounded flow in the tunnel. This

Table 6.5: Uncertainty in windmill experimental measurements.

Parameter	Value
Radius	$\pm 0.06\%$
Wind speed	$\pm 1.3\%$
Air density	$\pm 0.06\%$
Rotational speed	$\pm 0.34\%$
Thrust	$\pm 2.1\%$
Torque	$\pm 0.025\%$

variation is due, at least partly, to turbulence level spatial and temporal non-uniformity. Another reason for this variation is solid and wake blockage effect. These cause the flow velocity in the vicinity of the model in the wind tunnel to be different from that of the same model placed in an unbounded free airstream. For an open jet tunnel discussed in section 3.6, the effect of wake blockage is negligible [121, 146].

In this study and for experimental testing of wind rotors, the focus should be only on the solid blockage, which is defined as the ratio of the rotor swept area to the tunnel's cross-sectional area. Depending on the sizes of both the wind turbine and the test section, the effect of blockage can be substantial and is typically higher in a closed test section. Blockage has been shown to significantly affect wind tunnel performance results, particularly for blockage greater than 10% [87]. Due to the inverse cubic relation between the power coefficient and wind speed, an error as small as 1% in wind speed results in a 3% error in the performance coefficient.

Avoiding blockage would require selecting a small-scale test model, which, as noted by Jeong et al. [89], may not be feasible in test situations requiring high signal-to-noise ratio during measurements, a constraint due to the Reynolds scaling effect and the use of available test models amongst others. Thus, it is generally recommended to keep the  $B_R$  below and at around 10% [87]. However, for higher blockage, corrections must be applied to the upstream velocity utilized in computing the performance parameters of the wind turbine rotor model.

### 6.3.1 Blockage effect assessment and correction

Before testing in the OJF, the RWT measured  $C_T$  was higher than the BEM prediction and increased with  $N$ , which led to further investigation of this high discrepancy. Thus, the drag coefficients of simple geometries shown in Table 6.6 were investigated at an axial distance of 20–100 cm from the contraction outlet at different  $Re$ . While blockages of 5, 6, 10, and 20 % were examined, it was impossible to examine a  $B_R$  comparable to that of the windmill rotor. Such a rotor would experience a higher magnitude of thrust and be 100 cm in diameter,

which is, unfortunately, too large for the waterjet machine at the University of Calgary to cut out. Due to this constraint, a 50 cm disk was tested as shown in Figure 6.14. The use of porous discs, instead, would have been a realistic alternative to the solid disks [144].

Nonetheless, interesting findings were made from the drag coefficient measurements of the simple geometries, including the decrease in drag coefficient with increasing distance of the test specimen from the tunnel's exit. Later, the performance of the original windmill test setup was investigated at the same axial distances as the disks, which was the first attempt at understanding the unusually high thrust values recorded in the RWT testing. Note that the MPB was yet to be dynamically calibrated at this stage of the study, so the focus here would only be on the  $C_T$  because the torque measurements are deemed incorrect, as previously explained.

Unlike the closed jet tunnels, the OJT boundaries are not fixed; therefore, the flow can move easily around the tested specimen. While there are numerous mathematical models to correct the above errors, blockage corrections for OJT are not precisely known, unlike CJT. Thus, a complete correction method based on the measurement procedure reported in [146–149] is implemented in this study. Similar to the drag coefficient measurement previously described, rather than measure the free stream velocity,  $U_\infty$ , the free stream velocity experienced by a disk/plate at the test section of the wind tunnel,  $U_{\infty,d}$ , is computed from the experimentally measured drag force experienced by the geometries. With standard values of  $C_d$  at  $Re$  corresponding to that of the RWT at 0.3% turbulence level,  $U_{\infty,d}$ , is computed using

$$U_{\infty,d} = \sqrt{\frac{F_d}{\frac{1}{2}\rho A_d C_d}} \quad (6.11)$$

All the experimental test results on the windmill model for  $3 \leq N \leq 24$  and RWT blockage effects are presented and discussed in Chapter 7.

Table 6.6: Characteristics of flat plate and thin disks.

Geometry	Characteristic length (mm)	Blockage ratio (%)
Thin disk	250	5
Flat plate	250	6
Thin disk	360	10
Thin disk	500	20

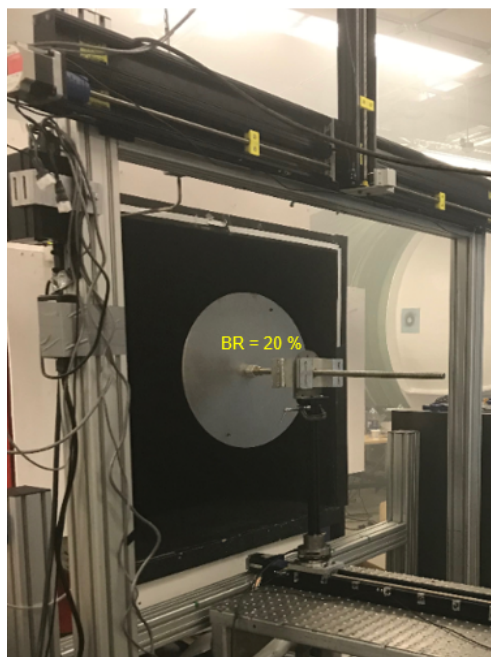


Figure 6.14: Drag measurement in RWT test section. Shown is the circular disk of  $\phi=50$  cm.

# Chapter 7

## Windmill and Blockage Experimental Results

In this chapter, the results of the experiments conducted on the 0.68 m windmill rotor with  $3 \leq N \leq 24$  that were described in Chapter 6 are presented. The aerodynamic performance measurements in the low (OJF) and high (RWT) blockage tunnels with the outcomes of blockage study on thin solid disks and the square flat plate are given in Section 7.1. The effects of blockage on the windmill rotor performance for large  $N$  are then discussed in Section 7.2. In section 7.3, the starting test performance results are analyzed. In both cases, the measured rotor performances are compared with the BEM aerodynamic and starting behavior prediction in Chapters 4 and 5, respectively.

### 7.1 Aerodynamic performance

#### 7.1.1 BEM comparison to Wegereef 1984 and OJF experiments

Since the model used in this study is a scaled replica of the model tested by Wegereef [25], its rotor performance for  $N = 6, 12$  and  $24$  denoted “WEG”, are compared to the OJF and BEM in Figures 7.1 and 7.2. As seen in Figure 7.1, significant differences can be observed

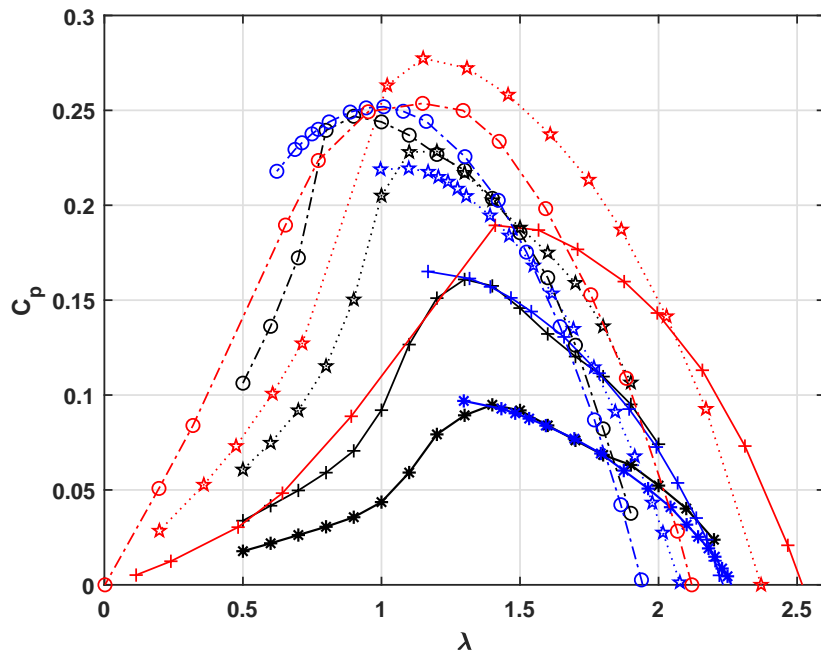


Figure 7.1: BEM power coefficient compared to the measurements made by Wegereef and in the OJF.

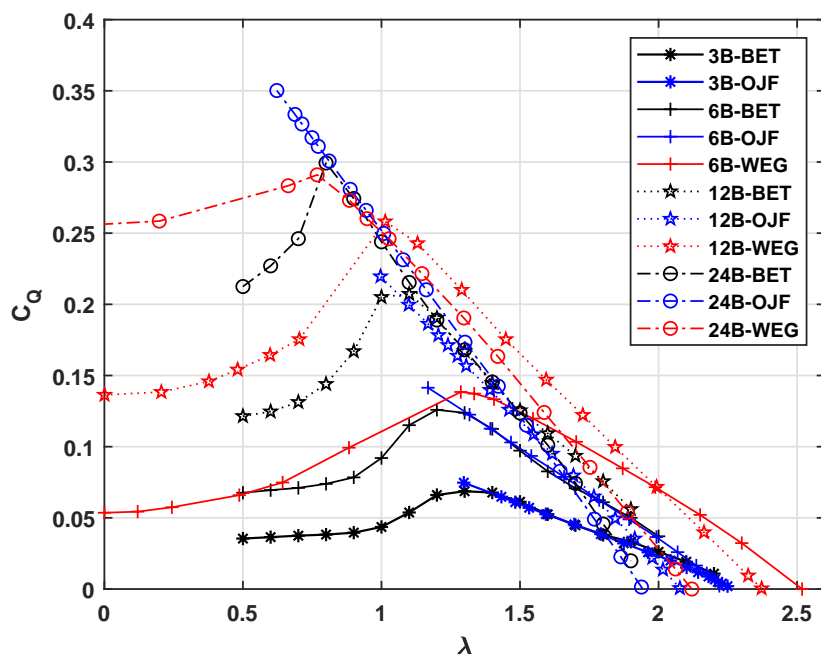


Figure 7.2: BEM torque coefficient compared to the measurements made by Wegereef and in the OJF.

between the OJF and WEG results. However, the closest match occurred for  $N = 24$ , where the maximum power coefficient,  $C_{P,max}$ , is 0.252 and occurs at  $\lambda_{opt} = 1.008$  for the former compared to  $C_{P,max} = 0.254$  at  $\lambda_{opt} = 1.148$  for the latter, a 0.71% difference. Generally, the  $C_P$  values for  $N = 6, 12$  and  $24$  are higher than the OJF, but curiously, a decrease in  $N$  from 24 to 12 in the data of Ref. [25] increased the maximum  $C_P$  by 9.34%. Wegereef's rotor model had  $B_R = 0.465$ , which probably explains the discrepancies, because no blockage correction was reportedly made to its  $C_P$  and  $C_Q$ .

Figure 7.1 also presents a performance comparison of the OJF experimental measurements and the BEM prediction for  $N = 3, 6, 12$  and  $24$  with  $\sigma$  defined as  $Nc/\pi R$  corresponding to 0.11, 0.22, 0.45, and 0.90 respectively. As expected, an increase in solidity by increasing  $N$ , shifts the  $C_P$  curves toward lower  $\lambda$ , while also decreasing  $\lambda_{opt}$ , which is consistent with previous studies, e.g., [38]. Further, there is good agreement between the OJF measurements and the BEM  $C_p$  values. The BEM predicted  $C_{P,max}$  to within  $\pm 4\%$  of measured OJF values, with no significant shift in  $\lambda_{opt}$  for all four rotor test cases as presented in Table 7.1. This is consistent with an analytical prediction of a high solidity, low-speed wind turbine reported by Duquette and Visser [150]. However, they did not correct for  $\sigma$ , implying that high  $\sigma$  effects are restricted to  $\lambda < \lambda_{opt}$ . The experimental results obtained here are promising. Glauert [99] gives the ideal  $C_p$  of a windmill as 0.288 at  $\lambda = 0.5$ . The case of  $N = 24$  rotor remarkably close to that limit despite its simple design suggests that improve performance can be achieved with an optimized blade.

It is important to note that runaway tip speed ratios,  $\lambda_{run}$  (equivalent to maximum  $\lambda$  at no load), are accurately predicted by BEM apparently because they occur at low  $\lambda$ , unlike low solidity rotors where  $\lambda_{run} \approx 15$ .  $\lambda_{run}$  reduces with increasing  $N$  and shows a good correspondence between the OJF and BEM, probably because of the low thrust at the runaway point. Wegereef's rotor had comparable chord-based  $Re$  to the present one, and because the OJF measurements match reasonably well with BEM, the OJF results can then be considered more accurate.

Table 7.1: Comparison of OJF and BEM torque and power coefficients.

Rotor/ Parameters	N=3		N=6			N=12			N=24		
	OJF	BEM	WEG	OJF	BEM	WEG	OJF	BEM	WEG	OJF	BEM
$C_{P,max}$	0.097	0.095	0.189	0.165	0.161	0.277	0.219	0.228	0.254	0.252	0.247
$\lambda_{opt}$	1.297	1.4	1.286	1.168	1.3	1.15	1.099	1.1	1.148	1.008	0.9
$C_{Q,max}$	0.075	0.069	0.138	0.141	0.126	0.2582	0.2196	0.207	0.291	0.350	0.299
$C_{Q,\lambda=0}$		0.023 <sup>a</sup>	0.054		0.0392 <sup>a</sup>	0.1364		0.095 <sup>a</sup>	0.258		0.21 <sup>a</sup>
$\lambda_{run}$	2.317	2.2	2.518	2.244	2	2.37	2.197	1.9	2.12	2.058	1.9
$C_W$		0.051	0.136		0.078	0.3235		0.1805	0.547		0.399

<sup>a</sup> obtained by extrapolating results to zero  $\lambda$ .

As with  $C_P$ , a similar trend can be observed with  $C_Q$  in Figure 7.2. The maximum  $C_Q$  generally increases with  $N$ , and a high  $C_Q$ , particularly at  $\lambda = 0$ , is advantageous for starting direct-drive waterpumping windmills. Unfortunately, measurements at lower and zero  $\lambda$  could not be obtained because while testing, the rotor stalls before reaching those values of  $\lambda$ , precluding OJF comparison with  $\lambda < \lambda_{opt}$ . However, following from Eq. (4.29), the computed  $C_W$  for WEG and BEM in Table 7.1 gives an indication of the water pumping potential, which obviously increases with  $N$ . Note that  $C_W$  values for OJF are missing due to lack of test data at  $\lambda = 0$  but are expected to follow the BEM and WEG trend. Furthermore, the discrepancy between the measured and predicted  $C_Q$  curves increases with  $N$  due to the increasing solidity, presumably altering the blade element lift and drag. The same can be observed for a comparable high solidity rotor of Figure 7.3 investigated by Kentfield [27]. Because no thrust measurements were done by Wegereef [25], low blockage experimental thrust data comparisons with BEM are deferred to the next section.

### 7.1.2 BEM Comparison to RWT and OJF experiments

The high blockage RWT measurements closely match that of the low blockage OJF at a limited range of  $\lambda$  beginning from  $\lambda_{run}$  up to a certain  $\lambda$  approaching  $\lambda_{opt}$  for each rotor case. Beyond this point, the measured model performances are comparatively greater over a much larger range of  $\lambda$  depending on  $N$ , which is possibly due to the effect of blockage as illustrated in Figures 7.4 and 7.5. As is evident from the plots, the measured  $C_P$  and

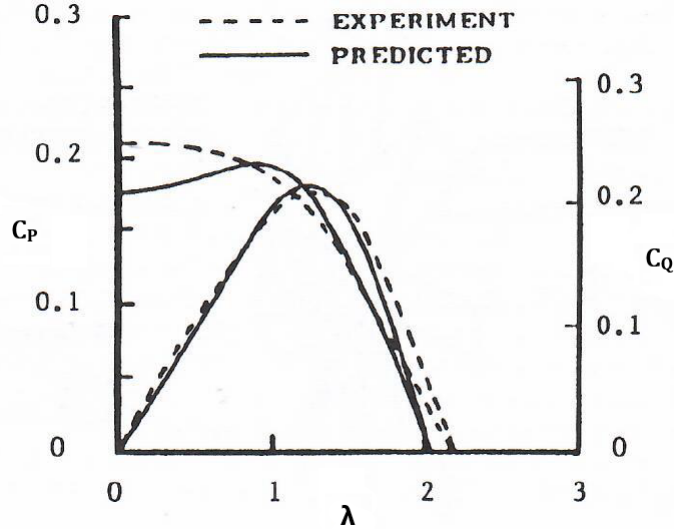


Figure 7.3: Predicted and measured performance of a high solidity, delta wing-bladed rotor, [27].

$C_Q$  values are greater than those of both the low blockage tunnel and the BEM prediction, with the discrepancies increasing with increasing  $N$  (or  $\sigma$ ). For example, compared to OJF, the RWT measured  $C_P$  is 13.3% higher for  $N = 24$  at  $\lambda = 1$ . At no load, equivalent to

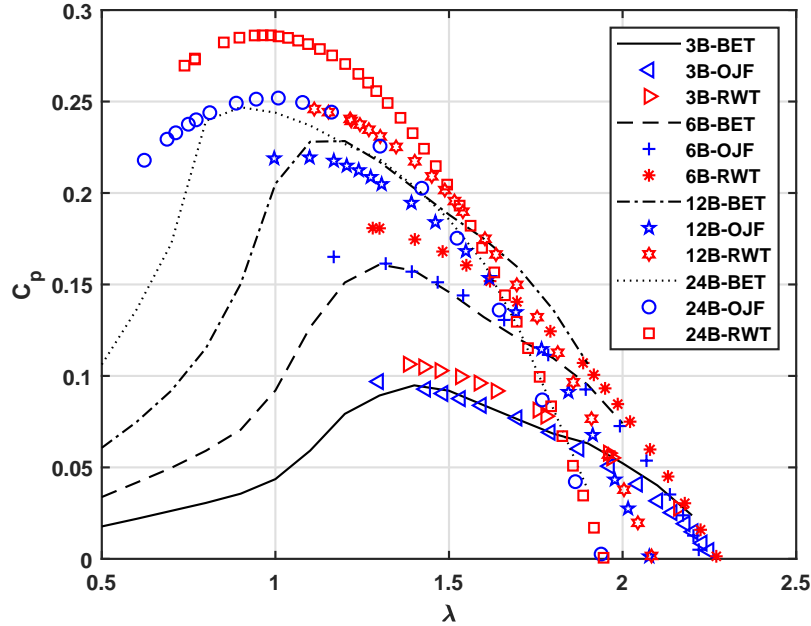


Figure 7.4: BEM and measured power coefficient with no blockage correction applied to the RWT results.

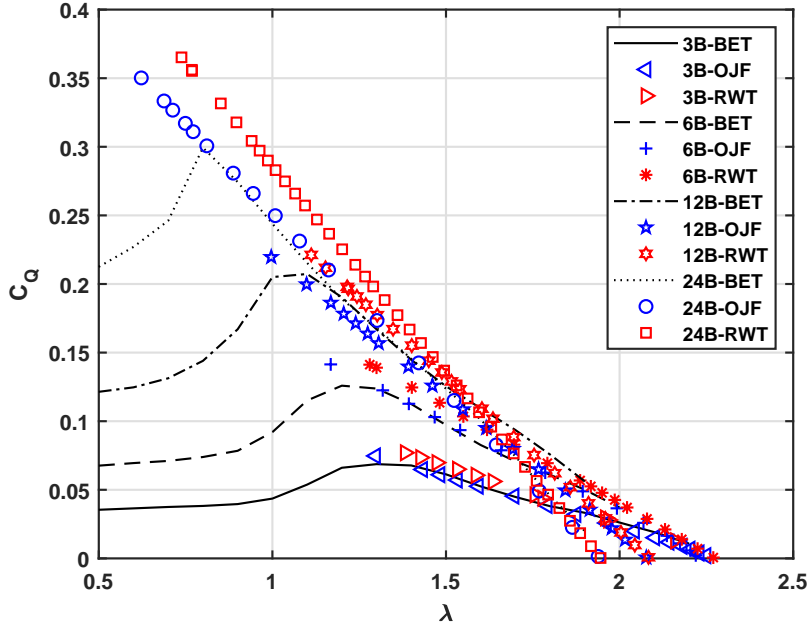


Figure 7.5: BEM and measured torque coefficient with no blockage correction applied to the RWT results.

$\lambda_{run}$ , an excellent match is obtained between the OJF and RWT. But as the rotor loading increases (decreasing  $\lambda$ ), the significance of the blockage appears to increase in such a way as to increase the model performance in the RWT. Interestingly, however, with reducing  $\lambda$ , the divergence becomes more pronounced, suggesting that the blockage and correction are  $\lambda$  dependent.

The  $C_T$  results are presented in Figure 7.6. Like  $C_P$  and  $C_Q$  after maximum torque (i.e., moving rightward of the curves), the OJF, in general, corresponds reasonably well with BEM. For  $N = 3, 6$  and  $12$ , the BEM slightly over-predicted the thrust, while for  $N = 24$ , starting at  $\lambda < 1.1$ , a noticeable divergence is seen, similar to the corresponding  $C_P$  and  $C_Q$  curves in Figures 7.4 and 7.5, respectively. This low  $\lambda$  behavior appears to be due to solidity effects not accounted for in the BEM calculations. However, the same cannot be said of the RWT. Disparities that are much larger than can be attributed to blockage or random measurement uncertainty are noticeable in the  $C_T$  curves of Figure 7.6. For example, the measured  $C_T$  due to the RWT is higher by a factor  $> 1.5$  for  $N = 3$  and  $N = 24$  at  $\lambda \approx 1.5$  and  $1.0$ ,

respectively compared to the OJF. The reasons for these high values were investigated by assessing the impact of blockage on thin solid disks and a flat square plate in the RWT described in Chapter 6. The results of the blockage test will be discussed in Section 7.2.

## 7.2 Blockage effect on flat disks/plate and windmill rotor

Based on the windmill model cross-sectional area and the test section sizes of the University of Calgary RWT and TU Delft OJF, their  $B_R$  correspond to 0.363 and 0.045, respectively, implying that blockage in the latter is negligible, which was confirmed from comparing measured  $C_T$  with BEM values (see Figure 7.6). For the RWT, the blockage effect is significant. Preliminary investigation of the effect of blockage was conducted using a flat plate and thin solid disks of varying sizes by measuring the drag force,  $F_d$ , experienced by them at increas-

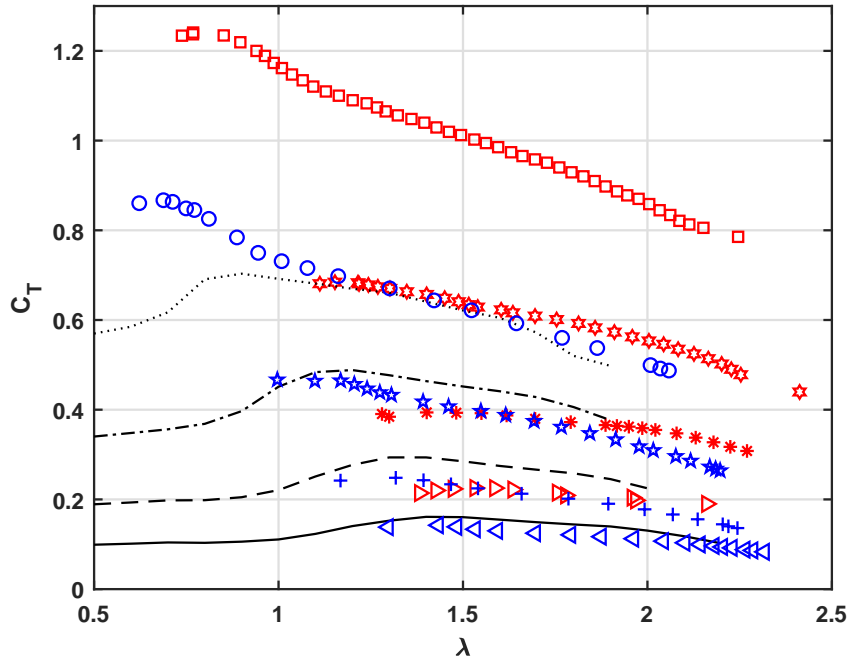
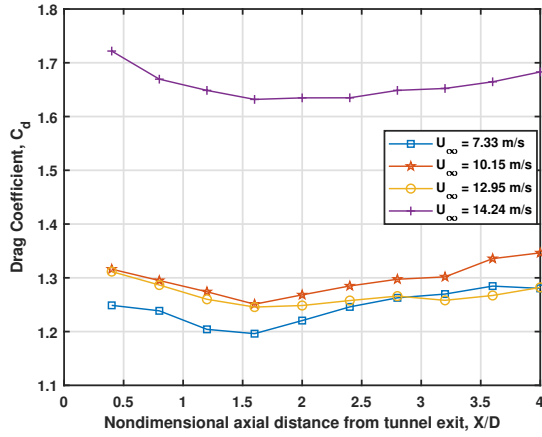


Figure 7.6: BEM and measured thrust coefficient with no blockage correction applied to the RWT results.

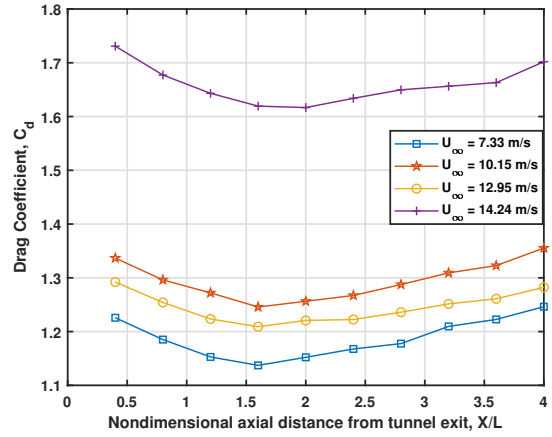
ing distances from the RWT exit in Section 6.3.1. These geometries were chosen because the sharp edges should ensure fixed flow separation as  $Re$  varies, and, therefore, the drag should be independent of  $Re$ . The results of the drag measurements are presented in Figures 7.7(a)–(d). Generally,  $C_d$  values are functions of the model projected areas,  $A_d$ , and distances,  $X$  from the tunnel exit. For  $U_\infty = 7.23, 10.15$  and  $12.95$  m/s, the  $C_d$  range between 1.0–1.5, which agrees with standard literature values for similar geometries tested; e.g., [146–148]. The slight variations in  $C_d$  between the wind speeds for  $B_R = 0.05, 0.06$  and 0.1 are possibly due to the effect of wind tunnel turbulence on the aerodynamic drag, which, according to Schubauer and Dryden [151], shifts the transition point from laminar to turbulent boundary layer flow resulting in different skin friction drag and point of separation. However, at  $U_\infty = 14.25$  m/s,  $C_d$  is much higher irrespective of the  $B_R$  and the axial distance of the geometry from the tunnel, reaching a maximum of 2 for the case of  $B_R = 0.2$ , as shown in Figure 7.7(d). Because the high drag is only observed at  $U_\infty = 14.25$  m/s for all  $B_R$ , the drastic increase is unlikely due to blockage or random error.

Small blockage effects can be seen as the  $B_R$  and the distance of the body from the tunnel exit increases and decreases, respectively, as indicated by a rapid drop in  $C_d$ , particularly for the 50 cm disk. At  $U_\infty \geq 14.25$  m/s, it is more likely that the measured high drag is due to a systematic error; perhaps the transducer's strain gauge stiffness changes owing to increased temperature resulting from internal friction. Therefore it is probable that the ATI F/T senses extraneous signals in addition to that of the wind load, which introduces a bias in the force measurements. Because of the limitation on the size of the test model, the windmill experiment could only be conducted at a wind speed of at least 14 m/s to maximize  $Re$  for which there are available  $C_l$  and  $C_d$  data. Consequently, the error in the windmill thrust measurements could not be obviated during testing. Due to time constraints, no further test was done to correct the RWT thrust measurements, particularly because the OJF external force balance gave accurate thrust values.

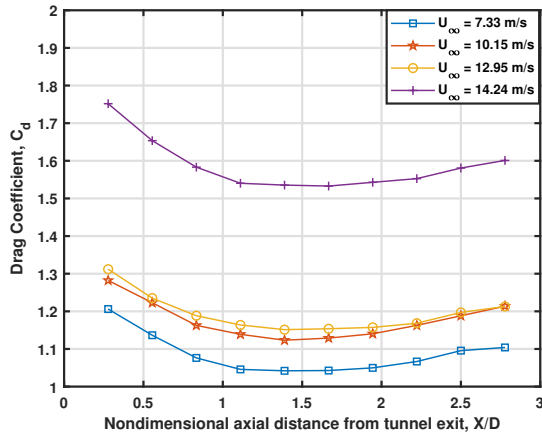
Based on the knowledge that the wind speeds at the tunnel exit and the vicinity of the



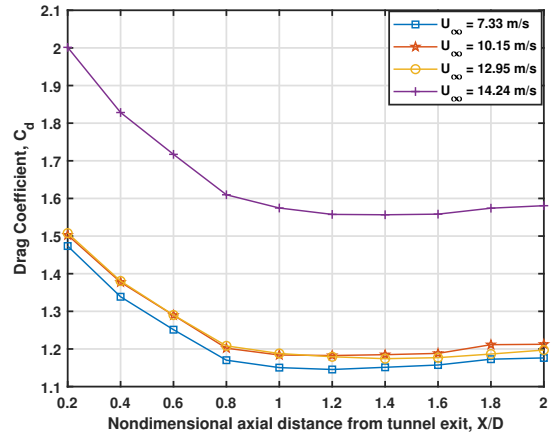
(a) Thin circular disk of  $\phi = 0.25$  m,  $B_R = 0.05$



(b) Flat square plate of  $\phi = 0.25$  m,  $B_R = 0.06$



(c) Thin circular disk of  $\phi = 0.36$  m,  $B_R = 0.1$



(d) Thin circular disk of  $\phi = 0.50$  m,  $B_R = 0.2$

Figure 7.7: Drag coefficients of simple geometries at varying distance from the RWT exit.

test model are different and using standard  $C_d$  values, the corrected upstream velocity at the disk was computed using Eq. (6.11). The velocity of the disk/plate at equivalent  $B_R$  as the windmill model was then used in calculating a blockage correction factor,  $B_F = U'_\infty/U_\infty$ , as given in [152]. Accordingly, the corrected  $C_P$ ,  $C_T$ ,  $\lambda$ , and  $C_Q$  are computed using

$$C'_P = C_p B_F^3 \quad (7.1)$$

$$C'_T = C_T B_F^2 \quad (7.2)$$

$$\lambda' = \lambda B_F \quad (7.3)$$

$$C'_Q = C'_P / \lambda' \quad (7.4)$$

Eqs. 7.1-7.4 were used to correct the RWT measurements. The resulting  $C'_P$  agrees well with both the OJF and BEM in Figure 7.8, although with a slight decrease in  $\lambda_{run}$ . The magnitude of difference increases as  $N \rightarrow 24$ . For all the studied rotor configurations,  $B_F$  drops with a rise in  $\lambda$ . At around  $\lambda = 1$  for  $N = 24$ , the correction of  $C_P$  due to blockage was 12.75% ( $B_F = 0.96$ ). Comparing Figure 7.4 to Figure 7.8 reveals that correction is not needed at and near the  $\lambda_{run}$  region. Although runaway is not practically important, it is an interesting test case for evaluating BEM accuracy. While the RWT correction for  $C_Q$  in Figure 7.9 is expected to have the same effect as  $C_P$  because of their direct relationship (i.e.,  $C_P = C_Q \lambda$ ), the corrections required in the case of  $C_T$  for  $N = 3, 6, 12$  and 24 are unsurprisingly greater than that of its corresponding  $C_P$  and  $C_Q$  values due to reasons cited earlier. This larger required correction is seen in the way the RWT and OJF results diverge at the runaway. Thus it appears that the required blockage corrections for  $C_P$ ,  $C_Q$  and even  $C_T$  are reasonably sufficient, but because of the ATI F/T transducer systematic error, Figure 7.6 corrected only for blockage is still far from matching the results of the OJF and BEM as depicted in Figure 7.10.

### 7.3 OJF experimental starting performance

Series of tests were done to ascertain the no-load instantaneous wind speed when rotation is first detected,  $U_s$ , i.e., starting wind speed and running/continuous speed, or the cut-in wind speed,  $U_c$ , for the windmill model starting from rest with  $N = 3, 6, 12$  and 24. Table 7.2 shows that as  $N$  increases,  $U_s$  decreases due to an increase in starting torque. When

$N$  increases from 3 to 24, a 71% decrease in starting wind speed is observed, which is a significant advantage of multi-bladed high solidity rotor in low wind speed locations. Note that the values of Table 7.2 are influenced by the azimuthal position of the individual blades at rest before starting and the operating condition (temperature) of the rotor model when measurements were conducted, i.e., if it is a cold or warm start. Successive increment of  $N$  from 3 to 6, 12 and 24 decreases the cut-in speeds by 22%, 37% and 48%, respectively.

Table 7.2: Starting and running speeds of rotors under no-load.

$N$	average $U_s$ (m/s)	$U_c$ (m/s)
3	5.25	> 2.7
6	3.5	> 2.1
12	2.5	> 1.7
24	> 1.7	> 1.4

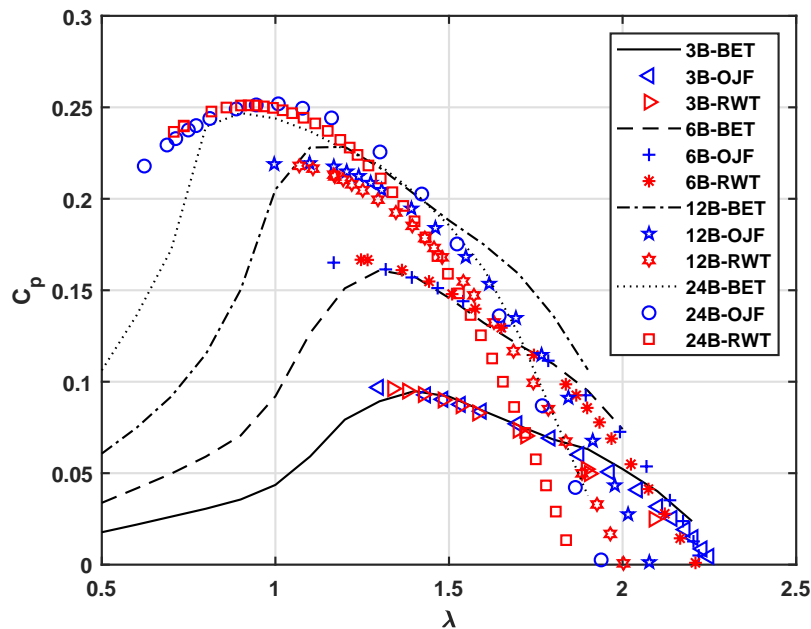


Figure 7.8: BET and measured power coefficient with correction applied to the RWT results.

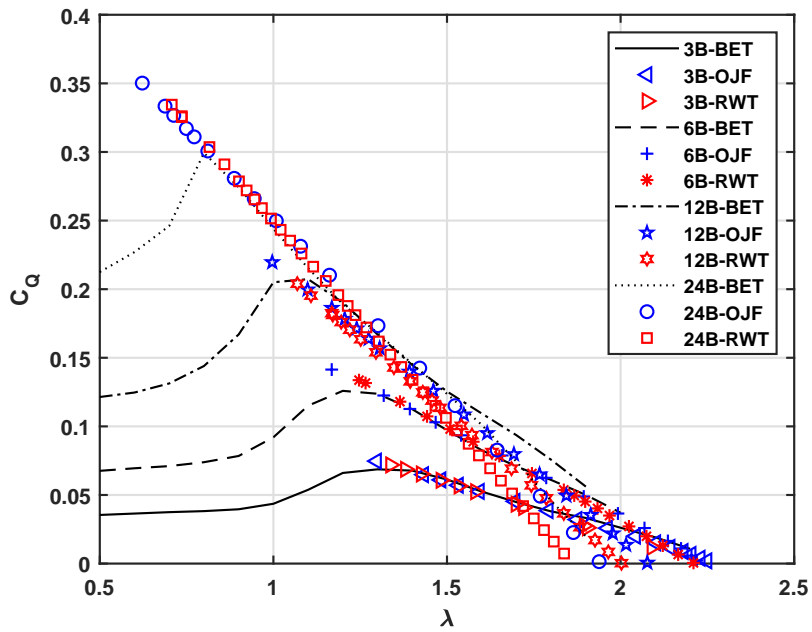


Figure 7.9: BET and measured torque coefficient with correction applied to the RWT results.

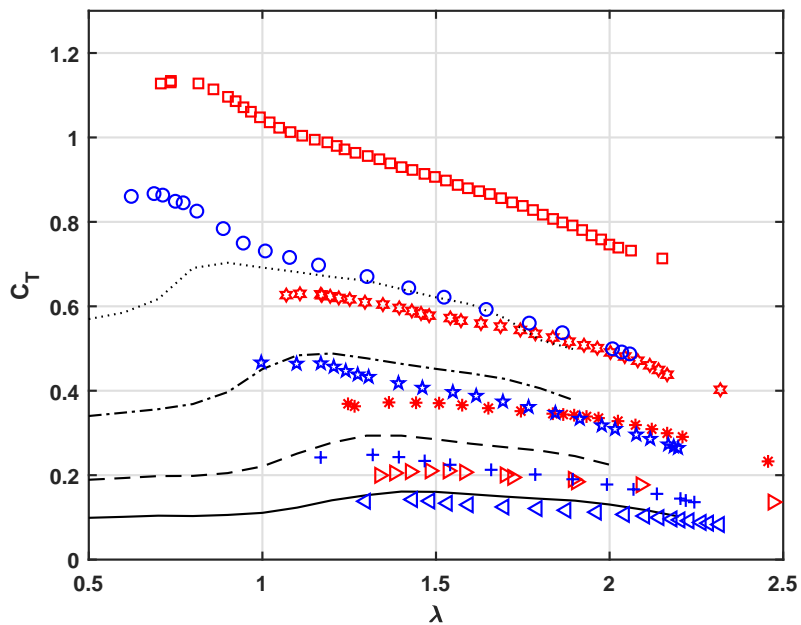
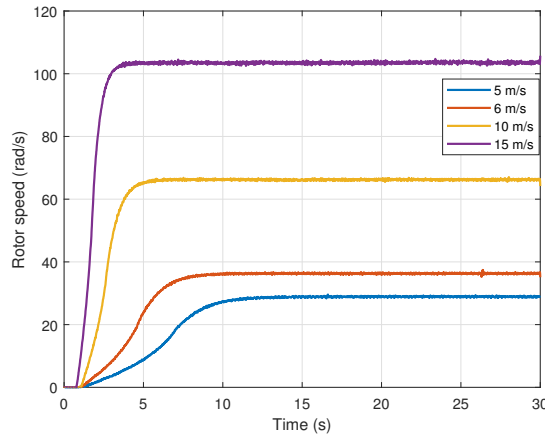


Figure 7.10: BET and measured thrust coefficient with correction applied to the RWT results.

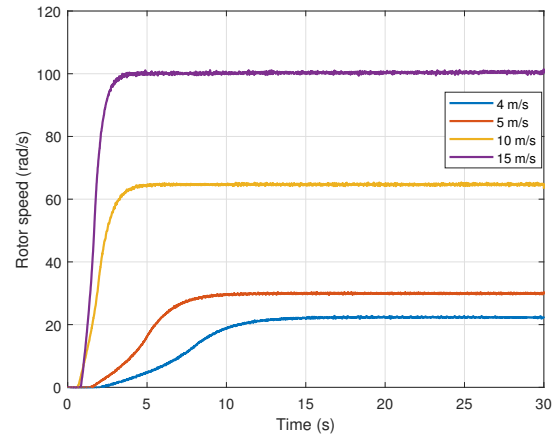
### 7.3.1 Rotor starting performance with different blade numbers

To clearly see the effect of changing  $N$  and wind speeds on the rotor starting performance, the rotors are started from rest in the wind tunnel and then stopped by applying braking force from the MPB70. Subsequently, the rotors are accelerated at constant wind speeds,  $U_\infty$  of 4, 5, 6, 10 and 15 m/s. Figure 7.11 shows the resulting final angular rotor speed,  $\Omega$ , corresponding to the wind speeds. In general, as  $U_\infty$  increases,  $\Omega$  increases, as does the rotor acceleration. However, for a given wind speed,  $\Omega$  decreases as  $N$  increases. For example, at a wind speed of 15 m/s, increasing  $N$  from 3 to 6, 12 and 24 reduces  $\Omega$  by 3.65%, 6.65% and 15.24%, respectively. Also, shown in Figure 7.11 is the improvement in starting performance due to a reduction in the idling period with an increase in  $N$  and wind speeds, particularly for high  $N$ . Realistically, there seems to be no idling because the rotors are designed for low  $\lambda_{opt}$  operation. Figure 7.12 gives a compressed view of Figure 7.11. For example, for  $N = 3$ , increasing the wind speed from 5 to 6, 10 and 15 increases the rotor speed by 26.56%, 127.29% and 256.48%, respectively.

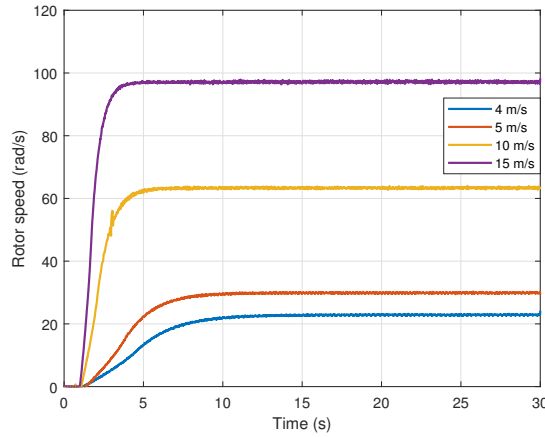
Recall that in this study, the solidity of the windmill is changed by varying  $N$  while keeping the blade chord length and radius constant. This is to allow for easier comparison with the BEM prediction study where the parameters are the same. The results of windmill starting experiments in Chapter 6 are compared with the BEM starting prediction reported in Chapter 5. As shown in Figure 7.13, the BEM calculations for  $N = 3, 6, 12$  and 24 agree with the corresponding experimental measurements. However, there are slight discrepancies. For  $N = 3$ , the region of acceleration shows significant discrepancy until the steady-state region. Probable reasons for this disagreement have been discussed in Chapter 5. With  $N > 3$ , the difference between the predicted and measured time-dependent rotor decreases in the transient phase of the starting sequence. Notice that when  $N = 24$ , excellent agreement is achieved. However, relative to the experiment, the BEM under-predicted its final rotor speed. This is probably due to solidity not accounted for in the simulation, which acts to alter the lift and drag of the airfoil and hence the torque resulting in an increased  $\Omega$  of the



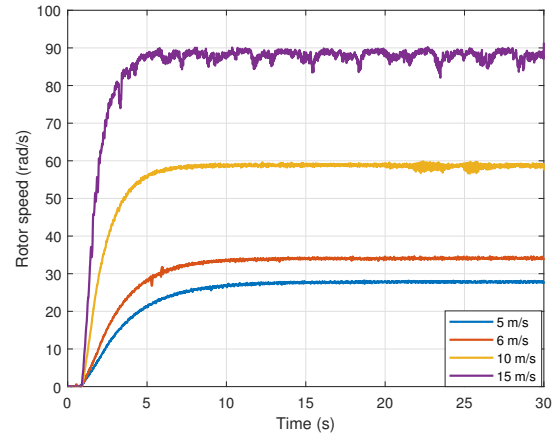
(a)  $N = 3$



(b)  $N = 6$



(c)  $N = 12$



(d)  $N = 24$

Figure 7.11: Model experimental rotor speed at constant wind speeds.

experiment.

## 7.4 Preliminary design considerations for waterpump-ing windmills optimization

This work is originally aimed at examining the significance of solidity and consequently modifying standard BEM code to account for its effect in the accurate performance prediction of high solidity machines. Optimization of rotor blade design for high performance (maximum starting torque) and rapid starting at slower wind speeds require useful design rules for the

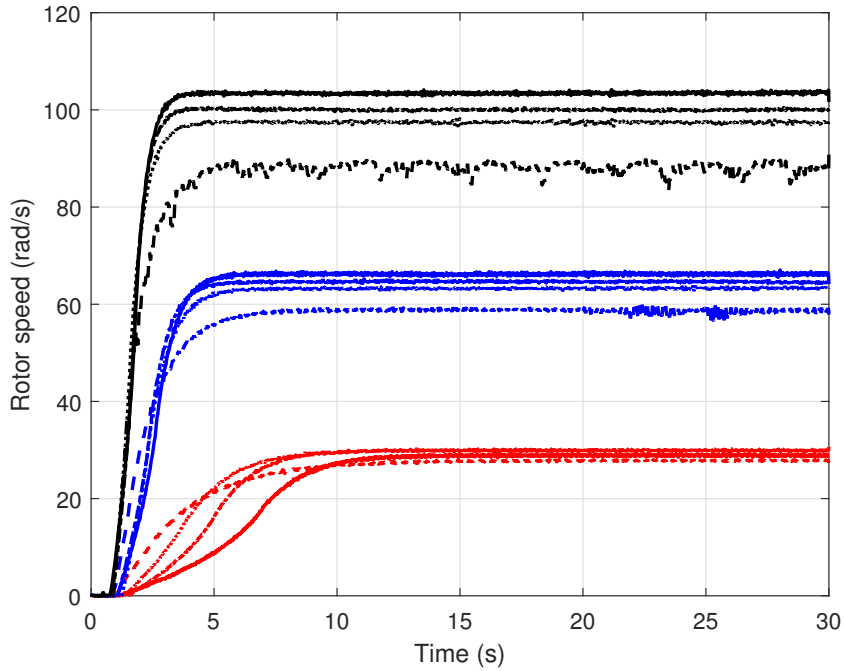


Figure 7.12: Comparison of rotational speeds at different wind speeds. Red lines show  $U_{\infty}=5$  m/s, blue lines show  $U_{\infty}=10$  m/s, black lines show  $U_{\infty}=15$  m/s, the solid line shows  $N = 3$ , the dash-dot line shows  $N = 6$ , the dotted line shows  $N = 12$  and the dashed line shows  $N = 24$ .

increased penetration of SWTs in general and waterpumping windmills in particular. An experimental rotor model of a cambered multi-bladed windmill was experimentally tested to investigate the effect of solidity (blade numbers) on the rotor aerodynamic and starting performance. Airfoil aerodynamic performance data were measured and used in the BEM prediction and then compared with the experimental results. Whereas BEM under-predicted the rotor torque at  $\lambda$  below that, giving maximum power, the predictions for power output were generally accurate for all  $N$ . In the light of this research, the following design considerations are proposed:

- Rotors with high solidity (large  $N$ ) start at wind speeds below 2.5 m/s for this configuration and quickly accelerate due to their higher aerodynamic torque. Thus, designs should consider  $12 \leq N \leq 24$ , equivalent to  $0.45 \leq \sigma \leq 0.9$ .
- The blade design tip speed ratio,  $\lambda_d$ , should be unity or slightly greater because the

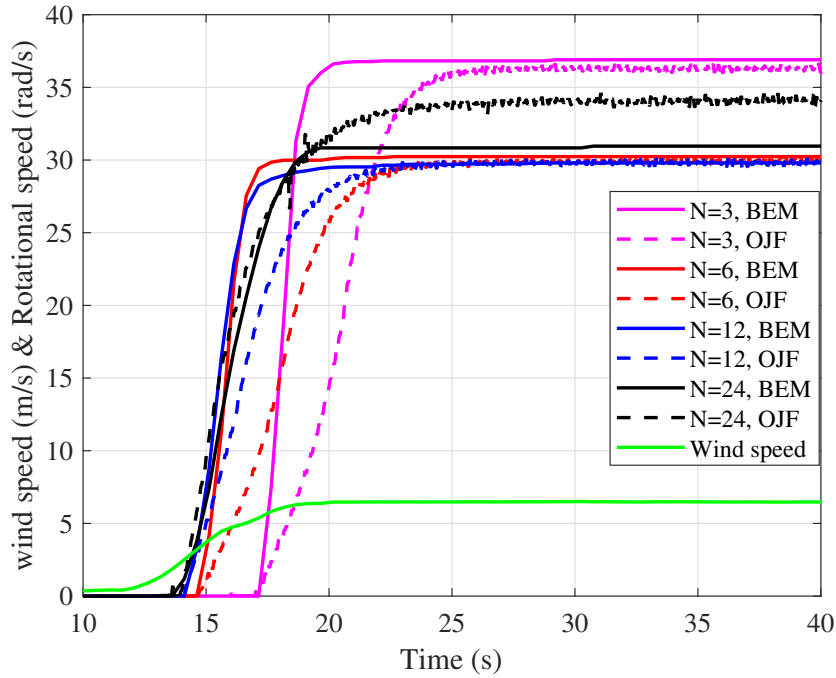


Figure 7.13: Comparison of rotational speeds with rotor experiment at constant wind speed.

optimum performance of the rotor with different  $N$  where obtained between  $1.0 \leq \lambda_d \leq 1.3$ .

- For ease of fabrication, the blade chord should be constant; however, a significant twist variation along the blade span is required for it to operate at or near-optimal value, i.e.,  $\lambda_d$ .
- Moderately thick and large cambered airfoils sections are also good choices for a water-pumping windmill blade in situations where they are the only available geometry in localities in developing countries. However, blade profiles with  $t/c \leq 6\%$  and  $h/c \leq 10\%$  are suggested.
- A blade aspect ratio of at least  $AR \geq 5$  is recommended subject to structural strength.

## 7.5 Summary

This chapter presented the rotor aerodynamic and starting performance results from both the OJF with negligible blockage and the RWT with a much higher blockage. Comparisons of the test data of the present rotor with that of Wegereef show discrepancies that were shown to be due to blockage. However, good agreement was obtained between the OJF and BEM except at the low  $\lambda$  range of the performance curve, possibly due to solidity effects not incorporated in BEM. High estimates of the performance in the RWT were found to be due to blockage. These results emphasize the importance of both blockage and solidity regarding rotor performance with varying  $N$ . Measurements of drag forces experienced by simple geometries indicate that the very high unusual rotor thrust values measured in the RWT were due to the systematic error of the ATI F/T. The experimental starting results are non-monotonic with  $N$ , suggesting a non-linearity response behavior in the MPB. Further, the MPB70 is not independent of speed, contrary to the manufacturers' claim. Finally, useful design guides from the experimental outcome were provided to optimize cambered blades for maximum torque and rapid starting in the future.

# Chapter 8

## Conclusions and Recommendations

Despite the fact that waterpumping windmills have been around for several centuries, the impact of increasing solidity (increasing blade number) is still not well understood due to limited studies, particularly for the commonly used cheap and easy to manufacture circular-arc blades (cambered plates). Understanding the influence of solidity helps to provide design guides for improved aerodynamic performance and better starting of waterpumping windmills at low wind speed locations. The present thesis makes notable contributions to circular-arc airfoils wind tunnel characterization, prediction of the aerodynamic performance and starting behavior, and wind tunnel blockage effect on rotor performance. The main research outcomes and contributions to knowledge and recommendations for future work are summarized in Sections 8.1 and 8.3, respectively.

### 8.1 Conclusions

BEM aerodynamic performance and starting predictions require accurate lift and drag data up to  $90^\circ$  for the HAWT or full incidence range for VAWT at the appropriate  $Re$  range, which is typically scarce in the literature, particularly for the circular arc airfoils with a mix of geometrical features. Therefore, static characterization of circular-arc airfoils (CAA) and NACA0012 for  $30000 \leq Re \leq 100000$  were measured in an open and closed (modified

open) wind tunnel. Steady measurements were made starting at  $\alpha = 0$  and finishing at  $180^\circ$ . Then measurements were made with decreasing  $\alpha$ . For the first time, unsteady lift and drag measurements were made on a sinusoidally pitching CAA. The airfoil geometrical features and wind tunnel configuration was shown to influence their performance, and that contrary to other studies, NACA0012 performance is low  $Re$  sensitive. The “second stall” phenomenon is dependent on  $Re$  and tunnel blockage and was observed for both tunnel test sections on CAA, unlike in NACA0012 studies [65,68] where it is limited to open tunnel test sections only. Open tunnel measurements evinced a large hysteresis loop compared to the closed tunnel occurring around the post-stall region. An order of magnitude change in  $Re$  in the unsteady measurements shows a non-monotonic increase in lift and monotonic rise in drag for reduced frequency,  $k \leq 0.06$ , suggesting that  $Re$  is important. As demonstrated in this work, hysteresis in the steady lift and drag is essential because starting goes from high to low  $\alpha$ . Thus, an adequate understanding of the low  $Re$  behavior of cambered blades can lead to improvements in design and cost reductions, critical factors to the increased use of SWTs for waterpumping application and possibly even for electricity generation.

The performance of the simulated rotor model was predicted using BEM with the traditional Prandtl tip loss,  $F_p$  and a helical vortex-based tip loss factor,  $F_u$  and  $F_w$ . The latter predicted the rotor performance with reasonable accuracy. In addition, it was shown that while  $F_p < 1$ ,  $F_u$  and  $F_w$  exceeds unity due to the inclusion of non-linear momentum terms typically excluded from standard BEM analysis.

A quasi-steady-state model with no induced velocities was developed to predict the starting wind speeds and the runaway rotor speed at no load of the experimental rotor model. At  $N > 3$ , the initial assumption of negligible induction was invalid because of the high values of kinetic energy ratio, KER. The implication is that the rotor absorbed a significant amount of kinetic energy from the wind, so the assumption of no induction was incorrect. Standard BEM that includes the effect of induction was then used. However, reduced frequencies,  $k$  for measuring unsteadiness effects, were within the acceptable range for all  $N$

cases. Unfortunately, the accuracy of the model is subject to the dynamics of the MPB, which is not provided by the manufacturer and could not be experimentally examined due to time constraints.

It was shown that at higher  $\lambda$  and lower  $\alpha$ , solidity effects are small, and BEM predicts  $\lambda_{run}$  with reasonable accuracy. For small  $\lambda$ , the significantly higher measured torque for high  $N$  implies that solidity effects have to be incorporated in BEM for operation below the point of maximum torque; unfortunately, measurements at lower and zero  $\lambda$  could not be obtained because while testing, the rotor stalls before reaching those values of  $\lambda$ . Otherwise, BEM accurately predicted the  $C_{P,max}$ , and the  $\lambda$  at which this occurred, and the  $\lambda_{run}$  for all  $N$ .  $C_{P,max}$  for  $N = 24$  is remarkably close to the ideal  $C_P$  of 0.288 at  $\lambda = 0.5$  obtained by Glauert; this is promising as better performance can be achieved with optimized blade design.

Blockage can be significant on rotor performance; the high blockage RWT computed  $C_P$  is 13.3% of the  $C_P$  measured at the low blockage OFJ. For a given rotor model and tunnel area, increasing solidity increases blockage. Standard blockage corrections were applied and shown to be insufficient to explain the behavior at and near the runaway, where corrections appear not to be required. The blockage factor, however, increases with reducing  $\lambda$ .

Based on the experimental outcome, the design rules for waterpumping windmill aerodynamics and starting performance are summarized as:

- Rotor designers should consider  $12 \leq N \leq 24$ , equivalent to  $0.45 \leq \sigma \leq 0.9$ .
- The design tip speed ratio,  $\lambda_d$ , of the rotor with different  $N$  should be unity or slightly greater.
- For ease of fabrication, it is suggested that the blade chord should be constant, while the blade twist should be varied along the blade span.
- Medium-thick and large cambered airfoil is also a good choice for waterpumping windmills blades, especially in localities where thinner and relatively cambered airfoils are

unavailable.

- Subject to structural strength consideration, the blade aspect ratio should be at least  $AR \geq 5$ .

## 8.2 Significant and original contributions

Low  $Re$  steady and quasi-steady ( $k \leq 0.06$ ) lift and drag data of circular-arc blades with a mix of camber and thickness were provided for  $0^\circ \leq \alpha \leq 90^\circ$  range for starting performance prediction and design process of SWTs. In addition, these data can be employed for other studies and relevant applications at similar  $Re$ s (see Appendix A).

The thrust and power performance of a rotor with identical blades and  $N = 3, 6, 12$ , and 24 have been obtained over a range of  $\lambda$  for the first time. The measurements were made in a large open jet wind tunnel with negligible blockage. Furthermore, the helical vortex theory-based tip loss factor has been employed for the first time to analyze the performance of the windmill rotor with a range of  $N$ . Its superiority to the traditional tip loss factor was demonstrated at low  $\lambda$  and high  $N$  ( $\sigma$ ).

It was also demonstrated that the low  $\lambda$  performance considerably exceeds BEM calculations at high  $N$ . At  $\lambda = 0.5$ , Glauert gives the maximum possible  $C_P$  as 0.288 [99]. The  $N = 24$  rotor gets remarkably close to that limit despite its simple design, suggesting that its performance can be improved significantly with an optimized blade design.

Blockage effect on a water-pumping windmill was accessed in detail in both low (negligible) and high blockage tunnels. This has never been presented by previous research works.

Because windmills are most efficient at very low speed, the starting performance as a function of  $N$  was determined for the first time. Additionally, a blade element prediction of the time dependence of rotor speed generally under-estimated the time required to reach runaway despite the steady BEM analysis under-estimating the blade torque at low tip speed ratios.

### 8.3 Future work

A better understanding of CA-series airfoil flow physics with a mix of geometrical parameters of camber, thickness, and AR should be performed using a pressure distribution method to better understand its low  $Re$  behavior. This technique can be supported by computational methods such as CFD modeling and PIV study. Moreso, solidity effects on the aerodynamic characteristics of circular-arc airfoils over a wide range of low  $Re$  and  $\alpha$  beyond stall should be investigated for a better understanding.

Further work on the effects of solidity on the rotor performance at the low  $\lambda$  range needs to be done. Improvements in the experimental test setup could be achieved using a small generator rather than the MPB to capture test data at this significant part of the performance curve. Multidimensional optimization of the windmill rotor design is required to maximize torque and reduce the starting time.

The starting model should be improved by using a small generator with characterized drivetrain resistance, or the dynamics of the MPB should be further explored. Alternatively, the use of an MPB or generator may be obviated in determining its drivetrain resistance. As demonstrated in the study, the starting experiments were non-monotonic in  $N$ , showing some non-linearity. Therefore, it is suggested that the MPB behavior during the acceleration phase of the starting and the aerodynamic influence of the spars need to be experimentally examined.

On a broader level, the influence of solidity on the aerodynamic and starting performance at load and no-load conditions should be determined and compared. Under load conditions, the reciprocating or positive displacement pump in a waterpumping windmill is subject to varying cyclic torque loads. This factor is responsible for the low overall conversion efficiency of wind turbines coupled to water pumbers. Therefore, further study is suggested to understand the effect of cyclical loads; this will help develop strategies for the optimal coupling of reciprocating piston pumps to wind turbines with blades of simple design. Optimum balance between critical design parameters such as torque, power, and low wind speed that

affect starting should be sought. Consequently, the waterpumping windmill system components should be matched, and the overall system also matched to the operating conditions to ensure operation within its performance envelope.

# Bibliography

- [1] S. Schmitz, *Aerodynamics of Wind Turbines: A Physical Basis for Analysis and Design*. John Wiley & Sons, 2019.
- [2] U. Nations, “The sustainable development goals report 2020,” accessed: 2020-09-30. [Online]. Available: <https://unstats.un.org/sdgs/report/2020/The-Sustainable-Development-Goals-Report-2020.pdf>
- [3] J. Sumanik-Leary, M. Delor, M. Little, M. Bellamy, A. Williams, and S. Williamson, *Engineering in Development: Energy*. Engineers Without Borders UK, 2014.
- [4] M. A. Rosato, *Small Wind Turbines for Electricity and Irrigation: Design and Construction*. CRC Press, 2018.
- [5] H. Ritchie, “Access to energy,” *Our World in Data*, 2019, <https://ourworldindata.org/energy-access>.
- [6] M. Roser, “Human development index (hdi),” *Our World in Data*, 2014, <https://ourworldindata.org/human-development-index>.
- [7] U. UNDP, “Human development indices and indicators: 2018 statistical update,” 2018.
- [8] R. S. Amano, “Review of wind turbine research in 21st century,” *Journal of Energy Resources Technology*, vol. 139, no. 5, p. 050801, 2017.

- [9] “2017 small wind world energy report summary,” Jun 2017. [Online]. Available: <http://small-wind.org/wwea-released-latest-global-small-wind-statistics> [Accessed:28-January-2018]
- [10] Administrator, “Kijito wind power limited,” 2018. [Online]. Available: <http://kijitowindpowerkenya.com/history.html>
- [11] 2010. [Online]. Available: <http://molinosjober.com/productos.htm> [Accessed: 14-January-2018]
- [12] Motherrulez, “Windpumps,” Mar 2017. [Online]. Available: <http://www.aureka.com/other-products/windpumps>
- [13] “The poldaw windpump,” 2016. [Online]. Available: <http://www.tribology.co.uk/poldaw-windpump/> [Accessed:14-January-2018]
- [14] N. Sönnichsen, “Cumulative installed capacity of small wind turbines worldwide from 2010 to 2018 (in megawatts),” accessed: 2020-09-25. [Online]. Available: <https://www.statista.com/statistics/269885/capacity-of-small-wind-turbines-worldwide/>
- [15] L. Soderholm, “Autonomous and grid-connected use of wind energy for structure heating,” in *Energy for Rural and Island Communities*. Elsevier, 1984, pp. 189–196.
- [16] M. Czajkowski, “Feasibility of a unique wind powered home heating system,” in *47th AIAA Aerospace Sciences Meeting including The New Horizons Forum and Aerospace Exposition*, 2008, p. 216.
- [17] G. Petersen, S. Fries, K. Kaiba, and D. Knünz, “A wind-powered water desalination plant for a small island community at the german coast of the north sea—design and working experience,” in *Energy for Rural and Island Communities*. Elsevier, 1984, pp. 173–180.

- [18] J. Cace, R. E. ter Horst, H. K. Syngellakis, and I. Power, “Urban wind turbines,” *Guidlines for small wind turbines in the built environment, Article online www. urbanwind. org*, pp. 1–41, 2007.
- [19] W. U. W. W. A. Programme), “The united nations world water development report 2019: Leaving no one behind,” 2019.
- [20] W. Kamkwamba and B. Mealer, *The boy who harnessed the wind.* Harper Collins, 2010.
- [21] O. Probst, J. Martínez, J. Elizondo, and O. Monroy, “Small wind turbine technology, wind turbines,” *InTech*, 2011.
- [22] K. Fagbenro, M. Mohamed, and D. Wood, “Computational modeling of the aerodynamics of windmill blades at high solidity,” *Energy for Sustainable Development*, vol. 22, pp. 13–20, 2014.
- [23] K. Singh, “Blade element analysis and experimental investigation of high solidity wind turbines,” Master’s thesis, University of Calgary, 2014.
- [24] J. R. Vaz, D. H. Wood, D. Bhattacharjee, and E. F. Lins, “Drivetrain resistance and starting performance of a small wind turbine,” *Renewable Energy*, vol. 117, pp. 509–519, 2018.
- [25] E. Wegereef, “Scale model of the itdg 6meter rotor wind tunnel tests for different blade setting angles,” in *Report of Twente University of Technology, Netherlands, windmill group. Report WM 076*, 1984.
- [26] A. Bruining, “Aerodynamic characteristics of a curved plate airfoil section at reynolds numbers 60000 and 100000 and angles of attack from-10 to+ 90 degrees,” Delft University of Techology, Tech. Rep., 1979.

- [27] J. Kentfield, *The Fundamentals of Wind-Driven Water Pumps*. Gordon and Breach Science Publishers. Amsterdam, Netherlands, 1996.
- [28] P. Action, 2008. [Online]. Available: <https://answers.practicalaction.org/our-resources/item/energy-from-the-wind>
- [29] N. C. E. Ltd, “The poldaw windpump,” accessed:14-January-2018. [Online]. Available: Available from:<http://www.tribology.co.uk/>
- [30] K. W. Van Treuren, “Small-scale wind turbine testing in wind tunnels under low reynolds number conditions,” *Journal of Energy Resources Technology*, vol. 137, no. 5, 2015.
- [31] L. Du, “Numerical and experimental investigations of darrieus wind turbine start-up and operation,” Ph.D. dissertation, Durham University, 2016.
- [32] A. Wright and D. Wood, “The starting and low wind speed behaviour of a small horizontal axis wind turbine,” *Journal of Wind Engineering and Industrial Aerodynamics*, vol. 92, no. 14-15, pp. 1265–1279, 2004.
- [33] D. H. Wood, *Small Wind Turbines: analysis, design and application*. Springer, 2011.
- [34] D. Wood, “Small wind turbines for remote power and distributed generation,” *Wind Engineering*, vol. 34, no. 3, pp. 241–254, 2010.
- [35] P. Ebert and D. Wood, “Observations of the starting behaviour of a small horizontal-axis wind turbine,” *Renewable energy*, vol. 12, no. 3, pp. 245–257, 1997.
- [36] N. Sarkis and A. E. Pinilla, “Experimental study on a model of a commercial wind-pumping rotor,” *Wind Engineering*, vol. 30, no. 6, pp. 511–520, 2006.
- [37] S. Worasinchai, G. L. Ingram, and R. G. Dominy, “Effects of wind turbine starting capability on energy yield,” *Journal of Engineering for Gas Turbines and Power*, vol. 134, no. 4, p. 042603, 2012.

- [38] D. A. Spera *et al.*, *Wind turbine technology: fundamental concepts of wind turbine engineering*. ASME press New York, 1994, vol. 3.
- [39] T. Wakui, Y. Tanzawa, T. Hashizume, and T. Nagao, “Hybrid configuration of darrieus and savonius rotors for stand-alone wind turbine-generator systems,” *Electrical Engineering in Japan*, vol. 150, no. 4, pp. 13–22, 2005.
- [40] E. Hau, *Wind turbines: fundamentals, technologies, application, economics*. Springer Science & Business Media, 2013.
- [41] “International electrotechnical commission 61400-2 wind turbines – part 2: Small wind turbines,” Dec 2013.
- [42] P. Fraenkel, F. Crick, and P. Cowley, “Wind power for pumping: The development of the itp windpump,” *Renewable energy*, vol. 16, no. 1-4, pp. 916–921, 1999.
- [43] N. Argaw, R. Foster, and A. Ellis, “Renewable energy for water pumping applications in rural villages; period of performance: April 1, 2001–september 1, 2001,” National Renewable Energy Laboratory (NREL), Golden, CO., Tech. Rep., 2003.
- [44] C. Gopal, M. Mohanraj, P. Chandramohan, and P. Chandrasekar, “Renewable energy source water pumping systems—a literature review,” *Renewable and Sustainable Energy Reviews*, vol. 25, pp. 351–370, 2013.
- [45] J. Dixon, “Improving the mechanical load matching of wind energy converters,” *1st BWEA Workshop*, pp. 181–189, 1979.
- [46] A. E. Pinilla, J. Burton, and P. Dunn, “Wind energy to water pumped: Conversion efficiency limits using single-acting lift pumps,” in *Proc. Conf. BWEA, Cambridge University Press*, 1984, pp. 334–345.
- [47] M. Selig, J. Donovan, and D. Fraser, *Airfoils at Low Speeds*. H.A. Stokely, 1989.

- [48] M. S. Selig, *Summary of low speed airfoil data*. SoarTech publications, 1995.
- [49] M. S. Selig and B. D. McGranahan, “Wind tunnel aerodynamic tests of six airfoils for use on small wind turbines,” *J. Sol. Energy Eng.*, vol. 126, no. 4, pp. 986–1001, 2004.
- [50] P. Migliore and S. Oerlemans, “Wind tunnel aeroacoustic tests of six airfoils for use on small wind turbines,” *J. Sol. Energy Eng.*, vol. 126, no. 4, pp. 974–985, 2004.
- [51] A. Kragten, “The 7.14%, 10% and 12.5% cambered plate as airfoil for windmill rotor blades. aerodynamic characteristics, geometry, moment of inertia i and moment of resistance w.” 2008.
- [52] A. Kummer, J. Dimeo, M. Hebel, and K. Visser, “On the use of cambered plate airfoils for small wind turbines,” in *Journal of Physics: Conference Series*, vol. 1618, no. 4. IOP Publishing, 2020, p. 042001.
- [53] M. Pandey, K. Pandey, and T. Ojha, “Aerodynamic characteristics of cambered steel plates in relation to their use in wind energy conversion systems,” *Wind Engineering*, pp. 90–104, 1988.
- [54] M. Okamoto, K. Yasuda, and A. Azuma, “Aerodynamic characteristics of the wings and body of a dragonfly,” *Journal of Experimental Biology*, vol. 199, no. 2, pp. 281–294, 1996.
- [55] M. Okamoto and A. Azuma, “Experimental study on aerodynamic characteristics of unsteady wings at low reynolds number,” *AIAA journal*, vol. 43, no. 12, pp. 2526–2536, 2005.
- [56] A. Tezuka, Y. Sunada, and K. Rinoie, “Surface pressure distributions on 4% circular arc airfoil at low reynolds number,” *Journal of Aircraft*, vol. 45, no. 6, pp. 2164–2167, 2008.

- [57] M. Okamoto and K. Ebina, “Effectiveness of large-camber circular arc airfoil at very low reynolds numbers,” *Transactions of the Japan Society for Aeronautical and Space Sciences*, vol. 59, no. 5, pp. 295–304, 2016.
- [58] R. G. Flay, A. Piard, and P. Bot, “Aerodynamics of a highly cambered circular arc aerofoil: experimental investigations.”
- [59] R. Wallis, “Wind tunnel tests on a series of circular arc plate aerofoils,” Aeronautical Research Labs Melbourne (Australia), Tech. Rep., 1946.
- [60] T. Ikui, M. Inoue, and K. Kaneko, “Two-dimensional cascade performance of circular-arc blades(circular arc blades two dimensional cascade performance test data for various cambers comparison with potential theory data),” in *Tokyo Joint International Gas Turbine Conference and Products Show, Tokyo, Japan*, 1971, pp. 57–64.
- [61] T. J. Mueller and J. D. DeLaurier, “Aerodynamics of small vehicles,” *Annual review of fluid mechanics*, vol. 35, no. 1, pp. 89–111, 2003.
- [62] S. Sunada, T. Yasuda, K. Yasuda, and K. Kawachi, “Comparison of wing characteristics at an ultralow reynolds number,” *Journal of aircraft*, vol. 39, no. 2, pp. 331–338, 2002.
- [63] T. J. Mueller, “Aerodynamic measurements at low reynolds numbers for fixed wing micro-air vehicles,” Notre Dame University in Dept of Aerospace and Mechanical Engineering, Tech. Rep., 2000.
- [64] R. E. Sheldahl and P. C. Klimas, “Aerodynamic characteristics of seven symmetrical airfoil sections through 180-degree angle of attack for use in aerodynamic analysis of vertical axis wind turbines,” Sandia National Labs., Albuquerque, NM (USA), Tech. Rep., 1981.

- [65] J. Rainbird, J. Peiró, and J. Graham, “Blockage-tolerant wind tunnel measurements for a naca 0012 at high angles of attack,” *Journal of Wind Engineering and Industrial Aerodynamics*, vol. 145, pp. 209–218, 2015.
- [66] D. Holst, B. Church, F. Wegner, G. Pechlivanoglou, C. Nayeri, and C. Paschereit, “Experimental analysis of a naca 0021 airfoil under dynamic angle of attack variation and low reynolds numbers,” in *Turbo Expo: Power for Land, Sea, and Air*, vol. 51180. American Society of Mechanical Engineers, 2018, p. V009T48A010.
- [67] S. Worasinchai, G. Ingram, and R. Dominy, “A low-reynolds-number, high-angle-of-attack investigation of wind turbine aerofoils,” *Proceedings of the Institution of Mechanical Engineers, Part A: Journal of Power and Energy*, vol. 225, no. 6, pp. 748–763, 2011.
- [68] L. Du, A. Berson, and R. G. Dominy, “Aerofoil behaviour at high angles of attack and at reynolds numbers appropriate for small wind turbines,” *Proceedings of the Institution of Mechanical Engineers, Part C: Journal of Mechanical Engineering Science*, vol. 229, no. 11, pp. 2007–2022, 2015.
- [69] G. Bragg and W. Schmidt, “Performance matching and optimization of wind powered water pumping systems,” *Energy Conversion*, vol. 19, no. 1, pp. 33–39, 1979.
- [70] G. Nathan, “A simplified design method and wind-tunnel study of horizontal-axis windmills,” *Journal of Wind Engineering and Industrial Aerodynamics*, vol. 6, no. 3-4, pp. 189–205, 1980.
- [71] H. Cleijne, P. Smulders, F. Verheij, and H. Oldenkamp, “Pump research by cwd: the influence of starting torque of single acting piston pumps on water pumping windmills,” in *European Wind Energy Association, Conference and Exhibition*, vol. 7, no. 9.10, 1986.

- [72] J. F. Manwell *et al.*, *Understanding wind energy for water pumping*. VITA, 1988, vol. 62.
- [73] R. Rijs and P. Smulders, “Blade element theory for performance analysis of slow running wind turbines,” *Wind Engineering*, pp. 62–79, 1990.
- [74] R. Rijs, P. Jacobs, and P. Smulders, “Parameter study of the performance of slow running rotors,” *Journal of Wind Engineering and Industrial Aerodynamics*, vol. 39, no. 1-3, pp. 95–103, 1992.
- [75] E. Lysen, “Introduction to wind energy cwd 82-1,” *Amerfoorst, The Netherlands*, 1983.
- [76] V. Morcos, “Aerodynamic performance analysis of horizontal axis wind turbines,” *Renewable energy*, vol. 4, no. 5, pp. 505–518, 1994.
- [77] H. Tokuyama, I. Ushiyama, and K. Seki, “Experimental determination of optimum design configuration for micro wind turbines at low wind speeds,” *Wind Engineering*, vol. 26, no. 1, pp. 39–49, 2002.
- [78] D. Wood, “Application of extended vortex theory for blade element analysis of horizontal-axis wind turbines,” *Renewable energy*, vol. 121, pp. 188–194, 2018.
- [79] E. Branlard and M. Gaunaa, “Development of new tip-loss corrections based on vortex theory and vortex methods,” in *The science of Making Torque from Wind 2012: 4th scientific conference*, 2012.
- [80] D. Wood, V. Okulov, and D. Bhattacharjee, “Direct calculation of wind turbine tip loss,” *Renewable Energy*, vol. 95, pp. 269–276, 2016.
- [81] S. Schmitz and D. C. Maniaci, “Methodology to determine a tip-loss factor for highly loaded wind turbines,” *AIAA Journal*, vol. 55, no. 2, pp. 341–351, 2017.

- [82] Q. I. Md and S. I. AKM, “The aerodynamic performance of a horizontal-axis wind turbine calculated by strip theory and cascade theory,” *JSME International Journal Series B Fluids and Thermal Engineering*, vol. 37, no. 4, pp. 871–877, 1994.
- [83] D. Wood, “A cascade model of blade element interaction for wind turbines with unequal blades,” *International Journal of Sustainable Energy*, vol. 35, no. 5, pp. 502–512, 2016.
- [84] S. Jafari, K. C. Kwok, F. Safaei, and B. Kosasih, “Aerodynamic analysis of a linear cascade wind turbine,” *Wind Energy*, vol. 21, no. 11, pp. 1141–1154, 2018.
- [85] H. Yan, “Computational modeling of cascade effect on blade elements with an airfoil profile,” Master’s thesis, University of Calgary, 2016.
- [86] M. O. Hansen, *Aerodynamics of wind turbines*. Routledge, 2015.
- [87] T. Chen and L. Liou, “Blockage corrections in wind tunnel tests of small horizontal-axis wind turbines,” *Experimental Thermal and Fluid Science*, vol. 35, no. 3, pp. 565–569, 2011.
- [88] J. Ryi, W. Rhee, U. C. Hwang, and J.-S. Choi, “Blockage effect correction for a scaled wind turbine rotor by using wind tunnel test data,” *Renewable Energy*, vol. 79, pp. 227–235, 2015.
- [89] H. Jeong, S. Lee, and S.-D. Kwon, “Blockage corrections for wind tunnel tests conducted on a darrieus wind turbine,” *Journal of Wind Engineering and Industrial Aerodynamics*, vol. 179, pp. 229–239, 2018.
- [90] A. Eltayesh, M. B. Hanna, F. Castellani, A. Huzayyin, H. M. El-Batsh, M. Burlando, and M. Becchetti, “Effect of wind tunnel blockage on the performance of a horizontal axis wind turbine with different blade number,” *Energies*, vol. 12, no. 10, p. 1988, 2019.

- [91] R. Lanzafame and M. Messina, “Optimal wind turbine design to maximize energy production,” *Proceedings of the Institution of Mechanical Engineers, Part A: Journal of Power and Energy*, vol. 223, no. 2, pp. 93–101, 2009.
- [92] R. Lanzafame, S. Mauro, and M. Messina, “Hawt design and performance evaluation: improving the bem theory mathematical models,” *Energy Procedia*, vol. 82, pp. 172–179, 2015.
- [93] A. L. A. Mesquita and A. S. Alves, “An improved approach for performance prediction of hawt using the strip theory,” *Wind Engineering*, vol. 24, no. 6, pp. 417–430, 2000.
- [94] D. Yu, H. Kwon, and O. J. Kwon, “Performance enhancement of hawt rotor blades by aerodynamic shape optimization,” in *50th AIAA Aerospace Sciences Meeting including the New Horizons Forum and Aerospace Exposition*, 2012, p. 1292.
- [95] C. Mayer, M. Bechly, M. Hampsey, and D. Wood, “The starting behaviour of a small horizontal-axis wind turbine,” *Renewable Energy*, vol. 22, no. 1-3, pp. 411–417, 2001.
- [96] P. Clausen and D. Wood, “Recent advances in small wind turbine technology,” *Wind Engineering*, vol. 24, no. 3, pp. 189–201, 2000.
- [97] C. Wichser and K. Klink, “Low wind speed turbines and wind power potential in minnesota, usa,” *Renewable Energy*, vol. 33, no. 8, pp. 1749–1758, 2008.
- [98] S. Khan, K. Shah, H. Khan, S. Ali, N. Ahmad, M. Abid, H. Ali, M. Sher *et al.*, “Observation of the starting and low speed behavior of small horizontal axis wind turbine,” *Journal of Wind Energy*, vol. 2014, 2014.
- [99] H. Glauert, “Airplane propellers,” in *Aerodynamic theory*. Springer, 1935, pp. 169–360.
- [100] T. O. Perry, *Experiments with Windmills*. US Government Printing Office, 1899.

- [101] M. Sanuki, “Experiments on the start and stop of windmill-and cup-anemometers with particular reference to their over-estimation factors,” *Papers in Meteorology and Geophysics*, vol. 3, no. 1, pp. 41–53, 1952.
- [102] G. M. Farias, M. A. Galhardo, J. R. Vaz, and J. T. Pinho, “A steady-state based model applied to small wind turbines,” *Journal of the Brazilian Society of Mechanical Sciences and Engineering*, vol. 41, no. 5, p. 209, 2019.
- [103] J. L. Moreira, A. A. Mesquita, L. Araujo, M. B. Galhardo, J. P. Vaz, and J. Pinho, “Experimental investigation of drivetrain resistance applied to small wind turbines,” *Renewable Energy*, 2020.
- [104] T. Aso, K. Seki, and I. Ushiyama, “Study on the bearing resistance in a wind turbine generator system,” *Wind Engineering*, vol. 39, no. 1, pp. 113–128, 2015.
- [105] T. Aso, T. Aida, and K. Seki, “Bearing resistance of wind turbine generator system,” *Electrical Engineering in Japan*, vol. 194, no. 2, pp. 64–73, 2016.
- [106] J. Winslow, H. Otsuka, B. Govindarajan, and I. Chopra, “Basic understanding of airfoil characteristics at low reynolds numbers (10<sup>4</sup>–10<sup>5</sup>),” *Journal of Aircraft*, vol. 55, no. 3, pp. 1050–1061, 2017.
- [107] P. Giguere and M. S. Selig, “Low reynolds number airfoils for small horizontal axis wind turbines,” *Wind Engineering*, pp. 367–380, 1997.
- [108] R. K. Singh, M. R. Ahmed, M. A. Zullah, and Y.-H. Lee, “Design of a low reynolds number airfoil for small horizontal axis wind turbines,” *Renewable energy*, vol. 42, pp. 66–76, 2012.
- [109] H. Shah, S. Mathew, and C. M. Lim, “A novel low reynolds number airfoil design for small horizontal axis wind turbines,” *Wind Engineering*, vol. 38, no. 4, pp. 377–391, 2014.

- [110] R. K. Singh and M. R. Ahmed, “Blade design and performance testing of a small wind turbine rotor for low wind speed applications,” *Renewable Energy*, vol. 50, pp. 812–819, 2013.
- [111] J. L. Tangler and D. M. Somers, “NREL airfoil families for hawts,” National Renewable Energy Lab., Golden, CO (United States), Tech. Rep., 1995.
- [112] P. Giguére and M. Selig, “New airfoils for small horizontal axis wind turbines,” *Journal of Solar Energy Engineering, Transactions of the ASME*, vol. 120, no. 2, pp. 108–114, 1998.
- [113] E. Y. Osei, R. Opoku, A. K. Sunnu, and M. S. Adaramola, “Development of high performance airfoils for application in small wind turbine power generation,” *Journal of Energy*, vol. 2020, 2020.
- [114] S. N. Leloudas, A. I. Eskantar, G. N. Lygidakis, and I. K. Nikолос, “Low reynolds airfoil family for small horizontal axis wind turbines based on rg15 airfoil,” *SN Applied Sciences*, vol. 2, no. 3, p. 371, 2020.
- [115] D. Wood, “Dual purpose design of small wind turbine blades,” *Wind Engineering*, vol. 28, no. 5, pp. 511–527, 2004.
- [116] L. Briggs and H. Dryden, *Aerodynamic Characteristics Circular-arc Airfoils at High Speeds*. US Government Printing Office, 1930.
- [117] R. Narasimha and S. Prasad, “Leading edge shape for flat plate boundary layer studies,” *Experiments in Fluids*, vol. 17, no. 5, pp. 358–360, 1994.
- [118] K. O. Granlund, M. V. Ol, and L. P. Bernal, “Unsteady pitching flat plates,” *Journal of Fluid Mechanics*, vol. 733, 2013.
- [119] R. J. Moffat, “Describing the uncertainties in experimental results,” *Experimental thermal and fluid science*, vol. 1, no. 1, pp. 3–17, 1988.

- [120] H. C. Garner, E. Rogers, W. Acum, and E. Maskell, “Subsonic wind tunnel wall corrections,” Advisory Group for Aerospace Research And Development, Neuilly-Sur-Seine (France), Tech. Rep., 1966.
- [121] J. B. Barlow, W. H. Rae, and A. Pope, “Low-speed wind tunnel testing,” 1999.
- [122] S.-H. Kang, E. S. Shin, K.-W. Ryu, and J.-s. Lee, “Separation blockage-correction method for the airfoil of a wind turbine blade,” *Journal of Mechanical Science and Technology*, vol. 27, no. 5, pp. 1321–1327, 2013.
- [123] P. Fuglsang, I. Antoniou, N. N. Sørensen, and H. A. Madsen, *Validation of a wind tunnel testing facility for blade surface pressure measurements*, 1998.
- [124] E. Maskell, “A theory of the blockage effects on bluff bodies and stalled wings in a closed wind tunnel,” Aeronautical Research Council London (United Kingdom), Tech. Rep., 1963.
- [125] T. Brooks, M. Marcolini, and D. Pope, “Airfoil trailing edge flow measurements and comparison with theory, incorporating open wind tunnel corrections,” in *9th Aeroacoustics Conference*, 1984, p. 2266.
- [126] B. Ewald, “Wind tunnel wall corrections (la correction des effets de paroi en soufflerie),” Advisory Group for Aerospace Research And Development, Neuilly-Sur-Seine (France), Tech. Rep., 1998.
- [127] B. K. Kirke, “Evaluation of self-starting vertical axis wind turbines for stand-alone applications,” Ph.D. dissertation, Griffith University Australia, 1998.
- [128] W. McCroskey, “A critical assessment of wind tunnel results for the naca 0012 airfoil,” NASA Ames Research Center Moffett Field, CA, United States, Tech. Rep., 1987.
- [129] A. Pelletier and T. J. Mueller, “Effect of endplates on two-dimensional airfoil testing at low reynolds number,” *Journal of aircraft*, vol. 38, no. 6, pp. 1056–1059, 2001.

- [130] C. C. Critzos, H. H. Heyson, and R. W. Boswinkle Jr, “Aerodynamic characteristics of naca 0012 airfoil section at angles of attack from 0 deg to 180 deg,” National Aeronautics and Space Administration, Washington DC, Tech. Rep., 1955.
- [131] S. F. Hoerner, “Fluid dynamic drag, published by the author,” *Midland Park, NJ*, pp. 16–35, 1965.
- [132] T. J. Mueller, “The influence of laminar separation and transition on low reynolds number airfoil hysteresis,” *Journal of Aircraft*, vol. 22, no. 9, pp. 763–770, 1985.
- [133] J. G. Leishman, *The Helicopter*. College Park, Maryland: College Park Press, 2007.
- [134] M. Sessarego, K. Dixon, D. Rival, and D. Wood, “A hybrid multi-objective evolutionary algorithm for wind-turbine blade optimization,” *Engineering Optimization*, vol. 47, no. 8, pp. 1043–1062, 2015.
- [135] R. E. Wilson, P. B. Lissaman, and S. N. Walker, *Aerodynamic performance of wind turbines*. Oregon State University Corvallis, Oregon, 1976.
- [136] T. Burton, D. Sharpe, N. Jenkins, and E. Bossanyi, *Wind energy handbook*. Wiley Online Library, 2001, vol. 2.
- [137] W. Z. Shen, R. Mikkelsen, J. N. Sørensen, and C. Bak, “Tip loss corrections for wind turbine computations,” *Wind Energy: An International Journal for Progress and Applications in Wind Power Conversion Technology*, vol. 8, no. 4, pp. 457–475, 2005.
- [138] M. Clifton-Smith, “Wind turbine blade optimisation with tip loss corrections,” *Wind engineering*, vol. 33, no. 5, pp. 477–496, 2009.
- [139] J. Chapman, I. Masters, M. Tognetti, and J. Orme, “The buhl correction factor applied to high induction conditions for tidal stream turbines,” *Renewable energy*, vol. 60, pp. 472–480, 2013.

- [140] D. H. Wood, “Helical vortices and wind turbine aerodynamics,” *International Journal of Mathematics for Industry*, p. 2050002, 2020.
- [141] M. Anderson, D. Milborrow, and N. Ross, *Performance and wake measurements on a 3 m diameter horizontal axis wind turbine: comparison of theory, wind tunnel and field test data*. Department of Energy Energy Technology Support Unit, 1982.
- [142] D. Wood and V. Okulov, “Nonlinear blade element-momentum analysis of betz-goldstein rotors,” *Renewable Energy*, vol. 107, pp. 542–549, 2017.
- [143] S. Worasinchai, “Small wind turbine starting behaviour,” Ph.D. dissertation, Durham University, 2012.
- [144] V. Hong, “Analysis of an actuator disc under unsteady loading: Validation of engineering models using experimental and numerical methods,” Master’s thesis, TU Delft, 2015.
- [145] N. Hosman, “Performance analysis and improvement of a small locally produced wind turbine for developing countries,” Master’s thesis, TU Delft, 2012.
- [146] A. Sayers and D. Ball, “Blockage corrections for rectangular flat plates mounted in an open jet wind tunnel,” *Proceedings of the Institution of Mechanical Engineers, Part C: Journal of Mechanical Engineering Science*, vol. 197, no. 4, pp. 259–263, 1983.
- [147] “Resistance of a fifteen-centimeter disk,” in *Technical note:United States. National Advisory Committee for Aeronautics, 252.*, 1926.
- [148] M. Knight, “Wind tunnel standardization disk drag,” in *Report/Patent Number NACA-TN-253*, 1936.
- [149] S. Mertens, “Wind energy in the built environment: concentrator effects of buildings,” Ph.D. dissertation, TU Delft, 2006.

- [150] M. M. Duquette and K. D. Visser, “Numerical implications of solidity and blade number on rotor performance of horizontal-axis wind turbines,” *J. Sol. Energy Eng.*, vol. 125, no. 4, pp. 425–432, 2003.
- [151] G. B. Schubauer and H. L. Dryden, *The effect of turbulence on the drag of flat plates*. US Government Printing Office, 1935.
- [152] J. M. Shoemaker, “Power and thrust measurements of marine current turbines under various hydrodynamic flow conditions in a cavitation tunnel and a towing tank,” *Renewable energy*, vol. 32, no. 3, pp. 407–426, 2007.
- [153] A. Palmgren, “Ball and roller bearing engineering,” *Philadelphia: SKF Industries Inc., 1959*, 1959.
- [154] H. Olsson, K. J. Åström, C. C. De Wit, M. Gäfvert, and P. Lischinsky, “Friction models and friction compensation,” *Eur. J. Control*, vol. 4, no. 3, pp. 176–195, 1998.
- [155] S. Andersson, A. Söderberg, and S. Björklund, “Friction models for sliding dry, boundary and mixed lubricated contacts,” *Tribology international*, vol. 40, no. 4, pp. 580–587, 2007.

## Appendix A

Lift and drag coefficients of  
NACA0012 and Circular-Arc airfoils  
(CA) series

NACA0012											
Re = 150,000											
Open tunnel						Closed tunnel					
Increasing $\alpha$			Decreasing $\alpha$			Increasing $\alpha$			Decreasing $\alpha$		
$\alpha$	$C_l$	$C_d$	$\alpha$	$C_l$	$C_d$	$\alpha$	$C_l$	$C_d$	$\alpha$	$C_l$	$C_d$
0.4935	-0.1611	0.0142	0.5305	-0.1471	0.0178	-0.0002	-0.2580	-0.0017	0.2498	-0.2396	-0.0018
3.6473	0.3887	0.0227	3.7500	0.4004	0.0230	4.9378	0.3286	0.0179	5.2503	0.3694	0.0187
7.6013	0.7038	0.0388	7.6895	0.7209	0.0391	9.9380	0.6524	0.0446	10.2505	0.6882	0.0496
12.9100	0.6014	0.1641	13.1358	0.5967	0.1735	14.9379	0.5147	0.1524	15.1879	0.5316	0.1593
17.7864	0.6392	0.2463	18.0344	0.6326	0.2498	19.9379	0.5421	0.2068	20.1880	0.5633	0.2152
22.6279	0.6914	0.3345	22.8302	0.6960	0.3431	24.9380	0.5987	0.2762	25.1880	0.6260	0.2908
27.4107	0.7607	0.4442	27.6433	0.7603	0.4458	29.9381	0.6906	0.3697	30.1881	0.6771	0.3696
32.1424	0.8495	0.5819	32.3547	0.8569	0.5878	34.9382	0.7400	0.4712	35.1882	0.7733	0.4955
37.0023	0.9174	0.7355	37.1490	0.9337	0.7404	39.9382	0.8091	0.6085	40.2508	0.8277	0.6274
41.9042	0.9523	0.8941	43.0840	0.6320	0.6269	44.9383	0.8093	0.7107	45.2508	0.8057	0.7180
47.0258	0.9122	1.0280	48.3048	0.5667	0.6599	49.9383	0.7777	0.8084	50.2507	0.7699	0.8046
52.1216	0.8857	1.1585	53.5054	0.5266	0.7239	55.0007	0.7306	0.8975	55.2507	0.7125	0.8771
57.3014	0.8397	1.3034	58.6337	0.4919	0.8036	60.0007	0.6977	0.9704	60.2507	0.6592	0.9644
62.8243	0.6790	1.2439	63.7415	0.4623	0.8871	65.0006	0.5944	1.0289	65.2506	0.5773	1.0134
68.6647	0.4221	0.9725	68.9157	0.4132	0.9605	70.0005	0.5019	1.0745	70.2505	0.4901	1.0736
73.8990	0.3548	1.0292	74.1391	0.3491	1.0233	75.0004	0.4117	1.1096	75.2504	0.4091	1.1297
79.1587	0.2797	1.0814	79.3927	0.2734	1.0672	80.0003	0.3113	1.1560	80.2503	0.3023	1.1464
84.4364	0.1991	1.1229	84.5886	0.1981	1.1172	84.9377	0.2058	1.1743	85.2502	0.1996	1.1767
89.6795	0.1092	1.1371	89.8927	0.1084	1.1310	89.9376	0.1029	1.1950	90.2501	0.0976	1.1822
94.9886	0.0167	1.1376	95.2046	0.0153	1.1423	94.9375	0.0066	1.1910	95.1875	0.0074	1.2013
100.3054	-0.0778	1.1382	100.5265	-0.0791	1.1242	99.9374	-0.0947	1.2051	100.1874	-0.0910	1.2062
105.5993	-0.1648	1.1051	105.8225	-0.1620	1.1216	104.9373	-0.1765	1.1979	105.1873	-0.1803	1.1632
110.8820	-0.2496	1.0727	111.6830	-0.3956	1.6430	109.8747	-0.2488	1.1685	110.1872	-0.2597	1.1583
116.0741	-0.3259	1.0149	117.0568	-0.5037	1.6099	114.8746	-0.3316	1.1335	115.1871	-0.3446	1.1608
121.3898	-0.4011	0.9492	122.4023	-0.6066	1.5170	119.8745	-0.4266	1.1325	120.1870	-0.4232	1.1248
126.6062	-0.4685	0.8920	127.8577	-0.7437	1.4606	124.8744	-0.5285	1.0883	125.1870	-0.4904	1.0040
131.6534	-0.4826	0.8058	133.1481	-0.8356	1.3434	129.9369	-0.6013	0.9849	130.1220	-0.6223	0.9865
137.4314	-0.7097	1.0412	138.3335	-0.8898	1.2349	134.9368	-0.6859	0.8881	135.0618	-0.6835	0.8834
142.9750	-0.8725	1.0235	143.5390	-0.9374	1.0676	139.9368	-0.7588	0.7823	140.0618	-0.7418	0.7744
147.8482	-0.8217	0.8263	148.4300	-0.9133	0.8800	144.9368	-0.7895	0.6623	145.1243	-0.7852	0.6412
152.6294	-0.7589	0.6422	153.0405	-0.8101	0.6976	149.9993	-0.7821	0.5271	150.1243	-0.7547	0.5065
157.1521	-0.6274	0.4847	157.6599	-0.7085	0.5123	154.9369	-0.7017	0.3902	155.1244	-0.6540	0.3677
161.9254	-0.5537	0.3792	162.5218	-0.6846	0.3877	159.9995	-0.5917	0.2932	160.1245	-0.6492	0.2337
167.1807	-0.6289	0.3043	167.6710	-0.7310	0.2868	164.9995	-0.5901	0.2187	165.1244	-0.6835	0.1274
172.5950	-0.7483	0.2301	172.9066	-0.7939	0.1752	169.9369	-0.6854	0.1762	170.1244	-0.7427	0.1147
176.7847	-0.5302	0.1548	177.1957	-0.6143	0.0786	174.9370	-0.6432	0.0971	175.0620	-0.6969	-0.0261
180.3399	-0.1325	0.0658	180.4040	-0.113	0.0467	179.9372	-0.3476	0.0053	179.9998	-0.2867	0.0158

NACA0012											
Re = 86,000											
Open tunnel						Closed tunnel					
Increasing $\alpha$			Decreasing $\alpha$			Increasing $\alpha$			Decreasing $\alpha$		
$\alpha$	$C_l$	$C_d$									
0.3941	-0.1211	-0.0102	0.3906	-0.1082	-0.0069	0.0623	-0.2509	-0.0229	0.0623	-0.2509	-0.0229
3.7869	0.3616	0.0051	3.8464	0.3657	0.0135	5.0628	0.3397	-0.0034	5.0628	0.3397	-0.0034
7.8771	0.6353	0.0420	7.8823	0.6555	0.0408	10.0630	0.6047	0.0307	10.0630	0.6047	0.0307
13.2581	0.5112	0.1534	13.3792	0.5120	0.1557	15.0629	0.4460	0.1277	15.0629	0.4460	0.1277
18.0157	0.5890	0.2115	18.1648	0.5792	0.2202	20.0629	0.5358	0.1631	20.0629	0.5358	0.1631
22.7643	0.6647	0.2925	22.8408	0.6638	0.2953	25.0630	0.6094	0.2358	25.0630	0.6094	0.2358
27.4488	0.7735	0.4064	27.4158	0.7984	0.4232	30.0631	0.7316	0.3527	30.0631	0.7316	0.3527
32.0490	0.9008	0.5592	32.0989	0.9209	0.5890	35.0632	0.8107	0.4729	35.0632	0.8107	0.4729
36.9032	0.9530	0.7161	37.0177	0.9464	0.7331	40.0633	0.8419	0.5864	40.0633	0.8419	0.5864
41.9969	0.9481	0.8558	43.1373	0.5997	0.5605	45.0633	0.8218	0.6749	45.0633	0.8218	0.6749
47.0622	0.9315	1.0012	48.3210	0.5439	0.5923	50.0633	0.7849	0.7678	50.0633	0.7849	0.7678
52.1554	0.9044	1.1551	53.4583	0.5089	0.6445	55.0796	0.7114	0.8132	55.0796	0.7114	0.8132
57.4875	0.8104	1.2423	58.6395	0.4721	0.7066	60.1256	0.6345	0.8922	60.1256	0.6345	0.8922
63.6311	0.4505	0.7911	63.8656	0.4083	0.7810	65.1256	0.5483	0.9481	65.1256	0.5483	0.9481
68.9050	0.3699	0.8322	69.0388	0.3588	0.8303	70.1255	0.4710	1.0079	70.1255	0.4710	1.0079
74.1494	0.2981	0.8832	74.2487	0.2979	0.8794	75.1254	0.3774	1.0372	75.1254	0.3774	1.0372
79.4033	0.2249	0.9309	79.4509	0.2184	0.9245	80.1253	0.2751	1.0643	80.1253	0.2751	1.0643
84.7073	0.1387	0.9525	84.6979	0.1484	0.9749	85.0627	0.1684	1.0928	85.0627	0.1684	1.0928
89.9975	0.0562	0.9700	89.9766	0.0628	0.9948	90.0626	0.0698	1.0871	90.0626	0.0698	1.0871
95.2076	-0.0254	0.9807	95.2653	-0.0234	1.0081	95.0625	-0.0372	1.1180	95.0625	-0.0372	1.1180
100.4926	-0.1082	0.9692	100.5019	-0.1149	1.0070	100.0623	-0.1481	1.1104	100.0623	-0.1481	1.1104
105.7864	-0.1933	0.9557	105.8121	-0.1928	1.0283	105.0622	-0.2510	1.1005	105.0622	-0.2510	1.1005
111.0922	-0.2846	0.9377	111.6386	-0.4166	1.5421	109.9996	-0.3443	1.0749	109.9996	-0.3443	1.0749
116.3220	-0.3546	0.8955	117.0866	-0.5492	1.5062	114.9995	-0.4448	1.0347	114.9995	-0.4448	1.0347
121.5427	-0.4224	0.8318	122.5794	-0.6905	1.4625	119.9994	-0.5476	1.0012	119.9994	-0.5476	1.0012
126.7078	-0.4720	0.7732	127.9302	-0.7990	1.3547	124.9994	-0.6146	0.9197	124.9994	-0.6146	0.9197
131.8695	-0.5227	0.7073	133.3791	-0.9152	1.2467	130.0618	-0.7243	0.8713	130.0618	-0.7243	0.8713
137.0918	-0.5910	0.6235	138.6159	-0.9971	1.1029	135.0617	-0.8318	0.7461	135.0617	-0.8318	0.7461
143.4553	-0.9764	0.8652	143.8436	-1.0621	0.8832	140.0616	-0.9332	0.5910	140.0616	-0.9332	0.5910
148.4224	-0.9671	0.7120	148.9075	-1.0968	0.5442	145.0617	-0.9694	0.4243	145.0617	-0.9694	0.4243
153.1671	-0.9028	0.5396	153.7208	-1.0451	0.3193	150.0617	-0.9647	0.2273	150.0617	-0.9647	0.2273
157.5305	-0.7168	0.3572	158.0590	-0.8595	0.1204	155.0618	-0.8624	0.0139	155.0618	-0.8624	0.0139
162.4050	-0.6866	0.2668	162.7048	-0.7585	0.0482	160.0619	-0.7361	-0.0722	160.0619	-0.7361	-0.0722
166.9292	-0.5495	0.2131	167.6624	-0.7408	0.0921	165.0620	-0.6843	-0.0720	165.0620	-0.6843	-0.0720
171.9353	-0.5488	0.1738	172.7234	-0.7567	0.0863	170.0620	-0.6261	0.0509	170.0620	-0.6261	0.0509
176.9278	-0.5519	0.0232	177.0563	-0.5895	-0.0074	175.0620	-0.6137	-0.1110	175.0620	-0.6137	-0.1110
180.2856	-0.1161	-0.0320	180.4248	-0.1134	-0.0024	179.9999	-0.0907	-0.0793	179.9999	-0.0907	-0.0793

CA1604												
Closed tunnel												
Increasing $\alpha$						Decreasing $\alpha$						
Spar			No spar			Spar			No spar			
$\alpha$	$C_l$	$C_d$	$\alpha$	$C_l$	$C_d$	$\alpha$	$C_l$	$C_d$	$\alpha$	$C_l$	$C_d$	
Re=30,000												
-10.0009	-0.6155	0.1720	-10.0002	-0.1378	0.2051	-9.8752	-0.1430	-0.8256	-9.8754	-0.2552	0.1632	
-5.0635	-0.7448	0.0123	-5.0629	-0.2578	0.1749	-4.9376	-0.0658	-0.8942	-4.8756	-0.4299	0.1383	
-0.0630	-0.3410	-0.0229	-0.0621	0.3092	0.1711	0.0632	0.6437	-1.0636	0.1253	0.2432	0.0800	
4.9381	0.4703	0.0219	4.8765	1.0421	0.2254	5.0661	4.7285	-2.6291	5.1264	0.9574	0.2215	
9.9390	1.0085	0.1876	9.8773	1.5055	0.3101	10.0669	5.5199	-2.2537	10.1271	1.4154	0.2669	
14.8773	1.6024	0.1949	14.8781	2.1058	0.2635	15.0678	5.8548	-1.6780	15.0653	1.8549	0.3787	
19.8774	1.6192	0.2922	19.8777	1.7002	0.5200	20.0053	5.6319	-1.4593	20.0647	1.3969	0.4739	
24.8765	0.9661	0.4456	24.8774	1.4582	0.5506	25.0050	4.4057	-0.6348	25.0647	1.3038	0.6060	
29.8767	1.0356	0.6433	29.8776	1.4454	0.7810	30.0052	4.1575	-0.2700	30.0648	1.2994	0.7698	
34.8771	1.1417	0.8581	34.8778	1.5070	0.9095	35.0678	3.8015	0.0995	35.0647	1.2159	0.8380	
39.9398	1.2376	0.8438	39.8777	1.4034	1.0118	40.0671	3.5530	-0.1602	40.0641	0.8821	0.8175	
44.9396	1.0933	0.9433	44.8776	1.2662	1.1098	45.0672	3.2311	0.2312	45.1265	0.8004	0.9059	
49.9395	1.0204	1.0086	49.9400	1.1688	1.1834	50.0674	3.2591	0.3194	50.1264	0.7219	0.9584	
54.9392	0.8616	1.0668	54.9396	0.9857	1.2047	55.0672	2.9346	0.5223	55.1264	0.7115	1.0131	
59.9390	0.7560	1.0883	59.9395	0.8830	1.3352	60.0670	2.6871	0.6531	60.1261	0.5425	1.0256	
64.9392	0.7794	1.2309	64.9392	0.7325	1.4088	65.0669	2.4352	0.8051	65.1260	0.4735	1.0810	
69.9389	0.6212	1.2526	69.9389	0.6148	1.3865	70.0665	2.1017	0.9583	70.1257	0.3315	1.0911	
74.9389	0.6142	1.2918	74.9386	0.4706	1.3875	75.0660	1.7413	1.0733	75.1254	0.2126	1.1250	
79.9383	0.3585	1.2804	79.9381	0.2737	1.2237	80.0656	1.4961	1.1412	80.0627	0.0910	1.1210	
84.9385	0.4440	1.3406	84.8754	0.1757	1.2490	85.0651	1.2547	1.1422	85.0625	-0.0155	1.1549	
89.8754	0.1763	1.3737	89.8751	0.0274	1.2393	90.0019	0.8920	1.1687	90.0000	-0.0085	1.1790	
Re=60,000												
-10.0006	-0.4416	0.1180	-10.0004	-0.2648	0.0841	-9.8755	-0.3616	0.0487	-9.9378	-0.2300	0.0398	
-5.0632	-0.5265	0.0928	-5.0630	-0.3765	0.0500	-4.9381	-0.4537	0.0071	-4.9379	-0.3084	0.0100	
-0.0627	-0.1781	0.0727	-0.0623	0.1600	0.0847	0.0628	0.2099	-0.1591	0.0629	0.2875	0.0382	
4.9383	0.5585	0.1536	4.9387	0.8667	0.0993	5.0638	0.9818	-0.0756	5.0638	0.9562	0.0925	
9.9389	0.9346	0.2021	9.9392	1.2098	0.1886	10.0643	1.3623	-0.0061	10.0644	1.3342	0.1672	
14.8770	1.3851	0.2366	14.8774	1.6763	0.1963	15.0650	1.8372	0.0700	15.0650	1.7229	0.1968	
19.8771	1.3866	0.3352	19.8771	1.3493	0.3622	20.0025	1.7314	0.1497	20.0020	1.3250	0.3646	
24.8765	0.9530	0.4474	24.8768	1.8119	0.4357	25.0021	1.3781	0.3279	25.0019	1.1859	0.4736	
29.8767	1.0209	0.6155	29.8771	1.2612	0.6059	30.0023	1.4419	0.5124	30.0021	1.2706	0.6001	
34.8769	1.0611	0.7607	34.8772	1.2679	0.7528	35.0649	1.3970	0.6791	35.0022	1.2584	0.7069	
39.9394	1.0697	0.8379	39.8772	1.1958	0.8501	40.0643	1.0985	0.5340	40.0016	0.9682	0.6293	
44.9393	0.9722	0.9228	44.8771	1.0867	0.9382	45.0643	1.0682	0.6099	45.0640	0.8807	0.6986	
49.9392	0.8845	0.9862	49.9395	1.0105	1.0221	50.0642	1.0123	0.6870	50.0639	0.8050	0.7830	
54.9391	0.7888	1.0524	54.9393	0.8862	1.0757	55.0641	0.9272	0.7616	55.0638	0.7127	0.8403	
59.9390	0.7150	1.1060	59.9391	0.7522	1.1272	60.0640	0.8352	0.8170	60.0637	0.6350	0.8904	
64.9387	0.5889	1.1022	64.9389	0.6484	1.1872	65.0638	0.7220	0.8763	65.0635	0.5256	0.9422	
69.9386	0.5149	1.1801	69.9386	0.5227	1.2244	70.0636	0.6077	0.9241	70.0634	0.4432	0.9758	
74.9383	0.3798	1.1939	74.9383	0.3900	1.2325	75.0634	0.4976	0.9489	75.0631	0.3296	1.0089	
79.9380	0.2334	1.2249	79.9380	0.2464	1.0158	80.0632	0.3776	0.9894	80.0630	0.2362	1.0290	
84.9378	0.1441	1.0909	84.8753	0.1508	1.0301	85.0630	0.2404	0.9976	85.0002	0.1173	1.0459	
89.8750	0.0230	0.9778	89.8751	0.0295	1.0409	90.0002	0.0726	1.2296	90.0001	0.0286	1.1147	
Re=100,000												
-10.0006	-0.4348	0.2038	-10.0004	-0.2590	0.0691	-9.8756	-0.3911	0.1402	-9.8754	-0.2573	0.0741	
-5.0632	-0.4769	0.1520	-5.0629	-0.3079	0.0478	-4.9381	-0.4277	0.1035	-4.8754	-0.2781	0.0416	
-0.0628	-0.2099	0.1370	-0.0622	0.2022	0.0579	0.0626	0.0386	0.0520	0.1254	0.2849	0.0481	
4.9383	0.5333	0.1989	4.9387	0.8873	0.1096	5.0636	0.7756	0.1123	5.1264	0.9648	0.1078	
9.9388	0.9170	0.2539	9.8768	1.2271	0.1691	10.0641	1.1443	0.1839	10.1274	1.6727	0.1324	
14.8771	1.3982	0.2741	14.8774	1.6580	0.1993	15.0647	1.5449	0.2194	15.0649	1.6885	0.1951	
19.8771	1.4018	0.3381	19.8772	1.4454	0.3525	20.0022	1.4405	0.3189	20.0645	1.3348	0.3668	
24.8766	1.0125	0.4823	24.8768	1.1711	0.4459	25.0018	1.1134	0.4516	25.0643	1.1733	0.4578	
29.8768	1.0613	0.6043	29.8770	1.2125	0.5837	30.0019	1.1605	0.5894	30.0646	1.2476	0.6020	
34.8770	1.1249	0.7624	34.8771	1.2207	0.7127	35.0645	1.1654	0.7294	35.0647	1.2411	0.7434	
39.9395	1.0719	0.8505	39.8771	1.1642	0.8372	40.0645	1.0852	0.8382	40.0641	0.9316	0.6302	
44.9394	0.9979	0.9329	44.8770	1.0831	0.9242	45.0639	0.8082	0.6852	45.1265	0.8574	0.7025	
49.9394	0.9571	0.9991	49.9394	0.9922	1.0151	50.0638	0.7529	0.7435	50.1264	0.7884	0.7640	
54.9392	0.8567	1.0632	54.9393	0.8854	1.0786	55.0637	0.6814	0.7996	55.1263	0.7119	0.8249	
59.9388	0.6604	0.9428	59.9391	0.7627	1.1150	60.0636	0.5973	0.8468	60.1262	0.6264	0.8756	
64.9385	0.5354	0.9021	64.9385	0.5437	0.9087	65.0635	0.5125	0.8948	65.1260	0.5352	0.9232	
69.9383	0.4370	0.9451	69.9383	0.4428	0.9545	70.0633	0.4162	0.9307	70.1258	0.4410	0.9610	
74.9381	0.3370	0.9745	74.9382	0.3497	0.9814	75.0631	0.3150	0.9575	75.1257	0.3391	0.9903	
79.9379	0.2305	0.9963	79.9380	0.2509	1.0061	80.0629	0.2110	0.9731	80.0630	0.2451	1.0078	
84.9377	0.1233	1.0022	84.8753	0.1515	1.0167	85.0627	0.0986	0.9854	85.0628	0.1401	1.0242	
89.8750	0.0220	1.0080	89.8751	0.0448	1.0234	90.0000	-0.0066	0.9923	90.0001	0.0370	1.0263	

CA1604												
Open tunnel												
Increasing $\alpha$							Decreasing $\alpha$					
Spar			No spar			Spar			No spar			
$\alpha$	$C_l$	$C_d$	$\alpha$	$C_l$	$C_d$	$\alpha$	$C_l$	$C_d$	$\alpha$	$C_l$	$C_d$	
Re=30,000												
-6.8973	-1.0390	1.4546	-10.0004	-0.2648	0.0841	-9.0045	-0.3042	0.0169	-11.7184	-0.7594	0.4712	
-1.8901	-1.1188	1.2463	-5.0630	-0.3765	0.0500	-4.0073	-0.3106	-0.0652	-6.7521	-0.7742	0.4026	
1.0856	-0.4343	1.0690	-0.0623	0.1600	0.0847	-0.4962	0.2027	0.1004	-0.7018	-0.2825	0.3616	
3.6674	0.3673	0.9958	4.9387	0.8667	0.0993	2.4579	0.8567	0.0978	5.6028	0.2940	0.3837	
6.9045	0.9714	0.9903	9.9392	1.2098	0.1886	6.2940	1.2489	0.0726	11.5543	0.7145	0.4487	
10.8696	1.3112	1.0070	14.8774	1.6763	0.1963	10.4260	1.5338	0.1267	17.7181	1.2288	0.5246	
13.9175	1.9249	1.1176	19.8771	1.3493	0.3622	14.1350	1.9396	0.2722	22.7632	1.2763	0.5659	
19.9707	1.5976	1.0995	24.8768	1.1819	0.4357	20.7688	1.4224	0.5037	26.7424	0.8252	0.7098	
25.2481	1.5085	1.2701	29.8771	1.2612	0.6059	26.3099	1.2458	0.4482	31.7843	0.8437	0.8301	
30.2647	1.5002	1.5630	34.8772	1.2679	0.7528	31.7570	1.1013	0.5466	37.0343	0.9542	1.0831	
34.8135	1.6700	1.7281	39.8772	1.1958	0.8501	36.8385	1.0779	0.6300	41.8451	0.8430	1.1350	
40.0341	1.6015	1.9952	44.8771	1.0867	0.9382	41.9067	1.0535	0.8405	45.7678	0.3669	0.7890	
46.8366	1.0426	1.8878	49.9395	1.0105	1.0221	47.4646	0.8752	0.9459	50.6473	0.3137	0.8673	
52.6046	0.7739	1.7012	54.9393	0.8862	1.0757	52.4775	0.8982	1.0647	55.5573	0.2739	0.8767	
58.0925	0.6177	1.8765	59.9391	0.7522	1.1272	57.8780	0.7700	1.1696	60.4278	0.2167	0.9203	
63.5680	0.4718	1.9198	64.9389	0.6484	1.1872	63.2102	0.6679	1.2604	65.3239	0.1431	0.9843	
69.1267	0.2895	1.9518	69.9386	0.5227	1.2244	68.2575	0.6538	1.3025	70.1528	0.0675	1.0052	
74.8337	0.0676	2.0105	74.9383	0.3900	1.2325	73.8785	0.4511	1.4355	74.9387	-0.0271	1.0183	
80.5297	-0.1567	1.9685	79.9380	0.2464	1.0158	79.0851	0.3673	1.4555	79.6685	-0.1189	1.0412	
86.8690	-0.6164	1.9451	84.8753	0.1508	1.0301	84.6034	0.2004	1.5342	84.5055	-0.1909	1.0288	
92.0950	-0.6800	1.8828	89.8751	0.0295	1.0409	89.8100	0.0885	1.5174	89.3001	-0.2541	1.0018	
Re=60,000												
-8.7879	-0.4003	0.3222	-11.7184	-0.7594	0.4712	-9.0030	-0.2964	0.0791	-11.5449	-0.7379	0.4231	
-3.5990	-0.5008	0.2591	-6.7521	-0.7742	0.4026	-3.8342	-0.3503	0.0267	-6.5969	-0.7609	0.3975	
0.0354	-0.0454	0.2978	-0.7018	-0.2825	0.3616	-0.1875	0.0898	0.0693	-0.4678	-0.2343	0.3492	
3.2429	0.5385	0.3529	5.6028	0.2940	0.3837	3.0500	0.6792	0.1211	5.7907	0.3218	0.3614	
7.0683	0.9350	0.4119	11.5543	0.7145	0.4487	6.8446	1.0759	0.1938	11.6767	0.7133	0.4622	
11.4275	1.1463	0.4522	17.7181	1.2288	0.5246	10.2215	1.5982	0.1892	17.8623	1.2372	0.4857	
15.1126	1.5670	0.4529	22.7632	1.2763	0.5659	15.0627	1.6437	0.2636	22.9798	1.2891	0.5638	
21.1705	1.2410	0.6525	26.7424	0.8252	0.7098	21.5712	1.6115	0.4520	26.8320	0.7819	0.6796	
26.1930	1.2262	0.6923	31.7843	0.8437	0.8301	27.0068	1.0176	0.4745	31.2942	0.5443	0.6401	
30.8303	1.3511	0.9232	37.0343	0.9542	1.0831	32.4163	0.8870	0.5573	36.0319	0.4284	0.6831	
35.6589	1.4191	1.1320	41.8451	0.8430	1.1350	37.6051	0.8267	0.6618	40.8824	0.3623	0.7307	
41.3772	1.1803	1.1866	45.7678	0.3669	0.7890	42.6609	0.8076	0.7192	45.7934	0.3230	0.7852	
47.6863	0.7410	0.9442	50.6473	0.3137	0.8673	47.7704	0.7748	0.8123	50.6991	0.2813	0.8077	
52.9755	0.6692	1.0348	55.5573	0.2739	0.8767	53.1162	0.6861	0.8889	55.6210	0.2468	0.8825	
58.1988	0.5983	1.1200	60.4278	0.2167	0.9203	58.3046	0.6280	0.9793	60.4783	0.1561	0.9327	
63.5423	0.4903	1.1906	65.3239	0.1431	0.9843	63.5489	0.5513	1.0831	65.2988	0.0768	0.9301	
68.8553	0.3904	1.2381	70.1528	0.0675	1.0052	68.9549	0.4225	1.1218	70.1172	0.0242	0.9491	
74.2301	0.2703	1.2948	74.9387	-0.0271	0.10183	74.2027	0.3458	1.1739	74.9147	-0.0653	0.9619	
79.5397	0.1727	1.3213	79.6685	-0.1189	0.1042	79.5167	0.2242	1.2202	79.7420	-0.1416	0.9493	
84.8949	0.0394	1.3740	84.5055	-0.1909	0.10288	84.9394	0.0905	1.2546	84.5697	-0.2178	0.9456	
90.2580	-0.0740	1.3796	89.3001	-0.2541	1.0018	90.1867	-0.0171	1.2597	89.3240	-0.2987	0.9584	
Re=100,000												
-8.8584	-0.3723	0.1994	-10.9069	-0.4008	0.1948	-8.9481	-0.3049	0.0978	-10.7562	-0.3894	0.1830	
-3.8275	-0.4098	0.1598	-5.8816	-0.3896	0.1713	-3.9028	-0.3219	0.0452	-5.6452	-0.3404	0.1352	
-0.0780	0.0101	0.1704	0.1882	0.1108	0.1495	-0.3499	0.1446	0.0627	0.4536	0.1728	0.1369	
3.0732	0.6092	0.2264	6.4941	0.6878	0.2249	2.8312	0.7499	0.1162	6.7771	0.7577	0.2039	
6.9434	0.9846	0.2820	12.3321	1.0582	0.3290	6.7269	1.1164	0.1657	12.5897	1.1168	0.3161	
10.3201	1.5068	0.2911	18.5037	1.6036	0.4255	10.1622	1.6149	0.1862	18.7590	1.6335	0.4169	
15.0861	1.5769	0.3469	23.6260	1.6576	0.5078	14.9416	1.6796	0.2626	23.7752	1.6406	0.4999	
21.3621	1.1780	0.5553	27.5242	1.1707	0.6267	21.3044	1.2517	0.4808	27.6293	1.1619	0.6129	
26.6640	1.0790	0.6357	32.1002	0.9833	0.6454	26.4335	1.2081	0.5974	32.2062	0.9473	0.5975	
30.9976	1.3067	0.8879	37.9246	1.3476	1.0353	32.2783	0.9281	0.5775	37.0104	0.8608	0.6416	
35.9582	1.3257	1.0587	42.9100	1.3136	1.1689	37.4418	0.8755	0.6516	41.9154	0.8188	0.7004	
42.1716	0.9170	0.9018	46.6743	0.7675	0.7857	42.5546	0.8410	0.7151	46.7997	0.7677	0.7668	
47.7804	0.7139	0.8355	51.5137	0.6965	0.8482	47.7138	0.7942	0.8041	51.6443	0.6990	0.8495	
53.0043	0.6634	0.9347	56.3907	0.6422	0.9307	53.0008	0.7229	0.8968	56.5279	0.6476	0.9182	
58.2697	0.5797	1.0122	61.2368	0.5742	0.9870	58.2103	0.6573	0.9838	61.3631	0.5747	1.0013	
63.5376	0.4957	1.0964	66.1039	0.4878	1.0728	63.4779	0.5722	1.0561	66.2150	0.4817	1.0450	
68.8251	0.4051	1.1626	70.8687	0.3839	1.0881	68.8326	0.4624	1.1365	70.9608	0.3970	1.1147	
74.1325	0.3075	1.2209	75.6701	0.2961	1.1653	74.1703	0.3557	1.1844	75.7136	0.2877	1.1355	
79.4886	0.1933	1.2452	80.3692	0.1908	1.1849	79.5151	0.2259	1.2131	80.4834	0.1860	1.1806	
84.7629	0.0874	1.2931	85.1294	0.0848	1.1853	84.9411	0.0908	1.2432	85.2321	0.0749	1.1958	
90.1382	-0.0327	1.2897	89.7858	-0.0394	1.2028	90.2224	-0.0232	1.2555	89.9392	-0.0269	1.1801	

CA1705												
Closed tunnel												
Increasing $\alpha$							Decreasing $\alpha$					
Spar			No spar			Spar			No spar			
$\alpha$	$C_l$	$C_d$	$\alpha$	$C_l$	$C_d$	$\alpha$	$C_l$	$C_d$	$\alpha$	$C_l$	$C_d$	
Re=30,000												
-10.0003	-0.2853	0.1052	-10.0003	-0.3118	0.1065	-9.9378	-0.2903	0.1023	-9.8753	-0.3154	0.0993	
-5.0628	-0.4455	0.0366	-5.0003	-0.4577	0.0350	-4.9379	-0.4319	0.0926	-4.8754	-0.4312	0.0694	
-0.0628	-0.0304	0.0443	-0.0627	-0.0695	0.1002	0.0625	0.0484	0.0952	0.0624	-0.0676	0.0538	
4.8750	0.7756	0.1339	4.9374	0.6884	0.1520	5.0633	0.7555	0.1191	5.0633	0.7491	0.1279	
9.8753	1.0899	0.1775	9.9377	1.0782	0.2083	10.0012	1.0841	0.2319	10.0637	1.0875	0.2156	
14.8760	1.5843	0.2287	14.9385	1.6039	0.2250	15.0017	1.5950	0.1767	15.0642	1.6428	0.1998	
19.8754	1.2257	0.3816	19.9379	1.2753	0.3780	20.0013	1.1348	0.3540	20.0639	1.2360	0.3397	
24.8753	1.2138	0.5144	24.8752	1.2343	0.5404	25.0013	1.1561	0.4985	25.0639	1.1889	0.4698	
29.8753	1.3522	0.7641	29.9377	1.3802	0.7284	30.0015	1.2118	0.6424	30.0640	1.2605	0.6516	
34.8751	1.3614	0.9491	34.9376	1.4065	0.9251	35.0016	1.2327	0.8004	35.0641	1.2762	0.8126	
39.8750	1.3515	1.1123	39.9375	1.4250	1.1133	40.0016	1.1852	0.9565	40.0642	1.2472	0.9343	
44.8748	1.2277	1.2303	44.9373	1.2948	1.2522	45.0014	1.0750	0.9821	45.0639	1.0684	1.0034	
49.9371	1.1689	1.4088	49.9371	1.1465	1.3931	50.0638	0.9623	1.0912	50.0638	0.9720	1.0702	
54.9369	1.0874	1.5623	54.9993	1.0204	1.4820	55.0637	0.8589	1.1617	55.1262	0.8569	1.1667	
59.9367	0.9101	1.5718	59.9991	0.8890	1.6216	60.0636	0.7202	1.2393	60.1261	0.7617	1.2521	
64.9364	0.7679	1.6972	64.9989	0.7481	1.7285	65.0634	0.5747	1.2870	65.1259	0.6256	1.2717	
69.9362	0.6232	1.7493	69.9986	0.6012	1.7606	70.0632	0.4591	1.3013	70.1258	0.5072	1.3468	
74.9360	0.4310	1.8191	74.9985	0.4512	1.8172	75.0630	0.3487	1.3240	75.1256	0.3617	1.3584	
79.9356	0.2729	1.9078	79.9356	0.2304	1.8279	80.0628	0.1809	1.3613	80.0628	0.2146	1.3878	
84.8734	0.0937	1.4472	84.9354	0.1296	1.9052	85.0001	0.0922	1.4245	85.0626	0.0683	1.3866	
89.8733	-0.0485	1.4339	89.9352	-0.0526	1.8906	89.9999	-0.0498	1.3624	89.9999	-0.0656	1.3802	
Re=60,000												
-10.0003	-0.2919	0.1061	-10.0003	-0.2918	0.0905	-9.9378	-0.2918	0.1005	-9.8753	-0.3021	0.1017	
-5.0628	-0.3933	0.0581	-5.0003	-0.4101	0.0432	-4.9379	-0.4139	0.0731	-4.8754	-0.4175	0.0653	
-0.0628	-0.0377	0.0639	-0.0628	-0.0692	0.0419	0.0625	-0.0005	0.0751	0.0625	-0.0382	0.0744	
4.9374	0.6714	0.1143	4.9374	0.6521	0.1137	5.0632	0.7041	0.1374	5.0632	0.6679	0.1354	
9.8752	0.9768	0.1859	9.9377	0.9910	0.1836	10.0635	0.9788	0.1921	10.0635	0.9892	0.1891	
14.8759	1.3794	0.1962	14.9384	1.4234	0.1946	15.0015	1.3783	0.2027	15.0640	1.4240	0.2028	
19.8754	1.1037	0.3540	19.9379	1.1686	0.3462	20.0012	1.0793	0.3318	20.0637	1.0900	0.3452	
24.8752	1.0474	0.4767	24.8752	1.0694	0.4791	25.0012	1.0182	0.4572	25.0012	1.0410	0.4562	
29.8752	1.1709	0.6695	29.8752	1.2025	0.6732	30.0013	1.0925	0.5977	30.0638	1.1114	0.5952	
34.8751	1.1952	0.8381	34.9376	1.2424	0.8545	35.0013	1.0830	0.7218	35.0639	1.1050	0.7232	
39.8749	1.1406	0.9571	39.9375	1.1947	0.9642	40.0013	1.0165	0.8237	40.0638	1.0474	0.8408	
44.8748	1.0887	1.0902	44.9373	1.1310	1.1290	45.0013	0.9581	0.9179	45.0638	0.9690	0.9176	
49.9371	1.0042	1.2240	49.9371	1.0323	1.2180	50.0637	0.8632	0.9960	50.0637	0.8767	0.9927	
54.9369	0.9034	1.3236	54.9369	0.9602	1.3471	55.0636	0.7635	1.0662	55.1261	0.7722	1.0529	
59.9367	0.7886	1.4253	59.9993	0.8337	1.4390	60.0634	0.6494	1.1026	60.1260	0.6751	1.1330	
64.9366	0.6583	1.4829	64.9991	0.7087	1.5336	65.0633	0.5396	1.1627	65.1258	0.5584	1.1704	
69.9363	0.5255	1.5797	69.9989	0.5640	1.5660	70.0631	0.4228	1.1932	70.1256	0.4369	1.2056	
74.9362	0.3771	1.5668	74.9986	0.4244	1.6411	75.0630	0.3087	1.2303	75.0630	0.3193	1.2281	
79.9359	0.2415	1.6512	79.9359	0.2581	1.6556	80.0628	0.1844	1.2541	80.0628	0.1940	1.2623	
84.8731	0.0823	1.6687	84.9357	0.1076	1.6913	85.0001	0.0652	1.2618	85.0626	0.0648	1.2392	
89.8730	-0.0676	1.6675	89.9355	-0.0508	1.6570	89.9999	-0.0615	1.2495	89.9999	-0.0504	1.2685	
Re=100,000												
-10.0003	-0.3214	0.1147	-10.0003	-0.3252	0.1142	-9.9378	-0.3256	0.1227	-9.8753	-0.3253	0.1228	
-5.0628	-0.4051	0.0737	-5.0003	-0.4031	0.0675	-4.9379	-0.3998	0.0859	-4.9379	-0.4120	0.0841	
-0.0628	-0.0324	0.0693	-0.0628	-0.0556	0.0664	0.0625	0.0069	0.0897	0.0625	-0.0251	0.0811	
4.8749	0.6687	0.1278	4.9374	0.6424	0.1239	5.0632	0.7015	0.1428	5.0632	0.6811	0.1387	
9.8752	0.9829	0.1849	9.9377	0.9955	0.1900	10.0015	1.3965	0.1584	10.0640	1.4437	0.1641	
14.8759	1.4087	0.1982	14.9384	1.4225	0.2000	15.0015	1.4064	0.2051	15.0015	1.4443	0.2090	
19.8755	1.1663	0.3487	19.9380	1.1980	0.3521	20.0012	1.1010	0.3425	20.0013	1.1489	0.3436	
24.8752	1.0373	0.4745	24.8752	1.0738	0.4900	25.0011	1.0016	0.4463	25.0012	1.0510	0.4517	
29.8752	1.1966	0.6810	29.8752	1.2233	0.6960	30.0013	1.1197	0.6144	30.0014	1.1472	0.6128	
34.8750	1.2378	0.8723	34.9375	1.2634	0.8784	35.0014	1.1310	0.7584	35.0014	1.1427	0.7457	
39.8749	1.1589	0.9843	39.9375	1.1694	0.9855	40.0013	1.0234	0.8237	40.0014	1.0590	0.8248	
44.8748	1.0978	1.1055	44.9373	1.1243	1.1133	45.0013	0.9513	0.9147	45.0638	0.9819	0.9228	
49.9371	1.0071	1.2198	49.9371	1.0696	1.2834	50.0637	0.8634	0.9805	50.0637	0.8919	1.0003	
54.9369	0.9271	1.3445	54.9995	0.9417	1.3515	55.0636	0.7684	1.0536	55.0636	0.7831	1.0505	
59.9368	0.7949	1.4242	59.9993	0.8259	1.4281	60.0634	0.6630	1.1292	60.0635	0.6809	1.1083	
64.9368	0.5070	1.1056	64.9991	0.7007	1.5208	65.0633	0.5518	1.1670	65.0633	0.5615	1.1578	
69.9367	0.4062	1.1606	69.9989	0.5539	1.5419	70.0631	0.4272	1.1746	70.0632	0.4491	1.2138	
74.9365	0.3020	1.2035	74.9986	0.4113	1.6289	75.0630	0.3137	1.2242	75.0630	0.3295	1.2302	
79.9363	0.1856	1.2341	79.9359	0.2537	1.6399	80.0628	0.1929	1.2467	80.0628	0.2062	1.2575	
84.8737	0.0723	1.2498	84.9357	0.1076	1.6890	85.0001	0.0810	1.2551	85.0087	0.0843	1.2735	
89.8735	-0.0403	1.2599	89.9354	-0.0501	1.6862	89.9999	-0.0387	1.2607	89.9999	-0.0437	1.2607	

CA1705											
Open tunnel											
Increasing $\alpha$						Decreasing $\alpha$					
Spar			No spar			Spar			No spar		
$\alpha$	$C_l$	$C_d$	$\alpha$	$C_l$	$C_d$	$\alpha$	$C_l$	$C_d$	$\alpha$	$C_l$	$C_d$
Re=30,000											
-10.3010	-0.1537	0.2061	-10.6937	-0.3542	0.1380	-10.3585	-0.2469	0.2080	-10.7156	-0.3956	0.1673
-5.7427	-0.3473	0.1718	-6.0580	-0.5083	0.1067	-5.6083	-0.3744	0.1413	-5.9991	-0.5397	0.1060
0.2721	0.1708	0.2259	-0.0479	0.0075	0.1330	0.3291	0.1042	0.1395	0.1148	0.0266	0.0870
6.5483	0.8544	0.3024	6.2942	0.7246	0.1866	6.7517	0.8306	0.2718	6.3983	0.6792	0.1963
12.3051	1.2408	0.4013	12.0682	1.1198	0.2792	12.4436	1.2158	0.4083	12.2557	1.1468	0.2913
17.6489	1.4163	0.5407	17.3977	1.2881	0.4098	17.7635	1.3791	0.4641	17.5936	1.3186	0.4168
23.6708	1.9381	0.6429	23.5542	1.8785	0.5289	23.7596	1.8877	0.6766	23.6811	1.8715	0.5509
27.5741	1.3781	0.8038	27.5035	1.3421	0.6756	27.6548	1.3236	0.7706	27.5665	1.3049	0.6823
32.9280	1.5588	1.0287	32.8327	1.5102	0.9057	33.0228	1.5115	1.0386	32.8376	1.4427	0.8410
37.9806	1.5857	1.2471	37.8258	1.5067	1.1487	37.1578	1.0698	0.7928	36.9584	0.9957	0.7274
42.9305	1.5601	1.4374	42.7309	1.4582	1.2530	42.0810	1.0306	0.9136	41.8636	0.9475	0.7998
47.6686	1.4264	1.5237	47.6719	1.4281	1.4630	46.9483	0.9629	1.0112	46.7289	0.8790	0.8811
52.4514	1.3155	1.7300	52.4167	1.2658	1.5297	51.7872	0.8487	1.1097	51.5995	0.7814	0.9839
57.2095	1.1600	1.7576	57.1924	1.1513	1.6718	56.5352	0.7200	1.1280	56.4663	0.7137	0.9968
61.5669	0.8319	1.4541	61.9004	1.0022	1.7479	61.3807	0.6411	1.2386	61.3326	0.6457	1.1242
66.0227	0.5541	1.3525	66.1319	0.6099	1.2453	66.1758	0.5365	1.2719	66.0537	0.5039	1.1768
70.7719	0.4260	1.4355	70.9153	0.4993	1.2973	70.9671	0.4299	1.3580	70.8068	0.3784	1.2524
75.7131	0.3960	1.4607	75.6016	0.3391	1.2936	75.6308	0.2902	1.3253	75.6705	0.3091	1.2565
80.2110	0.1716	1.4595	80.4319	0.2524	1.3151	80.4924	0.2195	1.4527	80.5305	0.2380	1.3551
84.9726	0.0499	1.4537	85.0935	0.1116	1.3751	85.0953	0.0167	1.4754	85.1459	0.0742	1.3323
89.7713	-0.0529	1.4912	89.8444	-0.0156	1.3529	89.8869	-0.0578	1.4595	89.9559	-0.0224	1.3627
Re=60,000											
-10.6322	-0.3228	0.1772	-10.6900	-0.3523	0.1462	-10.5375	-0.3064	0.1492	-10.5952	-0.3344	0.1416
-6.0250	-0.4915	0.1574	-5.9822	-0.4696	0.1187	-5.7699	-0.4250	0.1098	-5.8226	-0.4500	0.0998
-0.0449	0.0090	0.1582	-0.0744	-0.0061	0.1057	0.1843	0.0622	0.1082	0.1305	0.0346	0.0836
6.1128	0.6320	0.2441	6.1057	0.6284	0.1749	6.4316	0.6991	0.1857	6.3239	0.6731	0.1758
11.8389	1.0028	0.3322	11.8598	1.0134	0.2760	12.0478	1.0456	0.2893	12.0794	1.0572	0.2768
17.8356	1.5117	0.4397	17.9867	1.5888	0.3904	18.0444	1.5545	0.3991	18.1359	1.5943	0.3799
22.9953	1.5932	0.4880	23.0347	1.6133	0.4561	23.1207	1.5934	0.4762	23.2074	1.6307	0.4551
27.1614	1.1674	0.6391	27.2152	1.1949	0.6069	27.2830	1.1657	0.6444	27.3642	1.2020	0.6156
32.3603	1.2690	0.8278	32.4460	1.3127	0.8070	32.5520	1.3030	0.8535	32.5707	1.3070	0.8166
37.4495	1.3145	1.0269	37.5395	1.3604	1.0231	36.8953	0.9677	0.7403	36.8417	0.9363	0.6701
42.3912	1.2848	1.1873	42.4344	1.3068	1.1493	41.6249	0.8297	0.7522	41.6577	0.8428	0.7175
47.2605	1.2180	1.3004	47.3292	1.2531	1.3179	46.5178	0.7750	0.8175	46.5376	0.7817	0.7874
52.0595	1.0835	1.3707	52.1125	1.1105	1.3668	51.4788	0.7231	0.8791	51.4274	0.7257	0.8664
56.8689	0.9861	1.4807	56.8629	0.9831	1.4426	56.3324	0.6484	0.9487	56.3435	0.6513	0.9413
61.3794	0.7362	1.3275	61.0488	0.5674	1.0064	61.1784	0.5698	1.0075	61.1730	0.5646	0.9986
65.8635	0.4728	1.0561	65.9182	0.5007	1.0477	66.0210	0.4894	1.0713	66.0082	0.4808	1.0606
70.6706	0.3743	1.1081	70.6906	0.3845	1.1053	70.8167	0.3851	1.1245	70.8208	0.3855	1.1022
75.4895	0.2819	1.1626	75.5160	0.2954	1.1450	75.6073	0.2781	1.1603	75.6286	0.2878	1.1534
80.2738	0.1717	1.1908	80.3272	0.1990	1.1770	80.3207	0.1637	1.1928	80.3600	0.1830	1.1934
84.9985	0.0631	1.2031	85.0205	0.0743	1.2065	85.1395	0.0712	1.2127	85.1217	0.0619	1.1930
89.7960	-0.0403	1.2191	89.8101	-0.0331	1.1935	89.8881	-0.0572	1.2204	89.9185	-0.0414	1.2091
Re=100,000											
-10.7159	-0.3655	0.1595	-10.7320	-0.3737	0.1738	-10.6678	-0.3729	0.1464	-10.6004	-0.3688	0.1540
-5.9157	-0.4356	0.1180	-5.9558	-0.4561	0.1314	-5.7912	-0.4359	0.1105	-5.7359	-0.4377	0.1197
0.0216	0.0429	0.1080	-0.0053	0.0292	0.1250	0.2178	0.0793	0.1034	0.2475	0.0623	0.1095
6.2104	0.6818	0.1803	6.2276	0.6587	0.2004	6.4629	0.7150	0.1772	6.4291	0.6948	0.1911
11.9294	1.0489	0.2869	11.9386	1.0537	0.3095	12.1632	1.0726	0.2791	12.2216	1.0977	0.2963
17.9955	1.5933	0.3795	18.0189	1.6053	0.4002	18.1361	1.6013	0.3584	18.2738	1.6327	0.3902
23.0314	1.6116	0.4554	23.0748	1.6338	0.4771	23.1633	1.6152	0.4372	23.3177	1.6550	0.4696
27.2010	1.1876	0.6099	27.2284	1.2016	0.6301	27.3336	1.1915	0.5937	27.4630	1.2204	0.6244
32.4395	1.3094	0.8166	32.4910	1.3357	0.8401	32.6014	1.3282	0.8089	32.6761	1.3606	0.8539
37.6474	1.4155	1.0663	37.6747	1.4295	1.0829	37.3095	1.1792	0.8674	36.9124	0.9405	0.6867
42.4429	1.3112	1.1671	42.5277	1.3545	1.2066	41.6624	0.8488	0.7196	41.7843	0.8754	0.7459
47.2606	1.2180	1.2761	47.4137	1.2643	1.3236	46.5566	0.7948	0.7983	46.6737	0.8192	0.8269
52.0995	1.1358	1.4113	52.1813	1.1457	1.4258	51.4984	0.7332	0.8787	51.5258	0.7440	0.8957
56.3829	0.7380	1.0820	56.3132	0.7024	1.0167	56.3452	0.6549	0.9537	56.4302	0.6636	0.9677
61.0912	0.5891	1.0360	61.0803	0.5835	1.0283	61.1829	0.5720	1.0149	61.2732	0.5838	1.0379
65.9054	0.4942	1.0895	65.9192	0.5012	1.0892	66.0089	0.4832	1.0731	66.0980	0.4947	1.0930
70.7206	0.3999	1.1454	70.7200	0.3995	1.1383	70.8163	0.3849	1.1330	70.9015	0.3948	1.1383
75.5209	0.2979	1.1789	75.5252	0.3001	1.1846	75.6209	0.2851	1.1708	75.6308	0.2889	1.1826
80.3023	0.1863	1.2062	80.3082	0.1893	1.2092	80.3960	0.1703	1.2042	80.4097	0.1765	1.2110
85.0185	0.0733	1.2350	85.0909	0.0783	1.2246	85.1268	0.0648	1.2190	85.1840	0.0618	1.2328
89.7871	-0.0449	1.2248	89.8114	-0.0325	1.2347	89.9112	-0.0453	1.2160	89.9076	-0.0470	1.2407

CA2010												
Closed tunnel												
Increasing $\alpha$							Decreasing $\alpha$					
Spar			No spar			Spar			No spar			
$\alpha$	$C_l$	$C_d$	$\alpha$	$C_l$	$C_d$	$\alpha$	$C_l$	$C_d$	$\alpha$	$C_l$	$C_d$	
Re=30,000												
-10.0002	-0.5312	0.0310	-10.0002	-0.3837	0.1151	-9.9375	-0.5498	-0.0676	-9.8751	-0.3344	0.2348	
-5.0629	-0.5661	0.0878	-5.0627	-0.3854	0.0710	-4.9376	-0.5888	-0.0859	-4.8751	-0.3382	0.2069	
-0.0629	-0.2275	0.0938	-0.0627	-0.0640	0.0583	0.0624	-0.3196	-0.0982	0.0624	-0.0350	0.1963	
4.9371	0.5101	0.1126	4.9374	0.5656	0.1065	5.0625	0.5092	-0.0192	5.0625	0.5842	0.2517	
9.9372	1.0559	0.1975	9.9375	0.9838	0.1855	10.0001	1.0272	0.0245	10.0626	0.9730	0.3218	
14.8749	1.2665	0.2915	14.8751	1.2231	0.2778	15.0002	1.2153	0.0856	15.0627	1.1854	0.4219	
19.8752	1.8391	0.2081	19.8751	1.3280	0.3870	20.0001	1.2499	0.1884	20.0627	1.2712	0.5544	
24.8749	1.2803	0.4806	24.8751	1.2948	0.5082	25.0001	1.2103	0.2941	25.0626	1.2214	0.6708	
29.8750	1.4488	0.6467	29.8751	1.3857	0.7002	30.0002	1.2847	0.4966	30.0626	1.2911	0.8409	
34.8749	1.4142	0.8630	34.8750	1.3682	0.8694	35.0001	1.4730	0.7742	35.0626	1.2876	0.9909	
39.8748	1.4466	1.0114	39.8750	1.3771	1.0515	40.0000	1.4414	0.9868	40.0626	1.2290	1.1315	
44.9373	1.3185	1.1596	44.9374	1.2911	1.2084	44.9999	1.4308	1.2373	45.0625	1.2049	1.2727	
49.9372	1.2465	1.2652	49.9374	1.2486	1.3692	49.9999	1.1905	1.2792	50.0624	1.1202	1.4216	
54.9371	1.2004	1.4977	54.9373	1.1079	1.4333	55.0624	1.1142	1.3440	55.1249	1.0039	1.4785	
59.9371	0.9691	1.4098	59.9372	1.0030	1.5775	60.0623	1.0366	1.4378	60.1249	0.8839	1.5822	
64.9370	0.9282	1.5268	64.9371	0.8359	1.6244	65.0622	0.9152	1.6812	65.1248	0.7684	1.6936	
69.9370	0.8246	1.5870	69.9371	0.6289	1.6430	70.0622	0.7757	1.6864	70.1247	0.6885	1.7936	
74.9368	0.6538	1.7549	74.9370	0.4696	1.7020	75.0621	0.6702	1.8670	75.1246	0.5535	1.8920	
79.9367	0.4544	1.8443	79.9368	0.3048	1.7817	80.0620	0.4942	1.8031	80.1245	0.3844	1.9487	
84.9367	0.2746	1.7550	84.9367	0.1556	1.8228	84.9994	0.3259	1.8124	85.0619	0.1758	1.9467	
89.8740	0.1332	1.9242	89.8742	-0.0372	1.8558	89.9992	0.0543	2.2717	89.9993	0.0052	1.8934	
Re=40,000												
-10.0001	-0.4931	0.2931	-10.0002	-0.3582	0.1526	-9.9377	-0.5164	0.0212	-9.8752	-0.3732	0.1380	
-5.0628	-0.5001	0.0826	-5.0627	-0.3474	0.1046	-4.9376	-0.5622	-0.0176	-4.9377	-0.3554	0.0908	
-0.0628	-0.1818	0.0955	-0.0627	-0.0469	0.1011	0.0625	-0.2066	-0.0532	0.0623	-0.0346	0.0925	
4.9374	0.5958	0.1304	4.9374	0.5867	0.1519	5.0625	0.5660	0.0614	5.0624	0.6043	0.1522	
9.8750	1.0334	0.2245	9.8750	0.9726	0.2101	10.0000	1.0176	0.0770	10.0625	0.9697	0.2149	
14.8749	1.2643	0.3191	14.8751	1.2011	0.2952	15.0002	1.1606	0.1602	15.0626	1.2118	0.3071	
19.8752	1.8784	0.2392	19.8754	1.8696	0.3028	20.0004	1.7660	0.1284	20.0004	1.8504	0.2955	
24.8750	1.2415	0.5292	24.8751	1.2577	0.5492	25.0002	1.2434	0.3893	25.0000	1.2461	0.5385	
29.8749	1.3635	0.7330	29.8751	1.3394	0.7289	30.0002	1.3760	0.5681	30.0000	1.3207	0.7179	
34.8749	1.4530	0.8548	34.8750	1.3275	0.8696	35.0001	1.4347	0.7739	35.0000	1.3309	0.8730	
39.8749	1.4693	1.0815	39.8750	1.2971	1.0253	40.0000	1.4275	0.9660	40.0000	1.2866	1.0249	
44.8749	1.3829	1.2200	44.9149	1.2719	1.1909	45.0000	1.3398	1.1453	45.0624	1.2602	1.1960	
49.9374	1.3218	1.2800	49.9374	1.1508	1.2902	50.0624	1.2156	1.2192	50.0624	1.1428	1.2826	
54.9373	1.1458	1.4059	54.9373	1.0793	1.4604	55.0623	1.1547	1.3827	55.0623	1.0483	1.4054	
59.9372	0.9821	1.4844	59.9372	0.9344	1.5089	60.0623	1.0161	1.4787	60.0622	0.9222	1.5120	
64.9372	0.8493	1.5745	64.9372	0.7924	1.5732	65.0622	0.8769	1.6337	65.0622	0.7941	1.6068	
69.9371	0.6897	1.6182	69.9371	0.6427	1.6403	70.0621	0.7253	1.7038	70.0621	0.6650	1.6550	
74.9370	0.5509	1.7340	74.9370	0.4845	1.7067	75.0620	0.5706	1.8186	75.0620	0.5184	1.7479	
79.9369	0.3707	1.7580	79.9369	0.3365	1.7731	80.0619	0.4616	1.8767	80.0619	0.3516	1.7784	
84.9368	0.2177	1.7535	84.9368	0.1695	1.8363	84.9995	0.2444	1.6396	85.0618	0.1817	1.8351	
89.8740	-0.0422	1.8687	89.8742	-0.0109	1.8108	89.9991	0.0516	2.1312	89.9992	0.0186	1.8338	
Re=50,000												
-10.0001	-0.4368	0.2161	-10.0002	-0.3762	0.1653	-9.9377	-0.3469	0.1976	-9.8752	-0.3772	0.1620	
-5.0628	-0.5003	0.0831	-5.0627	-0.3420	0.1294	-4.9377	-0.4275	0.1573	-4.9377	-0.3460	0.1197	
-0.0628	-0.1491	0.0860	-0.0627	-0.0399	0.1246	0.0623	-0.0282	0.1189	0.0623	-0.0144	0.1100	
4.9372	0.5784	0.1623	4.9374	0.6070	0.1768	5.0624	0.6926	0.1978	5.0624	0.6193	0.1646	
9.8749	1.0062	0.2216	9.8750	0.9820	0.2426	10.0000	1.0973	0.2932	10.0625	0.9881	0.2304	
14.8750	1.1979	0.3082	14.8751	1.2336	0.3245	15.0001	1.2410	0.3484	15.0626	1.2370	0.3250	
19.8752	1.7918	0.2853	19.8754	1.8506	0.3148	20.0005	1.8281	0.3124	20.0004	1.8347	0.3107	
24.8749	1.2406	0.5052	24.8751	1.2448	0.5578	25.0002	1.2815	0.5765	25.0000	1.2416	0.5619	
29.8750	1.3197	0.6802	29.8751	1.3252	0.7387	30.0001	1.3591	0.7830	30.0000	1.3258	0.7379	
34.8750	1.4118	0.8796	34.8750	1.3278	0.8908	35.0000	1.4161	0.9825	35.0000	1.3239	0.8827	
39.8750	1.3597	1.0213	39.8750	1.2858	1.0392	39.9999	1.3724	1.1402	40.0625	1.3205	1.0762	
44.8749	1.2931	1.1835	44.8749	1.2573	1.2131	44.9999	1.2977	1.2678	45.0624	1.2290	1.1802	
49.9374	1.1967	1.2926	49.9374	1.1328	1.2880	50.0623	1.2439	1.4458	50.0624	1.1441	1.3223	
54.9373	1.0792	1.3617	54.9373	1.0440	1.4095	55.0622	1.1108	1.5245	55.0623	1.0117	1.3926	
59.9372	0.9700	1.4731	59.9372	0.9271	1.5295	60.0622	1.0022	1.6662	60.0622	0.9127	1.5284	
64.9372	0.8476	1.5397	64.9372	0.7821	1.6034	65.0621	0.8469	1.7717	65.0622	0.7717	1.5819	
69.9371	0.6681	1.6022	69.9371	0.6341	1.6579	70.0619	0.6942	1.8936	70.0621	0.6467	1.6643	
74.9370	0.5322	1.6840	74.9370	0.4819	1.7283	75.0619	0.5405	1.8868	75.0620	0.5040	1.7557	
79.9368	0.3611	1.7882	79.9369	0.3319	1.7876	80.0618	0.3471	1.8980	80.0619	0.3387	1.7776	
84.9368	0.1836	1.8539	84.9368	0.1575	1.7704	84.9992	0.1355	1.9401	85.0618	0.1657	1.8113	
89.8741	-0.0746	1.8645	89.8742	-0.0107	1.8069	89.9993	-0.0216	1.8813	89.9992	-0.0032	1.8240	

Re=60,000											
-9.9377	-0.3531	0.1792	-10.0002	-0.3677	0.1825	-9.9377	-0.3531	0.1792	-9.8752	-0.3717	0.1720
-4.9377	-0.4621	0.1502	-5.0627	-0.3236	0.1546	-4.9377	-0.4621	0.1502	-4.9377	-0.3292	0.1382
0.0623	-0.0150	0.1198	-0.0627	-0.0125	0.1370	0.0623	-0.0150	0.1198	0.0623	0.0098	0.1222
5.0624	0.6414	0.1853	4.9374	0.6015	0.1865	5.0624	0.6414	0.1853	5.0624	0.6287	0.1777
10.0625	1.0276	0.2469	9.8750	0.9819	0.2536	10.0625	1.0276	0.2469	10.0625	0.9968	0.2390
15.0001	1.2099	0.3393	14.8751	1.2332	0.3424	15.0001	1.2099	0.3393	15.0626	1.2438	0.3266
20.0005	1.8055	0.2984	19.8754	1.8311	0.3340	20.0005	1.8055	0.2984	20.0004	1.8433	0.3164
25.0001	1.2120	0.5559	24.8751	1.2281	0.5703	25.0001	1.2120	0.5559	25.0001	1.2391	0.5632
30.0000	1.3560	0.7855	29.8751	1.3123	0.7562	30.0000	1.3560	0.7855	30.0000	1.3196	0.7484
35.0000	1.4004	0.9729	34.8750	1.3120	0.8979	35.0000	1.4004	0.9729	35.0000	1.3334	0.9112
39.9999	1.3625	1.1432	39.8750	1.2914	1.0667	39.9999	1.3625	1.1432	40.0625	1.3099	1.0595
45.0623	1.2903	1.2702	44.8749	1.2248	1.2080	45.0623	1.2903	1.2702	45.0624	1.2464	1.2158
50.0623	1.2092	1.4009	49.9374	1.1242	1.3106	50.0623	1.2092	1.4009	50.0624	1.1367	1.3122
55.0622	1.0957	1.5230	54.9373	1.0090	1.3966	55.0622	1.0957	1.5230	55.0623	1.0391	1.4531
60.0621	0.9625	1.6314	59.9372	0.8934	1.5270	60.0621	0.9625	1.6314	60.0622	0.9008	1.5171
65.0620	0.8354	1.7645	64.9372	0.7642	1.6013	65.0620	0.8354	1.7645	65.0622	0.7606	1.5806
70.0620	0.6514	1.7703	69.9371	0.6318	1.6782	70.0620	0.6514	1.7703	70.0621	0.6366	1.6874
75.0619	0.4929	1.8693	74.9370	0.4764	1.7252	75.0619	0.4929	1.8693	75.0620	0.4846	1.7213
80.0618	0.3118	1.9093	79.9369	0.3104	1.7776	80.0618	0.3118	1.9093	80.0619	0.3196	1.7552
84.9992	0.1283	1.9421	84.9368	0.1418	1.8095	84.9992	0.1283	1.9421	85.0618	0.1540	1.7719
89.9992	-0.0209	1.8816	89.8742	-0.0252	1.7861	89.9992	-0.0209	1.8816	89.9992	-0.0096	1.7844
Re=70,000											
-10.0002	-0.4753	0.3279	-10.0002	-0.3478	0.1877	-9.8752	-0.3624	0.1567	-9.8752	-0.3445	0.1825
-5.0627	-0.4234	0.1690	-5.0627	-0.3162	0.1536	-4.9377	-0.3894	0.1038	-4.9377	-0.2984	0.1508
-0.0627	0.0449	0.1624	-0.0627	0.0148	0.1506	0.0623	-0.0431	0.1038	0.0623	0.0338	0.1393
4.9374	0.6590	0.2276	4.9374	0.6077	0.1934	5.0624	0.6034	0.1943	5.0624	0.6437	0.1932
9.8750	1.0650	0.2831	9.8750	0.9772	0.2585	10.0625	1.0509	0.2574	10.0625	1.0124	0.2512
14.8751	1.2636	0.3662	14.8751	1.2424	0.3448	15.0001	1.2191	0.3301	15.0626	1.2660	0.3362
19.8753	1.7994	0.2976	19.8754	1.8145	0.3440	20.0004	1.7397	0.2818	20.0004	1.8270	0.3350
24.8750	1.2561	0.5784	24.8751	1.2345	0.5829	25.0001	1.1873	0.5379	25.0001	1.2384	0.5736
29.8751	1.3055	0.7613	29.8751	1.2897	0.7495	30.0001	1.3332	0.7470	30.0000	1.3097	0.7506
34.8750	1.3836	0.9071	34.8750	1.3152	0.9155	35.0000	1.3646	0.9826	35.0000	1.3269	0.9186
39.8750	1.3316	1.0585	39.8750	1.2759	1.0528	39.9999	1.3633	1.1539	40.0625	1.2778	1.0506
44.8749	1.2707	1.1873	44.8749	1.2123	1.1854	45.0624	1.2800	1.2854	45.0624	1.2252	1.2027
49.9373	1.1919	1.3200	49.9374	1.1094	1.2919	50.0623	1.2014	1.4033	50.0624	1.1382	1.3389
54.9373	1.0874	1.4417	54.9373	1.0155	1.4265	55.0622	1.0919	1.5218	55.0623	1.0133	1.4133
59.9372	0.9687	1.5535	59.9372	0.8978	1.5376	60.0622	0.9445	1.5949	60.0623	0.8764	1.4832
64.9371	0.8086	1.6031	64.9372	0.7633	1.6071	65.0621	0.8018	1.7010	65.0622	0.7573	1.5945
69.9370	0.6668	1.7102	69.9371	0.6172	1.6645	70.0620	0.6444	1.7702	70.0621	0.6224	1.6723
74.9370	0.5001	1.7499	74.9370	0.4657	1.7329	75.0619	0.4898	1.8637	75.0620	0.4671	1.7116
79.9369	0.3356	1.8136	79.9369	0.3013	1.7476	80.0618	0.2972	1.8780	80.0619	0.3136	1.7890
84.9368	0.1642	1.8361	84.9368	0.1376	1.7930	85.0618	0.1251	1.8967	85.0618	0.1478	1.7917
89.8742	-0.0149	1.8374	89.8742	-0.0293	1.8132	89.9992	-0.0237	1.8665	89.9992	-0.0236	1.8143
Re=80,000											
-10.0002	-0.3271	0.3972	-10.0002	-0.2844	0.2042	-9.8751	-0.2579	0.1293	-9.8752	-0.3037	0.2003
-5.0628	-0.5344	0.2252	-5.0627	-0.3037	0.1799	-4.9376	-0.2902	0.1153	-4.9377	-0.2782	0.1253
-0.0628	-0.1645	0.2482	-0.0627	0.0094	0.2179	0.0624	0.1493	0.0866	0.0623	0.0497	0.1464
4.9374	0.5797	0.3042	4.9374	0.6273	0.2131	5.0626	0.8739	0.1513	5.0624	0.6572	0.1770
9.8749	0.9486	0.3343	9.8750	0.9238	0.3055	10.0626	1.1798	0.2399	10.0626	1.0690	0.2223
14.8751	1.2458	0.3868	14.8751	1.1820	0.3526	15.0626	1.3214	0.3349	15.0627	1.3560	0.3282
19.8754	1.8058	0.3726	19.8753	1.7084	0.3704	20.0004	1.7184	0.2848	20.0004	1.8640	0.3240
24.8751	1.2666	0.6144	24.8750	1.1676	0.5967	25.0001	1.2075	0.5512	25.0001	1.2955	0.5549
29.8751	1.2814	0.7671	29.8751	1.2850	0.7599	30.0001	1.3157	0.7502	30.0001	1.3862	0.7560
34.8750	1.3302	0.8987	34.8751	1.3050	0.9268	35.0000	1.3303	0.9832	35.0000	1.3086	0.9079
39.8750	1.3219	1.0760	39.8750	1.2282	1.0239	40.0624	1.3290	1.1436	40.0625	1.2808	1.0521
44.8749	1.2486	1.1906	44.8750	1.1906	1.1814	45.0624	1.2754	1.2865	45.0624	1.2026	1.1848
49.9373	1.1837	1.3426	49.9374	1.0986	1.2935	50.0623	1.1981	1.4186	50.0624	1.1185	1.3145
54.9373	1.0736	1.4484	54.9373	1.0001	1.4076	55.0622	1.0745	1.5219	55.0623	1.0067	1.4175
59.9372	0.9445	1.5327	59.9373	0.8688	1.4851	60.0622	0.9498	1.6283	60.0622	0.8907	1.5360
64.9371	0.7986	1.6177	64.9372	0.7548	1.5986	65.0621	0.8064	1.7337	65.0622	0.7600	1.6174
69.9371	0.6502	1.6839	69.9371	0.6145	1.6728	70.0620	0.6434	1.7863	70.1246	0.6109	1.6674
74.9370	0.4955	1.7729	74.9370	0.4569	1.7149	75.0619	0.4738	1.8325	75.0620	0.4551	1.6998
79.9369	0.3282	1.7983	79.9369	0.3030	1.7976	80.0618	0.3099	1.9031	80.0619	0.3021	1.7749
84.9368	0.1581	1.8501	84.9368	0.1362	1.7893	85.0617	0.1282	1.9322	85.0618	0.1377	1.7854
89.8742	-0.0196	1.8632	89.8742	-0.0329	1.8223	89.9992	-0.0199	1.8927	89.9993	-0.0270	1.7723

Re=90,000											
-10.0002	-0.3647	0.3172	-10.0002	-0.2674	0.2102	-9.8752	-0.3048	0.2659	-9.8752	-0.2810	0.1665
-5.0627	-0.4129	0.2198	-5.0627	-0.3231	0.2297	-4.9376	-0.3049	0.1034	-4.9377	-0.2329	0.1183
-0.0627	-0.0286	0.2403	-0.0627	0.0044	0.2123	0.0624	0.1220	0.1521	0.0624	0.1947	0.1170
4.9372	0.3938	0.3328	4.9374	0.5798	0.2507	5.0626	0.8983	0.1969	5.0625	0.7420	0.1861
9.8749	0.9260	0.3755	9.8750	0.9591	0.3120	10.0627	1.2649	0.2450	10.0626	1.1438	0.2093
14.8750	1.1120	0.3927	14.8750	1.1602	0.3899	15.0628	1.4801	0.3246	15.0627	1.3608	0.3351
19.8753	1.6609	0.3682	19.8753	1.6883	0.3914	20.0005	1.8998	0.3184	20.0629	1.8468	0.3351
24.8751	1.2085	0.6455	24.8751	1.2055	0.6185	25.0002	1.2923	0.5570	25.0002	1.3725	0.5764
29.8751	1.3307	0.8234	29.8750	1.2071	0.7890	30.0001	1.2637	0.7454	30.0001	1.3996	0.7824
34.8750	1.3516	0.9397	34.8751	1.2900	0.8974	35.0000	1.3231	0.9778	35.0626	1.3404	0.9478
39.8750	1.2900	1.0640	39.8750	1.2433	1.0404	40.0625	1.3058	1.1215	40.0625	1.2771	1.0771
44.8749	1.2298	1.1897	44.8750	1.1393	1.1345	45.0624	1.2371	1.2506	45.0624	1.2034	1.1923
49.9373	1.1817	1.3683	49.9374	1.0554	1.2563	50.0623	1.1769	1.3993	50.0624	1.0972	1.2780
54.9373	1.0451	1.4392	54.9374	0.9335	1.2894	55.0623	1.0625	1.4999	55.0623	0.9984	1.4046
59.9372	0.9397	1.5735	59.9373	0.8596	1.4756	60.0622	0.9306	1.5938	60.0623	0.8714	1.5027
64.9371	0.8081	1.6717	64.9372	0.7381	1.5714	65.0621	0.7935	1.7095	65.1247	0.7479	1.6018
69.9370	0.6570	1.7356	69.9371	0.6067	1.6566	70.0620	0.6352	1.7660	70.1246	0.6053	1.6693
74.9370	0.4912	1.7940	74.9370	0.4597	1.7393	75.0619	0.4755	1.8540	75.0620	0.4655	1.7478
79.9369	0.3301	1.8459	79.9369	0.2933	1.7710	80.0618	0.3066	1.8962	80.0619	0.2964	1.7800
84.9368	0.1523	1.8807	84.9368	0.1320	1.8147	85.0618	0.1299	1.9117	85.0618	0.1297	1.8089
89.8742	-0.0144	1.8539	89.8742	-0.0336	1.8036	89.9992	-0.0255	1.8944	89.9992	-0.0387	1.7887
Re=100,000											
-10.0002	-0.2373	0.4664	-10.0002	-0.2343	0.2326	-9.9377	-0.3082	0.2190	-9.8752	-0.2455	0.1929
-5.0628	-0.4499	0.2572	-5.0627	-0.2052	0.2519	-4.9376	-0.2011	0.1348	-4.9377	-0.2384	0.1619
-0.0627	0.0413	0.2303	-0.0627	0.0502	0.2676	0.0624	0.2080	0.1534	0.0624	0.1629	0.1454
4.8748	0.5067	0.3158	4.9374	0.6095	0.2725	5.0000	0.8107	0.2026	5.0625	0.7487	0.1720
9.8750	0.9314	0.3457	9.8750	0.9148	0.3287	10.0001	1.1895	0.2700	10.0626	1.1243	0.2547
14.8751	1.2270	0.4020	14.8751	1.1955	0.4097	15.0003	1.7954	0.2900	15.0627	1.4618	0.3367
19.8753	1.5920	0.3874	19.8753	1.7108	0.4132	20.0005	1.9237	0.3500	20.0630	1.8985	0.3694
24.8750	1.0871	0.6095	24.8750	1.1148	0.6036	25.0002	1.3636	0.5988	25.0002	1.3206	0.5780
29.8751	1.2553	0.8047	29.8751	1.2701	0.7897	30.0001	1.3419	0.8096	30.0626	1.3707	0.8030
34.8750	1.2683	0.9468	34.8750	1.1711	0.9171	35.0000	1.3454	1.0000	35.0626	1.3592	0.9434
39.8750	1.2779	1.0836	39.8749	1.0713	0.9861	40.0000	1.2902	1.1415	40.0626	1.3455	1.0788
44.8749	1.2349	1.1993	44.8750	1.1321	1.1530	44.9999	1.2405	1.2588	45.0625	1.1825	1.2128
49.9194	1.1455	1.3234	49.9374	1.0459	1.2095	50.0623	1.1524	1.3786	50.0624	1.0501	1.2733
54.9373	1.0332	1.4241	54.9374	0.9165	1.2589	55.0623	1.0416	1.5079	55.0624	0.9766	1.3169
59.9372	0.9266	1.5707	59.9373	0.8266	1.3829	60.0622	0.9274	1.6254	60.1247	0.8624	1.3880
64.9371	0.7849	1.6439	64.9372	0.6916	1.4605	65.0621	0.7729	1.6928	65.1247	0.6989	1.5126
69.9370	0.6372	1.7413	69.9371	0.5942	1.6228	70.0620	0.6285	1.7785	70.1246	0.5887	1.6398
74.9369	0.4863	1.8158	74.9370	0.4524	1.7184	75.0619	0.4660	1.8662	75.0620	0.4463	1.7081
79.9369	0.3194	1.8411	79.9369	0.2858	1.7305	80.0619	0.3013	1.8918	80.0619	0.2867	1.7417
84.9368	0.1404	1.8444	84.9368	0.1232	1.7765	85.0617	0.1243	1.9350	85.0618	0.1233	1.7610
89.8742	-0.0244	1.9015	89.8743	-0.0354	1.7663	89.9992	-0.0219	1.8466	89.9993	-0.0356	1.7881

CA2010											
Open tunnel											
Increasing $\alpha$						Decreasing $\alpha$					
Spar			No spar			Spar			No spar		
$\alpha$	$C_l$	$C_d$	$\alpha$	$C_l$	$C_d$	$\alpha$	$C_l$	$C_d$	$\alpha$	$C_l$	$C_d$
-10.4030	-0.3182	0.1724	-10.3751	-0.2949	0.2068	-10.4197	-0.4301	0.3134	-10.2853	-0.3226	0.1664
-5.5231	-0.4131	0.1466	-5.4270	-0.2866	0.1604	-5.4136	-0.4253	0.2601	-5.2995	-0.3338	0.1203
-0.0681	-0.0044	0.2049	-0.0915	0.0263	0.1750	0.1032	0.0322	0.2758	0.0859	0.0184	0.1431
5.7620	0.6511	0.2322	5.5889	0.5612	0.2330	5.8106	0.5907	0.2990	5.7961	0.5768	0.1960
11.4572	1.2001	0.3602	11.0715	0.9407	0.3115	11.3690	1.0317	0.3267	11.2474	0.9316	0.2686
16.7732	1.4496	0.5351	16.4167	1.2121	0.4021	16.3989	1.0553	0.3656	16.5984	1.2075	0.4312
21.8119	1.5295	0.6347	21.5767	1.3379	0.5510	21.5943	1.2097	0.5078	21.7468	1.3242	0.5345
26.6477	1.3999	0.7424	26.5202	1.2934	0.6684	26.6544	1.3050	0.7129	26.6550	1.2520	0.6522
31.8521	1.5613	1.0482	31.6216	1.3732	0.8632	31.7218	1.3103	0.9109	31.7901	1.3582	0.8686
36.8756	1.5798	1.1682	36.6242	1.3752	1.0050	36.9530	1.4929	1.0735	36.8257	1.3862	1.0141
41.8175	1.4846	1.2514	41.6208	1.3725	1.1526	41.8828	1.4374	1.3755	41.7539	1.3297	1.1597
46.8403	1.5026	1.5448	46.5833	1.3431	1.3366	46.8556	1.4160	1.4874	46.7496	1.3263	1.3446
51.7409	1.4241	1.6656	51.4315	1.2237	1.4410	51.7209	1.3096	1.5457	51.5919	1.2024	1.3876
56.4724	1.2120	1.5401	56.3456	1.1071	1.5056	56.0201	0.7562	1.0963	56.5526	1.1224	1.5285
61.3277	1.0978	1.9220	61.2244	1.0118	1.6523	60.9153	0.6734	1.1559	60.9342	0.6362	1.0381
66.1790	0.9311	1.9772	66.0347	0.8626	1.6927	65.9027	0.6141	1.3119	65.8252	0.5505	1.0551
71.0405	0.8217	2.1139	70.8307	0.7022	1.7299	70.7397	0.4854	1.3693	70.7167	0.4652	1.1118
75.7769	0.6135	2.0497	75.6958	0.5962	1.8026	75.4821	0.3314	1.3000	75.5884	0.3643	1.1774
80.4461	0.4016	2.1216	80.5003	0.4425	1.9148	80.3670	0.2405	1.4847	80.3716	0.2430	1.1613
85.2340	0.2341	1.7590	85.2177	0.2695	1.8931	85.1979	0.1069	1.4438	85.2427	0.1417	1.1833
90.0085	0.0561	2.3370	89.9864	0.0876	1.9353	90.0411	0.0324	1.3916	90.0648	0.0509	1.1723
Re=40,000											
-10.5210	-0.4114	0.3228	-10.4122	-0.3241	0.2009	-10.4892	-0.4850	0.1824	-10.3636	-0.3842	0.1566
-5.5925	-0.4679	0.1580	-5.4628	-0.3147	0.1683	-5.5251	-0.5133	0.1201	-5.3182	-0.3484	0.1250
0.0034	0.0520	0.2200	-0.1191	0.0046	0.1544	0.0163	-0.0365	0.1510	0.1011	-0.0188	0.1168
5.7195	0.6175	0.2495	5.5872	0.5599	0.2183	5.8196	0.5978	0.2047	5.7789	0.5632	0.1658
11.3796	1.1388	0.3528	11.0618	0.9330	0.2943	11.3684	1.0312	0.2633	11.2194	0.9095	0.2501
16.6342	1.3398	0.4774	16.3652	1.1716	0.4031	16.6128	1.2242	0.3334	16.5805	1.1934	0.3587
22.2260	1.8566	0.4458	22.1302	1.7730	0.4649	22.3493	1.8058	0.3749	22.3548	1.8022	0.4259
26.5646	1.3342	0.6862	26.4729	1.2562	0.6436	26.6072	1.2198	0.5364	26.6383	1.2389	0.6008
31.7101	1.4492	0.8942	31.5851	1.3445	0.8393	31.7199	1.3088	0.7132	31.7622	1.3363	0.7746
36.7748	1.5002	1.0593	36.6128	1.3662	0.9906	36.9720	1.5079	0.9682	36.7852	1.3544	0.9329
41.7801	1.4551	1.1913	41.5609	1.3254	1.1288	41.9171	1.4645	1.1742	41.7723	1.3442	1.1078
46.7116	1.4010	1.4473	46.5071	1.2831	1.2616	46.8688	1.4264	1.3708	46.6773	1.2696	1.2401
51.5841	1.3003	1.4252	51.4104	1.2071	1.3712	51.6727	1.2715	1.4132	51.5901	1.2010	1.3554
56.4393	1.1859	1.5890	56.2977	1.0694	1.4672	56.6164	1.2271	1.6429	56.5092	1.0883	1.4650
61.2234	1.0154	1.5583	61.1561	0.9580	1.5705	61.4572	1.0520	1.6431	61.3386	0.9541	1.5226
66.1339	0.9135	1.8383	65.9611	0.8047	1.5973	66.2570	0.8939	1.7368	66.1801	0.8295	1.5917
70.9186	0.7254	1.8212	70.8434	0.7122	1.7508	71.0053	0.6952	1.8290	71.0346	0.7151	1.7079
75.7715	0.6092	2.0889	75.6694	0.5754	1.7828	75.8635	0.5832	1.9476	75.8538	0.5730	1.7449
80.3397	0.3176	1.9671	80.4674	0.4166	1.8975	80.6031	0.4269	1.7630	80.6645	0.4241	1.8282
85.2037	0.2102	1.8949	85.1624	0.2260	1.9054	85.3792	0.2501	1.8116	85.3600	0.2339	1.8663
89.9570	0.0154	2.2894	89.9387	0.0501	1.8926	90.1277	0.1009	2.1913	90.0666	0.0524	1.8858
Re=50,000											
-10.5209	-0.4113	0.2837	-10.4779	-0.3757	0.1971	-10.4724	-0.4717	0.1642	-10.4315	-0.3884	0.1807
-5.6002	-0.4740	0.1680	-5.4810	-0.3290	0.1685	-5.5158	-0.5061	0.1359	-5.3701	-0.3401	0.1501
-0.1330	-0.0556	0.1653	-0.1197	0.0042	0.1519	-0.0042	-0.0526	0.1281	0.0868	0.0191	0.1431
5.6878	0.5925	0.2294	5.6032	0.5725	0.2090	5.8162	0.5952	0.2106	5.7491	0.5889	0.1919
11.2840	1.0633	0.3340	11.0691	0.9388	0.2815	11.3942	1.0516	0.2733	11.2053	0.9476	0.2720
16.5134	1.2444	0.4178	16.4046	1.2026	0.3870	16.5778	1.1966	0.3623	16.5293	1.2023	0.3719
22.2414	1.8687	0.4373	22.1898	1.8199	0.4556	22.3465	1.8036	0.3691	22.3341	1.8350	0.4353
26.5698	1.3384	0.6206	26.4785	1.2606	0.6323	26.5636	1.1854	0.5564	26.6116	1.2670	0.6185
31.6912	1.4342	0.8647	31.5875	1.3464	0.8325	31.7341	1.3200	0.7291	31.7123	1.3462	0.8021
36.7048	1.4449	0.9896	36.6052	1.3603	0.9668	36.9368	1.4801	1.0314	36.7432	1.3705	0.9781
41.7933	1.4655	1.2001	41.5848	1.3442	1.1393	41.9050	1.4549	1.1939	41.6987	1.3355	1.1285
46.6441	1.3477	1.3207	46.4953	1.2739	1.2620	46.7791	1.3556	1.2656	46.6322	1.2832	1.2836
51.6115	1.3219	1.4702	51.3773	1.1811	1.3746	51.7356	1.3212	1.4193	51.5043	1.1826	1.3668
56.4021	1.1565	1.5468	56.3307	1.0953	1.5107	56.5426	1.1688	1.5651	56.4115	1.0605	1.4695
61.2592	1.0437	1.6001	61.1491	0.9525	1.5887	61.4379	1.0368	1.6419	61.2565	0.9387	1.5480
66.0533	0.8811	1.7340	65.9762	0.8166	1.6293	66.3310	0.9523	1.7633	66.0980	0.8141	1.6337
70.9110	0.7194	1.7894	70.8262	0.6987	1.7492	71.0766	0.7515	1.8423	70.9504	0.6981	1.7142
75.7455	0.5887	2.0066	75.6318	0.5459	1.7767	75.9042	0.6153	1.8804	75.7685	0.5551	1.8100
80.4180	0.3794	1.9814	80.4166	0.3767	1.8477	80.5931	0.4190	1.8104	80.5532	0.3858	1.8526
85.1786	0.1904	2.0266	85.1335	0.2032	1.8967	85.3617	0.2363	1.9431	85.2630	0.2068	1.8881
89.9301	-0.0058	2.0276	89.9078	0.0258	1.8832	90.1454	0.1148	2.0383	90.0295	0.0232	1.9097

Re=60,000											
-10.5616	-0.4435	0.3382	-10.4615	-0.3628	0.2094	-10.4696	-0.4696	0.1782	-10.4071	-0.3692	0.2056
-5.6154	-0.4859	0.1986	-5.4691	-0.3197	0.1755	-5.4810	-0.4786	0.1249	-5.3522	-0.3260	0.1672
-0.0598	0.0021	0.2243	-0.1026	0.0176	0.1571	0.0176	-0.0355	0.1275	0.1071	0.0350	0.1513
5.7186	0.6168	0.2569	5.6200	0.5857	0.2227	5.7913	0.5755	0.1963	5.7467	0.5870	0.2134
11.2878	1.0663	0.3657	11.0809	0.9480	0.3007	11.3353	1.0051	0.2872	11.2245	0.9627	0.2874
16.5139	1.2448	0.4579	16.4258	1.2192	0.4003	16.5550	1.1786	0.3675	16.5634	1.2291	0.3969
22.2177	1.8500	0.4598	22.2334	1.8542	0.4628	22.3456	1.8029	0.3718	22.3587	1.8543	0.4429
26.5041	1.2865	0.6140	26.4683	1.2526	0.6405	26.6394	1.2453	0.5832	26.5882	1.2486	0.6347
31.6197	1.3778	0.8207	31.5932	1.3509	0.8461	31.8229	1.3901	0.8305	31.7172	1.3500	0.8323
36.7337	1.4677	1.0234	36.6043	1.3596	0.9867	36.8845	1.4387	1.0201	36.7372	1.3657	0.9926
41.7335	1.4182	1.1611	41.5858	1.3450	1.1491	41.9079	1.4573	1.2366	41.6939	1.3317	1.1446
46.6605	1.3606	1.3363	46.5166	1.2906	1.3010	46.8039	1.3751	1.3584	46.5975	1.2559	1.2632
51.5707	1.2897	1.4816	51.3679	1.1737	1.3854	51.6998	1.2930	1.5025	51.5130	1.1895	1.4036
56.4373	1.1843	1.5511	56.2925	1.0653	1.4983	56.5121	1.1447	1.5195	56.4276	1.0732	1.5100
61.2454	1.0328	1.6132	61.1350	0.9414	1.5800	61.4161	1.0196	1.6786	61.2467	0.9310	1.5722
66.0100	0.8469	1.6506	65.9561	0.8008	1.6492	66.2215	0.8659	1.7394	66.0628	0.7864	1.6231
70.9194	0.7262	1.8274	70.7833	0.6650	1.6921	71.0367	0.7200	1.8213	70.9322	0.6837	1.7617
75.7357	0.5809	1.9238	75.5962	0.5179	1.7847	75.8743	0.5917	1.9527	75.7398	0.5325	1.8347
80.4347	0.3926	1.9713	80.3841	0.3511	1.8354	80.5862	0.4135	1.9927	80.5205	0.3601	1.8509
85.1896	0.1991	1.9569	85.1064	0.1819	1.8761	85.2879	0.1780	1.9741	85.2325	0.1828	1.8476
89.9202	-0.0137	1.9673	89.8897	0.0116	1.8713	90.0746	0.0589	2.0200	90.0071	0.0056	1.8878
Re=70,000											
-10.5075	-0.4008	0.3321	-10.4245	-0.3337	0.2220	-10.4829	-0.4801	0.1899	-10.3475	-0.3224	0.2071
-5.5308	-0.4192	0.1839	-5.4426	-0.2988	0.1882	-5.5140	-0.5046	0.1477	-5.3181	-0.2992	0.1746
0.0811	0.1134	0.2318	-0.0710	0.0425	0.1743	0.0669	0.0035	0.1318	0.1457	0.0654	0.1628
5.7679	0.6558	0.2849	5.6217	0.5870	0.2304	5.8260	0.6029	0.2157	5.8452	0.6153	0.2240
11.3121	1.0855	0.3787	11.1045	0.9666	0.3118	11.3494	1.0162	0.2770	11.2515	0.9839	0.2975
16.5541	1.2766	0.4588	16.4421	1.2320	0.4170	16.5894	1.2058	0.3961	16.5937	1.2529	0.4039
22.2270	1.8573	0.4703	22.2264	1.8486	0.4764	22.2658	1.7399	0.3413	22.3554	1.8518	0.4632
26.5758	1.3430	0.6351	26.4770	1.2595	0.6430	26.6003	1.2143	0.5737	26.6032	1.2604	0.6430
31.6206	1.3784	0.8545	31.5942	1.3516	0.8479	31.7778	1.3545	0.8082	31.7245	1.3558	0.8454
36.7082	1.4477	1.0290	36.6022	1.3579	1.0074	36.8784	1.4339	1.0241	36.7156	1.3488	0.9906
41.7459	1.4280	1.1976	41.5726	1.3346	1.1580	41.8259	1.3925	1.1833	41.6855	1.3251	1.1430
46.6315	1.3377	1.3227	46.4599	1.2460	1.2558	46.7508	1.3332	1.3369	46.5817	1.2435	1.2578
51.5373	1.2633	1.4271	51.3278	1.1422	1.3631	51.6856	1.2817	1.4837	51.5325	1.1557	1.3811
56.4041	1.1581	1.5770	56.2781	1.0540	1.4887	56.4080	1.0625	1.4338	56.3869	1.0413	1.4765
61.2339	1.0237	1.6659	61.1101	0.9219	1.5772	60.9776	0.6733	1.0501	61.2157	0.9066	1.5475
66.0028	0.8413	1.6965	65.9355	0.7846	1.6587	65.8503	0.5728	1.0955	66.0476	0.7744	1.6273
70.8575	0.7190	1.8530	70.7831	0.6648	1.7473	70.7446	0.4892	1.1467	70.9051	0.6624	1.7156
75.7020	0.5544	1.9266	75.5820	0.5067	1.8055	75.6056	0.3796	1.1927	75.7020	0.5028	1.7717
80.4083	0.3718	1.9271	80.3703	0.3403	1.8394	80.3911	0.2595	1.2116	80.4982	0.3425	1.8607
85.1467	0.1652	1.9663	85.0926	0.1710	1.8983	85.2241	0.1276	1.2652	85.2136	0.1680	1.8714
89.9371	-0.0003	1.9361	89.8690	-0.0047	1.8701	89.9786	-0.0169	1.3344	89.9862	-0.0108	1.8554
Re=80,000											
-10.5195	-0.4102	0.3428	-10.3601	-0.2831	0.2320	-10.3320	-0.3609	0.1444	-10.3009	-0.2857	0.2141
-5.4981	-0.3933	0.2555	-5.4011	-0.2662	0.2083	-5.3280	-0.3578	0.1168	-5.2628	-0.2558	0.1861
0.1781	0.1900	0.2261	-0.0274	0.0767	0.1879	0.1364	0.0583	0.1277	0.1830	0.0947	0.1858
5.8458	0.7173	0.3169	5.6478	0.6075	0.2446	5.8571	0.6275	0.2354	5.8847	0.6464	0.2430
11.3279	1.0979	0.3837	11.1081	0.9694	0.3289	11.3547	1.0204	0.2972	11.3060	1.0268	0.3262
16.5903	1.3052	0.4844	16.4303	1.2227	0.4317	16.5904	1.2065	0.3797	16.6647	1.3087	0.4289
22.2067	1.8413	0.4923	22.2020	1.8295	0.4950	22.2348	1.7154	0.3390	22.3999	1.8868	0.4749
26.5939	1.3574	0.6691	26.4904	1.2700	0.6577	26.6063	1.2191	0.5698	26.6316	1.2827	0.6659
31.6350	1.3898	0.9168	31.5898	1.3482	0.8693	31.7135	1.3037	0.7628	31.7466	1.3732	0.8624
36.6693	1.4169	1.0233	36.5888	1.3474	0.9935	36.8490	1.4108	1.0353	36.7130	1.3467	0.9975
41.6907	1.3845	1.1484	41.5307	1.3017	1.1254	41.8479	1.4099	1.2290	41.6242	1.2769	1.1102
46.6108	1.3214	1.3126	46.4342	1.2259	1.2466	46.7430	1.3271	1.3488	46.5585	1.2253	1.2540
51.5426	1.2675	1.4786	51.3192	1.1354	1.3609	51.6402	1.2459	1.4674	51.4792	1.1138	1.3376
56.3991	1.1542	1.5955	56.2627	1.0418	1.4785	56.5470	1.1229	1.5755	56.3370	1.0020	1.4235
61.1978	0.9952	1.6617	61.0791	0.8975	1.5363	61.3614	0.9763	1.6579	61.1947	0.8901	1.5338
66.0319	0.8642	1.7349	65.9084	0.7633	1.6142	66.1800	0.8331	1.7152	66.0452	0.7726	1.6346
70.8176	0.6898	1.8335	70.7695	0.6541	1.7279	70.9986	0.6899	1.8400	70.8813	0.6437	1.7346
75.6857	0.5415	1.9401	75.5637	0.4923	1.8073	75.7714	0.5104	1.8774	75.6837	0.4883	1.8074
80.3726	0.3436	1.9422	80.3581	0.3307	1.8635	80.4885	0.3364	1.9381	80.4685	0.3192	1.8375
85.1393	0.1593	1.9456	85.0700	0.1533	1.8572	85.2632	0.1585	1.9763	85.1935	0.1522	1.8577
89.9287	-0.0070	1.9740	89.8542	-0.0164	1.8807	90.0145	0.0114	1.9991	89.9625	-0.0295	1.8720

Re=90,000												
-10.3676	-0.2903	0.3580	-10.3273	-0.2573	0.2293	-10.2912	-0.3287	0.1901	-10.2863	-0.2742	0.2298	
-5.6516	-0.5145	0.2915	-5.3911	-0.2583	0.2379	-5.1921	-0.2504	0.1449	-5.2600	-0.2536	0.2078	
-0.0958	-0.0263	0.2622	0.0286	0.1207	0.2078	0.2965	0.1848	0.1162	0.1792	0.0918	0.1888	
5.6425	0.5567	0.3463	5.6944	0.6442	0.2770	6.0890	0.8106	0.1847	5.9806	0.7218	0.2294	
11.1394	0.9491	0.4031	11.0898	0.9551	0.3505	11.5554	1.1789	0.2856	11.3368	1.0510	0.3144	
16.5001	1.2340	0.4956	16.3623	1.1693	0.4683	16.7517	1.3339	0.3807	16.7369	1.3655	0.4208	
22.2484	1.8742	0.5263	22.1673	1.8022	0.5123	22.2907	1.7596	0.3977	22.4234	1.9053	0.4875	
26.6258	1.3826	0.7090	26.6221	1.3736	0.6698	26.5892	1.2056	0.5681	26.7152	1.3484	0.6686	
31.7111	1.4499	0.9868	31.5049	1.2814	0.8583	31.7596	1.3401	0.8082	31.8353	1.4429	0.8899	
36.6548	1.4055	1.0346	36.5827	1.3426	1.0248	36.8374	1.4016	1.0422	36.7658	1.3882	1.0497	
41.6771	1.3737	1.1789	41.4576	1.2442	1.1065	41.7937	1.3671	1.2255	41.6494	1.2967	1.1447	
46.5717	1.2905	1.3118	46.3858	1.1877	1.2257	46.7055	1.2974	1.3215	46.4991	1.1786	1.2279	
51.4893	1.2254	1.4437	51.1724	1.0200	1.2757	51.6283	1.2365	1.4740	51.4433	1.0855	1.2816	
56.3460	1.1122	1.5352	56.1354	0.9418	1.3513	56.5298	1.1094	1.5635	56.3363	1.0014	1.3646	
61.2275	1.0187	1.7090	61.0291	0.8582	1.5139	61.3555	0.9717	1.6498	61.2002	0.8945	1.5116	
66.0163	0.8519	1.7584	65.7129	0.6096	1.3388	66.1857	0.8376	1.7860	65.9985	0.7359	1.5862	
70.8186	0.6933	1.8349	70.5081	0.4486	1.1813	70.9895	0.6827	1.8489	70.8776	0.6408	1.7533	
75.6312	0.4985	1.9006	75.3640	0.3353	1.2142	75.7975	0.5310	1.9035	75.6724	0.4795	1.7958	
80.3757	0.3460	1.9677	80.2204	0.2224	1.2328	80.5131	0.3559	1.9549	80.4531	0.3071	1.8380	
85.1344	0.1555	1.9923	85.0100	0.1061	1.2575	85.2944	0.1832	1.8751	85.1757	0.1381	1.8455	
89.8860	-0.0407	2.0400	89.8599	-0.0119	1.2597	90.0213	0.0168	2.0341	89.9557	-0.0348	1.8720	
Re=100,000												
-10.3537	-0.2793	0.3165	-10.3038	-0.2388	0.2504	-10.2528	-0.2984	0.2089	-10.2384	-0.2365	0.2407	
-5.5413	-0.4275	0.2935	-5.3631	-0.2363	0.2280	-5.1798	-0.2407	0.1737	-5.2156	-0.2186	0.1740	
-0.0674	-0.0039	0.2635	0.0004	0.0986	0.2315	0.3264	0.2084	0.1525	0.2337	0.1346	0.1913	
5.5228	0.4622	0.3479	5.7200	0.6643	0.2692	6.0687	0.7946	0.1961	5.9586	0.7045	0.2387	
11.0258	0.8594	0.4028	11.1214	0.9799	0.3857	11.6021	1.2158	0.2729	11.3744	1.0805	0.3040	
16.2937	1.0710	0.4850	16.4260	1.2194	0.4883	16.9431	1.4851	0.3936	16.7037	1.3394	0.4367	
22.0168	1.6914	0.5329	22.0944	1.7449	0.5393	22.5386	1.9553	0.4437	22.3621	1.8571	0.5025	
26.5618	1.3320	0.7028	26.6223	1.3737	0.6379	26.7027	1.2952	0.5896	26.6887	1.3277	0.6652	
31.6927	1.4354	0.9752	31.5597	1.3245	0.8816	31.7923	1.3660	0.8150	31.7753	1.3957	0.8687	
36.6498	1.4015	1.0878	36.5805	1.3409	0.9748	36.8066	1.3773	1.0268	36.8089	1.4221	1.0482	
41.6062	1.3177	1.1834	41.4538	1.2413	1.1189	41.7779	1.3546	1.2061	41.6608	1.3057	1.1524	
46.5660	1.2860	1.3144	46.3431	1.1542	1.2589	46.6416	1.2470	1.2858	46.5477	1.2168	1.2472	
51.4371	1.1842	1.4048	51.1520	1.0039	1.2064	51.5209	1.1517	1.3700	51.4453	1.0871	1.3456	
56.2446	1.0322	1.4453	56.0022	0.8370	1.2392	56.4450	1.0424	1.4782	56.2537	0.9365	1.3284	
61.1476	0.9556	1.6259	60.8485	0.7162	1.3883	61.3329	0.9538	1.6380	60.9349	0.6859	1.1390	
65.9649	0.8113	1.7268	65.8693	0.7326	1.5726	66.1487	0.8084	1.7176	65.7543	0.5439	1.1761	
70.7379	0.6320	1.7824	70.6105	0.5291	1.4514	70.9886	0.6820	1.8413	70.6809	0.4862	1.3717	
75.5992	0.4732	1.8850	75.3642	0.3354	1.2358	75.7827	0.5194	1.8365	75.6534	0.4646	1.7233	
80.3535	0.3285	1.9448	80.2191	0.2214	1.2603	80.5627	0.3457	1.9063	80.4548	0.3084	1.8379	
85.1334	0.1547	2.0102	85.0041	0.1015	1.2775	85.2500	0.1480	1.8737	85.1887	0.1484	1.8473	
89.8717	-0.0520	2.0173	89.8555	-0.0154	1.2734	89.9750	-0.0197	2.0038	89.9759	-0.0189	1.8374	

Quasi-steady measurements																				
CA1604, Re = 60,000																				
$\alpha = 45^\circ + 45^\circ \sin k\tau$																				
Averaging cycles = 5																				
$\alpha$	$C_l$	$C_d$	$\alpha$	$C_l$	$C_d$	$\alpha$	$C_l$	$C_d$	$\alpha$	$C_l$	$C_d$	$\alpha$	$C_l$	$C_d$	$\alpha$	$C_l$	$C_d$	$\alpha$	$C_l$	
k=0.01				k=0.02				k=0.03				k=0.04				k=0.05				k=0.06
0	0.1961	0.1219	0.0000	0.1785	0.1281	0.0001	0.2115	0.1345	0.0002	0.2826	0.0936	0.0002	0.3785	0.0591	0.0004	0.4717	0.0262			
0.0904	0.1911	0.1231	0.0901	0.1705	0.1266	0.0865	0.2087	0.1303	0.0933	0.2848	0.0977	0.0910	0.3789	0.0573	0.0976	0.4772	0.0177			
0.3614	0.186	0.1282	0.3604	0.1920	0.1229	0.3529	0.2279	0.1308	0.3658	0.2938	0.0985	0.3609	0.4018	0.0506	0.3725	0.5022	0.0096			
0.8119	0.2333	0.129	0.8101	0.2205	0.1253	0.7985	0.2575	0.1320	0.8167	0.3330	0.0969	0.8089	0.4308	0.0426	0.8268	0.5428	0.0031			
1.44	0.2908	0.1226	1.4374	0.2785	0.1290	1.4212	0.3129	0.1404	1.4453	0.3684	0.0953	1.4350	0.4809	0.0399	1.4568	0.5866	0.0000			
2.2433	0.3866	0.1328	2.2396	0.3566	0.1337	2.2187	0.3909	0.1487	2.2479	0.4408	0.0857	2.2349	0.5470	0.0398	2.2610	0.6533	0.0049			
3.2184	0.4906	0.1431	3.2138	0.4556	0.1389	3.1878	0.4874	0.1277	3.2216	0.5312	0.0829	3.2056	0.6271	0.0341	3.2362	0.7140	0.0111			
4.3616	0.6306	0.1542	4.3557	0.5755	0.1492	4.3246	0.5944	0.1268	4.3632	0.6381	0.0811	4.3446	0.7222	0.0461	4.3774	0.7988	0.0310			
5.6682	0.7921	0.1714	5.6609	0.7038	0.1632	5.6244	0.7322	0.1368	5.6670	0.749	0.0846	5.6457	0.8243	0.0617	5.6821	0.8884	0.0575			
7.1328	0.9183	0.1925	7.1242	0.8564	0.1817	7.0821	0.9023	0.1543	7.1284	0.8785	0.1085	7.1042	0.9354	0.0927	7.1424	0.9885	0.0934			
8.7497	1.0589	0.2269	8.7396	0.9990	0.2034	8.6921	1.0318	0.1741	8.7418	1.0093	0.1391	8.7151	1.0551	0.1330	8.7555	1.0983	0.1374			
10.5124	1.1641	0.2491	10.5007	1.1441	0.2300	10.4477	1.1860	0.2127	10.5000	1.1461	0.1925	10.4706	1.1809	0.1869	10.5120	1.2210	0.1918			
12.4137	1.289	0.2714	12.4004	1.2887	0.2670	12.3418	1.3322	0.2842	12.3963	1.2869	0.2522	12.3644	1.3215	0.2526	12.4073	1.3525	0.2584			
14.4459	1.448	0.3171	14.4309	1.4315	0.3302	14.3668	1.4744	0.3570	14.4235	1.4179	0.3297	14.3893	1.4543	0.3318	14.4321	1.4955	0.3392			
16.601	1.6116	0.3741	16.5843	1.5532	0.4109	16.5146	1.6076	0.4501	16.5572	1.5505	0.4228	16.5361	1.6046	0.4291	16.5792	1.6372	0.4376			
18.8702	1.7371	0.4545	18.8518	1.6698	0.5072	18.7766	1.7404	0.5548	18.8358	1.7164	0.5380	18.7971	1.7310	0.5384	18.8399	1.7600	0.5450			
21.2445	1.7875	0.5489	21.2243	1.7910	0.6210	21.1437	1.8577	0.6778	21.2038	1.8233	0.6540	21.1631	1.8381	0.6568	21.2047	1.8612	0.6634			
23.7141	1.8039	0.6542	23.6923	1.8571	0.7305	23.6065	1.9037	0.7235	23.6667	1.9294	0.7833	23.6242	1.9210	0.7815	23.6650	1.9333	0.7834			
26.2093	1.7288	0.7379	26.2457	1.8641	0.8268	26.1549	1.9069	0.8808	26.2151	1.9486	0.8973	26.1709	1.9679	0.9040	26.2098	1.9763	0.9037			
28.8998	1.5908	0.7949	28.8745	1.8311	0.9136	28.7790	1.9317	0.1004	28.8386	1.8931	0.1921	28.7839	1.9988	0.1026						
31.5949	1.4502	0.8496	31.5680	1.7549	0.9863	31.4680	1.8193	0.1099	31.5265	1.9759	0.1386	31.4798	1.9975	0.1143	31.5149	2.0043	0.1531			
34.3438	1.3877	0.9244	34.3154	1.6584	1.0508	34.2112	1.8721	1.1925	34.2683	1.9376	0.1474	34.2247	1.9883	0.1263	34.2533	1.9978	0.1282			
37.1534	1.3594	0.9995	37.1056	1.5342	1.1015	36.9976	1.8138	1.2762	37.0529	1.8909	1.3469	37.0048	1.9615	1.3876	37.0348	1.9715	1.4079			
39.9586	1.3337	1.0853	39.9274	1.4263	1.1622	39.8159	1.7424	1.3338	39.8691	1.8500	1.4542	39.8260	1.9170	1.5030	39.8479	1.9373	1.5320			
42.8019	1.3042	1.1763	42.7694	1.3328	1.2312	42.6550	1.6034	1.3966	42.7057	1.7693	1.5362	42.6571	1.8571	1.6071	42.6814	1.8877	1.6478			
45.654	1.2691	1.2641	45.6204	1.2672	1.3081	45.5033	1.4757	1.4423	45.5512	1.6633	1.5899	45.5028	1.7773	1.6994	45.5241	1.8288	1.7595			
48.5033	1.2223	1.346	48.4687	1.2028	1.3754	48.3495	1.3996	1.5231	48.3842	1.5606	1.6439	48.3465	1.6843	1.7766	48.3645	1.7516	1.8558			
51.3383	1.1529	1.3998	51.3029	1.1263	1.4287	51.1821	1.3118	1.6020	51.2234	1.4300	1.6683	51.1765	1.5722	1.8268	51.1915	1.6617	1.9370			
54.1478	1.067	1.4433	54.1116	1.0626	1.4954	53.9988	1.2064	1.6577	54.0273	1.3079	1.6941	53.9813	1.4507	1.8630	53.9933	1.5612	2.0013			
56.9203	0.9879	1.4778	56.8836	0.9955	1.5580	56.7612	1.1094	1.7038	56.7949	1.1910	1.7278	56.7509	1.3173	1.8709	56.7594	1.4498	2.0446			
59.6447	0.8904	1.4832	59.6077	0.9105	1.5586	59.4853	1.0139	1.7498	59.5148	1.0882	1.7723	59.4577	1.1906	1.8761	59.4780	1.3339	2.0741			
62.3101	0.7945	1.484	62.2730	0.8198	1.5933	62.1512	0.9241	1.7951	62.1762	0.9693	1.7938	62.1364	1.0688	1.8801	62.1388	1.2099	2.0880			
64.9057	0.7027	1.47	64.8686	0.7361	1.6152	64.7481	0.8399	1.8360	64.7687	0.8500	1.8473	64.7310	0.9526	1.8863	64.7310	1.0862	2.0873			
67.4211	0.617	1.4829	67.3843	0.6493	1.6186	67.2656	0.7343	1.8388	67.2813	0.7572	1.8197	67.2473	0.8425	1.8972	67.2440	0.9662	2.0841			
69.8461	0.5376	1.4732	69.8099	0.5633	1.5925	69.6937	0.6436	1.8901	69.7045	0.6633	1.8233	69.6738	0.7389	1.8974	69.6684	0.8543	2.0807			
72.1711	0.4667	1.4703	72.1355	0.4848	1.5700	72.0255	0.5516	1.8710	72.0285	0.5819	1.8233	72.0018	0.6402	1.8950	71.9934	0.7551	2.0866			
74.3866	0.3966	1.4356	74.3520	0.4145	1.5541	74.2428	0.4707	1.7751	74.2434	0.4967	1.8150	74.2207	0.5431	1.8851	74.2114	0.6591	2.0960			
76.4837	0.3332	1.408	76.4503	0.3463	1.5421	76.3455	0.4037	1.7660	76.3411	0.4269	1.8101	76.3228	0.4553	1.8630	76.3110	0.5673	2.1066			
78.454	0.2703	1.3791	78.4220	0.2812	1.5118	78.3222	0.3293	1.7472	78.3130	0.3597	1.7895	78.2996	0.3762	1.8470	78.2866	0.4780	2.1072			
80.2896	0.2238	1.3217	80.2593	0.2280	1.4787	80.1651	0.2703	1.7093	80.1793	0.2936	1.7590	80.1402	0.3060	1.8161	80.1281	0.3974	2.1118			
81.9831	0.1801	1.3132	81.9546	0.1792	1.4394	81.8667	0.2127	1.6559	81.8471	0.2306	1.7199	81.8442	0.2483	1.7855	81.8296	0.3211	2.0911			
83.5277	0.1366	1.2848	83.5012	0.1402	1.4022	83.4203	0.1624	1.6204	83.3958	0.1868	1.7692	83.3398	0.1935	1.7500	83.3386	0.2568	2.0659			
84.9171	0.1028	1.2627	84.8930	0.0921	1.3695	84.8195	0.1234	1.6024	84.7814	0.1412	1.7287	84.7304	0.1843	1.8463	84.7304	0.2404	2.0342			
85.7392	0.03	1.2547	85.7449	-0.0267	1.2287	85.7160	0.0233	1.3437	85.6934	-0.0027	1.4063	85.6762	0.0071	1.4244	85.7710	0.0181	1.8110			
89.3817	0.0091	1.2486	89.3916	-0.0201	1.2317	89.4194	0.0078	1.3189	89.3488	0.008	1.3946	89.2955	0.0184	1.4137	89.4387	0.0289	1.7916			
88.8455	0.0159	1.2442	88.8595	0.0013	1.2263	88.8994	0.0199	1.2928	88.8258	0.0173	1.3587	88.9141	0.0323	1.3792	88.9273	0.0449	1.7691			
88.1328	0.0298	1.2453	88.1510	0.0188	1.2198	88														

CA1604, Re = 100,000																	
$\alpha = 45^\circ + 45^\circ \sin k\tau$																	
Averaging cycles = 5																	
$\alpha$		$C_l$	$C_d$	$\alpha$		$C_l$	$C_d$	$\alpha$		$C_l$	$C_d$	$\alpha$		$C_l$	$C_d$		
k=0.01		k=0.02		k=0.03		k=0.04		k=0.05		k=0.06							
0	0.1927	0.1436	0	0.2781	0.128	0.0002	0.397	0.0481	0.0007	-0.5533	0.0085	0.0009	0.617	-0.0347	0.0011	-0.7145	0.0438
0.0919	0.193	0.1419	0.0937	0.2753	0.1303	0.0983	0.3805	0.0408	0.0792	0.5635	-0.0123	0.0757	0.6565	-0.0318	0.0818	0.7571	-0.0438
0.3643	0.2136	0.1421	0.3677	0.2912	0.129	0.3758	0.3849	0.0336	0.3372	0.5927	-0.0116	0.3292	0.6944	-0.0267	0.3384	0.8018	-0.0405
0.8163	0.2599	0.1434	0.8208	0.3267	0.1304	0.8316	0.4084	0.0289	0.7736	0.6287	-0.0067	0.7604	0.7359	-0.0193	0.7701	0.855	-0.0334
1.446	0.3228	0.1461	1.4513	0.3742	0.1241	1.4657	0.4463	0.0251	1.3866	0.6628	-0.0005	1.3677	0.7753	-0.012	1.3834	0.9222	-0.0223
2.2508	0.4098	0.1512	2.2566	0.4411	0.118	2.274	0.5025	0.0262	2.1738	0.7177	0.0092	2.1489	0.8205	0	2.1675	0.9907	-0.0062
3.2275	0.5136	0.1575	3.2335	0.5264	0.1151	3.2529	0.5732	0.0317	3.1321	0.7793	0.0233	3.1037	0.8962	0.0183	3.1196	1.0605	0.0167
4.3723	0.6334	0.1694	4.3785	0.6311	0.1148	4.4003	0.6532	0.0441	4.2576	0.8659	0.0449	4.2251	0.9599	0.0391	4.2436	1.1269	0.0432
5.6804	0.7622	0.1842	5.6857	0.7475	0.1195	5.71	0.7453	0.0643	5.5458	0.9584	0.0735	5.5088	1.0412	0.0698	5.5271	1.205	0.0782
7.1467	0.8984	0.1953	7.1511	0.8743	0.1364	7.1765	0.852	0.0929	6.9916	1.0153	0.1086	6.9496	1.1373	0.1074	6.9655	1.2906	0.1227
8.7652	1.031	0.2103	8.7685	1.0069	0.1685	8.7959	0.973	0.1316	8.5892	1.1717	0.1633	8.5424	1.2436	0.1566	8.56	1.3613	0.1716
10.5295	1.174	0.2384	10.5313	1.1431	0.217	10.5602	1.084	0.1797	10.3322	1.2894	0.2023	10.2824	1.3384	0.2134	10.2971	1.4234	0.2272
12.4324	1.3396	0.2787	12.4324	1.2766	0.2775	12.462	1.2155	0.2434	12.2136	1.4088	0.2859	12.1606	1.4217	0.2777	12.1703	1.4835	0.2879
14.4663	1.4788	0.3392	14.4642	1.4002	0.3498	14.4947	1.3428	0.3194	14.2259	1.5086	0.3631	14.1694	1.505	0.3524	14.1783	1.5355	0.3588
16.623	1.596	0.4189	16.6186	1.5288	0.4365	16.6497	1.4554	0.4057	16.3611	1.5938	0.4438	16.3009	1.5725	0.4325	16.3068	1.5829	0.4342
18.8938	1.6974	0.5129	18.8869	1.6358	0.5345	18.918	1.5936	0.5363	18.6107	1.6713	0.5349	18.547	1.6336	0.52	18.5479	1.6311	0.5169
21.2695	1.7507	0.6042	21.2599	1.6975	0.6277	21.2911	1.6039	0.5936	20.9656	1.7324	0.6288	20.1	1.6896	0.6163	20.8976	1.6781	0.6078
23.7408	1.7251	0.6734	23.7286	1.7397	0.7261	23.759	1.6481	0.6937	23.4165	1.7768	0.7294	23.3488	1.7374	0.7194	23.3414	1.7168	0.7077
26.2975	1.6622	0.7331	26.2818	1.7587	0.8219	26.3124	1.6318	0.7983	25.9535	1.8141	0.83	25.8866	1.7752	0.8328	25.8703	1.7471	0.814
28.9295	1.5736	0.7899	28.9108	1.7512	0.9113	28.9405	1.6903	0.9022	28.5665	1.8335	0.9495	28.4945	1.8024	0.9487	28.4776	1.7658	0.9254
31.6261	1.4631	0.8401	31.6037	1.7267	0.9986	31.633	1.6881	1.0084	31.245	1.8398	1.0644	31.1713	1.8141	1.0624	31.1494	1.7793	1.0436
34.3765	1.3672	0.8926	34.3505	1.6859	1.0837	34.3788	1.6741	1.1125	33.9784	1.8266	1.1761	33.994	1.8053	1.1755	33.8756	1.7762	1.1615
37.1696	1.2876	0.9619	37.1401	1.6338	1.1624	37.1672	1.6464	1.2154	36.7557	1.793	1.27	36.6805	1.7821	1.2863	36.6473	1.7571	1.2729
39.9942	1.2296	1.0295	39.9611	1.5743	1.2393	39.987	1.599	1.3073	39.5659	1.7525	1.3792	39.4901	1.7464	1.3934	39.4515	1.7292	1.3848
42.8389	1.1981	1.114	42.8022	1.4849	1.2981	42.8267	1.533	1.3897	42.3976	1.7019	1.4774	42.3215	1.7019	1.5001	42.2775	1.6966	1.5009
45.6923	1.1627	1.193	45.652	1.3936	1.3556	45.675	1.4601	1.4631	45.2396	1.6356	1.5675	45.1636	1.6456	1.5979	45.1146	1.6456	1.6065
48.5429	1.1093	1.2571	48.4991	1.3114	1.423	48.5204	1.3274	1.5262	48.0805	1.561	1.6495	48.0409	1.5777	1.6891	47.9509	1.5832	1.7072
51.3793	1.0497	1.3148	51.332	1.2234	1.4855	51.3516	1.2864	1.5737	50.909	1.4704	1.7124	50.834	1.501	1.7711	50.7757	1.5158	1.8039
54.1901	0.9797	1.3586	54.1393	1.3127	1.54	54.1576	1.3877	1.6078	53.7138	1.3729	1.760	53.6397	1.4154	1.8422	53.5767	1.4379	1.8905
56.9638	0.8884	1.37	56.9058	1.0317	1.582	56.9259	1.0991	1.6401	56.4836	1.2755	1.8041	56.1045	1.3258	1.9053	56.3437	1.3486	1.9619
59.6895	0.7967	1.3666	59.6323	0.9369	1.6124	59.6467	0.9959	1.6767	59.2073	1.1616	1.816	59.1363	1.2282	1.9534	59.0663	1.2557	2.023
62.3561	0.7007	1.3502	62.2959	0.8434	1.6301	62.3087	0.8999	1.7112	61.8741	1.052	1.8187	61.8047	1.1255	1.9855	61.7309	1.1657	2.0817
64.9528	0.61	1.3162	64.8895	0.7551	1.6413	64.9007	0.8087	1.8747	64.4734	0.9486	1.8129	64.4059	1.0253	2.0094	64.3297	1.0716	2.13
67.4694	0.5265	1.292	67.4039	0.6645	1.6398	67.413	0.7168	1.7703	66.9947	0.8515	1.808	66.9296	0.9226	2.0171	66.8527	0.9746	2.1616
69.8955	0.4517	1.2586	69.8277	0.5778	1.6273	69.8355	0.6297	1.7938	69.4248	0.7551	1.8105	69.366	0.8185	2.0016	69.2858	0.8749	2.1729
72.2216	0.3827	1.2297	72.1517	0.4978	1.6105	72.1576	0.5453	1.8071	71.6735	0.6655	1.8016	71.6047	0.7193	1.9737	71.6224	0.78	2.181
74.4381	0.3295	1.2125	74.3665	0.4246	1.5927	74.3760	0.4645	1.8069	73.9919	0.5819	1.7907	73.9354	0.6294	1.9617	73.8566	0.6855	2.1763
76.5363	0.2753	1.2081	76.4632	0.3534	1.5956	76.4666	0.3921	1.8024	76.1042	0.498	1.7786	76.0607	0.5474	1.9425	75.9712	0.597	2.1594
78.5076	0.2284	1.204	78.4333	0.2927	1.5296	78.4355	0.3265	1.791	78.0922	0.4198	1.7575	78.0424	0.4727	1.9199	77.964	0.5109	2.1205
80.3441	0.1872	1.2041	80.260	0.2368	1.5039	80.2693	0.2683	1.7804	79.9477	0.3483	1.7372	79.9024	0.4067	1.9083	79.8276	0.4359	2.083
82.0385	0.1501	1.2064	81.9629	0.1867	1.4865	81.963	0.2174	1.7124	81.6634	0.2845	1.7124	81.622	0.3438	1.8911	81.548	0.3709	2.0641
83.584	0.1176	1.207	83.5082	0.141	1.4401	83.5071	0.17	1.7424	83.2325	0.2285	1.688	83.1941	0.2856	1.858	83.1248	0.3107	2.043
84.9743	0.0873	1.2022	84.8987	0.1015	1.3979	84.8986	0.1277	1.7147	84.6486	0.1814	1.6571	84.614	0.2333	1.8355	84.5521	0.2593	2.0105
86.2038	0.0628	1.201	86.1288	0.0676	1.3263	86.1268	0.0964	1.6003	85.9061	0.1308	1.6206	85.8750	0.1849	1.8076	85.8167	0.2151	1.9857
87.2676	0.0395	1.2013	87.1935	0.0424	1.3249	87.191	0.0699	1.6639	87	0.11	1.5937	86.975	0.1408	1.7672	86.9212	0.1752	1.9683
88.1614	0.0244	1.1981	88.0886	0.0212	1.3018	88.0858	0.0502	1.6442	87.9259	0.0835	1.5586	87.9054	0.1038	1.7398	87.8611	0.1418	1.9403
88.8816	0.0057	1.1989	88.8104	0.0046	1.2809	88.8081	0.0348	1.6269	88.6868	0.068	1.5248	88.663	0.0726	1.7212	88.6249	0.1136	1.9057
89.4253	-0.0052	1.2086	89.3562	-0.007	1.258	89.354	0.0269	1.5956	89.2955	0.0343	1.6022	89.2463	0.0503	1.6862	89.2174	0.0902	1.8837
89.7903	-0.014	1.2137	89.7236	-0.031	1.2411	89.7217	0.0251	1.5726	89.6619	0.0339	1.4743	89.6536	0.0362	1.6625	89.6364	0.0736	1.8482
89.7592	-0.019	1.2183	89.9112	-0.0186	1.2313	89.9108	0.0277	1.5469	89.8857	0.0277	1.4484	89.8831	0.0281	1.6342	89.872	0.0615	1.8142
89.9793	-0.0217	1.2274	89.918	-0.0154	1.2268	89.9183	0.0254	1.5308	89.								

## Appendix B

### Drivetrain resistance model

This appendix presents the MPB drive train resistance model equation based on the extensive development of Vaz et al. [24]. Under moderate load and speed operation, the MPB bearing frictional torque is given by the following empirical formula based on Palmgren's model [153]

$$Q_{R,p} = Q_l + Q_v \quad (\text{B.1})$$

where  $Q_l$  and  $Q_v$  are the load and viscous friction torques, respectively. With  $Q_l$  expressed as

$$Q_l = f_1 F_\beta d_m \quad (\text{B.2})$$

where  $f_1$  is a factor dependent on the bearing design and relative bearing load.  $F_\beta$  is the force depending on the axial and radial loads, and  $d_m$  is the bearing pitch diameter.  $f_1$  is defined as

$$f_l = z \left( \frac{F_s}{C_s} \right)^y \quad (\text{B.3})$$

where  $F_s$  and  $C_s$  are respectively the static equivalent load and static load rating.  $F_s$  is given as

$$F_s = X_s F_r + Y_s F_a \quad (\text{B.4})$$

Therefore  $f_l$  becomes

$$f_l = z \left( \frac{X_s F_r + Y_s F_a}{C_s} \right)^y \quad (\text{B.5})$$

Here,  $F_r$  and  $F_a$  are the radial and axial load corresponding to the overhanging load on the rotor shaft and rotor thrust determined from BET calculations.  $X_s$  and  $Y_s$  in Eq. B.5 are given in the manufacturer's datasheet as well as parameters  $z$  and  $y$  which are a function of the applied load magnitude and direction. For a deep-groove ball bearing with a nominal contact angle of 0,  $F_\beta$  can be approximated as

$$F_\beta = 3F_a - 0.1F_r \quad (\text{B.6})$$

Similarly, Palmgren [153] established the following empirically based equation to compute the viscous component of the bearing friction torque at moderate speeds.

$$Q_v = \begin{cases} 10^{-7} f_0 (v_0 n)^{2/3} d_m^3, & v_0 n \geq 2000 \\ 160 \times 10^{-7} f_0 d_m^3, & v_0 n < 2000 \end{cases} \quad (\text{B.7})$$

where  $v_0$  is the lubricant kinematic viscosity measured in centistokes and  $n$  is the speed in revolutions per minute (rpm). For the two cases in Eq. B.7,  $f_0$  is a factor depending on the bearing type and lubrication method.

However, the Palmgren model does not fully characterize the resistance of lubricated drivetrains, particularly at very low or zero speeds, especially on the transition from significantly high static to lower dynamic resistance. Accordingly, Ref. [24] modified the Palmgren model to include an additional term to Eq. B.1 given as

$$Q_R = Q_{r,str} + Q_l + Q_v \quad (\text{B.8})$$

$Q_{r,str}$  is the Stribeck frictional torque experienced during starting, i.e. from ( $n = 0$ ), which is heavily dependent on the static frictional torque. For most lubricated sliding contact surfaces, the frictional torque varies with the velocity depending on the magnitude to which interacting surfaces are running under the regimes of lubrication: boundary, mixed or partial and full film. Like lubricated contact surfaces, dry ones exhibit static friction torque higher than the dynamic or sliding frictional torques. Frictional torque in lubricated sliding contacts decreases with an increase in velocity up until either a mixed or full film condition is achieved, then the frictional torque can either increase, decrease, or remain constant for increasing speed. This behavior is referred to as the *Stribeck effect* and its model illustrated in Figure B.1. A simplified form of the Stribeck formulation is expressed as [154, 155]

$$Q_{R,st} = Q_c + (Q_s - Q_c) \exp \left[ - \left( \frac{n}{n_{st}} \right)^i \right] + k_v n \quad (\text{B.9})$$

where  $Q_c$  is the Coulomb frictional torque,  $Q_s$  the maximum static frictional torque,  $n$  the speed of the wind turbine,  $n_{st}$  the Stribeck speed,  $k_v$  the viscous friction coefficient, and  $i$  the exponent.

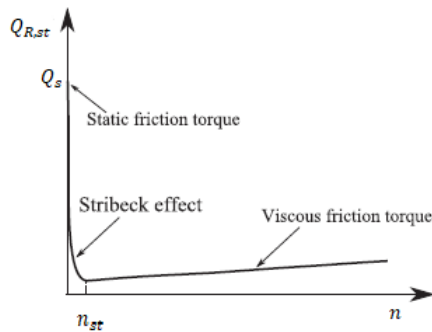


Figure B.1: Schematic of a generalized Stribeck curve.

Combining Eqns.(B.2), (B.5),(B.6), (B.7) and (B.9), the total drivetrain resistance for the windmill rotor is

$$Q_R = z \left( \frac{X_s F_r + Y_s F_a}{C_s} \right)^y (3F_a - 0.1F_r)d_m + 10^{-7} f_0 (v_0 n)^{2/3} d_m^3 \\ + Q_c + (Q_s - Q_c) \exp \left[ - \left( \frac{n}{n_{st}} \right)^i \right] + k_v n \quad (B.10)$$

Using the values of the parameters in Table B.1, Eq. B.10 is as given by Eq. (25) of Ref. [24] in terms of the turbine thrust,  $T_a(n)$  computed from BET, constant drag torque of MPB70,  $Q_{MPB}$ , turbine rotational speed (rpm),  $n$  and Stribeck rotational speed (rpm),  $n_{st}$ .

Table B.1: Drivetrain resistance model parameters

Parameter	Value
$X_s$	0.6
$Y_s$	0.5
$F_r$	4.38N
$F_a$	0.0 N
$C_s$	4000 N
$z$	0.0004
$y$	0.55
$d_m$	31 mm
$f_0$	2
$v$	315.6 mm <sup>2</sup> /s
$k_v$	0.0157 Ns/mm

$$Q_R = \left[ 2.15 \left[ 0.0794 + \frac{0.0132 T_a(n)^4}{\sin[3.3 T_a(n)^{0.24}]} \right]^{0.333} + 40.5 \right] \exp \left[ - \left( \frac{n}{n_{st}} \right)^{0.26} \right] \\ + 15.0954n + 0.0134 [3T_a(n) - 0.3801] [0.00053042 + 0.0001163T_a(n)]^{0.55} \quad (B.11) \\ + 0.0967n^{0.67} + 0.5Q_{MPB}$$

Note that Eq. B.10 is strictly for the MPB bearings, however in Eq.B.11, an additional term  $Q_{MPB}$  was included to account for the constant drag of the brake, and parameters  $i$  and  $n_{str}$  used here were values determined from experimental data by [24] using regression analysis.

## Appendix C

# Contribution of the spars to the windmill blade's thrust and torque

Because the BEM program does not consider the effect of the spars from the rotor hub to the root of the blades which constitutes 42% of the windmill rotor radius, a correction is required to compare with experimental results. In this appendix, the thrust and torque contributions of the spars not part of the blade are computed to correct the measured thrust and torque data.

### C.1 Thrust calculation

The thrust force produced by the spars not part of the blade is

$$T_{b'} = \frac{1}{2} \rho U_{b'}^2 A_{b'} \quad (\text{C.1})$$

here,  $U_{b'}$  is the component of the total velocity in the axial direction

$$U_{b'} = U_\infty \left( 1 + \frac{\lambda^2 r^2}{R_s^2} \right)^{1/4} \quad (\text{C.2})$$

$U_{b'}$  is obtained as derived in Chapter 5, neglecting axial, and rotational induction factors.

The area of the spar,  $A_{b'}$ , is defined as

$$A_{b'} = dsR_s \quad (\text{C.3})$$

where  $ds$  is the spar diameter and  $R_s$  is the spar length up to the blade root. Substituting Eq.C.2 and Eq.C.3 into Eq.C.1 the contribution of drag to thrust at radius,  $r$  along the spar

$$dT_{b'} = \frac{1}{2}\rho C_d U_\infty^2 d_s \left(1 + \frac{\lambda^2 r^2}{R_s^2}\right)^{1/2} \quad (\text{C.4})$$

By integrating between the inner radius of spar,  $r_b$  to outer radius of spar  $r_r$ , Eq. C.4 becomes

$$T_{b'} = \frac{1}{2}\rho C_d U_\infty^2 d_s \int_{r_b}^{r_r} \left(1 + \frac{\lambda^2 r^2}{R_s^2}\right)^{1/2} dr \quad (\text{C.5})$$

Eq. C.5 is then given as

$$T_{b'} = \frac{1}{2}\rho C_d U_\infty^2 d_s \left[ \frac{r\lambda \sqrt{\frac{r^2\lambda^2}{R_s^2} + 1} + R_s \sinh^{-1} \left( \frac{r\lambda}{R_s} \right)}{2\lambda} \right]_{r_b}^{r_r} \quad (\text{C.6})$$

## C.2 Torque calculation

Following the same approach for obtaining  $T_{b'}$ , Eq. C.5 is modified for torque, hence

$$Q_{b'} = \frac{1}{2}\rho U_\infty^2 d_s \int_{r_b}^{r_r} \left(1 + \frac{\lambda^2 r^2}{R_s^2}\right)^{1/2} r dr \quad (\text{C.7})$$

on integration Eq.C.7 becomes

$$Q_{b'} = \frac{1}{2}\rho U_\infty^2 d_s \left[ \frac{R_s^2 \left( \frac{r^2\lambda^2}{R_s^2} + 1 \right)^{3/2}}{3\lambda^2} \right]_{r_b}^{r_r} \quad (\text{C.8})$$